



HAL
open science

Study of the micro-discharges / metallic surfaces interactions for a better understanding of the growth mechanisms within the PEO process

Vitalios Ntomproukidis

► **To cite this version:**

Vitalios Ntomproukidis. Study of the micro-discharges / metallic surfaces interactions for a better understanding of the growth mechanisms within the PEO process. Plasma Physics [physics.plasm-ph]. Université de Lorraine, 2020. English. NNT : 2020LORR0077 . tel-02961871

HAL Id: tel-02961871

<https://hal.univ-lorraine.fr/tel-02961871>

Submitted on 8 Oct 2020

HAL is a multi-disciplinary open access archive for the deposit and dissemination of scientific research documents, whether they are published or not. The documents may come from teaching and research institutions in France or abroad, or from public or private research centers.

L'archive ouverte pluridisciplinaire **HAL**, est destinée au dépôt et à la diffusion de documents scientifiques de niveau recherche, publiés ou non, émanant des établissements d'enseignement et de recherche français ou étrangers, des laboratoires publics ou privés.



AVERTISSEMENT

Ce document est le fruit d'un long travail approuvé par le jury de soutenance et mis à disposition de l'ensemble de la communauté universitaire élargie.

Il est soumis à la propriété intellectuelle de l'auteur. Ceci implique une obligation de citation et de référencement lors de l'utilisation de ce document.

D'autre part, toute contrefaçon, plagiat, reproduction illicite encourt une poursuite pénale.

Contact : ddoc-theses-contact@univ-lorraine.fr

LIENS

Code de la Propriété Intellectuelle. articles L 122. 4

Code de la Propriété Intellectuelle. articles L 335.2- L 335.10

http://www.cfcopies.com/V2/leg/leg_droi.php

<http://www.culture.gouv.fr/culture/infos-pratiques/droits/protection.htm>

UNIVERSITE DE LORRAINE**Ecole Doctorale : Chimie – Mécanique – Matériaux - Physique****Institut Jean Lamour****Département Chimie et Physique des Solides et des Surface****THESE**

Soutenue le 15 Juillet 2020

Pour obtenir le grade de Docteur de l'Université de Lorraine

Spécialité : Physique – Physique des plasmas et applications

par

Vitalios NTOMPROUGKIDIS

Etude de l'interaction micro-décharges / surfaces métalliques pour une
meilleure compréhension des mécanismes de croissance lors du procédé PEO

(Titre en anglais)

Study of the micro-discharges / metallic surfaces interactions for a better
understanding of the growth mechanisms within the PEO process

Jury

Rapporteurs	ARURAUULT Laurent	Professeur, CIRIMAT, Université de Toulouse
	LAVISSE Luc	Maître de conférences, ICB, Université de Bourgogne
Examineurs	CHAMPEAUX Corinne	Professeure, IRCER, Université de Limoges
	BESLAND Marie-Paule	Directrice de recherche, IMN, Université de Nantes
	VEYS-RENAUX Delphine	Maître de conférences, IJL, Université de Lorraine
Directeur de thèse	HENRION Gérard	Directeur de recherche, IJL, Université de Lorraine
Co-directeur	MARTIN Julien	Maître de conférences, IJL, Université de Lorraine

Acknowledgements

First of all, I would like to express my sincere gratitude to my supervisor, Gérard Henrion, for accepting me in this project, for putting his trust and belief in my capability to carry out this research. I am grateful for his guidance, mentorship and support during these three years, from which I have learned a lot. One could not ask for a better supervisor. Thank you very much.

I would also like to thank my co-supervisor, Julien Martin, with whom we had an excellent collaboration conducting all the experiments of this work. For his guidance and tutoring on experimental procedures, for all our discussions analysing our results and all the advices he provided on multiple occasions.

A very special thanks to Alexandre Nominé for all the work we have done together, particularly for the discussions we had and his scientific advices and help. It was a real pleasure to share an office in a very friendly and enjoying environment both professionally and personally.

I would like to acknowledge the members of the CC3M competence cluster for their contributions in this work. I am thankful to Sandrine Mathieu and Christine Gendarme for their tutoring and their advices on the SEM microscope, to Stéphanie Bruyère and Sylvie Migot for their contributions with the TEM analysis, Erwan Etienne for his help in metallurgical post-treatments. For their help and advices on XRD measurements and analysis, I would like also to thank Pascal Boulet and Sebastien Diliberto from the x-gamma competence cluster. I would like to thank Ilya Bardin from MISIS university of Moscow, with whom I had the pleasure to work in person, discuss and learn from.

A great amount of this work involved people from within the Institute Jean Lamour as well as outside the laboratory. I would like to thank Pauline Haraux, Komlan Akoda, Alexandre Bastien, Pascal Brenot, Guillaume Ezo'o, A. Maizeray, O. Ferry and Julien Jourdan for their contributions in this thesis. Charles Roux-Pertus for his help in thickness and porosity calculations.

I would very much like to thank all the colleagues of the laboratory for their help, each one in their own way. Vincent Guigoz, Stephane Cuyenet, Thierry Czerwec, Mohammed Belmahi, Maïke Thal for their input in my work with occasional discussions to resolve some of the problematics concerning this research. A great thanks to Cédric Noël for his tutoring, support and constant availability on spectroscopic measurements and analysis methods and to Régis Reigner for his technical support.

I would like to express my appreciation to Christine Sartori, Georges Billant, Martine Tailleur, Nathalie Niclas, Valerie Frank and Anne-Marie Airault for their help in administrative procedures.

Acknowledgements

These three years would have not been the same without the friends I met and from whom I received a warm welcome in and outside the laboratory. Fahad, Joseph, Christophe, Alejandro, Claudia at first and later on Alexis, Marianna, Ferial, Agathe, Shantanu. Thank you guys for all the wonderful moments we have spent. I would like also to thank the Greek community of Nancy, Katerina Cael, Ortho Salomon, Alexandros Petrelis, for their help and support from the very moment of my arrival to Nancy.

I am grateful to LabEx DAMAS (Laboratoire d' Excellence Design of Alloy Metals for low-mAs Structures) for financing this doctoral scholarship.

Finally, I would like to thank my family in Greece, my brother and particularly my parents. Their constant support, encouragement, love and care was invaluable during all this period.

Table of Contents

General Introduction	1
Chapter I - State of the art	5
I.1 Introduction	5
I.2 Plasma Electrolytic Oxidation.....	5
I.2.1 Historical development of PEO.....	5
I.2.2 Processing principle	6
I.2.3 Supplying modes	7
I.2.4 Influence of PEO processing parameters	8
I.2.4a Effect of the electrolyte	9
I.2.4b Influence of the electrical parameters	12
I.3 “Soft” regime	14
I.4 Properties of micro-discharges.....	16
I.4.1 Spatial characteristics	17
I.4.2 Temporal characteristics	17
I.4.3 Physical properties of the micro-discharges.....	19
I.5 Structural properties of PEO oxide coatings	21
I.6 Growth mechanisms	24
I.7 Conclusions of Chapter I.....	26
Chapter II - Experimental considerations	29
II.1 Introduction of the chapter II	29
II.2 Experimental installation	29
II.2.1 The electrical generator.....	29
II.2.2 The electrolytic cell.....	31
II.2.3 The electrodes	32
II.3 <i>In situ</i> diagnostic of the PEO process	33
II.3.1 Electrical time-response.....	33
II.3.2 Optical characterisation	34

Table of Contents

II.3.2a Photomultiplier	34
II.3.2b Optical emission spectroscopy (OES)	35
II.3.2c Fast video imaging	36
II.4 <i>Ex situ</i> characterisation of the PEO coatings	37
II.4.1 Scanning electron microscopy (SEM) and EDX measurements.....	37
II.4.2 X-ray Diffraction (XRD) and grazing incidence X-ray diffraction (GIXRD).....	37
II.4.3 Transmission Electron Microscopy (TEM) and Scanning (STEM)	38
Chapter III - Sequential run of the PEO process.....	39
III.1 Introduction of the chapter III	39
III.2 Specific experimental procedure	39
III.2.1 Material and electrolyte.....	39
III.2.2 Variation of the electrical conditions	39
III.2.3 <i>In situ</i> diagnostic of the PEO process.....	40
III.2.4 <i>Ex-situ</i> characterization of the PEO coatings	41
III.3 Results on the in-situ diagnostic of the PEO process	41
III.3.1 Establishment of the “soft” regime.....	41
III.3.2 Delay in the micro-discharges appearance	43
III.3.3 Time constant of the anodic voltage-time response	46
III.3.4 Properties of the micro-discharges	48
III.4 Results on the ex-situ characterization of the PEO coatings	50
III.4.1 Morphology of the PEO coatings	50
III.4.2 Crystallographic phases in PEO coatings	52
III.4.3 Element distribution in PEO coatings	53
III.5 Discussion of the results	55
III.5.1 Discussion about a mechanism of charge accumulation	55
III.5.2 Discussion about coatings improvement using sequenced PEO treatments.....	59
III.5.3 Discussion about energy efficiency using sequential PEO treatments	60
III.6 Conclusions of Chapter III	61
Chapter IV - Understanding the “soft” regime.....	63

IV.1 Introduction of the chapter IV	63
IV.2 Specific experimental conditions	63
IV.2.1 Materials and electrolytes	63
IV.2.2 PEO processing conditions	64
IV.2.3 <i>In situ</i> characterisation of the PEO process.....	64
IV.2.4 <i>Ex situ</i> characterisation of the PEO coatings	65
IV.3 Effect of the electrolyte on the PEO process.....	65
IV.3.1 Effect of the electrolyte on the voltage-time response	66
IV.3.2 Effect of the electrolyte on the PEO coatings	68
IV.4 Specific effect of the aluminium alloy on the PEO process in “soft” regime	70
IV.4.1 Fast video imaging	70
IV.4.2 <i>In situ</i> characterisation by optical emission spectroscopy.....	71
IV.4.2a Presence of broad emission continuum.....	72
IV.4.2b Electron (T_e), rotational (T_{rot}) and gas (T_{gas}) temperatures.....	75
IV.4.2c Electron density T_e	78
IV.5 Ex-situ characterisation of the PEO coatings	83
IV.5.1 X-ray diffraction measurements.....	83
IV.5.2 Morphology and elemental composition of the PEO coatings	84
IV.6 Interaction of MDs with the surrounding environment.....	88
IV.6 Phenomenological interpretation.....	93
IV.7 Conclusions of Chapter IV	97
Chapter V - Formation of PEO coatings in the “soft” regime conditions	99
V.1 Introduction of the chapter V.....	99
V.2 Specific experimental conditions.....	100
V.2.1 Elaboration of specific samples in the PEO “soft” regime conditions.....	100
V.2.2 <i>Ex situ</i> characterisation of the PEO coatings.....	101
V.2.3 <i>In situ</i> characterisation of the PEO process.....	101
V.3 Results on the <i>ex situ</i> characterisation of the PEO coatings	102
V.3.1 Characterisation at the micrometre scale.....	102

Table of Contents

V.3.2 Characterisation at the sub-micrometre scale	105
V.4 Results on the <i>in situ</i> characterisation of the PEO process	110
V.4.1 Estimation of the electron temperature in the plasma of the micro-discharges	110
V.4.2 Estimation of the rotational temperature in the plasma of the micro-discharges.....	112
V.5 Discussion.....	113
V.5.1 Estimation of the heating rate (HR).....	114
V.5.2 Estimation of the crystallisation temperature (T_c)	115
V.5.3 Estimation of the cooling rate (CR).....	117
V.5.4 Mechanism of melting and metastable solidification route	117
V.6 Conclusions of Chapter V.....	120
Chapter VI - New opportunities for the Plasma Electrolytic Oxidation process.....	121
VI.1 Introduction of the chapter VI.....	121
VI.2 Formation of metallic oxide particles using the PEO process.....	121
VI.2.1 Introduction	121
VI.2.2 Specific experimental conditions	122
VI.2.3 Results and discussion.....	124
VI.2.3a Morphology of the particles	124
VI.2.2b Chemical composition of the particles.....	126
VI.2.2c Crystallographic phases of the particles.....	128
VI.2.2d Discussion about the formation mechanism of the particles.....	131
VI.2.4 Intermediate conclusion	134
VI.3 Duplex surface treatment using cold-spray and PEO processes.....	135
VI.3.1 Introduction	135
VI.3.2 Specific experimental conditions	136
VI.3.2a Metallic substrates.....	136
VI.3.2b Cold-spray processing conditions	137
VI.3.2c PEO processing conditions.....	138
VI.3.2.d Ex-situ characterization of the coatings.....	139
VI.3.3 Results and discussion.....	139

VI.3.3a Establishment of the “soft” sparking regime.....	139
VI.3.3b Morphology and growth kinetic of the coatings	140
VI.3.3c Chemical and crystallographic compositions of the duplex coatings	143
VI.3.3d Discussion about the growth mechanism of the duplex coatings.....	148
VI.3.4 Intermediate conclusion	152
VI.4 Conclusions of Chapter VI.....	153
General conclusions	155
Bibliography	159

General Introduction

Lightweight structures have always been of a particular interest to the manufacturing industry, especially in the domains of aeronautic and automotive. Nowadays, more than ever, the need of reduction in weight, and consequently, in fuel consumption and exhaust emissions, imposes the implementation of lightweight metallic alloys, such as the aluminium, titanium and magnesium. When exposed to atmospheric conditions, specifically in contact with oxygen, these materials form a thin oxide layer that protects themselves against corrosion. In their pure form, they exhibit relatively good anti-corrosion properties. However, in order to improve the mechanical properties, alloying elements are usually added to these light-weight metals which in turn degrade their corrosion resistance. Indeed, the incorporation of these alloying elements into the aluminium matrix creates defects which act as nucleation centres for corrosion. Thus, with the aim to combine good mechanical properties in bulk as well as good corrosion resistance at the surface, surface treatments are usually applied in order to produce protective coatings on aluminium, magnesium and titanium alloys.

For decades, anodising processes (mild or hard anodising) have been used to grow protective oxide ceramic coatings on Al, Mg and Ti based alloys. This leads to significant improvement of corrosion resistance, but limited changes of mechanical properties. In addition, conventional anodising technologies face serious environmental and health issues since, in some cases, they involve the use of hazardous carcinogenic, mutagenic and reprotoxic (CMR) compounds (acids, borates, heavy metals and hexavalent chromium), which are forbidden in EU [1,2]. Although surface treatments in gas phase, such as physical vapour deposition (PVD) and chemical vapour deposition (CVD), could overcome this problem, their application is limited in small scales and cannot satisfy the needs of the industry in processing large surfaces. Thus the need for an alternative process in accordance with the European regulations and the requirements of the modern industry is required.

A solution to the aforementioned issues can be provided by the plasma electrolytic oxidation (PEO). PEO is a surface engineering process suitable for lightweight metals (Al, Mg, Ti) and their alloys to form protective ceramic coatings [3]. It is historically related to anodising as it shares similarities in experimental installations, such as the liquid processing environment (electrolyte) and the application of electrical potential between two electrodes, one of which is the treated element. However, major differences separate conventional anodising and the PEO process. Firstly, PEO processing is run in diluted alkaline electrolytes free of toxic substances and CMR compounds, that meets the recent EU regulations concerning health and environment. Secondly, PEO operates in much higher voltage and current density (hundreds of volts and tens of $\text{A}\cdot\text{dm}^{-2}$, respectively) than anodising,

General Introduction

allowing a higher growth rate ($\sim 100 \mu\text{m}\cdot\text{h}^{-1}$) of the final coatings in the range of hundreds of micrometres. Moreover, the application of high voltage leads to dielectric breakdown phenomena of the growing oxide layer and the appearance of micro-discharges (MDs) over the processed surface, which promote the coating growth. Hence, the oxide growth takes place in highly non-equilibrium plasma conditions.

From the resulting coating point of view, the oxide layers produced by PEO exhibit superior thickness, hardness and better adhesion to the substrate. Moreover, the well crystallised oxide phase offers improved thermal, wear and corrosion resistance [4–8].

However, and contrary to conventional anodising processes, one of the drawbacks of PEO is still the limited knowledge of the fundamental mechanisms that govern the process. Despite the fact that discharge phenomena have been first observed more than a century ago by Sluginov, they were systematically studied during the 1960s and 1970s mainly by research teams in the former USSR [3]. In the recent years, the interest in PEO processing has been constantly increasing and great effort has been done to understand and provide a descriptive model of the growing mechanism. However, its wider industrial application is still restricted due to high energy consumption and lack of understanding of the interrelationship between processing conditions, discharge characteristics and resulting coating microstructure.

This thesis aims to contribute to a better understanding of the physico-chemical reactions and the growth mechanisms that govern the process. To achieve this, the adopted experimental approaches consisted mainly in studying the behaviour and properties of micro-discharges with respect to the applied electrical parameters in order to correlate them with the resulting oxide coatings and provide a descriptive model of the process. This thesis is organised in six chapters as follows:

In chapter I, a short review of the plasma electrolytic oxidation process is presented. After a brief presentation of the history and evolution of the PEO process, the main features and principles are described to facilitate the comprehension of the following chapters. The progress in the field of PEO is presented through recent work of international research groups, regarding various physical properties of the micro-discharges (spatial, temporal) and the associated resulting oxide layers (microstructure).

Chapter II briefly describes all the technical details related to this work, including the processed materials, the experimental installation, as well as the characterisation techniques used.

Chapter III focuses on both the behaviour of micro-discharges and the morphology of the produced PEO coatings with the sudden change of the applied electrical parameters. Switching from one

condition to another in the course of treatments, reveal particular and interesting behaviour of MDs in terms of size, distribution and their appearance. These results are correlated with the grown oxide layers. A synergetic effect is observed under certain combinations which is beneficial to the growing oxide in terms of total thickness and microstructure. Lastly, the specific energy consumption of these sequential treatments is considered and compared to their single-sequenced counterparts.

In chapter IV a comparative study of the process between two different alloys and under different types of electrolyte composition is presented at first. The results clearly show the effect of the electrolyte composition and concentration on the distribution of the micro-discharges over the processed surface, and consequently on the resulting oxide coating, as well as the anodic voltage. The results also show that the light emission during a particular “soft” regime is also affected by the processed substrate. To understand this, further studies were conducted by means of optical emission spectroscopy and high speed video recording. Observations of the interactions between the micro-discharges and gas bubbles located at the vicinity of the processed surface indicate that the source of light emission during “soft” regime is localised deep in the inner parts of the growing oxide layer.

Chapter V is focused on the structural study of the particular “pancake” morphology which appears during “soft” regime. The PEO coatings were investigated mainly at the sub-micrometre scale revealing a peculiar nanometre sized lamellar arrangement, consisting of Al_2O_3 lamellae alternating periodically with metastable 1:1 mullite lamellae. Along with results from optical emission spectroscopy during the transition to “soft” regime and based on the phase diagram for the Al_2O_3 - SiO_2 binary system, a growth mechanism is proposed which explains the formation of this particular arrangement.

The final chapter VI focuses on potential new opportunities for the PEO process. The chapter is divided into two parts. The first part describes the feasibility of producing metal oxide particles during PEO treatment. The second part investigates the possibility to elaborate protective coatings on materials that are difficult or even impossible to produce (e.g. magnesium and steel, respectively). This is done by implementing a duplex treatment which involves a first treatment by the cold-spray technique followed by a second one by plasma electrolytic oxidation.

Finally, a general conclusion summarising the main results and perspectives of this work is given.

Chapter I - State of the art

I.1 Introduction

Almost in every application of lightweight materials, such as aluminium, magnesium and titanium, surface treatment is necessary to modify its properties in accordance with the specific needs of their use. This is particularly evident in the aerospace industry, where the parts of the aircraft are exposed to extreme conditions. As stated previously, to this day this modification is mainly performed by anodising processes, which, besides the restrictions imposed by the EU, has reach also some technical limits, such as low growth rate and overall coating thickness.

Plasma electrolytic oxidation, although similar in some basic experimental principles to the anodising, exhibits many differences in growing mechanisms, kinetics, as well as the microstructure of the resulting oxide layers. Despite the fact that plasma electrolytic oxidation is known for more than a century, it remains still not completely understood and thus, not yet implemented in large scale industrial applications. Despite the fact that in the past decades great progress has been achieved and various models have been proposed, the relationship between the processing conditions, the discharge characteristics and the microstructure of the resulting oxide layer are still not clear.

The objective of the following chapter is to provide an overview of the recent achievements in the PEO process. After a brief presentation of the historical development of PEO, followed by the description of basic principles regarding the processing conditions, a particular attention will be paid to the so called “soft” regime. Description of both the physical properties of the micro-discharges and the microstructural characteristics of the elaborated coatings under different conditions will be given. Finally, some of the proposed growth mechanisms in the literature will be described.

I.2 Plasma Electrolytic Oxidation

I.2.1 Historical development of PEO

The first observation of luminescent phenomena that are associated with electrolysis were observed in 1880 by N. Sluginov [3]. However, it took almost another 50 years until Günterschultze and Betz studied the phenomenon in detail and observed sparking on the anode by anodising in high voltage [9] and called the process as “*anodic spark deposition*”. The next stage of research in this direction came in the 1960s when W. McNeil and L. Gruss deposited cadmium niobate ($\text{Cd}_2\text{Nb}_2\text{O}_7$) on cadmium substrate [3,10] and opened new opportunities to synthesize complex oxide coatings

from components of substrate and electrolyte. From 1970s research has been conducted by many groups from USSR [11], Germany [12], England [13] and USA [14]. However, the research was mainly focused on optimising parameters to improve the resulting coatings and their structural properties. Since the 1990s and with the wide spread of the researches conducted internationally, PEO attracted much attention and the number of works in this field increased, particularly focused to the understanding of the growth mechanisms. A tenfold increase in the number of publications is noted between 2000 and 2019¹.

Many terminologies are used to name this surface treatment technology: “anodic spark deposition” [14], “micro-arc discharge oxidation (MDO)” [15], “anodic oxidation by spark discharge (ANOF)” [12], “micro-arc oxidation” [4,16,17] and “plasma electrolytic oxidation (PEO)” [18–22], the latter being most broadly used.

I.2.2 Processing principle

As mentioned previously, PEO shares similarities with anodising technologies. From a technical point of view, it involves two electrodes, *i.e.* a working electrode that faces one or more counter-electrodes, an electrolytic cell in which the electrodes are immersed and a power supply. A cooling system is also integrated to the electrochemical cell in order to keep the temperature constant and to ensure homogeneity of the electrolyte.

As depicted in Fig. I-1, four typical stages can be identified during plasma electrolytic oxidation process [23]. When processing in galvanostatic mode, current is applied between the electrodes. At the beginning, the potential gradually increases and an initial insulating thin oxide layer is formed at the metal surface, commonly called “barrier layer”. This is associated with the release of gaseous oxygen at the anode. When the potential reaches the dielectric breakdown voltage of the oxide, the stage II starts with the ignition of numerous tiny micro-discharges that move rapidly over the whole processed surface. Additionally, Fig.I-2 illustrates the physical appearance of the micro-discharges at different processing stages. This second stage is also characterised by a sharp drop of the voltage slope. As the process continues, the slope of the voltage decreases even more (stage III) due to gradual thickening of the oxide layer and the increase in its impedance. The micro-discharges become larger in size and more persistent at same locations. Stage IV is characterised by even smaller variation of the voltage and intensification of the micro-discharges which decrease in number, but become even larger and long lasting.

¹ Data based on search in Science Direct containing the terms “Plasma electrolytic oxidation” and “Micro-arc oxidation”

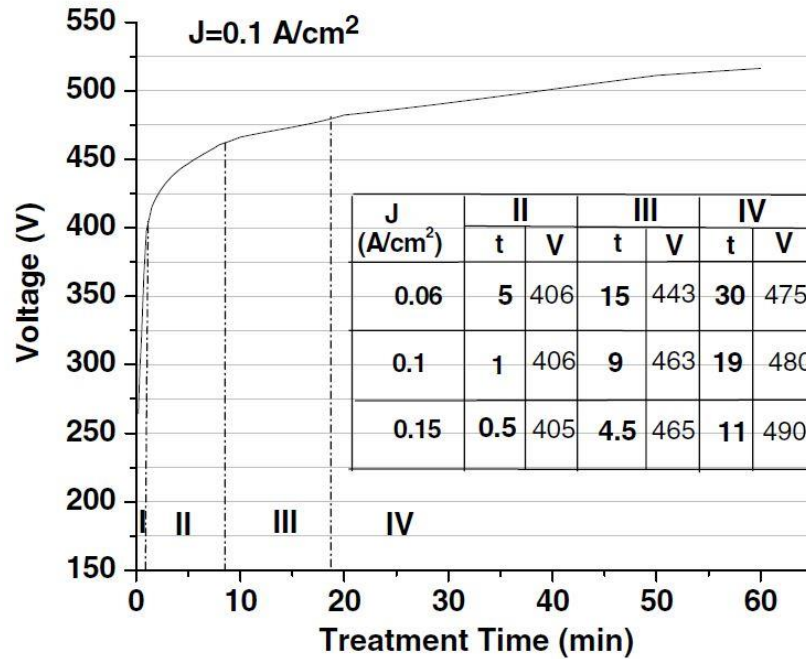


Figure I- 1. Voltage evolution with processing time for $J = 0.1 \text{ A}\cdot\text{cm}^{-2}$. The inset depicts the beginning time (min) and voltage (V) of each stage for different current densities. [23]

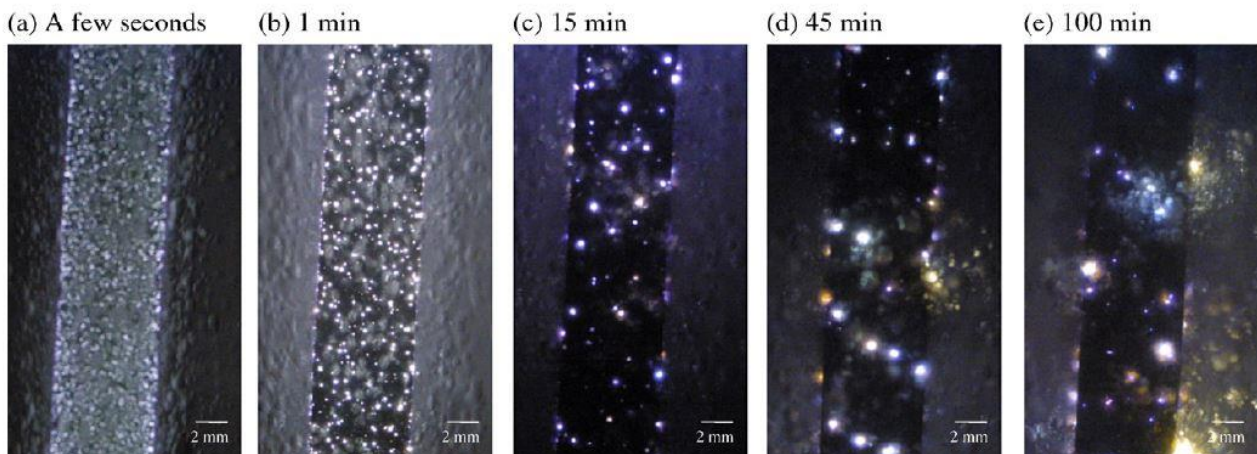


Figure I- 2. Evolution of visual aspect of micro-discharges with PEO processing time [19].

I.2.3 Supplying modes

Generally, PEO can be conducted under either potentiostatic [10,14] or galvanostatic [13,24] mode. Within the potentiostatic supplying mode, an overall voltage is applied to the electrolyser system while the current is controlled within the galvanostatic mode. By using a potentiostatic mode, S. D. Brown *et al.* [14] showed that under constant voltage, as the coating thickness increases, and hence its electrical resistance, the current gradually decays, leading to quenching of the discharges and termination of the process (shown in Fig. I-3). Thus, to ensure continuation of the oxide growth under a spark regime, a constant increase of voltage is needed [10]. However, this can be avoided by

using a galvanostatic supplying mode where the voltage is continuously adjusted to maintain the desired current value.

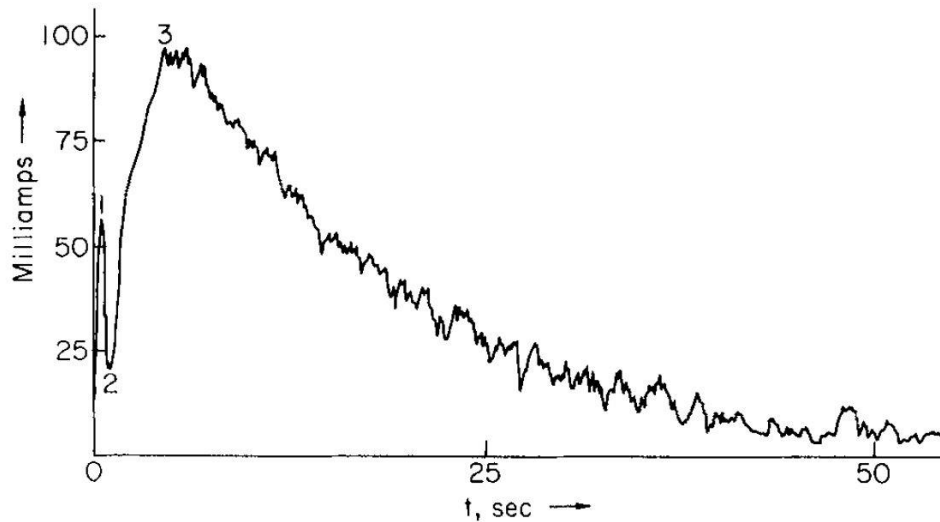


Figure I- 3. Current variation under potentiostatic supplying mode where a constant voltage is applied during the process [14].

PEO process within DC mode was firstly proposed but it presents the major drawback to promote the appearance of strong micro-discharges that lead to highly porous coatings with poor end-use properties. [3,25]. This issue was partially solved with the use of pulsed DC supplies, which allow the control over the heat conditions during the treatment, thus, changing the coating composition and structure. However, this can lead to additional surface polarisation by the electrical double layer created at the solid/liquid interface [3]. To overcome this problem, AC power supplies can be employed. It has been shown that treatment in alternating mode offers better processing conditions which are more beneficial and lead to improvement of the coating microstructure [26]. In the recent years, pulsed bipolar current mode is preferred, as it offers the flexibility to control the pulse waveforms by adjusting their amplitudes and durations [3].

I.2.4 Influence of PEO processing parameters

The processing parameters of the PEO process have a significant effect on the discharge phenomena and, consequently, on the resulting oxide layers. Indeed, besides the supplying modes described previously, crucial other parameters such as the nature of electrolyte and the electrical conditions play an important role in the PEO process [19,27–34].

The geometry of the PEO electrochemical cell, more specifically, the distance between the working electrode and the counter-electrode has also been found to have an influence on the elaborated coatings [35,36]. Melhem *et al.* [35] showed that, within given electrical conditions, the total thickness and density of the coating can be increased by the proper adjustment of the distance between the electrodes (Fig. I-4). They found that considerable improvement can be achieved within “soft” sparking (as will be described later) conditions (compact symbols in Fig. I-4). However, by applying intense “arcing” conditions, the resulting coatings seems to be unaffected by the distance of the electrodes (open symbols in Fig. I-4). Additionally, investigation of the geometry of the system by implementing rectangular processed sample, faced by two counter-electrodes opposite both surfaces, they illustrated an inhomogeneity of discharge distribution during the process which leads to higher growth at the edges compared to the centre of the sample.

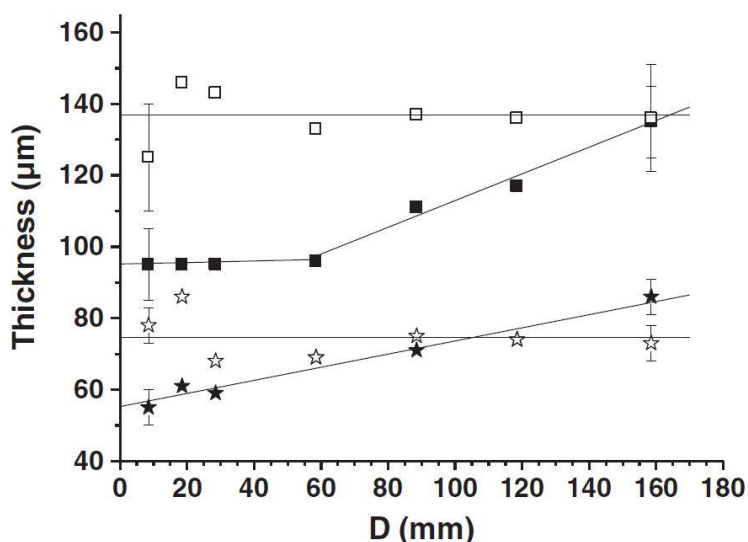


Figure I- 4. Coating thickness variation with inter-electrode distance for two different electrical conditions (open and compact symbols). Squares represent the total thickness, while stars correspond to the dense layer. [35]

I.2.4a Effect of the electrolyte

Among many parameters, the proper choice of the electrolyte is of great importance for the PEO process, as a careful matching is necessary between the metal and the electrolyte. A large variety of electrolytes can be used in PEO, from alkaline electrolyte containing mainly species such as potassium hydroxide (KOH) and sodium silicate (Na_2SiO_3) [5,19,29,30,37–39] to acidic electrolytes, such as phosphoric and citric acids, particularly used for the PEO processing of Ti and Zr [40–42]. The composition of the electrolyte affects the total thickness as well as the surface morphology and microstructure of the coatings [43–46]. Kai Wang *et al.* [44] showed that treatment in aluminate

electrolyte results in smoother surface, while the addition of silicate leads to an increased surface roughness. Moreover, the addition of sodium hexafluorosilicate (Na_2SiF_6) in the solution in both cases significantly enhanced the thickness and the microhardness of the coatings.

Additives in electrolytic solutions are common practice to incorporate elements into the coating for surface modifications, improved performance or new properties for biomedical use [47–53]. One of the main purposes of particle addition, especially in PEO of magnesium is sealing and waterproofing. Chen *et al.* [54] incorporated PTFE particles in coatings formed on Mg alloy and showed that the resulting layers exhibited high sealing degree and ultra-low friction coefficient. Similar results were demonstrated by Mohedano *et al.* [55] and Mashtalyar *et al.* [56] who added CeO_2 and TiN particles in the electrolyte, respectively. Duan *et al.* [49] performed PEO treatments on magnesium substrates adding phosphate, fluoride or borate in typical alkaline electrolytes and demonstrated their effect in enhancing the corrosion protection of magnesium against corrosive artificial seawater (3.5% NaCl). Figure I-5 the morphological changes induced to the resulting coating made on magnesium substrate by the addition of TiN particles in various concentrations.

Furthermore, reactive incorporation of particles can lead to the formation of new phases in the coating resulting to composite-like structures [57]. Other fields of interest lie in the enhancement of the photocatalytic properties of the surface [52], surface coloration [53], dental and orthopaedic implants [58].

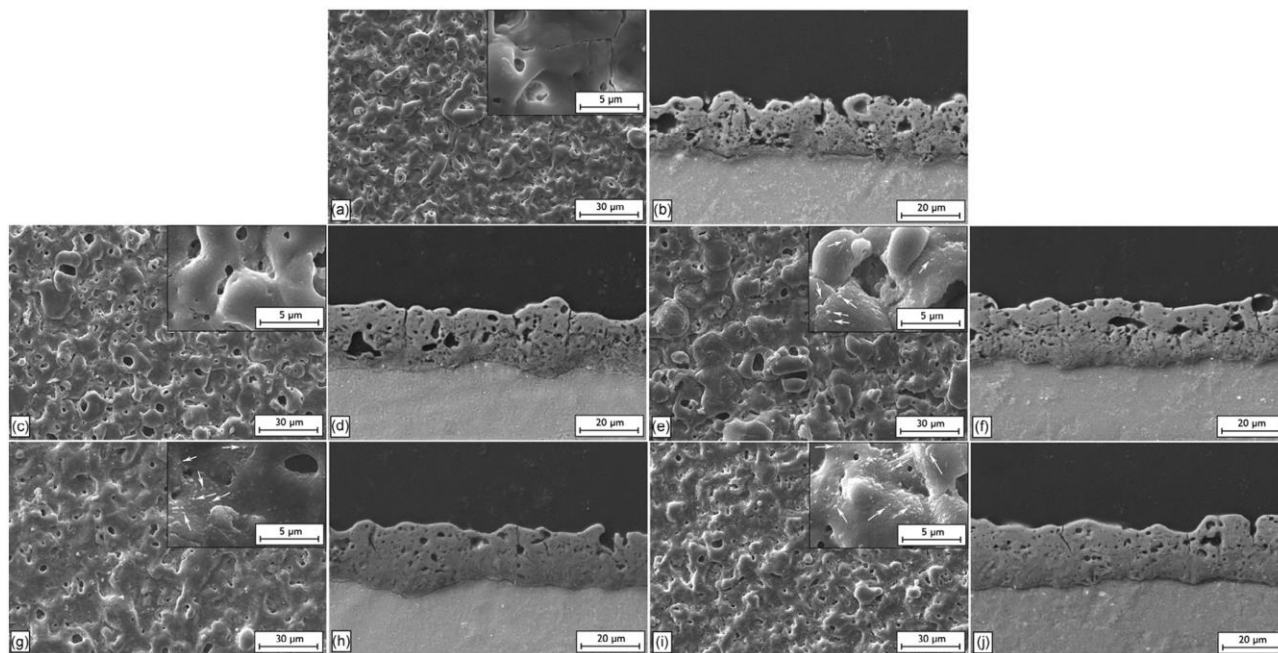


Figure I- 5. SEM surface and cross-section images of coating obtained without (a, b) and with addition of TiN nanoparticles in the electrolyte for concentrations of $1 \text{ g}\cdot\text{L}^{-1}$ (c, d), $2 \text{ g}\cdot\text{L}^{-1}$ (e, f), $3 \text{ g}\cdot\text{L}^{-1}$ (g, h), $4 \text{ g}\cdot\text{L}^{-1}$ (i, j). [56]

The concentration of a given electrolyte can also influence both the growth rate of the oxide layer and its mechanical properties. As shown by A. A. Voevodin *et al.* [4], the increase in concentration of Na_2SiO_3 leads to the enhancement of the overall thickness, but decrease of the hardness, due to the formation of larger amounts of alumina-silicate phase (Table I-1). On the other hand, Khan *et al.* [43] illustrated that higher concentration of potassium hydroxide leads to coating dissolution at the surface and, hence, lower growth rate (Fig. I-6).

Table I- 1. Al-O-Si stoichiometry, ratio of Si/Al content, ratio of alumina and aluminasilicate phases, and Vickers hardness of the PEO coatings produced at different concentrations of sodium silicate in the electrolyte. Table reproduced from [4].

Na_2SiO_3 concentration ($\text{g}\cdot\text{L}^{-1}$)	Al-Si-O stoichiometry	Si/Al ratio	Ratio of Al_2O_3 and Al-Si-O phases	Vickers hardness (GPa)
2	$\text{Al}_{0.26}\text{Si}_{0.08}\text{O}_{0.66}$	0.3	1.0	17 ± 2.5
4	$\text{Al}_{0.23}\text{Si}_{0.10}\text{O}_{0.67}$	0.4	0.6	14 ± 2.5
6	$\text{Al}_{0.22}\text{Si}_{0.12}\text{O}_{0.67}$	0.5	0.4	11 ± 2.0
10	$\text{Al}_{0.20}\text{Si}_{0.14}\text{O}_{0.65}$	0.7	0.2	12 ± 2.0
20	$\text{Al}_{0.13}\text{Si}_{0.19}\text{O}_{0.68}$	1.5	0.1	6 ± 1.5

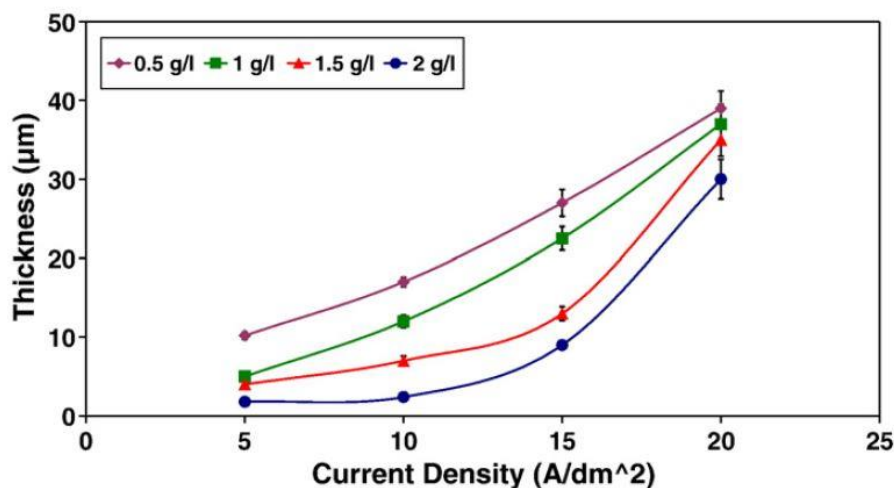


Figure I- 6. Thickness dependence on current density and KOH concentration in DC PEO treatments of 6082 aluminium alloy. [43]

Another factor to account for is the ageing of the electrolyte, as it has been demonstrated by Martin *et al.* [28]. They have shown that ageing of the electrolyte occurs approximately after 2-3 hours of processing, leading to depletion of ionic species in the electrolyte and decrease of its electrical

conductivity, which in turn affects the characteristics of micro-discharges and consequently the forming oxide layer.

I.2.4b Influence of the electrical parameters

As mentioned in the previous section, it has been established that the use of pulsed bipolar current (PBC) to supply the electrodes results in a better control of the PEO process, resulting in a higher quality of the coatings in terms of thickness and compactness [20,31,59]. According to Snizhko *et al.* [32] and Khan *et al.* [43] the thickness of the coating is increasing with current density. Moreover, in the case of aluminium processing, the increased current density can lead to higher local temperatures and induce transformation to the stable α -alumina phase, which exhibits superior hardness.

In AC or pulsed mode processes, a typical parameter that can be adjusted is also the pulse frequency. Various studies have been conducted on the effect of the input frequency on PEO processing and the resulting coatings [20,34,60,61]. By performing PEO treatments on magnesium samples in pulsed DC mode, Lv *et al.* [34] and Srinivasan *et al.* [60] illustrated that the increase in frequency leads to reduction of the surface roughness and improvement of the coating microstructure. However, within low frequencies, the longer pulse duration increases the lifetime of the micro-discharges, leading to higher temperatures which provide better sintering conditions for formation of phases that are not observed in high frequencies. On the other hand, these long lasting micro-discharges are usually detrimental for the coating since they tend to generate large pores throughout the oxide coating. Additionally, they supported that in these conditions, the growth rate is rather increased compared to higher frequencies. Similar result were observed by Zhang *et al.* [61] on titanium oxide coatings prepared by PEO in DC pulsed mode.

On the other hand, in processes involving aluminium as treated material, Martin *et al.* [20] investigating the frequency influence within the range of 100 – 900 Hz, showed that the growth rate increases with frequency. Figure I-7 illustrates the effect of the pulse frequency and the current density on the microstructure of the oxide layers at two different locations, the centre and the edge of the sample. Moreover, as can be seen from Fig. I-8, the surface roughness decreases with frequency and increases with current density. This is typically more pronounced at the edges of the sample.

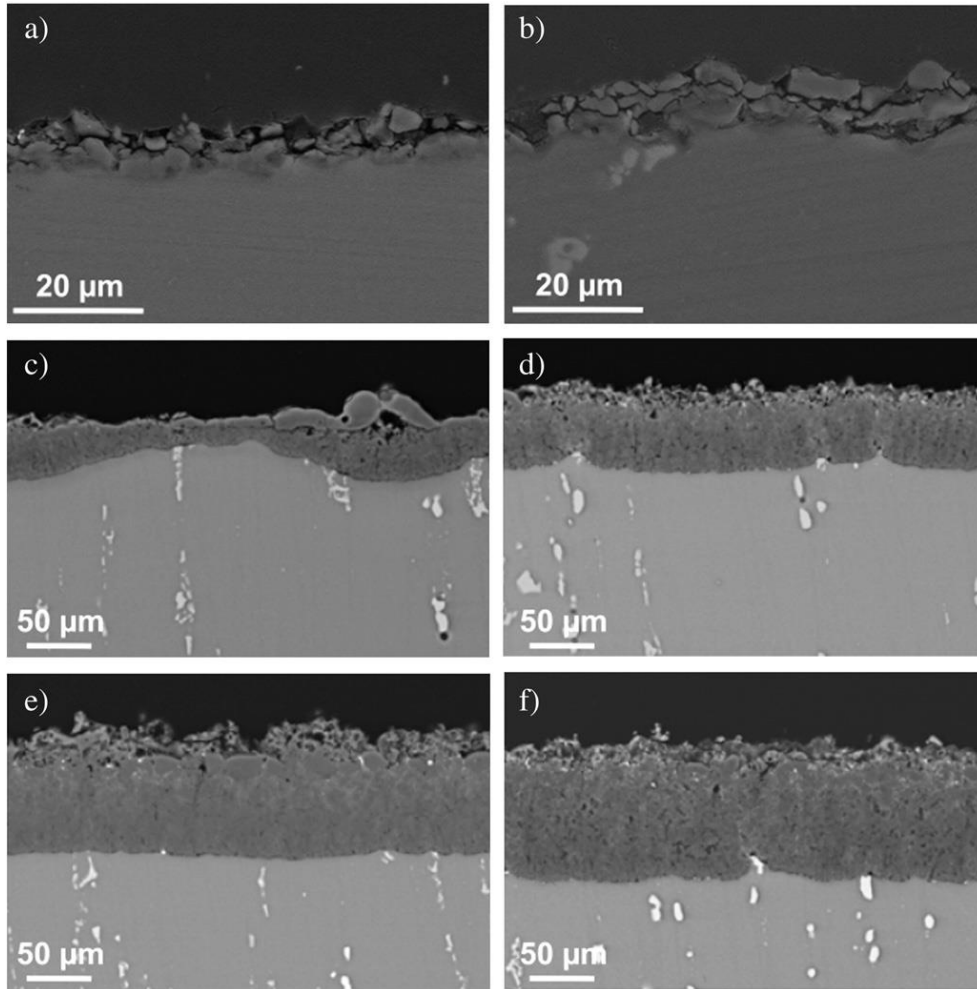


Figure I- 7. Cross-section micrographs of aluminium oxide coatings elaborated in various processing conditions: a), b) with $j = 12.5 \text{ A.dm}^2$, $f = 100 \text{ Hz}$, $t = 100 \text{ min}$, at the centre and edge of the sample respectively, c), d) with $J_p = 75.5 \text{ A.dm}^2$, $f = 100 \text{ Hz}$, $t = 40 \text{ min}$, at the centre and edge of the sample respectively and e), f) with $j = 75.5 \text{ A.dm}^2$, $f = 900 \text{ Hz}$, $t = 40 \text{ min}$, at the centre and edge of the sample respectively. [20]

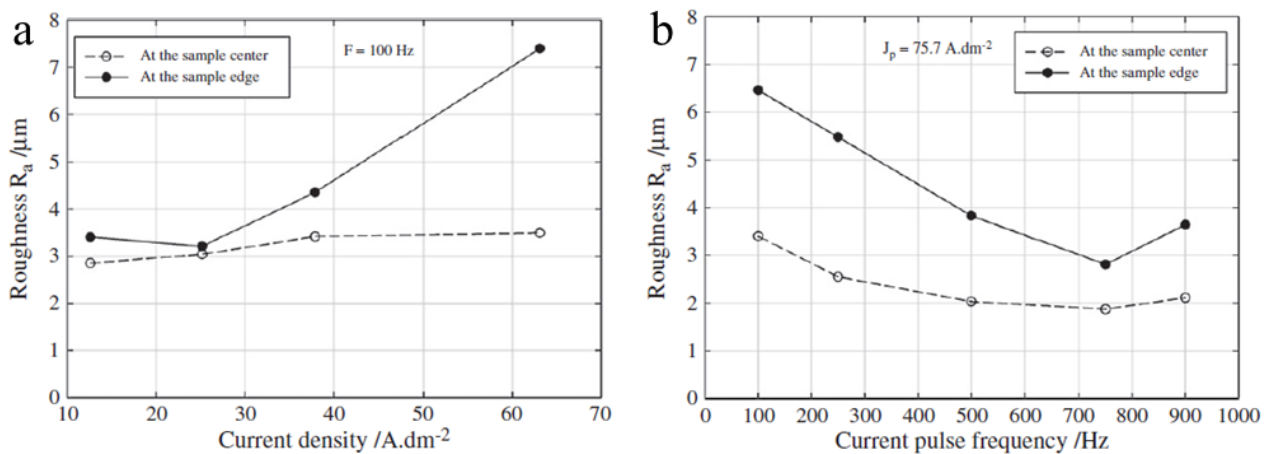


Figure I- 8. Dependence of the roughness of the oxide layer at the centre and the edge of PEO processed samples on a) the current density J_p (for samples processed at $f = 100 \text{ Hz}$ for $t = 70 \text{ min}$ and b) the current pulse frequency f (for samples processed with $J_p = 75.5 \text{ A.dm}^2$ for $t = 40 \text{ min}$). [20]

However, it is worth mentioning that these results were obtained under pulsed bipolar current mode (PBC), in which the negative (cathodic) pulse plays a significant role in the process development. Rogov *et al.* [62] highlighted the role of the cathodic current in PEO by associating its effect on the electrical double layer (EDL) formed at the oxide-electrolyte interface. By considering the process in terms of potential barriers in the metal-oxide (active zone) and the oxide-electrolyte interfaces, they suggested that the cathodic polarisation could decrease the EDL potential barrier through local acidification of the surface. According to Lukes *et al.* [63], the potential barrier of the EDL strongly depends on the pH of the electrolyte with respect to the isoelectric point of the surface. This can lead to promotion of discharges during either anodic or cathodic polarisation. More recently, investigation of Nominé *et al.* [33] in pulsed bipolar mode showed that cathodic discharges can be induced, alongside with the anodic ones, at high frequencies. The nature of these MDs was put in question, as no delamination effect was observed (which is typical of cathodic MDs). However, a potential contribution to the growth rate or facilitation of energy transfer to promote high temperature phases was assumed.

I.3 “Soft” regime

Generally, PEO was associated with micro-discharges which gradually decrease in number and increase in size and with the processing time. This is accompanied with intensification of the MDs and strong acoustic emission, as well as gradual increase of the anodic voltage. However, when operating in PBC mode, it was found that the suitable adjustment of the waveforms of the current pulses, that is the anodic and cathodic amplitudes, the pulse duration and the frequency, can affect significantly the behaviour of the process. Particularly, Mécuson *et al.* [19] showed that the right control of the ratio of the applied positive to negative charge ($RCQ = Q_p/Q_n$) can induce drastic changes to the process leading to what they called “soft” regime (mentioned also as “soft” sparking regime). The appearance of this regime is mainly conditioned by maintaining the RCQ in the range between 0.8 and 1 and it typically occurs after a certain initial period of time following the conventional PEO “arc” regime. One significant observation that was made is the gradual decrease of the anodic voltage after a certain period of processing time and its stabilisation at lower values (up to 200V lower) (Fig. I-9). In their work, Martin *et al.* [28] showed that transition to this “soft” regime appears earlier by using higher current density and frequency.

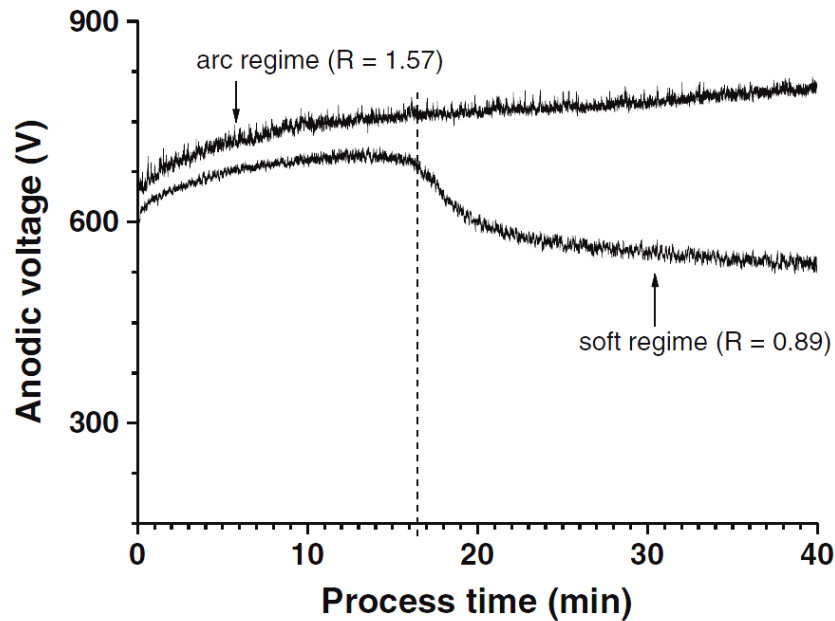


Figure I- 9. Variation of anodic voltage amplitude with processing time for two different electrical conditions applied, $RCQ = 1.57$ and $RCQ = 0.89$. [35]

Transition to “soft” regime is also accompanied with disappearance of visible MDs that in turn is associated with a decrease in acoustic and light emissions. Indeed, bright MDs tend to disappear and only small dots remains visible in deep darkness. This is particularly obvious in Fig. I-10 that shows the visual aspect of the MDs before (at 30 min) and after (at 45 min) the “soft” regime occurrence. Note that the camera integration time for the last image (Fig. I-10d) is 200 times higher than the previous ones. Moreover, from optical emission spectroscopy, the transition to “soft” regime is also accompanied with the disappearance of all atomic emission lines.

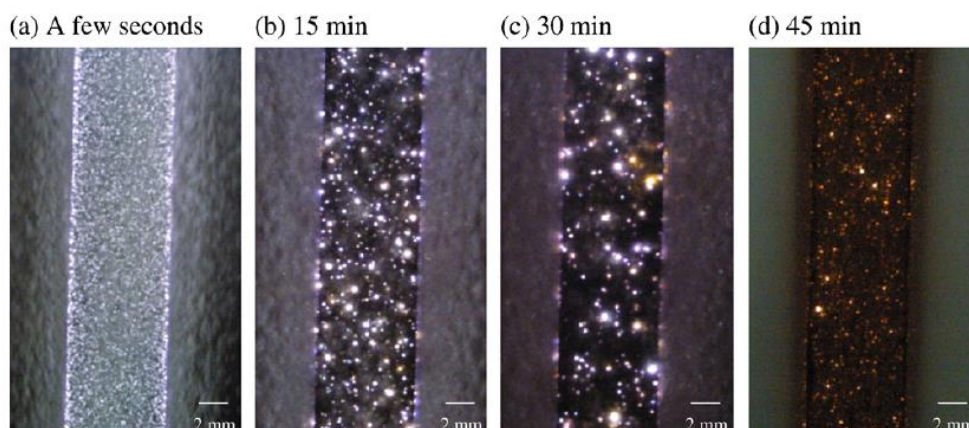


Figure I- 10. Visual aspect of micro-discharges during PEO processing of aluminium under "soft" regime conditions. [19]

Despite these observations, Mécuson *et al.* [19] showed that the growth kinetic is enhanced after the transition to “soft” regime. Figure I-11 depicts the thickness dependence on processing time for two conditions: arcing ($RCQ = 1.57$) and “soft” regime ($RCQ = 0.89$). At the beginning of the process and until the transition occurs, the growth rate is identical for both electrical conditions and it increases right after the transition, in a rather parabolic way, for “soft” regime conditioned treatment.

The “softening” of the micro-discharges has also a beneficial impact on the growing oxide layer, to its microstructure and phase composition, which improve its structural properties, as will be described later in this chapter.

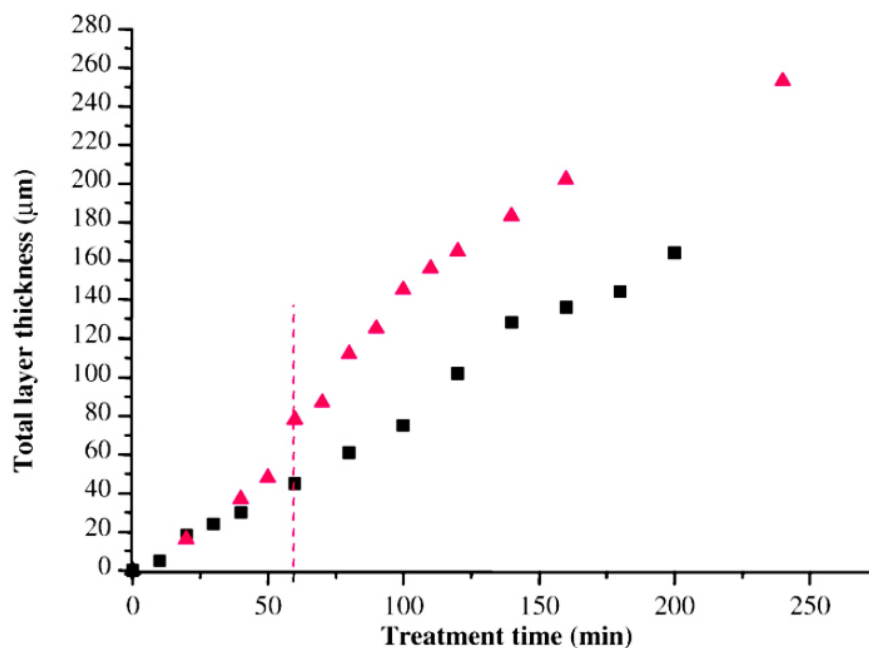


Figure I- 11. Variation of the thickness of aluminium oxide coating with PEO processing time treated in “arcing” ($RCQ = 1.57$) and “soft” regime conditions. [Reproduction from [19]]

I.4 Properties of micro-discharges

As the growth of the oxide layers is defined by the nature of the micro-discharges and their properties, it is clear that their characterisation is of paramount importance to understand and optimise the PEO process. Thus, many research teams have focused on studies regarding the physical properties of the micro-discharges, such as electron density and temperature in the plasma, as well as macroscopic characteristics related to their size, lifetime and distribution over the surface. The appearance of micro-discharges on the treated surface is a phenomenon that is constantly evolving during the treatment, as can be seen from Fig. I-2 and Fig. I-10.

I.4.1 Spatial characteristics

The spatial characteristics of micro-discharges have been extensively studied by various research teams [20,22,64–67]. Regarding the size of the MDs, in the literature, values have been reported to vary between 35–800 μm in diameter. One should consider that this is strongly affected by the operating mode and the applied electrical conditions. For example, Fig. I-12b illustrates the size evolution with processing time for five different values of charge quantity ratio (RCQ) operated in PBC mode. Similarly, their density is also affected by the imposed parameters, as seen in Fig. I-12a. One can notice that although at the beginning of the process all the cases exhibit similar characteristics, the one that is conditioned by a very high ratio ($RCQ = 6.0$) undergoes drastic changes in the course of the process. The micro-discharges decrease rapidly in number and increase in size.

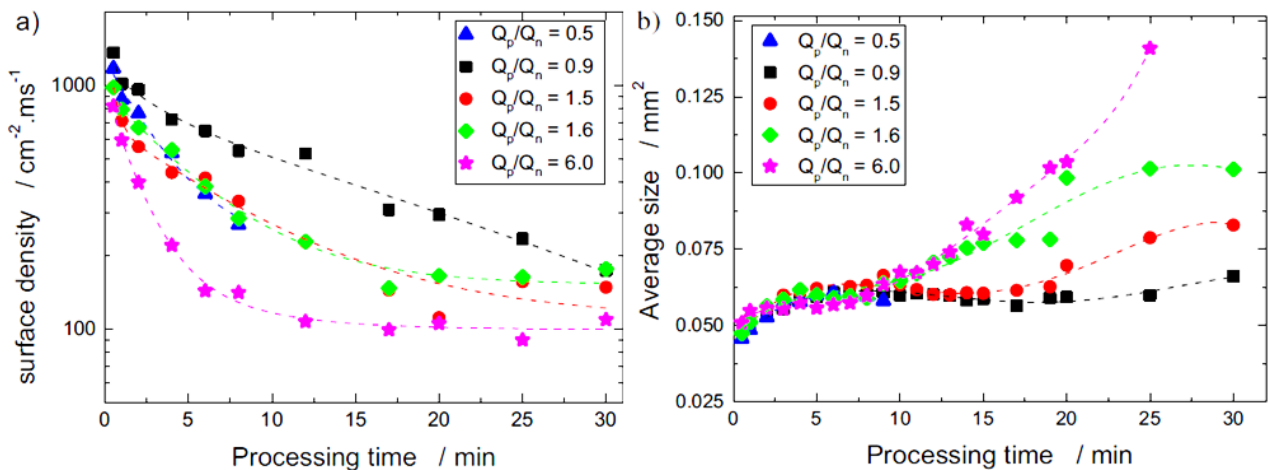


Figure I- 12. Evolution of a) Surface density and b) average size of the micro-discharges with processing time for PEO treatments with various values of charge quantity ratio ($RCQ = Q_p/Q_n$). [67]

I.4.2 Temporal characteristics

Physical observations of the PEO process, typically give the impression that the micro-discharges appear continuously. However, processing in AC mode, time-resolved studies have shown that the appearance of MDs occurs only during the anodic half period [21,68]. Of course this applies to most common PEO treatments in usual electrolytes. Under certain conditions, cathodic discharges may also be present [33,63,69].

Regarding the appearance of the micro-discharges which is accompanied with light emission from the processing surface, Martin *et al.* [67] conducted a systematic study by synchronised recording of the emitted light with the applied current pulses. They showed that the appearance of MDs is delayed with respect to the rise of the anodic current pulse (Fig. I-13). Moreover, it increases with processing time and is higher for lower values of charge quantity ratio (RCQ) (Fig. I-14).

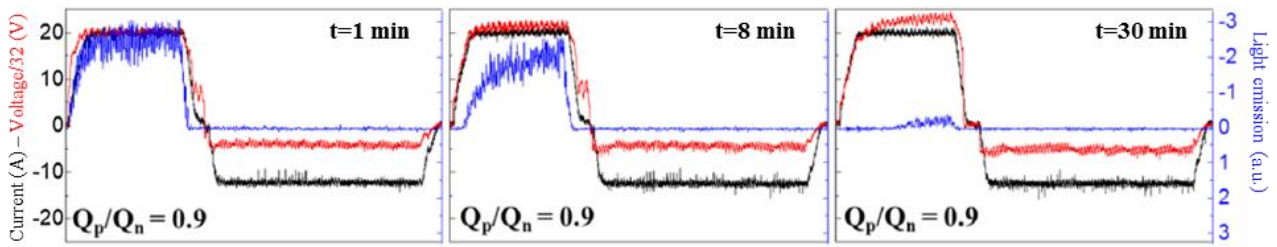


Figure I- 13. Light emission and voltage response to the applied current pulse at various moments of the PEO process. [67]

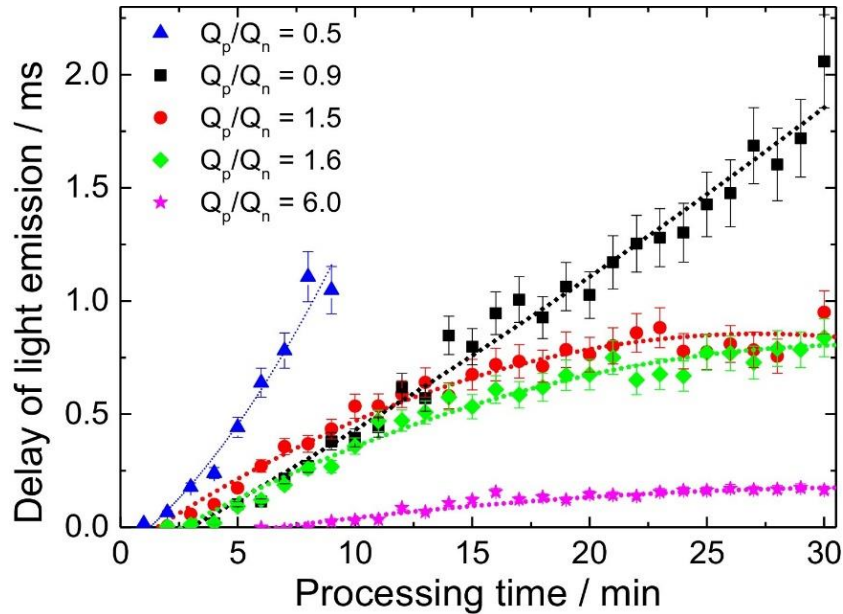


Figure I- 14. Evolution of delay in the appearance of micro-discharges with processing time for various electrical conditions applied. [67]

Regarding the lifetime of the micro-discharges, time-resolved investigations result in a broad range of values reported in the literature, spanning from few microseconds to some hundreds of milliseconds [20,65,68,70,71]. Mehlem [70], conducting PEO experiments in pulsed bipolar mode at a frequency of 100 Hz, reported MDs duration as low as 8 μ s, while Matykina *et al.* [65] found values as high as 800 ms when operating in DC mode. Typically, at the beginning of the process, the majority of MDs are short-lived (less than 200 μ s), with a very small percentage exceeding a lifetime of 300 μ s, as shown in Fig. I-16. However, it should be noted that the detection of very short-lived discharges might be limited by the temporal resolution of the detectors, while in cases of AC operating mode, the micro-discharges are limited by the imposed frequency.

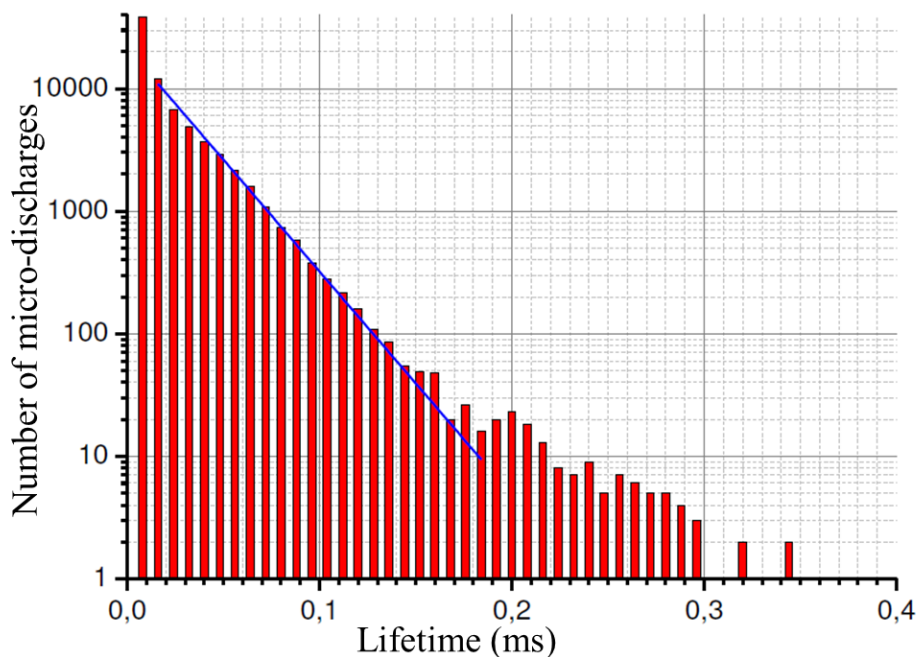


Figure I- 15. Distribution of duration of micro-discharges in PEO at processing time $t = 1$ min in PBC mode at $f = 100$ Hz and “soft” regime conditions ($RCQ = 0.89$). [70]

I.4.3 Physical properties of the micro-discharges

Optical emission spectroscopy is a common diagnostic tool that provides information related to the species that are present in the plasma, their (excitation?) state, as well as the electron density and temperature.

Typically, an emission spectrum reveals the presence of species that originate from the processed material and the electrolyte. The elements from the material are present in the plasma in atomic or ionised state. The electrolyte species generally decompose when diluted and provide ions such as oxygen (O^+) or hydroxyl radicals (OH). Atomic hydrogen (H) and oxygen (O) are also present [21,23,38,42,66,72–75]. Fig. I-16 shows a typical emission spectrum obtained at 110 s of oxidation time during PEO process of aluminium 7075 alloy in alkaline electrolyte consisting of potassium hydroxide and sodium metasilicate [75]. Al, Zn, Cu and Mg originate from the substrate, while O, H, Na and OH come from the electrolyte.

Besides the identification of species, optical emission spectroscopy can also give access to quantitative information in the plasma, such as electron density and excitation temperature (T_{exc}). Moreover, analysis of molecular emission lines can provide values on rotational (T_{rot}) and vibrational (T_{vib}) temperature. The spectroscopic studies typically require the plasma to be in thermodynamic

equilibrium (TE) or at least in local thermodynamic equilibrium (LTE). Under these conditions, the excitation temperature is considered to be representative of the electron temperature (T_e).

The reported values of electron temperature in literature range between $T_e = 3500 - 33000$ K [38,70]. For example, Jovovic *et al.* [38] conducting PEO processing on aluminium alloy, determined the electron temperature of $T_e \approx 4000$ K using Mg I lines, while the corresponding value from O II lines was found to be $T_e \approx 33000$ K. Yang *et al.* [75] investigated the variation of electron temperature with PEO processing time by measuring the relative intensities of Al I lines and found it to range between $T_e = 3000 - 15000$ K. Stojadinovic *et al.* [73] calculated the rotational temperature using the emission lines of MgO, AlO and OH and reported the values of $T_{rot} = 11000$ K, $T_{rot} = 8000$ K and $T_{rot} = 3500$ K, respectively.

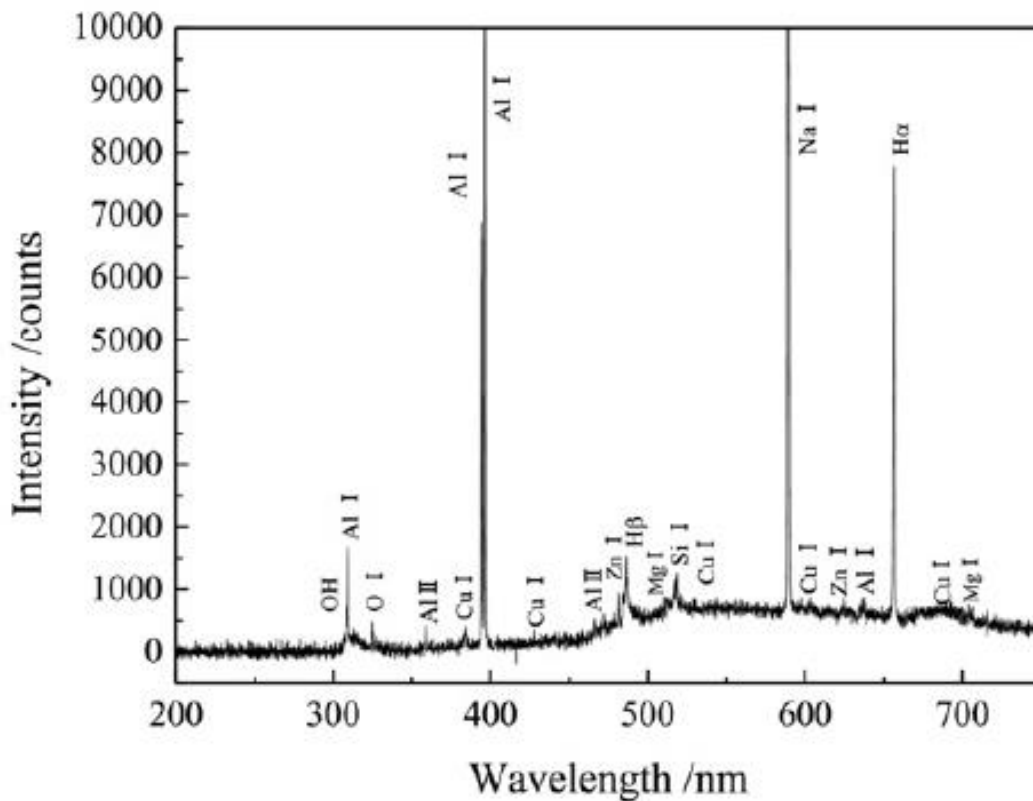


Figure I- 16. Typical emission spectrum during PEO of aluminium alloy. [38]

Such discrepancies in the reported values, reflects a probable deviation from the thermodynamic equilibrium and can, at best, correspond to partial local thermodynamic equilibrium limited to each species.

The electron density is determined by the analysis of the broadening of a given emission line, particularly from the contribution of the Stark broadening. This is done by interpolation of the

experimental profile with a mathematical function (Gauss, Lorentz, Voigt) and extraction of the component due to Stark effect.

Among others, hydrogen is the most frequent element used to determine the electron density [21,38,72,76]. However, interpolation of the experimental profile of these lines is done by using two functions, as it was found that adjustment with one single function is not satisfactory. This leads to two different values of FWHM, resulting to corresponding two values of electron densities (Fig. I-17). Non-hydrogenic species (*e.g.* Al, Al⁺) originating from the substrate can be also used for the determination of electron density. In this case the fitting process does not involve such issues and can be resolved by the use of only one function. In the literature, the reported values of electron density range between $N_e = 1 \cdot 10^{15} - 5 \cdot 10^{17} \text{ cm}^{-3}$ [21,23,38,42,66,72–74,76].

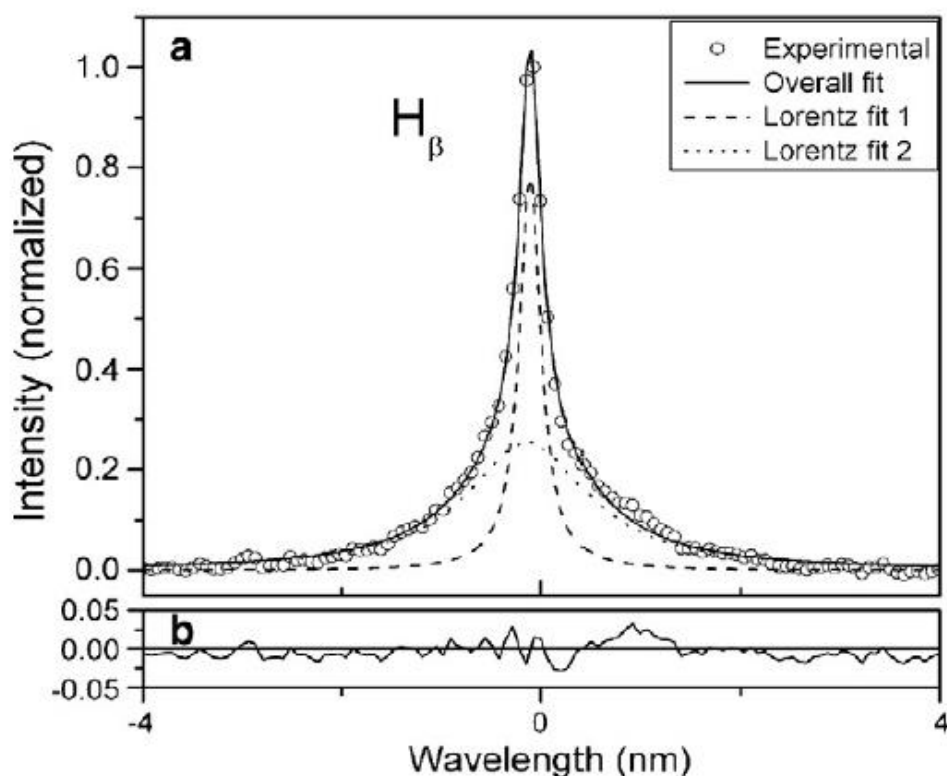


Figure I- 17. Interpolation of H_β emission line from PEO processing of tantalum with two Lorentzian functions. [66]

I.5 Structural properties of PEO oxide coatings

The oxide coatings that are formed with PEO processing typically exhibit a multilayer structure consisting of 3 distinct sublayers. A porous outer layer, which consists usually of low temperature phases, a dense inner layer, formed by high temperature modifications, and a thin oxide layer of few hundred nanometres that is formed at the interface with the metal substrate below the dense layer

[3,7,77]. This is usually called “barrier” layer. Figure I-18 illustrates cross-section image of typical PEO coating depicting the multi-layered structure. The relative size of the dense and porous region is generally affected by the substrate and electrolyte composition and the applied electrical conditions [3].

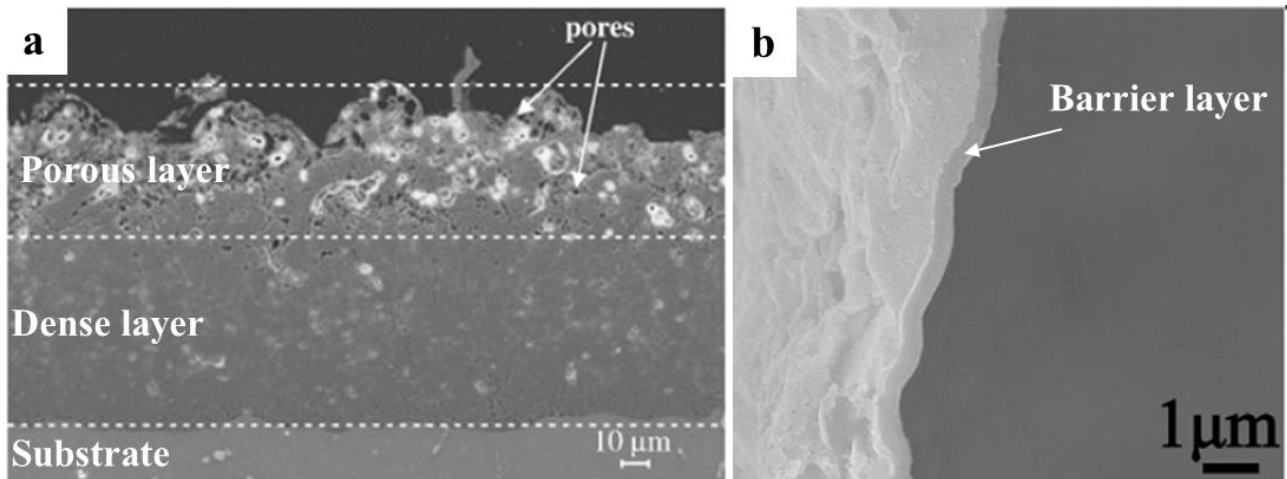


Figure I- 18. Cross-section SEM micrograph of PEO coating produced on Al substrate, depicting a) the two main sublayers [19] and b) the barrier layer located at the oxide/substrate interface [78].

Depending on the processing conditions, a variety of surface morphologies can be observed. Fast solidification processes lead to the so-called “pancake”-like structures [44,79] (Fig. I-19a, b) on the surface. These can be either completely closed or exhibiting open cavities in the centre of the pancake. According to Sundararajan *et al.* [79], they are the result of discharges that took place at this location and as the molten alumina was ejected through the discharge channel, it was solidified around it, forming the pancake-like structure. Usually micro-cracks appear on these “pancakes”, as a result of internal stresses [80–83]. Moreover, nodular structures of various sizes can be present (Fig.I-19c, d). Intense micro-discharges, can also sometimes lead to crater-like structures. The surface roughness reported for aluminium oxide coatings ranges between $R_a = 0.75 - 7 \mu\text{m}$ [20,31,84] and depends on processing conditions (AC/DC mode, frequency, electrolyte composition) and also on the geometry of the sample, as edge effects can lead to preferential discharge-sites and inhomogeneous growth [35].

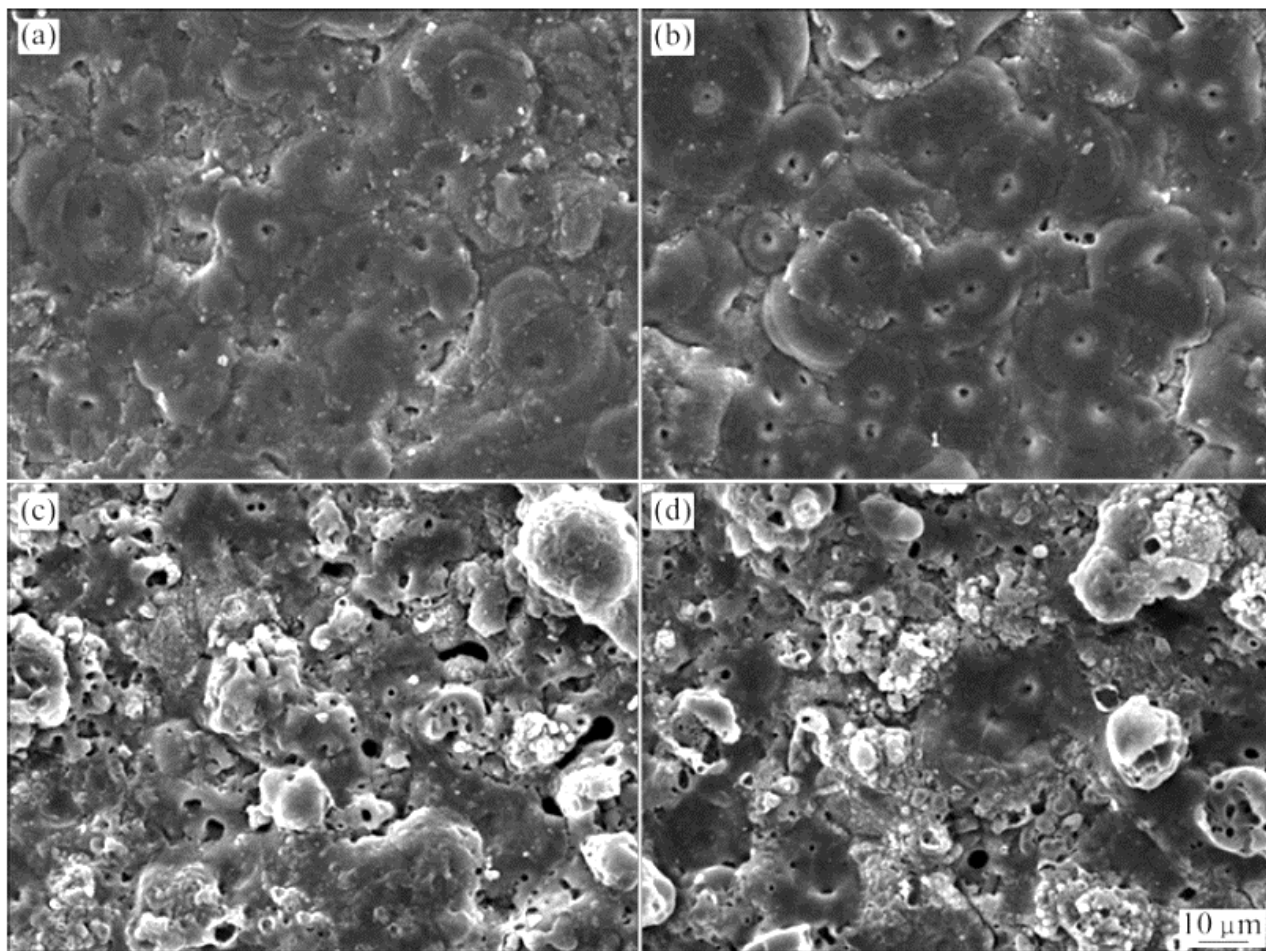


Figure I- 19. SEM micrographs of the surface morphology of aluminium oxide coatings PEO processed in four different electrolytes depicting various morphological characteristics of the surface. [44]

Typically, aluminium oxide coatings produced by PEO exhibit complex microstructure. Due to rapid solidification processes, some regions may be quenched by the electrolyte at very high rates, producing amorphous phases, while others, at the vicinity of the discharges may have effectively been heat treated, leading to high crystallisation. This leads to formation of transition phases, such as γ -, η - or δ - Al_2O_3 and α - Al_2O_3 phase [3,4,7,85,86]. The α -alumina is more desirable since it is the most stable phase and it exhibits increased hardness compared to the other phases. In coatings formed from copper rich aluminium alloys, the content of the α -phase can reach up to 60% [3]. Tillous *et al.* [7] showed that the α -phase of alumina is mainly located at the intermediate dense layer of the coating, where it reaches its maximum content. In addition, some complex phases might be also present in the outmost porous layer, due to incorporation of elements from the electrolyte, such as silicon, potassium, sodium. In silicate rich electrolytes this usually leads to the formation of various mullite (Al-Si-O) phases, which can serve as thermal barriers as they exhibit much lower thermal conductivity compared to the bulk crystalline material [6,87].

PEO coatings are considered generally porous. However, their overall porosity levels may range from less than 5% to more than 30% [88–90], depending on the elaboration parameters. As seen in Fig. I-18a and Fig. I-19, these pores are typically within the micrometre scale and located mainly at the outer sublayer. Fig. I-20 illustrates the porosity distribution obtained from X-ray microtomography for two coatings produced on pure aluminium and on the 2214-T6 aluminium alloy [84]. Nevertheless, Curran *et al.* have reported the existence of nanometre size surface connected network of porosities that reaches until the substrate/oxide interface [91]. Galvis *et al.* [92] and Han *et al.* [93] investigated highly porous titania coatings, reporting an average pores size of 1-1.7 μm in diameter.

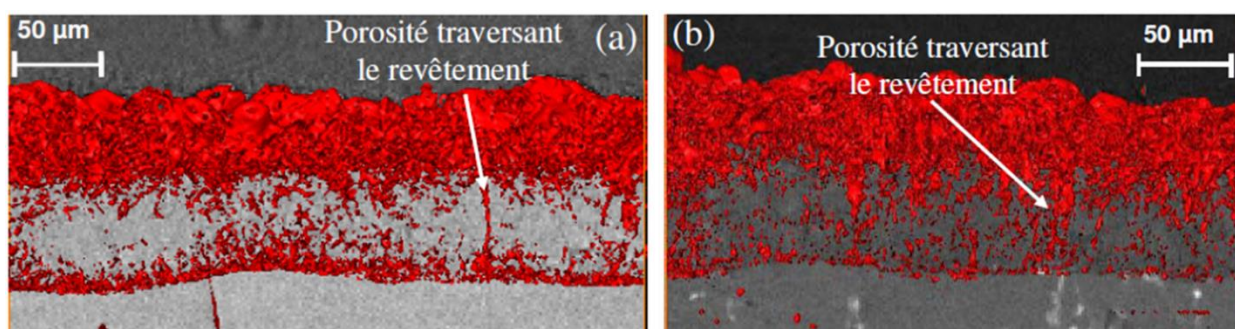


Figure I- 20. Porosity distribution in PEO coatings of a) pure aluminium and b) 2214-T6 aluminium alloy produced in PBC mode at $f = 100$ Hz.[84]

I.6 Growth mechanisms

The growth of oxide layers during PEO is the result of complex and concomitant mechanisms involving matter in plasma state which is confined in very small volumes, high pressure and temperature conditions and interactions with liquid environment. Besides PEO, discharges in and in contact with liquids are of interest to many other domains (e.g. medical use and chemical analysis of liquids) and their rather complex ignition mechanisms are studied intensively [94–96]. However, in PEO processing, clear relationship between the process parameters, the properties of the micro-discharges and the coating growth has not yet been established.

Generally, the suggested mechanisms can be divided in to two groups: those that describe the oxidation process of the metal under electrical discharge conditions [18,79,97–100] and those that describe the dielectric breakdown processes of the insulating coating when surrounded with conductive liquid and under electric polarisation [23,64,101–105].

In the first group, based on the gas steam vial model, Klapkiv [98] suggested a single discharge model with a core-shell structure (Fig. I-21). According to this model, the plasma temperature and

electronic density exhibit a gradient. Consequently, the elements that constitute the plasma vary depending on the different zones and thus, different reactions take place for the formation of aluminium oxide. Under such conditions of high temperature and pressure, Sundararajan *et al.* [79] showed that the molten material is ejected through the discharge channel, oxidised, rapidly solidified and deposited on the surface, promoting the growth of the oxide layer.

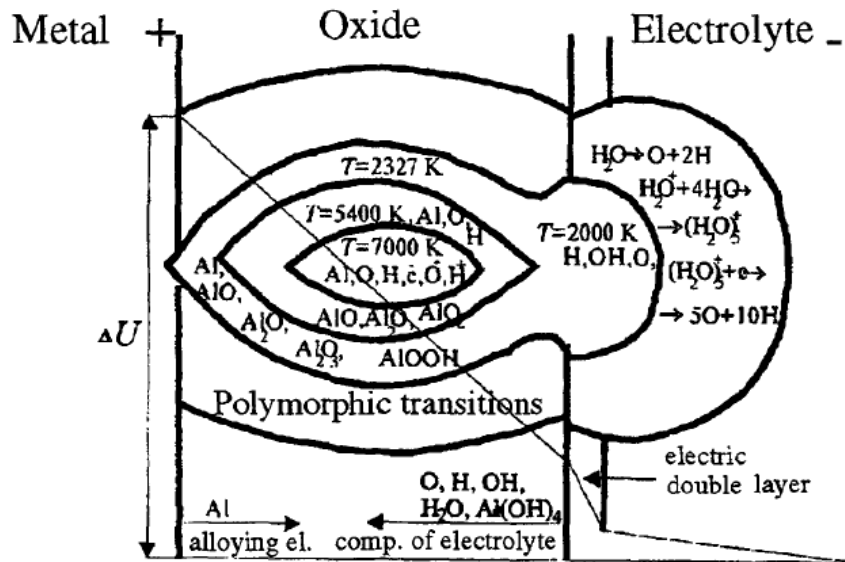


Figure I- 21. Schematic representation of the alumina formation in the discharge channel. [98]

For Yerokhin *et al.* [18], two simultaneous mechanisms of the metal oxidation take place through the discharge channels including a plasma-assisted oxidation and an electrochemical-assisted oxidation. More recently, by using ^{18}O isotope tracers through PEO coatings, Matykina *et al.* [100] concluded that migration of oxygen is the result of two concomitant mechanisms, *i.e.* one by the solid-state diffusion of oxygen and another due to water molecules trapped in cavities which, within the plasma, decompose and form ions and radicals.

For the second group of mechanisms, Hussein *et al.* [23] suggested a multi-discharge model including three types of discharges igniting at several locations and at different times through the coating thickness:

- A-type discharges that appear on the fine impurities located on the top surface of the coating
- B-type discharges that cross the overall thickness of the coating
- C-type discharges that occur in the micro-sized porosities of the coatings

Based on optical emission spectroscopy measurements, Jovović *et al.* [102] were able to confirm these three types of discharges. Using a silicate-based electrolyte, Dehnavi *et al.* [103] established that A-type discharges are caused by the presence of silicon anions adsorbed on the topmost surface of the growing oxide layer.

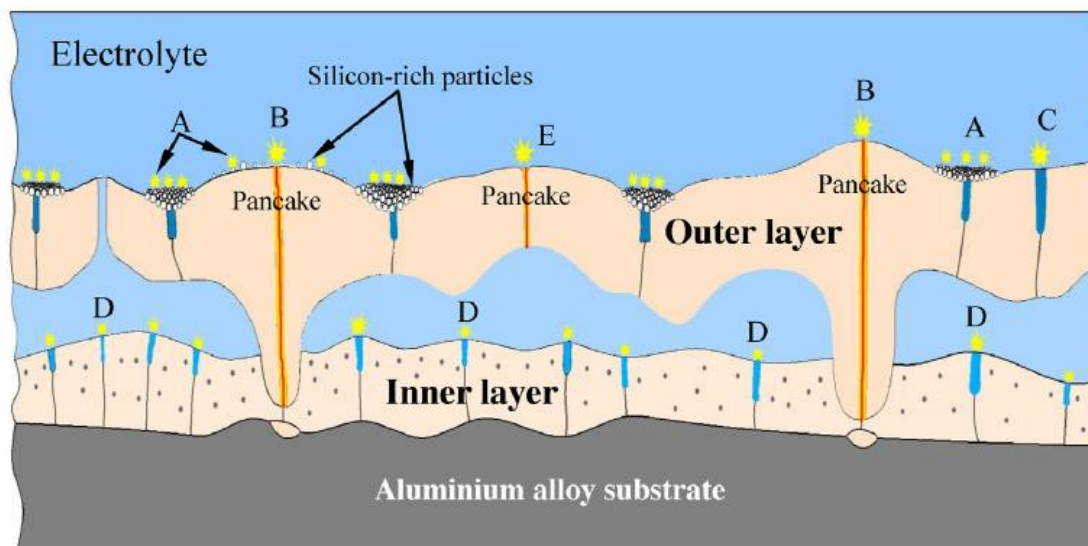


Figure I- 22. Schematic representation of the multi-discharge model.[104]

Later, Cheng *et al.* [104] enriched Hussein's model (Fig. I-22) by including D- and E-type discharges in order to explain the typical morphology of the PEO coatings, *i.e.* the presence of an outer porous sublayer filled with electrolyte and an inner dense sublayer, as will be described in next section. D-type discharges are assumed to take place in large cavities inside the growing oxide layer and are considered to be responsible for the formation of the compact inner layer, while the E-type traverse partially the outer porous sublayer of the coating. Recent work of Wu *et al.* [78], investigating the coating/substrate interface, illustrate the formation of protrusions on the oxide that develop towards the substrate, suggesting an inward growth during the PEO process.

I.7 Conclusions of Chapter I

This chapter introduced the main principles of the plasma electrolytic process, highlighting its advantages over the conventional processes used until now. A brief documentation of the work and progress that has been done to the present day was summarised. As described, PEO is a complex procedure, in which a multitude of reactions and phenomena take place under high potential. Although great progress has been achieved, the knowledge regarding the fundamental principles that drive the process and define the coating growth is still limited. The “soft” regime, though commonly

admitted to enhance and improve the resulting coating, is still not well understood in terms of what are the factors that induce the transition into this regime and how does this alter the growth of the coating. A deeper understanding is necessary for both the optimisation of the process as well as the reduction in energy consumption to facilitate a potential large scale industrial use.

The work of this thesis aims to contribute to a better understanding of the PEO process by:

- investigating the nature and behaviour of the micro-discharges under various electrical regimes, particularly in connection to their appearance during the anodic pulse and establish a correlation between the electrical parameters, the coating's micro-structure and the ignition of micro-discharges.
- studying of the micro-discharges during the "soft" regime and investigating their interactions with the surrounding environment above the discharge channel by means of high speed video.
- Experimenting with various parameters, such as the substrate and the electrolyte composition, and their influence on the processing characteristics (electrical and optical).
- Regarding the micro-structural properties of the PEO coatings elaborated in "soft" regime conditions, a detailed and in depth multi-scale investigation of the "pancake" cavity structure is performed to explain the presence of a particular lamellar arrangement.

Finally, new opportunities and possibilities are sought through the investigation of potential metallic oxide micro- and nano-particles production during PEO processing. Additionally, an attempt for a duplex procedure involving the combination of cold spray and the PEO process is made to elaborate protective coatings on unconventional substrates.

Chapter II - Experimental considerations

II.1 Introduction of the chapter II

This chapter provides a description of the experimental set-up used in this study, as well as details about the different techniques used to *in situ* characterise the PEO process and to *ex situ* characterise the microstructure of the produced coatings.

II.2 Experimental installation

As illustrated in Fig. II-1, the PEO treatment unit mainly consists of an electrolytic cell, an electrical generator controlled by a computer and the electrodes. In addition, Fig. II-1b provides a schematic illustration of the set-up with the main equipment used for the *in situ* characterisation of the PEO process. These main parts are detailed in the following sections.

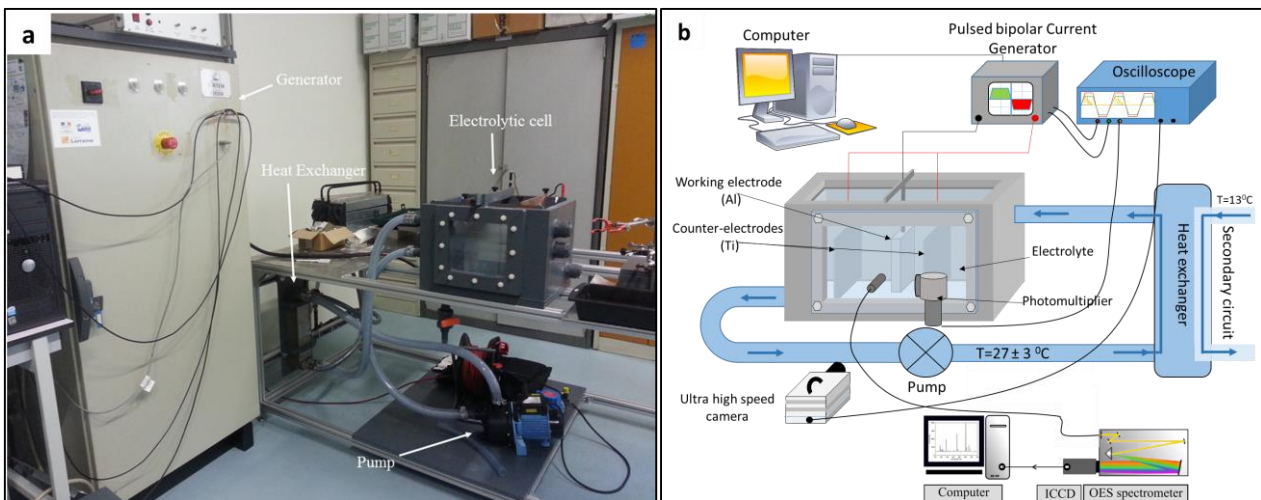


Figure II-1. a) Picture of the PEO treatment unit and b) schematic illustration depicting the set-up with the equipment used for the *in situ* characterisation.

II.2.1 The electrical generator

The electrodes are supplied by using a current generator (Ceratron[®]) working in a current-controlled galvanostatic mode and operated via Cockpit Ceratron v.1.5 software. In this mode, the current is applied to the electrodes while the voltage is continuously adapted according to the oxide growth. In addition, the generator provides the possibility to supply the electrodes with a pulsed bipolar current where all the waveform parameters over one pulse period can be adjusted in a wide range [106]. Indeed, by using a computer-controlled environment, this can be done by not only

adjusting the amplitude and the frequency of the current pulses, but also all the temporal parameters related to the bipolar waveforms (T_i). A schematic description of the bipolar waveform is depicted in Fig. II-2. All time and amplitude parameters are adjustable within ranges according to Table II-1. By this way, the anodic and the cathodic charge quantities (Q_i in fig. II-2) that are delivered to the electrodes, and thus, their ratio ($RCQ = Q_p / Q_n$) can be controlled. As previously reported in the literature, this ratio of the charge quantities is crucial for both the growth kinetics and the microstructure of the producing oxide layer [19].

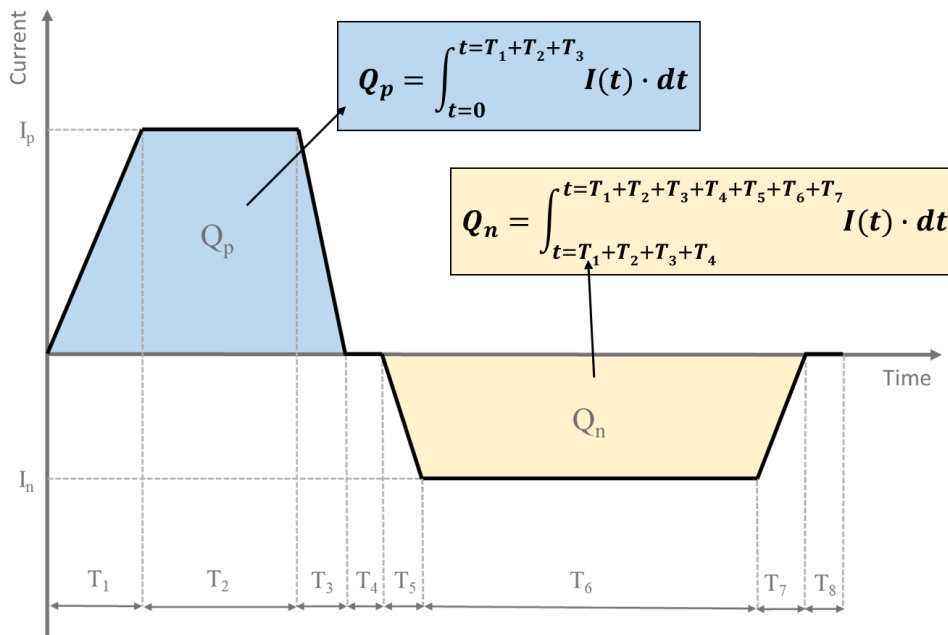


Figure II-2. Schematic illustration of a current waveform applied in the present study.

Mainly, the amplitude of the anodic and the cathodic currents is provided in the range of [5 – 35 A] and the available pulse frequencies are in the range of [100 – 1000 Hz] [107]. For the different investigations conducted in this work, various electrical conditions were used. In order to avoid confusion, details on the different electrical parameters used will be given at the beginning of each chapter.

Table II-1. Technical specifications of the electrical generator CERATRONIC®.

Parameter	Definition	Min	Max
I_p (A)	Amplitude of positive current	5	35
I_n (A)	Amplitude of negative current (defined by R)	5	35
R (%)	Ratio of I_n/I_p	1	250
F (Hz)	Frequency	100	1000
T_1 (μ s)	Current rising duration of positive pulse	300	$T = \sum T_i$
T_2 (μ s)	Duration of maximum current of the positive pulse	100	$T = \sum T_i$
T_3 (μ s)	Current decrease duration of positive pulse	100	$T = \sum T_i$
T_4 (μ s)	Dead time	100	$T = \sum T_i$
T_5 (μ s)	Current rising duration of negative pulse	100	$T = \sum T_i$
T_6 (μ s)	Duration of maximum current of the negative pulse	100	$T = \sum T_i$
T_7 (μ s)	Current decrease duration of negative pulse	100	$T = \sum T_i$
T_8 (μ s)	Dead time	100	$T = \sum T_i$

II.2.2 The electrolytic cell

The PEO experiments were conducted in a rectangular tank made of a PVC polymeric material. Dimensions of the tank were 300 mm \times 400 mm \times 300 mm which represents a volume capacity less than 36 L. Two glass windows located on opposite sides allow the observation and the study of the processed samples using different optical diagnostic techniques. As illustrated in Fig. II-1, a cooling system allows maintaining the electrolyte temperature at a constant value of 27 °C \pm 3 °C. By using a hydraulic pump, the electrolyte is circulated in a closed circuit through a heat exchanger. In turn, the heat exchanger is connected to a secondary closed cooling water circuit of the laboratory where the temperature is maintained below 15 °C. The circulation of the electrolyte also allows agitating the electrolyte which ensures its chemical homogeneity during the process. PEO treatments were performed in alkaline conductive electrolytes (pH in the range of [12 - 12.5] and conductivity in the range of [2.5 - 6.5] mS·m⁻¹ depending on the chemical species dissolved). These electrolytes were prepared by using various chemical components dissolved in deionised water. For the present study, the following chemical compounds were mainly used in different concentration:

- Potassium hydroxide [KOH], [1 - 2] g·L⁻¹ = [17.8 - 35.6] mMol·L⁻¹
- Anhydrous sodium silicate [Na₂SiO₃], [1.65 - 10] g·L⁻¹ = [13.5 - 82] mMol·L⁻¹
- Sodium hexametaphosphate [Na₆P₆O₁₈], 2 g·L⁻¹ = 3.3 mMol·L⁻¹

From a practical point of view, each electrolyte was prepared by mixing the deionised water with the required chemical compounds in a 4 litre beaker and applying magnetic stirring until the salts were completely dissolved and the mixture was homogeneous. A total of 25 litres was used to fill the electrolytic tank. To ensure reproducibility of the results and to avoid any ageing effect, the electrolyte was frequently replaced with a fresh one. Finally, details on the different electrolytes used in this study will be given at the beginning of each chapter.

II.2.3 The electrodes

The electrodes used in the PEO process consist of a working electrode and two counter electrodes. The working electrode is made of the metal to be protected by the growth of a PEO oxide layer and located between two metallic counter electrodes. In the present study, various substrates were used as working electrodes. Alloys of aluminium Al 2024 and Al 1050 were mainly used. Their chemical composition is reported in Table II-2. All the samples were cut in rectangular shapes (50×30×5 mm) providing a processing surface of ~0.38 dm². Additionally, some other materials were also processed such as zirconium (M5), pure titanium and in specific case a low carbon steel (presented in chapter VI). The detailed composition of these materials as well as their geometry will be given in the dedicated chapter.

Table II - 2. Chemical composition of aluminium alloys employed in the current study.

Elements (wt%)	Cu	Mg	Mn	Si	Fe, Ti, Zn	Al
Al 1050	0.05	0.05 max	0.05 max	0.25 max	<0.5	Balance
Al 2024	3.8-4,9	1.3-1.5	0.5-0.6	0.5 max	<0.5	Balance

Concerning the counter-electrodes, and whatever the different treatment conducted in this study, two rectangular titanium plates of 200 mm × 200 mm × 1 mm in dimensions are used. The two plates are symmetrically set to face both sides of the processed sample at an adjustable distance and maximize the homogeneity of the electric field at the surface of the working electrode. For all the experiments, the distance between the counter electrodes and the working electrode was fixed at 90 mm.

II.3 *In situ* diagnostic of the PEO process

II.3.1 Electrical time-response

The electrical signals applied to the electrodes were recorded in real time during the PEO process. Recordings of the output electrical signals were performed using a 4 channel/1GHz bandwidth oscilloscope (Agilent 54832B) and a data acquisition card (Keithley KPCI 3102). Fig. II-3a shows a typical current signal with the corresponding voltage time-response over two current pulses of the current (recorded after 5 min PEO processing time).

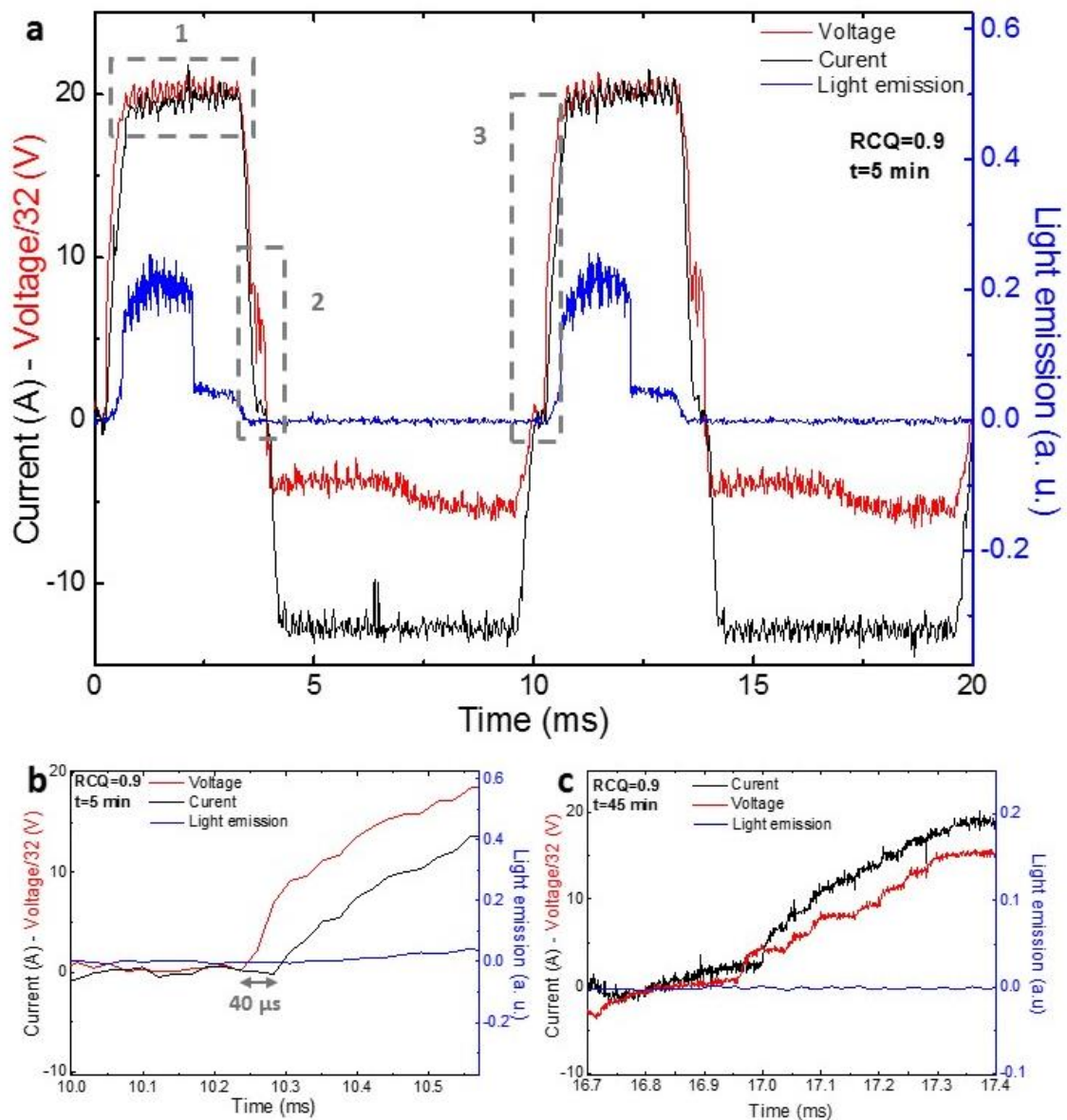


Figure II-3. Example of a typical chronogram recording during *in situ* characterisation of the PEO process. a) Voltage response (red) to the applied current pulse (black) and light emission (blue). b) and c) are magnified depictions of area 3 in (a) obtained at 5 min and 45 min of processing time, respectively.

Three main observations can be done. Firstly, high frequency oscillations of both the current and the voltage during their maximum values (anodic or cathodic) are observed (box area 1 in Fig. II-3a). This is associated to the control-loop frequency of the current regulation which is set at 8 kHz. Secondly, as the anodic current starts, the voltage increases earlier, about 40 μs ahead of the respective current rise (Fig. II-3b). Melhem [70] showed that this constant mismatch is not due to the PEO process itself, but is inherent to the electrical generator. This conclusion was made by investigating the current-voltage plots after connecting a pure resistive load to the generator. This rather represents the system quite well during the early stage of the process. Nevertheless, it has been observed that the system displays a more complex behaviour, exhibiting not only resistive but also capacitive characteristics [67], resulting eventually to a change of the voltage response curve to the applied current. With this in mind, it was observed, and as shown in voltage-current response of Fig. II-3c obtained at 45 min, that this phase shift is diminishing to zero as the process continues. In any case, for the purposes of this study and since the timescale of this shift is negligible compared to the timescale of the pulse period (10 ms at 100 Hz) and the duration of the different phenomena observed in the present study (from 100 μs to 1-2 ms), current and voltage are considered to be in phase, whatever the applied operating conditions. Finally, some peaks of the voltage during the decrease of the positive current are observed (area 2 in fig. II-3a). According to F. Jaspard [106], this is due to reaction of the regulating system to maintain the current value when the latter rapidly drops.

II.3.2 Optical characterisation

II.3.2a Photomultiplier

The need of a high temporal resolution monitoring is required when dealing with events (typ. micro-discharges or dynamic of bubbles) that take place simultaneously and have short durations ($\sim 10 \mu\text{s}$) and small size ($\sim 5 \mu\text{m}$ in diameter). In the present study, a photomultiplier (PM) was used as an optical diagnostic tool to detect light emission during the PEO processing with a high time resolution. The one used in this work was a Hamamatsu R928 which exhibits a time resolution of 2.2 ns (see Table II-3 which presents the main characteristics of the photomultiplier used). Once collected, the output signal of the photomultiplier is then amplified by a 300 MHz bandwidth current amplifier (Stanford Research Systems SR445) and recorded by the oscilloscope, together with the current and voltage signals. It is also worth noting that light emission recorded by the PM is synchronised with the applied current. Such a recording is illustrated in Fig. II-3a (blue line).

Table II-3. Main specifications of the Hamamatsu R928 photomultiplier.

Spectral Range (nm)	185-900
Maximum response wavelength (nm)	400
Gain	10^7
Time response Anode pulse rise time (ns)	2,2

II.3.2b Optical emission spectroscopy (OES)

In addition to the time-resolved detection of light, optical emission spectroscopy was also applied in the present study to provide various information on the plasma state, from the identification of chemical species to the electronic density and temperature. As described in details in chapter IV, the physical principle of the OES technique is based on the relaxation of excited species to lower energy states that produced photon emissions. To briefly remind, if a species (atom or molecule) is found at an excited energy state E_j , it can, if the quantum selection rules are respected, relax by transition to a lower energy state E_i . The exceeding energy, $\Delta E = E_j - E_i$, is then emitted as a photon

$$h\nu_{ji} = E_j - E_i = \frac{hc}{\lambda_{ji}} \quad (\text{Eq. II - 1})$$

where h is the Planck constant ($h = 6.62 \cdot 10^{-34} \text{ J}\cdot\text{s}$), ν_{ji} the transition frequency, c the speed of light in vacuum ($c = 3 \cdot 10^8 \text{ m}\cdot\text{s}^{-1}$) and λ_{ji} the wavelength of the emitted photon.

Due to the fact that the wavelengths of the detected light correspond to specific transitions of different species, the analysis of a spectrum emitted by the plasma allows identifying those radiative species and their state in the plasma. Moreover, analysis of discrete spectral lines of a given species gives access to quantitative information, such as electronic density and temperature.

Two spectrometers were used. The first one is a Horiba Jobin-Yvon TRIAX 550 monochromator with a focal distance of 550 mm. It is equipped with 3 diffraction gratings (100, 1200 and 1800 grooves/mm which offer different spectral resolutions (1, 0.1, 0.07 nm, respectively). The second spectrometer used in this work is an OceanOptics USB2000 using a diffraction grating of 1200 grooves/mm which covers a spectral range from 200 nm to 900 nm with a resolution of approximately 1 nm. Whatever the spectrometer used, light was collected by an optical fibre located in front of the processed sample, guided to the entrance of the monochromator, diffracted and finally collected by the ICCD detector.

II.3.2c Fast video imaging

Despite of providing valuable information on micro-discharges, the photomultiplier and the optical emission spectroscopy are unable to individually discriminate light from discrete events, but give rather collective information based on time integrated recordings. To overcome this, fast video imaging was used in the present study to characterised short-lived and small-sized events such as the micro-discharges and the gas bubbles. For example, fast video imaging provides complementary information on the number of micro-discharges, their spatial distribution over the processed surface, their size and their life-time.

During this work, two cameras were used. A Photron FastCam SA 1.1 and Photron FastCam SA5. Both provide a spatial resolution of 1024×1024 pixels for acquisition frequencies up to 5400 frames per second (fps) and decrease to 64×16 pixels at maximum frame rates (675 kfps for SA1.1 and 1.3 Mfps for SA5). Spatial resolutions of ~ 6.5 and $\sim 15 \mu\text{m}^2/\text{px}$ are achieved for frames rates of 100 kfps and 125 kfps, respectively. The main advantage of the SA5 version is that it offers better spatial resolution at higher acquisition frequencies. Both of the cameras are equipped with a CMOS (Complementary Metal Oxide Semiconductor) sensors which encodes the images on 12 bits. A lens with a 55 mm focal distance and an aperture of $f/1.2$ was implemented for the experiments. Depending on the nature of the investigation, we used various acquisition frequencies during the PEO treatments. To avoid confusion, information on every case will be given at their respective sections in this manuscript.

As previously mentioned, the oscilloscope is also used to perform synchronised recordings of current and voltage simultaneously with other techniques. The high speed camera is connected to the TRIGGER output of the oscilloscope. Once triggered, a signal is sent to the input of the camera to start the recording with a delay of 40 ns with respect to the oscilloscope. This allows simultaneous recording of current and voltage values and the corresponding images of micro-discharges taking place at that moment.

Upon recording, an analysis of the images that are recorded is necessary to obtain quantitative and statistical information regarding the micro-discharges. Due to very high acquisition frequencies, manual analysis of these images is inconceivable (50-125 frames per ms, depending on the settings). An automated analysis was used with an image processing software (TRACK by Aprex Solutions), which allows detecting events on every individual frame and tracking their evolution throughout successive frames of the video. Having set the proper parameters, it is possible to record all the geometric details of these events (localisation, size, shape) as well as some of their physical properties

such as life time, velocity and acceleration (for non-stationary events). Once the analysis is performed, the results are saved in the form of tables and can be further exploited for any statistical analysis, providing mean values or distributions of the above mentioned properties.

II.4 *Ex situ* characterisation of the PEO coatings

For the *ex situ* characterisation of the produced oxide coatings, the samples were rinsed immediately after the treatment with ethanol, dried and stored in a dry environment before analysis by means of various techniques which are described in the following sections.

II.4.1 Scanning electron microscopy (SEM) and EDX measurements

Scanning electron microscopy (SEM) was mainly used to observe the morphology of the produced PEO coatings at the micrometre scale. Top views and cross-sections were examined by a field emission gun scanning electron microscope (FEG Philips XL 30 S). Cross-section observations were performed in the backscattered electron imaging mode at an acceleration voltage of 25 kV. Such observations provide information on the thickness of a coating, and the morphology regarding its density and the existence of porosities. Prior to be examined in the cross-section view, the samples were cut, mounted in resin, polished through successive grades of SiC abrasive papers, and finely polished with diamond paste. Top-views are examined in the secondary electron imaging mode at an acceleration of 5 kV. Prior to their examination, and in order to avoid charge accumulation at the oxide surface, a thin gold coating (~ 50 nm) is deposited by using PVD technique.

In addition, the microscope is equipped with an EDS SDD detector (X-Max, Oxford Instruments) which allows investigating the chemical composition of the PEO coatings as well as performing element distribution maps.

II.4.2 X-ray Diffraction (XRD) and grazing incidence X-ray diffraction (GIXRD)

For the X-ray diffraction (XRD) characterisation a Bruker D8 Advance diffractometer was used in a $\theta/2\theta$ Bragg – Brentano configuration with a copper crystal source emitting an X-ray beam of $\lambda = 1.5406 \text{ \AA}$ in wavelength corresponding to the Cu $k_{\alpha 1}$ radiation. X-ray diffraction patterns were obtained in the range of $20^\circ - 80^\circ$ with a step size of $0,02^\circ$. Additionally, an INEL CPS 120 diffractometer (Co k_{α} incident radiation $\lambda = 1.7903 \text{ \AA}$) was implemented to perform grazing incidence x-ray diffraction (GIXRD) with an incidence angle of 3° and a step size of 0.027° over the range of $20^\circ - 120^\circ$. This technique achieves a very small penetration depth (about $6 \mu\text{m}$), allowing in such way the examination of the thin outmost top layer of the coating.

II.4.3 Transmission Electron Microscopy (TEM) and Scanning (STEM)

At the micro- and nanometre scales, the structure of the produced oxide layers was investigated by high-resolution transmission electron microscopy (HR-TEM). The different specimens for HR-TEM were cross-cut slices prepared by means of a focused ion beam (FIB) technique on a SEM dual beam facility (FEI Helios 600). The slices were extracted at an acceleration voltage of 30 kV and different beam currents. The last polishing step was done at 5 kV in order to reduce possible material amorphisation and defect formation. A JEOL ARM 200F – cold FEG UHR – transmission electron microscope operating at 200 kV and equipped with a Cs corrector was used for HR-TEM observations.

In scanning mode (STEM), EDX analyses were obtained using a JEOL CENTURIO energy-dispersive X-ray spectrometer with a probe size of 1 nm. The quantification limit of the EDS detector is ± 1 at.%. EDX/STEM element distribution maps recorded over various areas were usually produced by using 1 measurement point per nm, an acquisition time of 1 ms per data point and by repeating 20 scans over the same area. In addition, EDX line-scan profiles were also performed with an acquisition time of 1 min per measurement point.

Chapter III - Sequential run of the PEO process

III.1 Introduction of the chapter III

The present chapter aims at contributing to a better understanding of the physical mechanisms that allow the coating growth under discharge regime while keeping in mind the necessity to decrease the energy consumption of the PEO process, as well as improving the produced coating quality in terms of its microstructure. For this purpose, the main idea consists in investigating the PEO process by using sequential treatments with various set of electrical parameters, mainly by applying various ratio of charge quantity (RCQ) to the electrodes. Particularly, two very different RCQ were considered in this study, RCQ = 0.9 and 6.0. They were selected because they are known to result in opposite effects in terms of the produced PEO coating morphology and the electrical energy consumption. The effects of a sudden modification of the electrical conditions in the course of a PEO process is closely investigated and discussed by taking into account the correlation between several criteria based on the process monitoring data (voltage- and current-time responses), the MDs behaviour (light emission, surface density, spatial distribution and size) and the material characterization (thickness, porosity and element composition). Comparisons with results collected from reference treatments run within a single sequence are also considered for discussion.

III.2 Specific experimental procedure

III.2.1 Material and electrolyte

In the present work samples made of a Al2024 aluminium alloy were PEO processed. Their chemical composition of the alloy is reported in Table II-2. They were processed in a solution of potassium hydroxide ($[\text{KOH}] = 1 \text{ g}\cdot\text{L}^{-1} \cong 0.018 \text{ mol}\cdot\text{L}^{-1}$) and anhydrous sodium silicate ($[\text{Na}_2\text{SiO}_3] = 1.65 \text{ g}\cdot\text{L}^{-1} \cong 0.014 \text{ mol}\cdot\text{L}^{-1}$) diluted in deionized water. The electrical conductivity and pH values were $2.8 \text{ mS}\cdot\text{cm}^{-1}$ and 12.5, respectively.

III.2.2 Variation of the electrical conditions

As reported in Table III-1 and illustrated in the adjacent corresponding figures, various sequential PEO treatments were performed by changing the value of the charge quantity ratio (RCQ) during the

process. The anodic current amplitude was set at $I_p = 20$ A for a duration of 3.5 ms, providing thus an anodic current density of $50.5 \text{ A}\cdot\text{dm}^{-2}$ and delivering to the sample surface an anodic charge of $Q_p = 61$ mC per period. It is also worth noting that the two RCQ values considered in this study were designed by adjusting only the waveform of the cathodic current pulse, while maintaining the waveform of the anodic one unchanged. In such a way, treatments with $\text{RCQ} = 0.9$ were conducted at a frequency of 100 Hz, a negative pulse amplitude of $I_n = 11.8$ A and a duration of $t_c = 6.1$ ms, thus providing a cathodic charge of $Q_n = 68.4$ mC. For $\text{RCQ} = 6.0$ the respective values were 200 Hz, $I_n = 11.9$ A, $t_c = 1.15$ ms and $Q_n = 10.2$ mC. For all the sequenced treatments investigated, the samples were systematically processed for 20 min with a first RCQ value. At 20 min processing, the current supply was switched to the second RCQ value without stopping the PEO treatment. Process continued with this second RCQ value for 30 min. Consequently, the total duration of all the sequential PEO treatments investigated was equal to 50 min. In parallel, and for comparison reasons, four reference treatments were also conducted and they consisted of single PEO treatment runs with the same RCQ values for 20 and 50 min (see Table III-2).

Table III- 1. Electrical parameters depicting numerical values of charge quantity, current amplitude, frequency and duration of the applied pulses.

RCQ	Q_p (mC)	Q_n (mC)	Waveform
0.9	61	68.4	
6	61	10.4	

III.2.3 *In situ* diagnostic of the PEO process

As described in chapter II, *in situ* diagnostic of the PEO process was performed by recording current and voltage waveforms simultaneously with light emission. As a complement, by using a high

speed camera (Photron SA1.1), video recordings of the MDs were precisely conducted at time when the transition from the first RCQ to the second one occurs. Only the lower part of the sample is filmed over an area of 5.4 cm^2 ($30 \times 18 \text{ mm}^2$) providing a spatial resolution of $0.015 \text{ mm}^2/\text{pixel}$, which is at least three times lower than the average area of MDs that were detected in the experiments. The acquisition rate was fixed at 150 000 frames per second that corresponds to a time resolution of $6.6 \text{ }\mu\text{s}$.

III.2.4 Ex-situ characterization of the PEO coatings

Identification of the crystallographic phases through the coatings was made by means of X-ray diffraction measurements while SEM microscopy was used for the observation of the surface and cross-section morphology. Estimations of the thickness and the void fraction of the coating were conducted on cross-section SEM micrographs by using image processing that discriminates the coating from the substrate and the surrounding molding resin. The thickness and the fraction of voids were determined as the average values of 10 measures taken on cross-section over 10 different positions (every $500 \text{ }\mu\text{m}$). Moreover, it is necessary to clarify that voids correspond to cavities throughout the coatings that are larger than $1 \text{ }\mu\text{m}$ in diameter, finer porosities being not detected after image processing. Finally, the chemical composition and the distribution of elements through the synthesized oxide layers were determined by EDX analyses on sample cross-sections.

III.3 Results on the in-situ diagnostic of the PEO process

III.3.1 Establishment of the “soft” regime

Figure III-1 shows the time evolution of the anodic voltage amplitude for the sequential treatments investigated as well as their reference treatments consisting in a single sequence. As the process starts, all curves show a quite similar trend with a strong increase in the voltage amplitude within the first seconds. As previously reported in the chapter I, during this early stage, an initial amorphous oxide thin film grows with no visible micro-discharges (MDs) while a bluish luminescence and an intense gas release are visible all over the sample surface [101]. The point at which the slope of the voltage curves significantly reduces (at about 620 V) is commonly designated as the dielectric breakdown voltage of the formed oxide layer. Once this specific voltage value is reached, the ignition of small blue-white MDs starts over the processed surface [32,60,64]. As the process goes on, the anodic voltage amplitude continues to increase with a much lower rate and the visible MDs become fewer and larger and they gradually turn into orange-red colour.

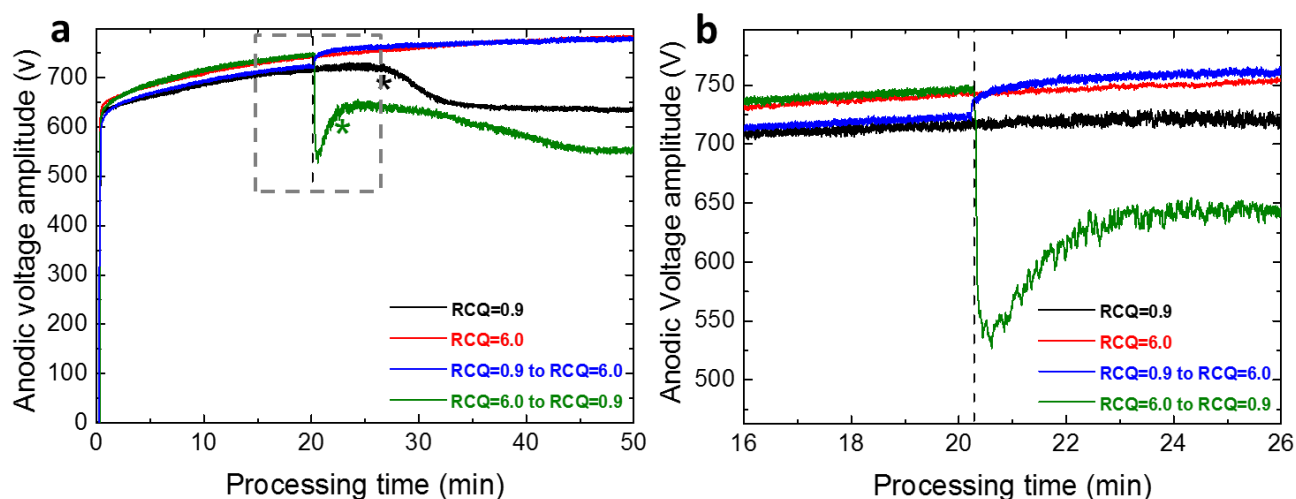


Figure III - 1. a) Time evolution of the anodic voltage amplitude for a set of treatments involving RCQ = 0.6 and RCQ = 6.0 conditions. The vertical dash line indicates the switching time from first to the second sequence. Stars (*) indicate the time of transition into “soft” regime. b) Close-up of the switching point.

It can also be noticed that during this stage, the anodic voltage amplitude exhibits slight differences depending on the applied electrical conditions. Indeed, right before the switching point that occurs at 20 min, the anodic voltage reaches 726 ± 5 V for the treatment performed with the low RCQ (RCQ = 0.9) while it reaches 755 ± 5 V for the treatment performed with the high RCQ (RCQ = 6.0). Right after 20 min, a significant anodic voltage drop is observed for the treatment that switches from the high RCQ to the low one while a slight voltage jump is noted for the reverse sequence (highlighted in Fig. III-1b). Particularly for the first, the anodic voltage decreases suddenly from 755 ± 5 V to 540 ± 10 V over less than 5 s following the transition, then increases for a period of 3 min and finally decreases with a much lower rate to stabilize at about 558 ± 10 V until the end of the treatment. For this specific sequence treatment, it is also worth noting that from the switching time at 20 min to the end of the process at 50 min, the anodic voltage amplitude constantly remains lower than for all the other PEO treatments investigated. The opposite behaviour is observed for the process that switches from low RCQ (RCQ = 0.9) to the high one (RCQ = 6.0). Indeed, the anodic voltage amplitude increases rapidly within few minutes after the switch to values close to the corresponding reference process and gradually reaches approximately 770 ± 10 V by the end of the treatment.

Table III- 2. PEO treatments performed with the associated time of the "soft" regime appearance, the average thickness and the porosity of the overall coatings and the specific energy consumption.

	First sequence from 0 to 20 min	Second sequence from 20 to 50 min	t_{SR}^* (± 1 min)	Overall Thickness (± 5 μm)	Average growth rate ($\mu\text{m}/\text{min}$)	Void fraction (± 3 %)	Specific Energy Consumption (± 1 $\text{kWh}\cdot\text{m}^{-2}\cdot\mu\text{m}^{-1}$)
Reference treatments	RCQ = 0.9	-	-	35	1.75	7	12
	RCQ = 6.0	-	-	53	2.65	15	13
	RCQ = 0.9	RCQ = 0.9	32	62	1.24	3	17
	RCQ = 6.0	RCQ = 6.0	-	70	1.4	13	25
Sequenced treatments	RCQ = 0.9	RCQ = 6.0	-	76	1.52	12	15
	RCQ = 6.0	RCQ = 0.9	21	109	2.18	5	11

* t_{SR} = Time of the "soft" regime appearance

As previously reported, the transition to the "soft" regime is associated with a gradual decrease in the maximum anodic voltage [19,35]. For the reference treatment conducted only with RCQ = 0.9, which is until now the well-established condition that promotes the appearance of the "soft" regime, Fig. III-1 shows that this transition starts at approximately 27 min (marked with *) and is fully established at about 32 min. Table III-3 reports the time at which the "soft" regime appears for all the PEO treatment investigated in this study (noted as t_{SR} in Table III-3). On the other hand, by using sequential treatment, especially when switching from the high RCQ (RCQ = 6.0) to the low one (RCQ = 0.9), Fig. III-1 evidences a sudden drop of the anodic voltage right after the switching point at 20 min. It suggests an almost immediate transition into the "soft" regime at approximately 21 min. Although, the voltage gradually increases for the next 4 min after the switching point, before it starts to decrease again, it remains that optical and acoustic observations confirm the fact that the process has really entered the "soft" regime mode right after 20 min (a sudden noise reduction and light emission attenuation was noted). Thus, it is apparent that this specific sequenced treatment (from RCQ = 6.0 to 0.9) triggers earlier the transition to the particular PEO "soft" regime, which could have a beneficial effect for both the morphology of the final produced coating and the energy consumption. This aspect will be addressed later in this chapter.

III.3.2 Delay in the micro-discharges appearance

During a PEO treatment, micro-discharges usually appear during the anodic polarization of the processed sample. More recently, by using time-resolved optical techniques, it was established that their ignition is delayed with respect to the applied anodic current [67]. It was further proved that this

delay evolves with processing time and is strongly dependent upon the electrical parameters applied, mainly the RCQ. As shown in Fig. III-2, this delay in the micro-discharges appearance, (noted Δt) was defined as the time difference between the rise of the anodic current and the detection of light emitted from the processed surface. Fig. III-2a and b also illustrate the reproducible measuring protocol that allows evaluating this delay for all the conducted experiments, regardless the conditions or the moment of measurement.

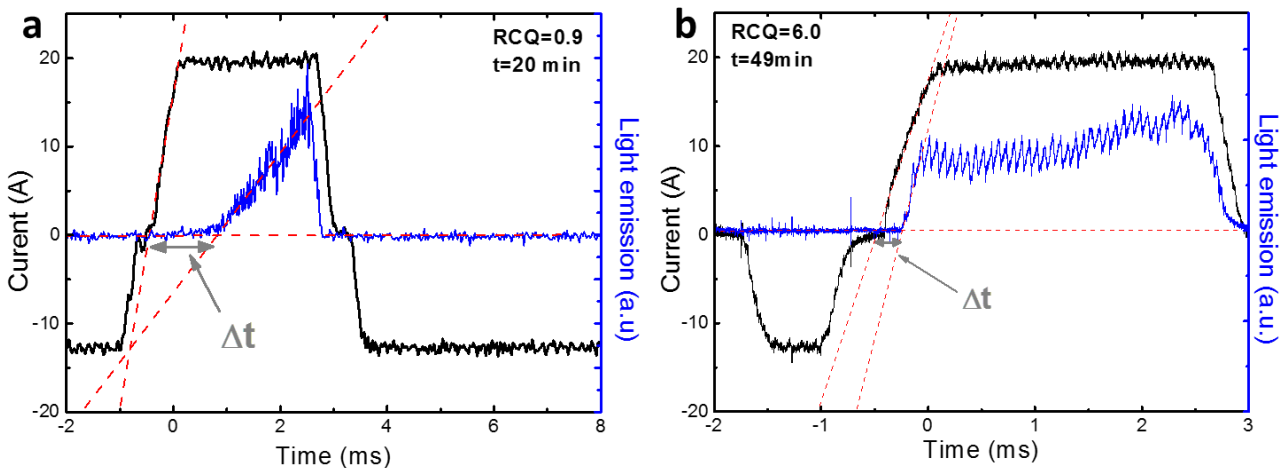


Figure III - 2. Delay in MDs ignition with respect to the applied anodic current.

Chronograms in Fig. III-3 show the variations of the light emission, the current and the voltage over a period of 10 ms for the two different sequenced treatments investigated and at different processing times *e.g.* after starting the process at 5 min, right before the switching point at 19 min 55 s, right after the switching point at 20 min 05 s and at the end of the process at 49 min 55 s. The first row corresponds to the treatment starting with the high RCQ value (RCQ = 6.0) and switching to low one (RCQ = 0.9), while the second row is associated to the reverse sequence.

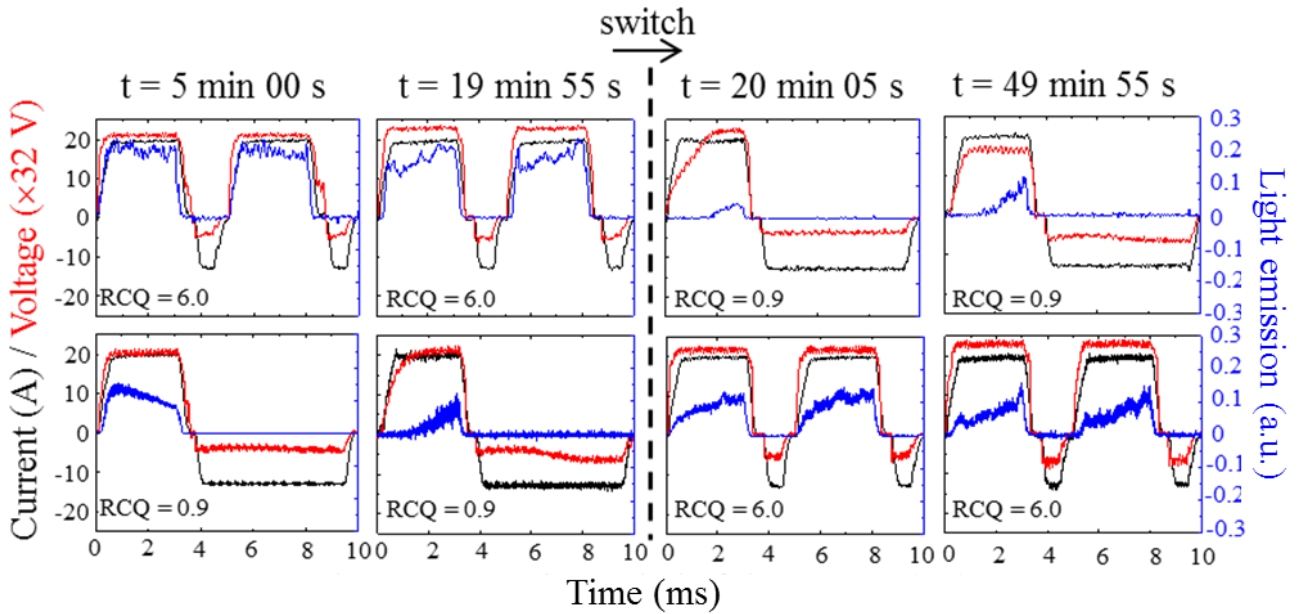


Figure III - 3. Evolution of the light emission (blue) with the corresponding current (black) and voltage (red) signals recorded over 10 ms for the sequenced PEO treatments involving RCQ = 6.0 and RCQ = 0.9. The vertical dash line (---) indicates the switching time of the RCQ conditions at 20 min.

Concerning the light emission, and as usually encountered under the processing conditions used in this study, light is only detected during the anodic polarization since MDs only appear during the anodic alternation of the current pulse [33,35,108]. Chronograms also evidence that the detected light is more or less delayed with respect to the rising edge of the anodic current pulse. In parallel with these chronograms, Fig. III-4 reports the evolution of this delay Δt as a function of the processing time for each PEO treatment carried out.

At the beginning of the process (at 1 min), and irrespective of the investigated conditions, the delay is quite negligible (less than 10 μ s) which means that MDs appear quite simultaneously with the applied anodic current. Until the switching point that will occur at 20 min, Fig. III-4a shows that the delay gradually increases with the processing time. It increases faster using the low RCQ (RCQ = 0.9) than the high one (RCQ = 6.0). Right before 20 min (at 19 min 55 s), the delay is long and reaches 1.19 ± 0.01 ms for the treatment performed with the low RCQ while it remains short and reaches only 0.14 ± 0.01 ms for the treatment conducted with the high RCQ.

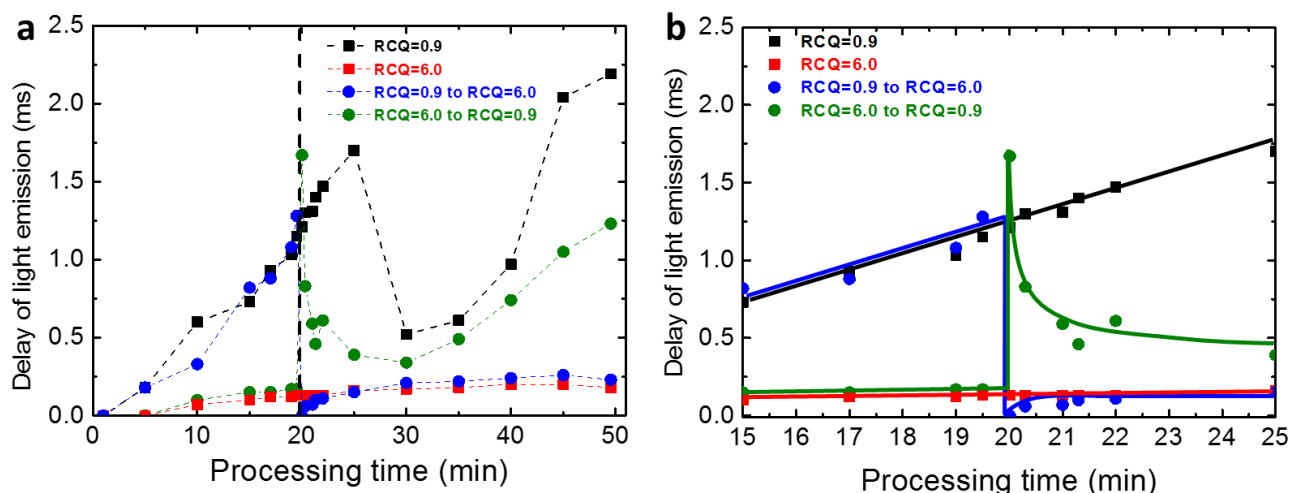


Figure III - 4. a) Evolution of the delay of light emission as a function of processing time for the different PEO processing conditions. Vertical dash line (---) indicates the switching time of the RCQ conditions. b) Close-up of the delay evolution close to the switching point at 20 min.

Right after 20 min, Fig. III-4b clearly shows that the delay Δt suddenly changes in different proportions depending on the sequenced treatment used. When switching from the low RCQ to the high one, the delay Δt instantaneously drops from 1.19 ± 0.01 ms to about 0.02 ± 0.01 ms. More interestingly, the delay Δt reached right after the switching time is largely lower than the delay measured at the same processing time with the corresponding reference treatment conducted with the high RCQ only ($\Delta t = 0.14 \pm 0.01$ ms). The opposite behavior is strictly observed for the reverse sequenced treatment. Indeed, when the process switches from the high RCQ to the low one, the delay Δt suddenly jumps from 0.14 ± 0.01 ms to 1.62 ± 0.01 ms. Similarly, it is also worth noting that the delay Δt reached right after the switching time is largely higher than the delay Δt measured at the same processing time with the corresponding reference treatment conducted with the low RCQ only ($\Delta t = 1.19 \pm 0.01$ ms).

Finally, after a certain period of time following the switching time - from a few to tens of minutes depending on the sequenced treatment used - Fig. III-4a shows that the delay in the MDs appearance tends to converge and to recover the value that it would have attained by using the corresponding reference treatment.

III.3.3 Time constant of the anodic voltage-time response

Concerning the voltage-time response recorded over one pulse period of the anodic current, chronograms in Fig. III-5 show that the voltage signal exhibits a transient regime during the first milliseconds following the beginning of the anodic pulse. The duration of this transient regime may be short or long, depending on the applied electrical conditions. As reported in a previous study, the

experimental data of the anodic voltage-time response were adequately fitted by an exponential function giving access to the time constant (noted τ) of this transient regime [67].

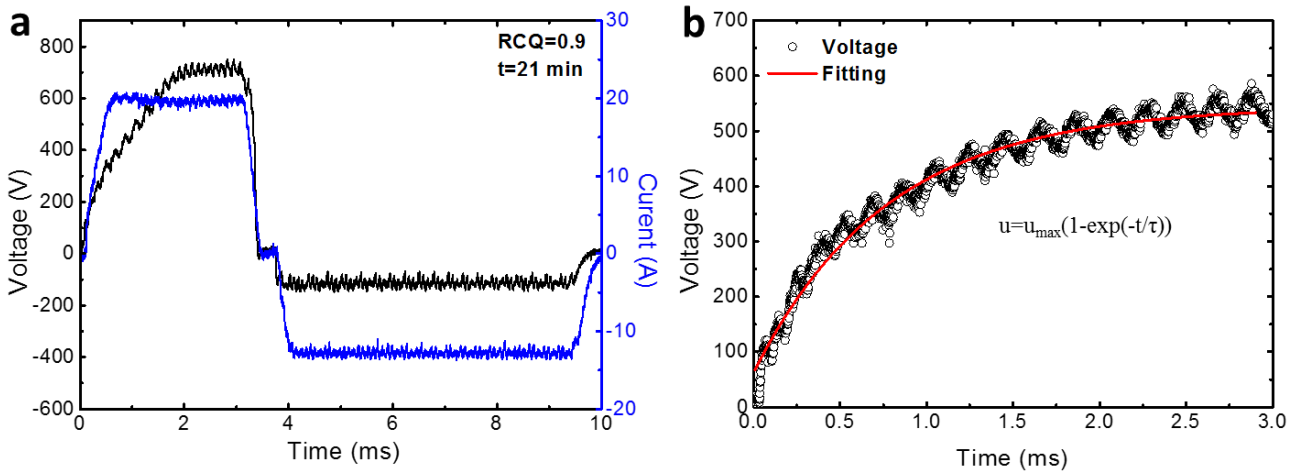


Figure III- 5. a) Voltage response to the applied current waveform and b) fitting example of experimental data during the voltage transient regime.

Fig. III-6 reports the evolution of this time constant τ as a function of the processing time for each PEO treatment performed in this study. At the beginning of the process (at 1 min), and irrespective of the investigated conditions, the time constant τ is low (less than 0.1 ms). Until the switching point at 20 min, the time constant gradually increases with processing time. It increases more rapidly using the low RCQ (RCQ = 0.9) than the high one (RCQ = 6.0). Right before 20 min (at 19 min 55 s), the time constant τ is long and reaches 0.43 ms for the treatment performed with the low RCQ while it remains short and reaches only 0.16 ms for the treatment conducted with the high RCQ. In addition, it is also worth noting that the evolutions of the delay Δt (Fig. III-4) and the time constant τ (Fig. III-6) for the different RCQ investigated are similar which is in good agreement with previous observations [67].

Right after 20 min, Fig. III-6b evidences that the time constant τ suddenly changes in different proportions depending on the sequenced treatment applied. When switching from the low RCQ to the high one, the time constant τ behaves like the delay Δt in the MDs appearance since it suddenly drops from 0.43 ms to about 0.09 ms. Interestingly, the time constant τ reached right after the switching time is significantly lower than the time constant measured at the same processing time with the corresponding reference treatment conducted with the high RCQ only ($\tau = 0.16$ ms). In addition and as already observed for the delay Δt , the opposite behaviour is strictly observed for the reverse sequence. Indeed, when the process switches from the high RCQ to the low one, the time constant suddenly jumps from 0.16 ms to 1.06 ms. For this specific sequenced treatment, the time constant τ

reached right after the switching time is largely higher than the time constant τ measured at the same processing time with the corresponding reference treatment conducted with the low RCQ only ($\tau = 0.43$ ms). Finally, it is observed that after a certain period of time following the switching time - from a few to tens of minutes depending on the sequenced treatment used - the time constant of the voltage-time response tends to converge and to recover the value that it would have attained by using the corresponding reference treatment.

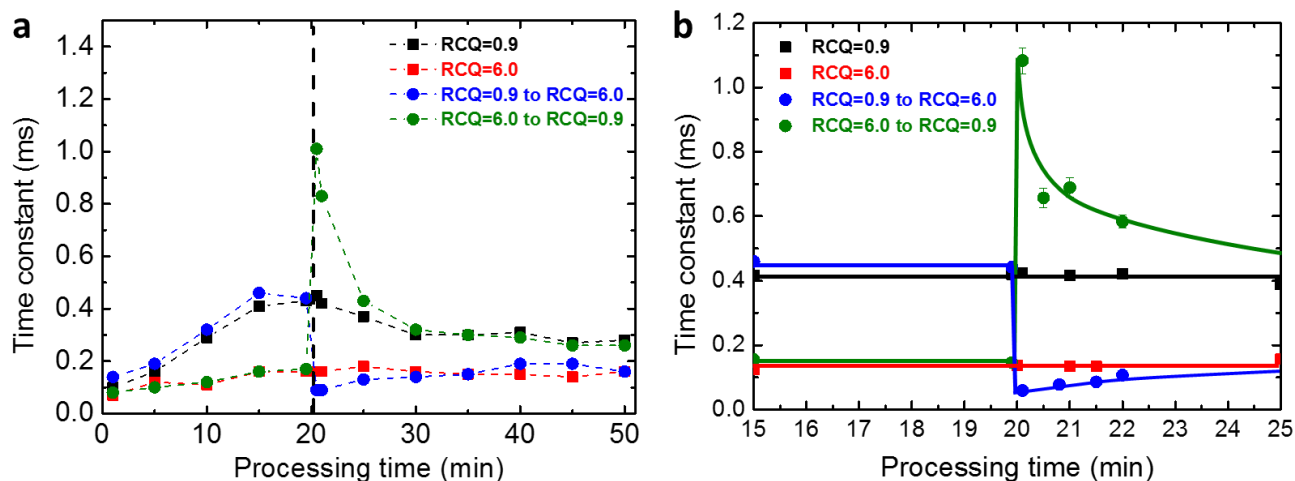


Figure III-6. a) Evolution of the time constant of the anodic voltage transient as a function of processing time for a pair of different PEO processing conditions investigated (RCQ = 6,0 and RCQ = 0,9). The vertical dash line (---) indicates the switching time of the RCQ conditions. b) Close-up of the time constant evolution at the switching point at 20 min.

III.3.4 Properties of the micro-discharges

In order to investigate the behaviour of the micro-discharges during PEO sequenced treatments, synchronised fast video recordings and electrical measurements were conducted exactly during the transition from one RCQ to another. Fig. III-7 shows the evolution of the number of MDs (blue) that were detected as a function of the corresponding current waveforms (black) right before and right after the switching point at 20 min for the two different sequenced treatment investigated. Fig. III-7a is associated to the sequenced treatment that switches from the low RCQ (RCQ = 0,9) to high RCQ (RCQ = 6,0) while Fig. III-7b corresponds to the reverse sequence. Additionally, for each sequence, an inset illustrates a captured frame from the recorded video, providing a good insight into the behaviour and properties of the MDs, such as their size and intensity.

Right before the switching point at 20 min, the sample processed with the low RCQ (RCQ = 0,9) undergoes much more MDs than the one processed with the high RCQ (RCQ = 6,0). Indeed, right before the switching point, the surface density of the MDs is about $6.5 \text{ mm}^{-2}\text{ms}^{-1}$ and $1.12 \text{ mm}^{-2}\text{ms}^{-1}$

for a RCQ of 0.9 and 6.0, respectively. In contrast, and as it can be seen from the captured frames, the size of the MDs increases with the increase in the RCQ. Indeed, right before the switching point, the average area of the MDs is about 0.057 mm^2 and 0.105 mm^2 for a RCQ of 0.9 and 6.0, respectively. This behaviour is consistent with previous work which established that the surface density of MDs decreases as the process goes on, this decrease being much faster as the RCQ gets higher, while the average size of the MDs gradually increases with the process, this increase being much faster for higher RCQ [20,35,67]. In addition, and as mentioned previously concerning detection of the light emitted from the processed samples, chronograms in Fig. III-7 also confirm that the occurrence of the MDs is delayed with respect to the anodic current pulse, this delay remaining higher for the low RCQ.

Right after 20 min, when the process enters into the second sequence, Fig. III-7 evidences that transition is associated with a sudden change in the MDs behaviour. Indeed, when the process switches from low RCQ to the high one, both the surface density and the average size of the MDs suddenly increase from $6.5 \text{ mm}^2\text{ms}^{-1}$ to $10.5 \text{ mm}^2\text{ms}^{-1}$ and from 0.057 mm^2 to 0.091 mm^2 , respectively. The opposite behaviour is observed for the reversed sequence since both the surface density and the average size of the MDs suddenly decrease from $1.12 \text{ mm}^2\text{ms}^{-1}$ to $0.28 \text{ mm}^2\text{ms}^{-1}$ and from 0.105 mm^2 to 0.022 mm^2 , respectively. Said differently, numerous and large MDs are promoted by switching from the low RCQ to the high one in the course of the process while less numerous and smaller size MDs are promoted with the reverse sequence.

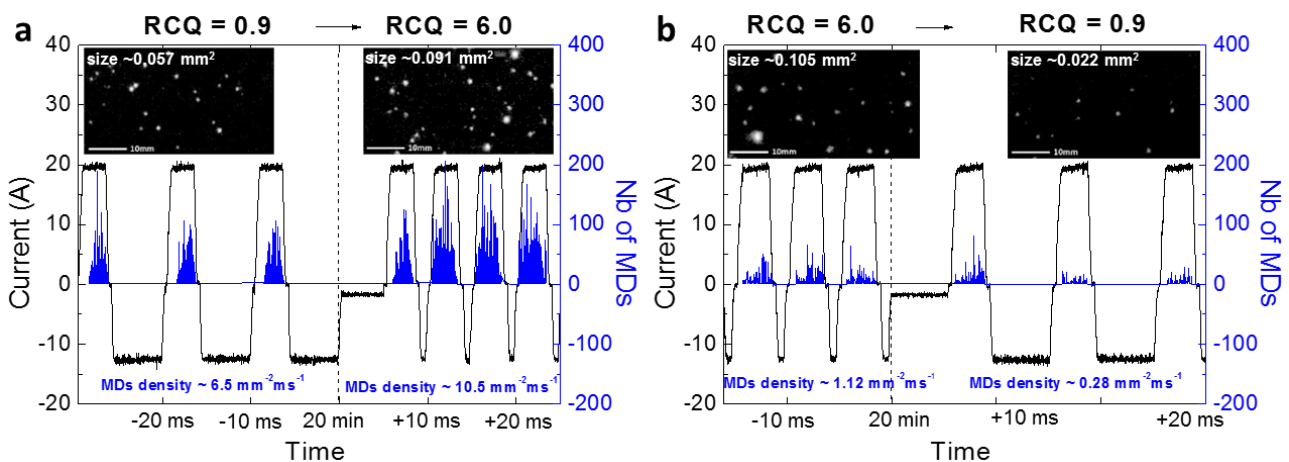


Figure III-7. Evolution of the number of micro-discharges (blue lines), detected using fast video imaging, with the corresponding current signal (black lines) recorded exactly when the PEO process switches from one RCQ to the second one. Vertical dash lines (---) indicate the switching points. The insets are frames captured from the movie of the processed sample recorded with fast video camera. a) For the sequenced treatment that switches from the low RCQ = 0.9 to the high RCQ = 6.0. b) For the sequenced treatment that switches from the high RCQ = 6.0 to the low RCQ = 0.9.

A point worth mentioning here is the effect of the cathodic polarisation on the ignition of the MDs and, thus, their delay in appearance. Nominé *et al.* [109] highlighted the significance of cathodic polarisation on anodic micro-discharges. By comparing the PEO process under unipolar and bipolar current modes they showed that the overall light emission and the size of MDs are decreased when the anodic alternation follows a previously generated cathodic one. Here a clear effect of the cathodic polarisation can be seen in Fig. III-7a. Before the transition to the second sequence (RCQ = 0.9), the MDs are delayed with respect to the applied current, as it is evidenced by the detections during the three anodic pulses before the switch (20 min). Once the transition to the second sequence is established, the first anodic pulse has not been preceded yet by a cathodic one in the new conditions (RCQ = 6.0). As a consequence, MDs still exhibit a similar delay in their appearance during this first pulse. It is only after the first cathodic pulse is generated that the micro-discharges appear almost simultaneously with the current rise of the subsequent anodic pulse and maintain this behaviour for all the pulses that follow in Fig. III-7a. Similar effect also appears in Fig. III-7b, where the intensity of the emitted light is much higher at the first half period after the switching than for the subsequent ones. This clearly shows that cathodic polarisation plays a key role in the PEO process and particularly in the properties of the micro-discharges.

III.4 Results on the ex-situ characterization of the PEO coatings

III.4.1 Morphology of the PEO coatings

SEM micrographs in Fig. III-8 compare the top-surface views of the different PEO coatings produced in the present study. All surfaces exhibit the typical morphology of the PEO coatings consisting in “pancake”-like structures with voids of about 1 to 100 μm in diameter. These voids are usually associated with discharge channels that take place during the PEO process [7,31,35]. This is particularly obvious for the oxide layer grown for 20 min under the high RCQ (RCQ = 6.0) which exhibits a “crater”-like structure with large voids up to 10 μm in diameter. In contrast, the use of the low RCQ (RCQ = 0.9) for 20 min results in the formation of a “sponge”-like structure with fine open pores less than 1 μm in diameter. After 50 min processing time, these differences are much more pronounced. Moreover, Fig. III-8 also shows that the implementation of sequenced treatments has a significant effect on the morphology of the top-most surface compared to the associated reference treatments. Interestingly, by switching from low RCQ to the high one, the fine “sponge-like” structure observed at 20 min turns into a rough “crater”-like structure at 50 min. The opposite morphological transformation is strictly observed for the reverse sequence.

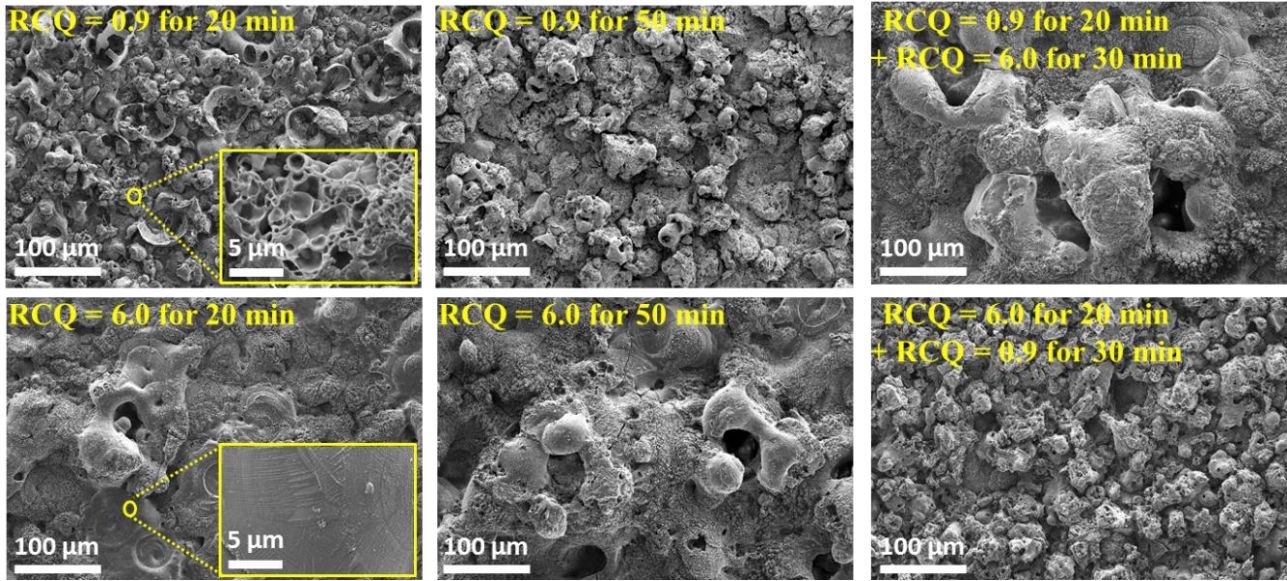


Figure III-8: SEM top-surface views of the PEO oxide layers elaborated under the different PEO processing conditions investigated and summarized in Table II-2.

SEM micrographs in Fig. III-9 show the corresponding cross-sectional views of the same samples. From a general point of view, the synthesized oxide layers exhibit the typical morphology of PEO coatings usually consisting of three distinct regions, more or less dependent on the processing conditions: a thin “barrier” layer adjacent to the aluminium substrate (not visible at the current magnification of Fig. III-9), a thick compact inner sublayer and a highly porous outer sublayer with large cavities. In parallel with these cross-sectional views, Fig. III-10 reports both the overall thickness of the oxide layer (thickness of the inner and the outer sublayers) and the fraction of voids (up to 1 μm in diameter) for the treatments carried out for 50 min. Concerning the reference treatments, the use of the high RCQ results in a thick overall coating ($70 \pm 5 \mu\text{m}$) with large cavities through the outer sublayer (void fraction $13 \pm 3 \%$) while the use of low the RCQ leads to a slightly thinner ($62 \mu\text{m} \pm 5 \mu\text{m}$) but much more compact coating (void fraction $\sim 3 \pm 3 \%$). Moreover, and as already observed from the top-surface views, Fig. III-9 and Fig. III-10 also put in evidence that the use of sequenced treatments affect the final cross-sectional morphology of the coatings compared to the corresponding reference treatments. The sequence treatment involving the transition from the low RCQ to the high one has a detrimental effect on the morphology of the oxide layer. Indeed, although the overall thickness slightly increases ($76 \pm 5 \mu\text{m}$), the fraction of voids significantly increases ($12 \pm 3 \%$) due to the presence of large cavities throughout the thickness. In contrast, the reverse sequence has a beneficial effect on the morphology of the oxide layer since the overall thickness significantly increases ($\sim 109 \pm 5 \mu\text{m}$) while maintaining a low fraction of voids ($\sim 5 \pm 3 \%$).

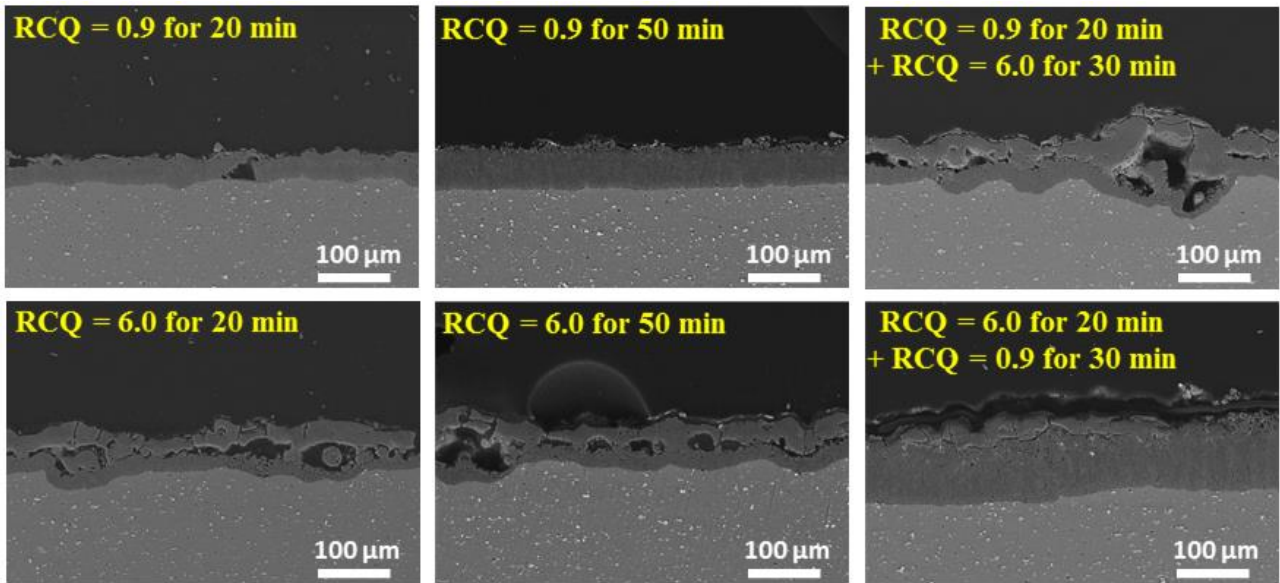


Figure III-9: SEM cross-sectional views of the PEO oxide layers elaborated under the different PEO processing conditions investigated and summarized in Table III-2.

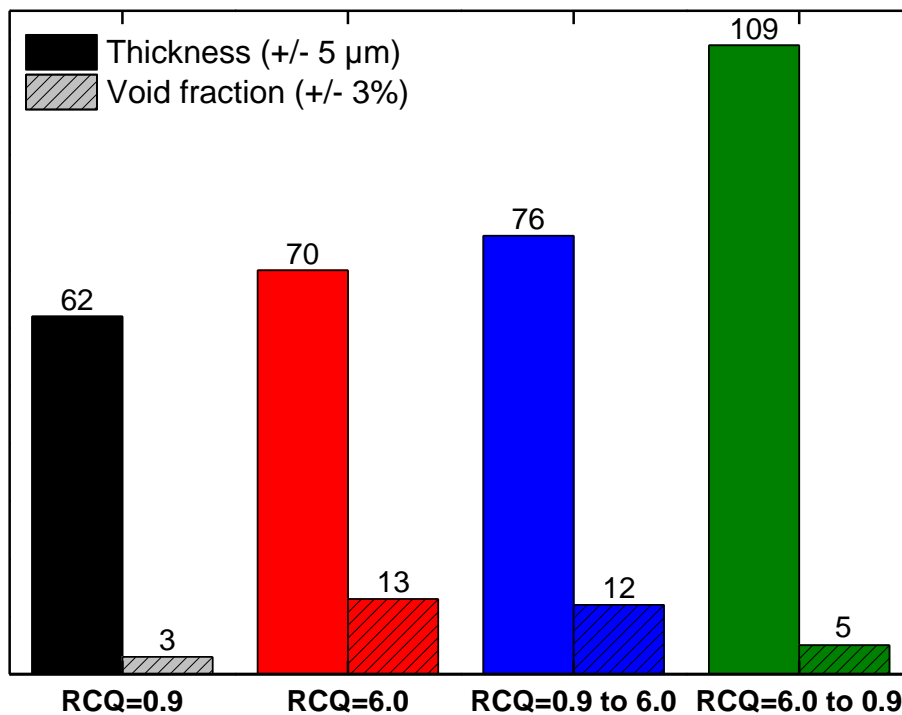


Figure III-10. Measured thickness and estimated void fraction of the PEO oxide layers elaborated for 50 min under the different processing conditions investigated and summarized in Table III-2.

III.4.2 Crystallographic phases in PEO coatings

Figure III-11 shows XRD patterns collected on oxide layers produced from single RCQ treatments with values of 0.9 and 6.0, as well as sequential treatments involving these two RCQ values. Analysis of these patterns shows that all the produced coatings are mainly composed of α - and γ -phases of

alumina. In addition, it is seen that the relative intensity of peaks corresponding to α -phase is largely increasing with respect to γ -phase when high charge ratio is involved in the process, i.e. single treatment with RCQ = 6.0 and sequenced treatments. Moreover, transitional δ -phase was observed, which also exhibited an increase in these cases. These findings are consistent with the existing literature [85].

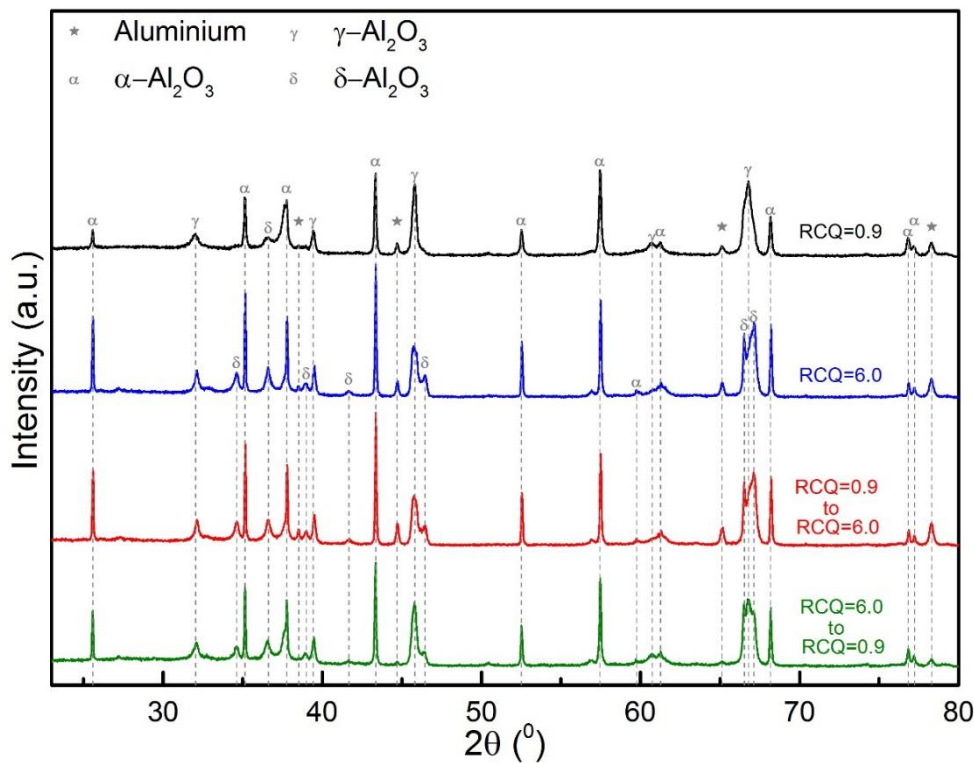


Figure III-11. XRD patterns of the PEO oxide coatings produced under different experimental conditions (Table III-2).

III.4.3 Element distribution in PEO coatings

Figure III-12 compares the EDX element distribution maps recorded on the cross-section of the samples processed with the reference treatments performed for 50 min and with the specific sequenced treatment (RCQ = 6.0 for 20 min followed by RCQ = 0.9 for 30 min) that provides the thickest coating with a compact morphology. Whatever the applied conditions, the oxide layers mainly contain Al, O, Si and K elements. Al comes from the Al2024 aluminium alloy substrate while O, Si and K come from the electrolyte. EDX maps also evidence that Si and K species are preferentially located throughout the outer porous sublayer while the inner sublayer is mainly composed of Al and O. This observation is consistent with previous studies which also showed that open cavities, in contact with the electrolyte, incorporate elements from the electrolyte [110–112].

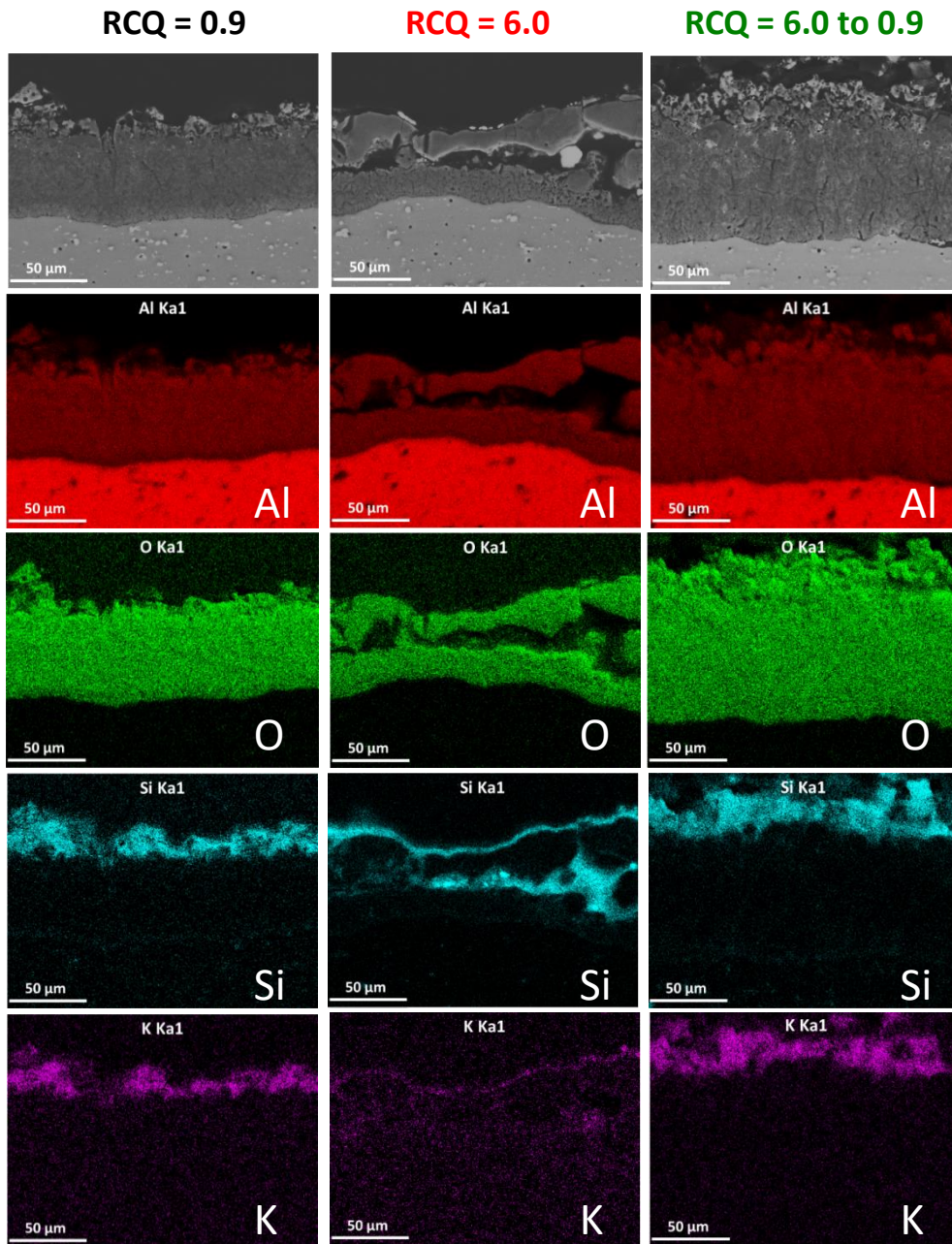


Figure III-12. SEM cross-sectional views and the associated EDX element maps (Al, O, Si and K) of the PEO oxide layers elaborated for 50 min with the reference treatments (RCQ = 0.9 and RCQ = 6.0) and with the sequenced treatment (RCQ = 6.0 for 20 min followed with RCQ = 0.9 for 30 min)

Nevertheless, some differences in the element distribution throughout the oxide layer are significant when comparing the different treatments investigated. In the case of the reference treatment conducted with the low RCQ, Si and K are quite evenly distributed throughout the outer sublayer, which is not the case for the reference treatment performed with the high RCQ. In the specific case of the sequenced treatment that switches from the high RCQ to the low one, Si and K seem to be more concentrated and they are homogeneously distributed throughout a thicker outer

sublayer, which could certainly provide a better corrosion protection of the aluminium alloy substrate. Indeed, some works that carried out PEO processes of aluminium in electrolyte with various amount of diluted silicate have established that the presence of such a silicon-rich barrier layer, mainly made of an amorphous silica SiO_2 or alumino-silica phase (typically $(\text{AlO}_3) \cdot (\text{SiO}_2)$), improve both wear resistance and the corrosion resistance of the aluminium alloys [110–112]. On that point, further corrosion experiments, mainly conducted via electrochemical impedance spectroscopy, should be devoted to verify a potential enhancement of the corrosion resistance of the samples processed with sequenced treatments, especially the one that switches from the high to the low RCQ.

III.5 Discussion of the results

The present discussion focuses on the explanation of the experimental results by establishing relationship between the optical characterization of the micro-discharges, the morphological characterization of the produced PEO coatings and the various applied electrical conditions. In particular, making more explicit the link between the delay Δt in the MDs appearance, the time constant τ of the voltage-time response and the MDs properties is needed first to a better understanding of the key role played by the MDs on the morphology of the growing oxide layers. Finally, on the basis of the combined experimental results, the interest in using sequential PEO treatments will be discussed from the point of view of the energy consumption.

III.5.1 Discussion about a mechanism of charge accumulation

Fig. III-13 shows a schematic representation of the proposed mechanism of charge accumulation that could explain the relationship between the delay Δt in the MDs appearance, the time constant τ of the voltage-time response and the MDs properties, especially when the process suddenly switches from one RCQ to the second one in the course of the PEO treatment.

At the beginning of the process, results have shown that the delay in the MDs appearance - correlated to the time constant of the voltage-time response – gradually increases with the processing time (Fig. III-4 and Fig. III-6). It also increases more rapidly using the low RCQ than the high one. It was previously established that the ratio of charge quantity controls the dynamic of establishment of a stable electrical double layer (EDL) at the electrolyte / oxide interface, which in turn, once established, governs the dielectric breakdown of the oxide layer and therefore the ignition of the MDs [67]. The dynamic of establishment of this EDL is mainly affected by the mechanism of charge accumulation taking place at the interface between the oxide and the electrolyte. Depending on the substrate polarization, charges (cations (H^+) and anions (OH^-)) that are expected to be the most

important species in terms of number density and mobility) are accumulated at this interface during every alternation of the current pulse. Namely OH^- species are accumulated during the anodic alternation and they are relaxed during the cathodic one, while the opposite occurs for H^+ species. As reported previously by Martin *et al.* [67], the mechanism of charge accumulation during anodic alternation of the current can be more or less balanced by a charge relaxation process during the following cathodic alternation. This relaxation of charges depends on the cathodic current waveform, more precisely on a combined effect of the cathodic amplitude and the time it is applied. When processing with high RCQ (RCQ = 6.0), the low value of these cathodic current parameters makes the accumulated charges relax incompletely. So, charges remain close to the interface and they accumulate much more rapidly during the subsequent anodic alternation. It results that the time needed to accumulate charge is short and breakdown occurs earlier with a short delay between the applied anodic current and the MDs appearance. It gives rise to large and long-lived MDs. In contrast, with the low RCQ - the amplitude of the cathodic current and the cathodic part duration being higher compared to the high RCQ - the charges that were accumulated during an anodic alternation are highly relaxed during the subsequent cathodic alternation. It results that accumulation of charges takes longer time. Consequently, the discharge ignition consecutive to the dielectric breakdown of the oxide layer occurs with a longer delay with respect to the rising edge of the anodic current. In this case, it gives rise to small and short-lived MDs. Moreover, the fact that both the delay in the MDs appearance and the time constant of the voltage-time response gradually increase with the processing time is explained by taking into account some evolutions in the morphological aspects of the growing oxide layer, particularly its gradual thickening and the development of fine porosities, the latter exhibiting a higher specific area and a higher charge storage capacity. Therefore, as the process goes on, more accumulated charges are needed to reach the dielectric breakdown voltage of the growing oxide layer resulting in a longer delay Δt and in a longer time constant τ .

Right before the switching point, although the oxide layer elaborated with the low RCQ remains quite compact (no large cavities up to 10 μm in diameter are visible throughout the thickness), SEM observations have revealed the presence of a fine “sponge”-like structure with very small porosities less than 1 μm in diameter at the top-most surface (Fig. III-8). This sponge-like structure exhibits a high specific area associated with a high charge storage capacity. In this case, right before the switching point, the accumulation of charges at the oxide / electrolyte interface is therefore mainly limited due to two joint effects, *i.e.* the application of a low RCQ (high extraction of electric charges during the high magnitude of the cathodic regime) onto a “sponge”-like top-most surface (high dispersion of charges through the fine porosities filled with the conductive electrolyte) (Fig. III-13a).

This explains why, right before the switching point, the delay in the MDs appearance and the time constant of the voltage-time response reached high values (Fig. III-4 and Fig. III-6). It is also in good agreement with experimental results on the MDs behaviour which are numerous and with small size (Fig. III-7) since they are finely distributed through the sponge-like structure. In contrast, SEM observations conducted on the sample processed for 20 min with the high RCQ have revealed large open cavities up to 10 μm in diameter throughout the outer oxide sublayer but no fine porosities at the top-most surface (Fig. III-8). Contrary to the “sponge”-like structure that develops under the low RCQ, this “crater”-like structure presents a lower specific area and a lower charge storage capacity. In this case, right before the switching point, the accumulation of charges is therefore strong due to the combined effects of a high RCQ (low extraction of electric charges during the low magnitude of the cathodic regime) and the thinness of the inner compact oxide sublayer underneath the open cavities (Fig. III-13b). This explains why the delay in the MDs appearance and the time constant of the voltage-time response remains short with the development of fewer MDs with larger size.

Interestingly, by suddenly switching the RCQ in the course of the process, the results have shown that the delay in the MDs appearance, the time constant of the voltage-time response and the MDs behaviour also suddenly change in opposite proportions depending on the sequenced treatment applied. If the electrical condition suddenly changes from the low RCQ to the high one, the previous oxide layer grown under the low RCQ – known to exhibit a sponge-like structure as previously discussed - is thus suddenly submitted to the high RCQ. In this case, right after the switching point, the electrical and the morphological conditions are met to promote the strongest and the most rapid accumulation of charges at the oxide / electrolyte interface. Indeed, on one hand, the dynamic of charge extraction from the surface suddenly becomes low due to the low magnitude of the cathodic current alternation, and, on other hand, the number of charges involved is high due to the high storage charge capacity of the sponge-like structure. Consequently, and as illustrated in Fig. III-13a, the MDs appear quite instantaneously with the rising edge of the anodic current that is in good agreement with the sudden drop of the delay in the MDs appearance and the time constant of the transient regime of voltage-time response. These combined effects also explain why this delay and this time constant reached lower values than the values obtained at the same processing time with the corresponding single treatment conducted at high RCQ. In addition, when the process suddenly turns into the new RCQ, the accumulation of charge becomes so strong that it results in the development of numerous and large-size MDs. MDs are numerous due to the fact that they develop throughout the network of fine porosities at the top-most surface of the oxide layer.

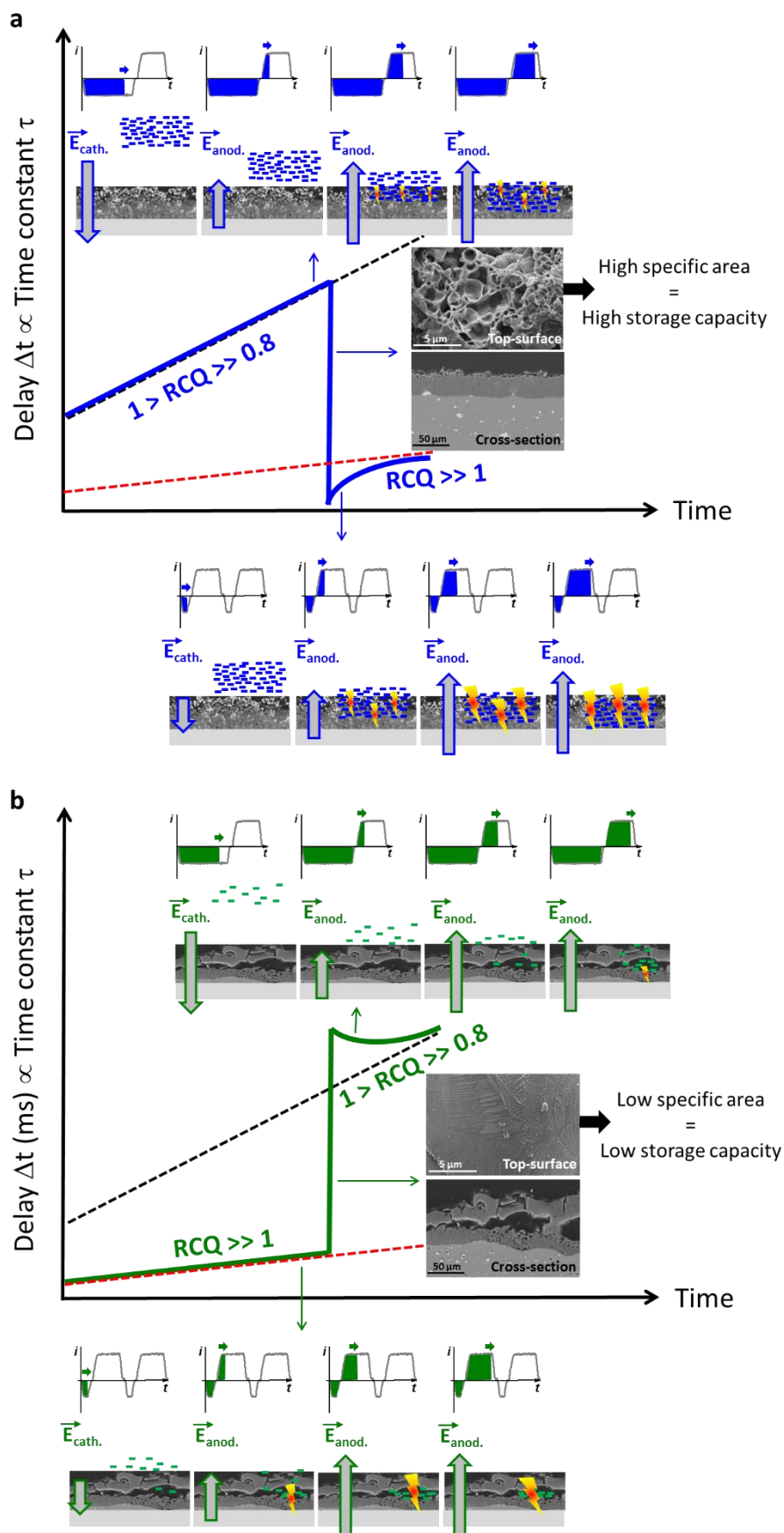


Figure III-13. Schematic model of combined effects of the ratio of charge quantity (RCQ) and the coating morphology on the micro-discharges properties exactly when the PEO process suddenly switches a) from a high RCQ (RCQ = 6.0) to a low RCQ (RCQ = 0.9) (blue line) and b) for the reverse sequence (green line)

For a similar reason, and as illustrated in Fig. III-13b, if the electrical conditions suddenly change from high to low RCQ, the mechanism of charge accumulation becomes inhibited by the combined effects of a high extraction of electric charges due to the high magnitude of the cathodic current alternation and by the limited number of charges involved in this dynamic of charge accumulation due to the lower storage capacity of the “crater”-like structure. Consequently, the dielectric breakdown is strongly delayed explaining why the delay in the MDs appearance and the time constant of the voltage-time response remains long, largely higher than the values obtained at the same processing time within the corresponding reference treatment at high RCQ (Fig. III-4 and Fig. III-6). Finally, for this specific sequenced treatment (from RCQ = 6.0 to RCQ = 0.9), the mechanism of charge accumulation is so inhibited at the oxide / electrolyte interface by the aforementioned causes that it gives rise to smoother MDs as experimentally observed (few and small-sized MDs right after the switching point in Fig. III-7).

III.5.2 Discussion about coatings improvement using sequenced PEO treatments

The results clearly show that the implementation of sequenced treatments has a significant effect on the coatings morphology compared to the associated reference treatments. These effects can be explained by considering the previous explanations on the relationship between the delay in the MDs appearance, the time constant τ of the voltage-time response and the MDs behaviour.

The sequenced treatment that switches from the high to the low RCQ value results in the thickest coating (109 μm) combined with a low fraction of voids (5 vol. %). Within this specific sequenced treatment, it is as if the thick overall oxide layer ($\sim 53 \mu\text{m}$) formed during the first sequence (RCQ = 6.0 for 20 min in Fig. III-9) is kept while the large cavities formed (up to 10 μm in diameter) are completely filled with alumina during the second sequence. These observations can be explained by considering the earlier transition into the beneficial "soft" regime during which the processed sample experiences smoother MDs regarding both their limited number over the processed surface and their smaller size (Fig. III-7b). During this “soft” regime, Cheng *et al.* [64,104] also proposed the ignition of internal D-type MDs that are expected to occur in the pancake-like cavities allowing these cavities to be gradually filled with solidified alumina. Said differently, the experimental results seem to support a repairing mechanism that takes place inside the large cavities of the thick oxide layer elaborated during the first sequence at high RCQ. When the process switches to the low RCQ, this mechanism is suddenly triggered and experimentally confirmed by the sudden changes in the MDs behaviour, the latter becoming less numerous ($\sim 0.28 \text{ mm}^{-2}\text{ms}^{-1}$) with smaller average size (~ 0.022

mm²) (Fig. III-7b) due to the low aforementioned mechanism of charge accumulation at the oxide / electrolyte interface.

In contrast, results have shown that the reverse sequenced treatment involving the transition from low to high RCQ values has detrimental effects on the produced oxide layer. Indeed, although the thickness of the overall oxide layer is slightly higher than that produced with the reference treatment at low RCQ for 50 min, larger cavities are even visible throughout the coating providing a more irregular and rugged aspect of the top most surface (Fig. III-9). Within this sequenced treatment, the previously formed oxide layer (RCQ = 0.9 for 20 min) continued to grow, yet the deteriorating effects caused by intense and large MDs of the second sequence (RCQ = 6.0) are clearly visible. One can observe that porosities have been enlarged and cracks have appeared in the sublayer of the sequenced sample (RCQ = 0.9 to RCQ = 6.0), compared to RCQ = 0.9 for 20 min. Moreover, large cavities have been developed in the vicinity of the oxide/substrate interface, as a result of strong B-type micro-discharges, taking place throughout the total of the oxide layer. The presence of such large cavities that are usually considered as discharge channels is directly correlated with the MDs behaviour (Fig. III-7a). Indeed, switching from low to the high RCQ value is associated with the sudden ignition of more numerous and larger-size MDs due to the strong aforementioned mechanism of charge accumulation at the oxide / electrolyte interface (Fig. III-13).

III.5.3 Discussion about energy efficiency using sequential PEO treatments

To all the processes described in this work the electrical energy provided to the system was calculated by the integral:

$$E = \int [U(t)_{an} \cdot I(t)_{an} \cdot dt_{an} + U(t)_{cat} \cdot I(t)_{cat} \cdot dt_{cat}] \quad (\text{Eq. III-1})$$

where U(t) is the measured voltage, I(t) the current and Δt the duration of application for the anodic and cathodic pulse, respectively. The specific energy consumption is then defined as the electrical energy provided to grow 1 μm of coating over 1 m² of surface.

$$SEC = \frac{\text{Energy}}{\text{Surface} \cdot \text{Thickness}} \quad \frac{(kWh)}{(m^2 \cdot \mu m)} \quad (\text{Eq. III-2})$$

Volumetric measurements were performed by numerical analysis of SEM cross-section images using a specific processing software. This made it possible to discriminate the coating from the substrate and the surrounding resin, and, finally, measure the total average thickness of the coating, including porosities and large cavities. The volume of oxide was then determined using this thickness value and the macroscopic known sample surface.

The values of specific energy consumption for every PEO treatment conducted in this work are provided in Table III-2, along with total thickness and porosity, reported previously. As it can be seen, the sequential treatment which starts with a high RCQ value and switches to the low one exhibits the lowest specific energy consumption ($11 \text{ kWh}\cdot\text{m}^{-2}\cdot\mu\text{m}^{-1}$) among all processes. Particularly, by comparing with the single treatment performed under the beneficial “soft”-regime conditions (RCQ = 0.9 during 50 min), the growth rate can be increased by $\sim 40\%$ while maintaining a low level of porosity ($\sim 5\%$). Interestingly, this improvement is not made at the expense of energy consumption that is actually reduced by $\sim 35\%$. Consequently, using this virtuous sequenced treatment, the produced oxide layer is the thickest and the most compact and needs the lowest energy to grow.

In contrast, when a sequenced treatment starts with the low RCQ value and is then followed with the high one, an “arc” regime is triggered and more numerous and larger-sized MDs are ignited, which gradually damage the previously formed dense layer. Moreover, this regime is known to be highly energy consuming and although the overall thickness is slightly increased, this sequenced treatment leads eventually to a higher specific energy consumption ($17 \text{ kWh}\cdot\text{m}^{-2}\cdot\mu\text{m}^{-1}$).

III.6 Conclusions of Chapter III

The work presented in this chapter mainly focused on the effect of sequenced treatments on the plasma electrolytic oxidation (PEO) of aluminium. The main conclusions are given hereafter.

Firstly, the singular variations of the delay in the micro-discharges appearance and the time constant of the voltage-time response were explained by a mechanism of charge accumulation taking place through the electrical double layer (EDL) located at the oxide/electrolyte interface. It was further established that this mechanism depends not only on the applied electrical conditions, but is also affected by the morphology of the growing oxide, particularly by the specific surface area in contact with the electrolyte.

In addition, it was shown that by sequentially processing a sample with different RCQ conditions in the course of the treatment, it is possible to promote an earlier transition into the beneficial “soft” regime. Nevertheless, it is necessary to keep in mind that a careful selection of the RCQ values and a proper combination of the sequences involved is needed to achieve the acceleration of transition into this regime.

Implementation of a first high RCQ and then switching to the lower optimal one (RCQ = 0.9) led to a fast growth at first and a “repairing” mechanism afterwards during the second sequence, which filled the large cavities and resulted in a significant enhancement of the produced coating, by

Chapter III - Sequential run of the PEO process

increasing the total thickness (up to ~ 40%) while, simultaneously, maintaining a compact and dense structure of the oxide layer.

Finally, the specific energy consumption of these sequenced PEO treatments was investigated. It was shown that it is possible to increase the efficiency of the process by optimising the combination of the RCQ conditions that are involved in the sequential treatment. Particularly, in the case of transition from a high RCQ = 6.0 to the lower of RCQ = 0.9, we have demonstrated that a significant decrease (~35% compared to reference) in specific energy consumption can be achieved.

Chapter IV - Understanding the “soft” regime

IV.1 Introduction of the chapter IV

The present chapter is dedicated to a deep investigation of the mechanisms of micro-discharges in PEO mainly during the “soft” regime. It is divided in two main parts.

The first part is devoted to a comparative study between two different substrates used in PEO in two different electrolytes. Their respective influence on the properties of the micro-discharges, on the transition to “soft” regime and on the resulting coating is investigated. Additionally, spectroscopic studies during PEO processes conducted in both “arc” and “soft” regimes are presented. Through this optical investigation, information on chemical species and excited their state in the plasma are obtained. The results, as well as limitations and problematics will be discussed.

The second part focuses on the interactions between micro-discharges and their surrounding environment. This is addressed mainly by means of high speed video camera recordings which allows us to simultaneously follow the discharge events and the dynamics of the gas bubbles located at the vicinity of the processed oxide surface. This indirect approach enables us to draw conclusions on the nature of the micro-discharges, through their effect on the gas bubbles dynamics.

IV.2 Specific experimental conditions

IV.2.1 Materials and electrolytes

For the purpose of this study, two aluminium alloys were PEO processed. They consist in the low-alloyed 1050 grade of aluminium and the copper-rich 2024 grade of aluminium. Their respective chemical composition is given in Table II-2.

As summarized in TableIV-1, two different electrolytes were prepared. The first one, called *electrolyte 1*, consists in a solution of potassium hydroxide [KOH] and anhydrous sodium metasilicate [Na_2SiO_3] diluted in deionised water. This first electrolyte is widely used in PEO processes [6,19,29,113,114]. The second electrolyte, called *electrolyte 2*, consists in a solution of anhydrous sodium metasilicate [Na_2SiO_3] and sodium hexametaphosphate [$\text{Na}_6\text{P}_6\text{O}_{18}$] diluted in deionised water. The chemical concentration, pH and electrical conductivity of these two electrolytes are reported in Table IV-1.

Table IV-1. Chemical composition and concentration of the two electrolytes used in the current study, along with their respective pH and conductivity values.

	[KOH]	[Na ₂ SiO ₃]	[Na ₆ P ₆ O ₁₈]	pH	Conductivity σ
<i>Electrolyte 1</i>	1 g/L [0.018 mol/L]	1.65 g/L [0.014 mol/L]	-	12.5	2.8 mS/cm
<i>Electrolyte 2</i>	-	2 g/L [0.016 mol/L]	10 g/L [0.016 mol/L]	11.3	6.5 mS/cm

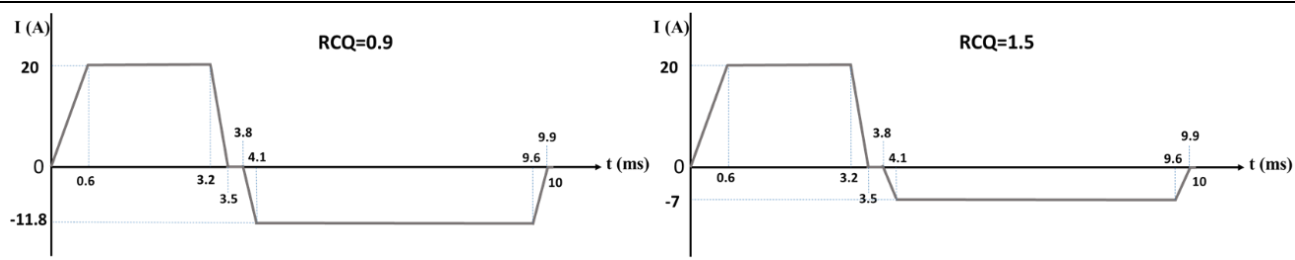
IV.2.2 PEO processing conditions

Two electrical conditions were used by applying two different charge quantity ratios (*RCQ*), $RCQ = 0.9$ and $RCQ = 1.5$. The first one is known to promote the appearance of “soft” sparking regime during the PEO treatment. Oppositely, the second ratio leads to intense “arcing” conditions during the process. As reported in Table IV-2, these two *RCQ* were designed by changing only the pulse parameters of the cathodic alternation of the current waveform.

The PEO study in the present chapter was conducted in two electrical conditions, that is with charge quantity ratio (*RCQ*) of $RCQ = 0.9$, which promotes the “soft” regime, and with $RCQ = 1.5$, which leads to intense “arcing” conditions during the process. The respective numerical values of the electrical parameters and the corresponding waveforms are reported in Table IV-1.

Table IV-2. Electrical parameters of the different current waveforms applied in the present study.

<i>RCQ</i>	Q_p (mC)	I_p (A)	T_p (ms)	Q_n (mC)	I_n (A)	T_n (ms)	f (Hz)
0.9	61	20	3.5	68.4	-11.7	6.1	100
1.5	61	20	3.5	40.7	-7	6.1	100



IV.2.3 *In situ* characterisation of the PEO process

The *in situ* characterisation of the process was performed by recording the variations of the voltage amplitude with processing time. Additionally, simultaneous recording of the current waveforms

synchronised with high speed video were conducted for investigation of the interactions of MDs with the gas bubbles. For the spectroscopic studies, the OceanOptics spectrometer, with diffraction grating of 1200 grooves/mm was used to follow the spectral evolution with processing time within the range of 250-850 nm. The integration time was set to 4 s and the signal was averaged over two consecutive measurements. For the time-resolved spectra, the TRIAX 550 spectrometer was implemented, the diffraction grating was set to 100 grooves/mm. The integration time during acquisition was set to 0.4 ms and was averaged over 10 measurements. All acquisition parameters (integration time, slit, gain, etc.) were kept constant for all the recorded spectra.

IV.2.4 Ex situ characterisation of the PEO coatings

The PEO coating’s phase composition was identified by X-ray diffraction, cross-section images were examined by SEM and EDX analysis was performed to determine the chemical composition and perform profile scans on the resulting oxide layer. Additionally, thickness measurements were carried out with the use of an Eddie’s current sensitive probe (Fischer Isoscope® FMP10).

IV.3 Effect of the electrolyte on the PEO process

As reported in the previous bibliographic chapter, the electrolyte plays a significant role in the PEO process. It defines the nature of the MDs, the breakdown voltage, as well as the growth and the microstructure of the resulting coating [32,43,44]. Dissolved species in the aqueous-based electrolyte regulates its pH value which in turn, with respect to the isoelectric point (IEP) of the processed material, determine the nature of the charges accumulated at its surface, and consequently, control the type of micro-discharges [62,63,115] that ignites (anodic or cathodic).

Until now, all the experiments were conducted in *electrolyte 1*, which consists of potassium hydroxide [KOH] and anhydrous sodium silicate [Na₂SiO₃] (Table IV-1). In views of increasing the concentration of “active” species in the electrolyte and enhance the supply of ions during PEO, a new composition of electrolyte was chosen to be prepared (*Electrolyte 2* in Table IV-1). The effect of electrolyte was studied in two ways; as to its impact on the process itself, on one hand, in terms of electrical characteristics (e.g. voltage amplitude) of the system and the properties of micro-discharges (e.g. their spatial distribution), and, on the other hand, as to its effect on the resulting coating

morphology and properties. This investigation was conducted on both aluminium alloys (Details reported in Table II-2).

IV.3.1 Effect of the electrolyte on the voltage-time response

From a processing point of view, the effect of the electrolyte on the electrical characteristics of the PEO process, mainly the voltage-time response, is illustrated in Fig. IV-1. For each electrolyte investigated, the figure IV-1 shows the evolution of the anodic and the cathodic voltage amplitudes when the PEO process is performed within the “soft” regime conditions (Table IV-2). At the beginning of the process, all the curves follow a similar trend with a rapid increase of the anodic voltage during the the first seconds of the treatment. The point at which the slope of the anodic voltage reduces significantly is designated as the dielectric breakdown voltage. At this point the micro-discharges (MDs) ignite over the processed surface. Whatever the processed aluminium alloy, it appears that MDs ignite at much lower anodic voltage (~430 V) in the *electrolyte 2* (green and blue in Fig. IV-1) than in to *the electrolyte 1* (black and red in Fig, IV-1). In addition, this difference in voltage remains more or less constant during the whole processing. This difference approximately reaches up to 300-350V at the end of treatment (~350 V for *electrolyte 2* against 630-700 V for *electrolyte 1*). This observation could be explained by the larger supply in ionic species in the system, due to higher concentration of both sodium silicate and sodium hexametaphosphate in the solution. Taking into account the charge accumulation mechanism proposed by Martin *et al.* [67], a higher concentration of ions in the electrolyte can facilitate a faster accumulation of these charges at the oxide/electrolyte interface during each anodic pulse and lead to the dielectric breakdown, and thus the ignition of MDs, at lower applied voltages.

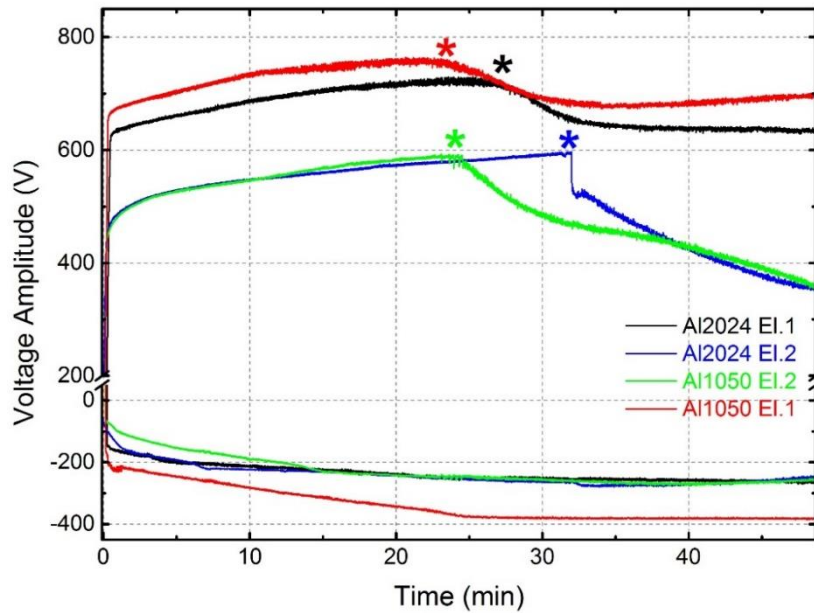


Figure IV-1. Evolution of anodic and cathodic voltage amplitude. Effect of the electrolyte composition on the electrical characteristics of the process during PEO of Al1050 and Al2024 in “soft” regime conditions. EI 1 and EI 2 correspond to *electrolyte 1* and *electrolyte 2*, respectively.

Regarding the transition from the “arc” to the “soft” sparking regime (marked with stars (*) in Fig. IV-1), Fig. IV-1 shows that this transition is more affected by the processed aluminium alloy rather than the electrolyte composition. Generally, this transition is taking place gradually within a period of time, starting with a progressive decrease in anodic voltage and is fully established once the voltage is relatively stabilized at this lower value (red and black curves).

For the quite pure 1050 aluminium substrate (red and green curves in Fig. IV-1), and whatever the electrolyte used, the transition to the “soft” regime starts at approximately 24 min and is fully established at about 31 min. As described in chapter I, establishment of the “soft” regime is usually associated to a gradual drop in the anodic voltage amplitude as well as to a gradual decrease in both the optical and acoustic emissions. Surprisingly, for the PEO of the specific 1050 aluminium alloys, attenuation of the acoustic emission was clearly noted at 30 min but the emission of light still continued until the end of the treatment. In addition, by using specifically the *electrolyte 2*, the drop in the anodic voltage amplitude is steeper and continues to decrease until the end of the treatment. Unfortunately, the processing duration (50 min) did not allow to confirm the further decline of the voltage amplitude or its stabilisation later in the process. Thus, the full establishment of “soft” regime in this case is based only on the voltage drop at 24 min and the observations of changes in acoustic emission. In contrast, for the *electrolyte 1* the anodic voltage stabilizes at about 700 V after switching to the “soft” regime.

For the copper-rich 2024 aluminium alloy, a difference in the transition to the “soft” regime is noted between the *electrolyte 1* and the *electrolyte 2*. Using the *electrolyte 1* (black curve), a usual transition is observed (starting at about 27 minutes and fully established at about 32 min). In contrast, when using the *electrolyte 2* (blue curve), the PEO process is accompanied with intense micro-discharges until 32 min and then instantaneously switches to the “soft” regime at 32 min. This is noted by the sudden sharp drop in voltage as well as a sudden sound and light extinction. Nevertheless, this moment still coincides with the full establishment of “soft” regime in the *electrolyte 1*.

On the other hand, and whatever the electrolyte used, the transition to the “soft” regime also appears to depend on the treated material since it takes place earlier for the quite pure 1050 aluminium than the copper-alloyed 2024 aluminium.

Contrary to anodic voltage amplitude behaviour, no significant differences were observed for the cathodic voltage for most of the cases, with the exception of the increase (in absolute value) for the case of pure aluminium processed in electrolyte 1 (red curve) which reached at approximately -380 V.

IV 3.2 Effect of the electrolyte on the PEO coatings

We have seen that the composition of electrolyte influences the PEO process, mainly the time at which the “soft” regime appears. In turn, it is also expected that such processing changes affect the resulting oxide coating as well. This is illustrated in Fig. IV-2 which shows the visual aspect of two 1050 aluminium samples processed in two different electrolytes.

The sample processed in the *electrolyte 1* (Fig. IV-2a) exhibits a non-homogeneous growth of the coating. At the centre of this sample presents some darker spots are observed, while a number of small crater-like dots are located at the edges and corners (indicated with arrows). A close up of these crater-like dots is shown in Fig. IV-2a1 and a2. They are probably the result of a higher discharge activity due to an amplification of the electrical field at these sharp edges. This was also reported previously by Melhem *et al.* [35], who complementary showed that this edge effect also depends on both the distance between the electrodes, the current pulse frequency and slightly by the RCQ value [70].

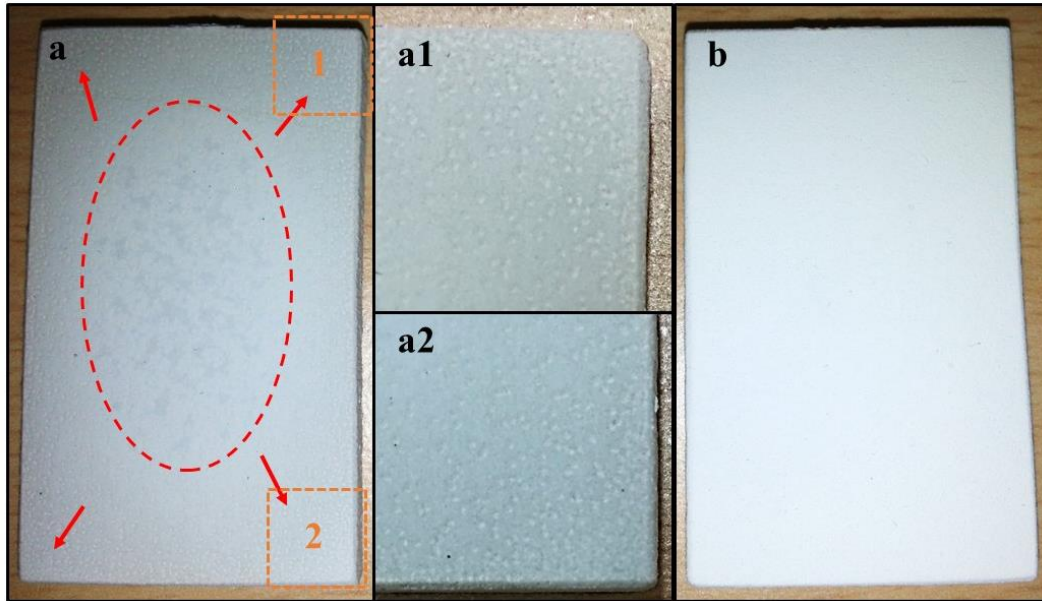


Figure IV- 2. Visual aspect of the 1050 aluminium alloy samples PEO processed under the “soft” regime conditions ($RCQ = 0.9$) in a) the *electrolyte 1* and b) in the *electrolyte 2*. Pictures a1) and a2) are magnified pictures of the sample corners.

On the other hand, the sample processed in the *electrolyte 2* (Fig. IV-2b) exhibits a visually homogeneous coating with no marks suggesting a uniform growth between the centre and the edges of the sample.

To confirm these differences in treatment between the *electrolyte 1* and the *electrolyte 2*, the coating thickness were measured over the complete sample surfaces. Fig. IV-3 presents a cartography showing the topology of the two obtained surfaces. A measurement point was performed each 5 mm over one flat surface of the samples. As expected, thickness of the oxide coating produced in the *electrolyte 1* is highly heterogeneous over the surface (Fig. IV-3a). Indeed, the central area of the surface exhibits a much lower thickness, as low as $38 \mu\text{m}$, compared to the edges, at which it reaches values as high as $109 \mu\text{m}$. Oppositely, when processed in the *electrolyte 2* (Fig. V-3b), thickness of the oxide coating shows a much more homogeneous over the entire surface. Low variations in the thickness are noted between the centre and the edges of the sample. The measured thicknesses vary in the range between $150 \mu\text{m}$ and $180 \mu\text{m}$. In addition, the standard deviation from the mean thickness is much lower for this second electrolyte than for the first one. Finally, the oxide coating elaborated in the electrolyte 2 is thicker and more homogeneous ($h_2 = 165 \pm 8 \mu\text{m}$) than the one produced in electrolyte 1 ($h_1 = 68 \pm 16 \mu\text{m}$).

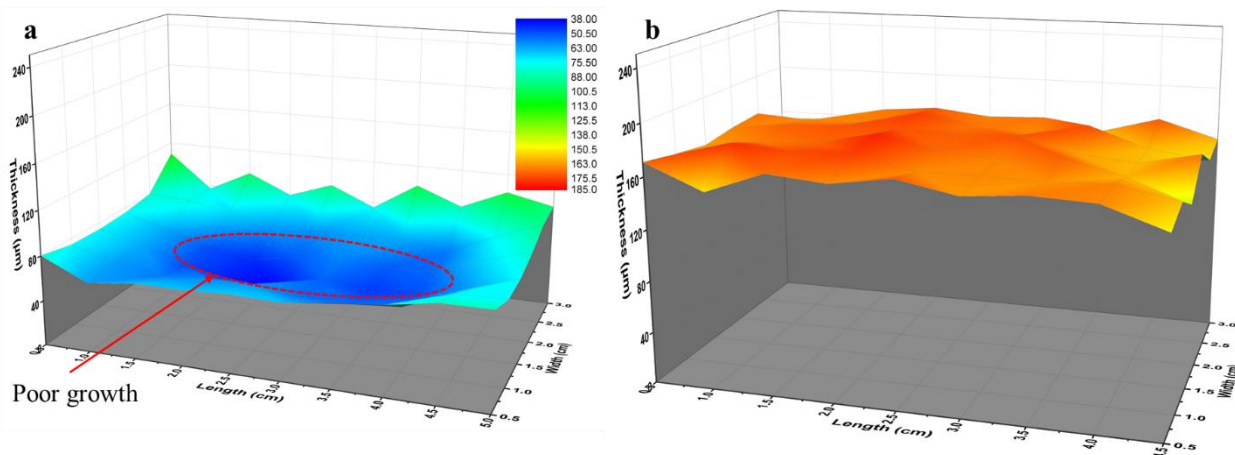


Figure IV-3. 3-dimensional representation of the thickness of the PEO oxide produced on a 1050 aluminium substrate under the “soft” regime conditions in a) the *electrolyte 1* and b) in the *electrolyte 2*. Composition of each electrolyte is provided in Table IV-2.

A plausible explanation could lay, once again, in the higher concentration of available charges in the electrolyte, which facilitates a faster and even distribution of ions at the oxide/electrolyte interface during anodic polarisation. As a consequence, MDs take place all over the surface, resulting in homogeneous growth. Regarding the increased growth rate, considering the mechanism of charge accumulation, it is possible that the higher amount of ions in the electrolyte could lead to longer discharge events. As micro-discharges manifest as cascades or “chains of individual sparks”, an increased concentration of charges could result either in an increase of discharge sites (density of MDs) or in prolonged durations of these cascades within the time frame of one anodic pulse.

IV.4 Specific effect of the aluminium alloy on the PEO process in “soft” regime

The above observations clearly evidence differences between the low-alloyed 1050 grade aluminium and the copper-alloyed 2024 grade aluminium. These differences were deeply investigated by studying in detail the behaviour of the micro-discharges that develop over the two different alloys during the PEO process conducted in the “soft” regime. For this purpose, fast-video imaging and optical emission spectroscopy measurements were performed.

IV.4.1 Fast video imaging

Fig. IV-4 shows a couple of frames that were obtained from fast video imaging at 10 and 40 min processing times for the 1050 and 2024 aluminium alloys.

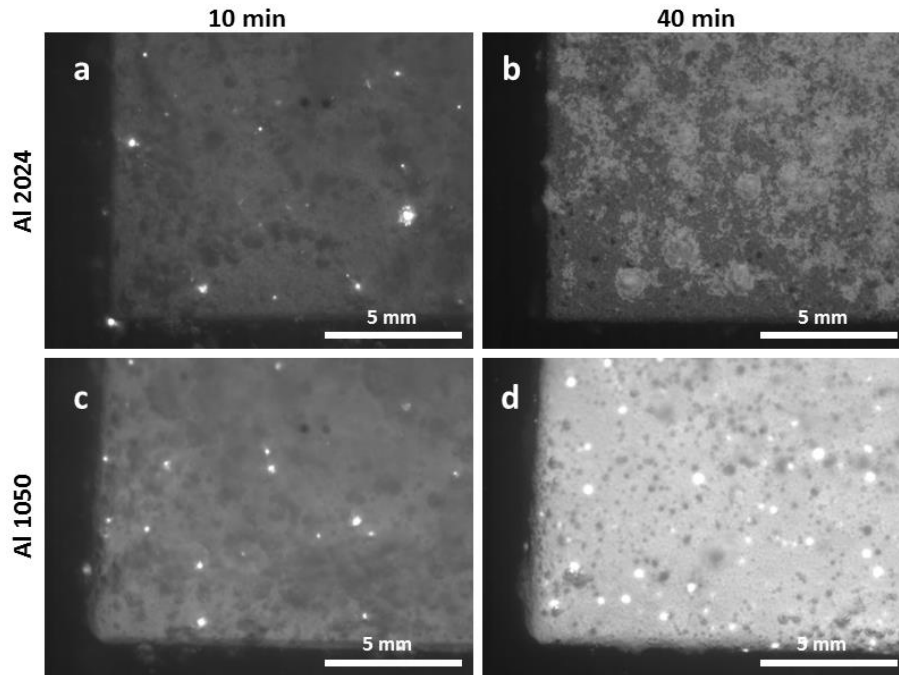


Figure IV-4. Pictures recorded from fast-video imaging on a), b) Al 2024 and c), d) Al 1050 aluminium alloys PEO processed in the *electrolyte 2* under the “soft” regime conditions. Fast video recordings were performed at a frame rate of 20 kfps under an external illumination. Each picture depicts the treated surface during an anodic polarisation of the pulsed bipolar current.

At the first stage of the PEO process, before the transition to the “soft” regime, intense micro-discharges appear at the surface of both aluminium alloys during each anodic pulse of the current (Fig. IV-4 a and IV-4c). With the transition to the “soft” regime, large micro-discharges on the copper-rich 2024 aluminium gradually extinguish and finally disappear (Fig. IV-4 b). It is worth mentioning that few residual tiny spots remain randomly visible but only in a deep darkness (after extinction of the light illumination). This is in agreement with previous reports in the literature [19,20,26]. However, in the case of the low-alloyed 1050 aluminium substrate, even under light illumination, one can clearly see large shiny spots occurring over the processed surface. Contrary to the 2024 aluminium alloy, these spots still appear periodically during every anodic pulse of the current.

IV.4.2 *In situ* characterisation by optical emission spectroscopy

With the aim to investigate the nature of these light spots that appear unusually on the low-alloyed 1050 aluminium substrate during the “soft” regime, optical emission spectroscopy (OES) measurements were conducted. For comparison reasons, OES measurements were also performed on the 2024 aluminium alloy. As it has been previously mentioned, OES is a powerful diagnostic in the field of plasma physics. Nevertheless, although recordings of emission spectra are relatively easy, interpretation of the results and extraction of plasma parameters from the recorded spectra still remains a challenging task. A series of spectral acquisitions in various wavelength ranges were

performed for PEO treatments conducted in the *electrolyte 1* within the “soft” regime conditions (see Table IV-1).

IV.4.2a Presence of broad emission continuum

Fig. IV-5 and Fig. IV-6 present the time evolution of the emission spectra recorded during the PEO treatment of the 2024 and 1050 aluminium alloys, respectively. Whatever the processed substrate, as the process starts and during the first “arcing” stage that extends to about 28 min, all the typical emission lines are present, originating either from the sample (Al, Al⁺, Cu, Mn) or from the electrolyte (Na, H, OH, Si). The emission line intensity gradually decreases with processing time and eventually disappears once the “soft” regime is established (approximately after 30 min). One can observe the emission of a broad underlying continuum, spanning from ~ 400 to 850 nm in wavelength, for both the treated aluminium alloys. However, a distinct difference in these two sets of spectra is observed between the two alloys investigated. For the copper-rich 2024 aluminum alloy, despite the fact that the intensity of this continuum slightly increases at the beginning (until 5 min), it gradually decreases with the processing time and no emission continuum is observed at the end of the treatment (Fig. IV-5). In contrast, for the quite pure 1050 aluminium substrate, the overall intensity of this continuum increases with the processing time reaching its maximum intensity at the end of the treatment (Fig. IV-6).

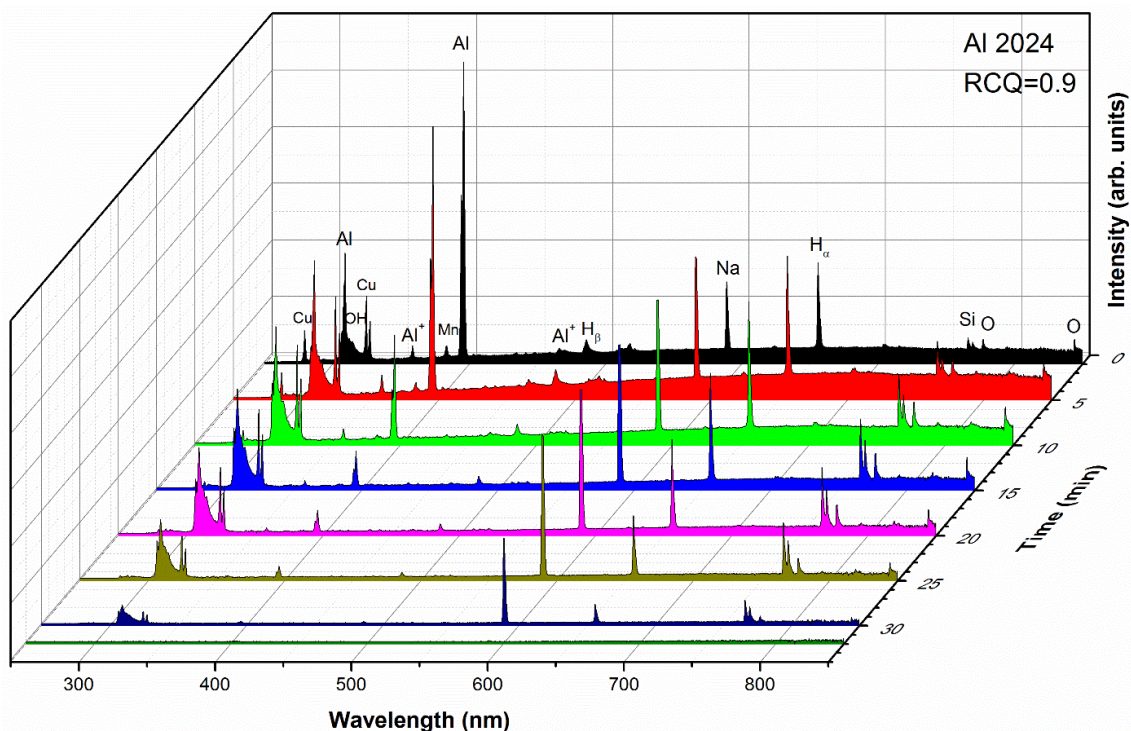


Figure IV-5. Evolution of the emission spectra during the PEO process of a 2024 aluminium alloy under the “soft” regime conditions in the *electrolyte 1*.

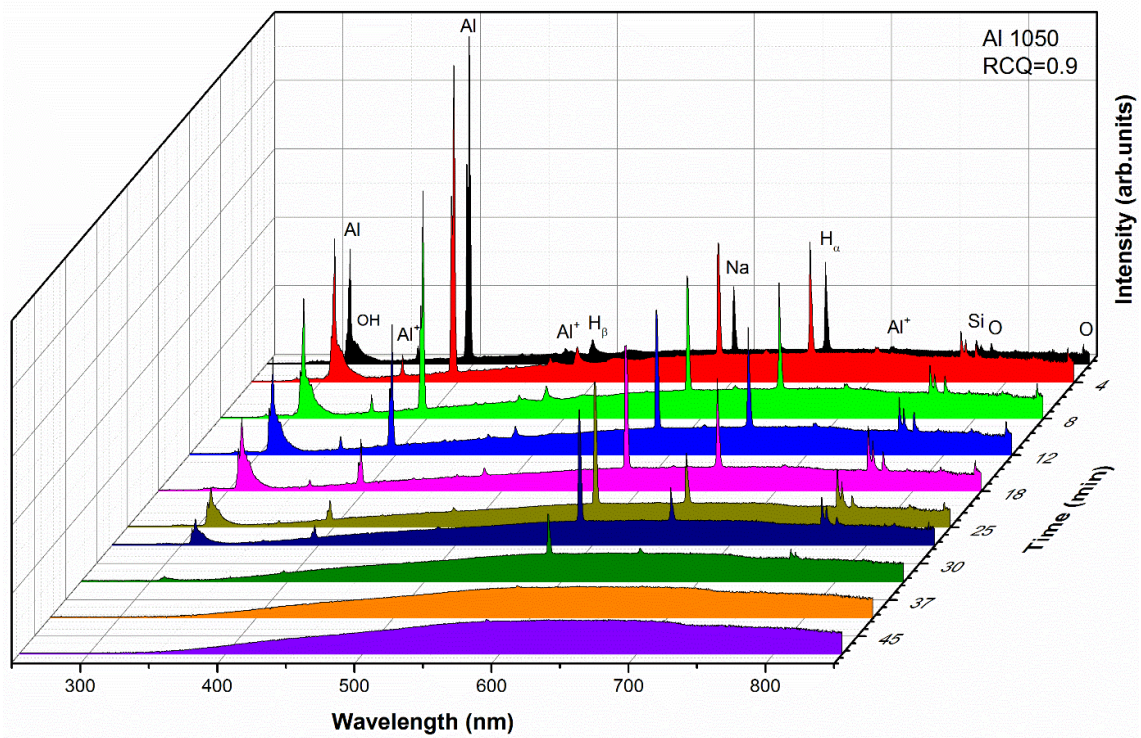


Figure IV-6. Evolution of the emission spectra during the PEO process of a 1050 aluminium alloy under the “soft” regime conditions in the *electrolyte 1*.

This difference in the emission spectra between the two aluminium alloys investigated is also illustrated in Fig. IV-7. For the 1050 aluminium substrate, the fact that an emission light continuum remains during the “soft” regime is unusual. The interpretation of such a broad continuum spectrum is generally difficult. This interpretation is even more difficult due to the fact that distinctive light spots remains visible over the processed surface (Fig. IV-4d) while no of individual emission lines can be observed (Fig. IV-6 and 7). This puts the nature of this light emission continuum in question.

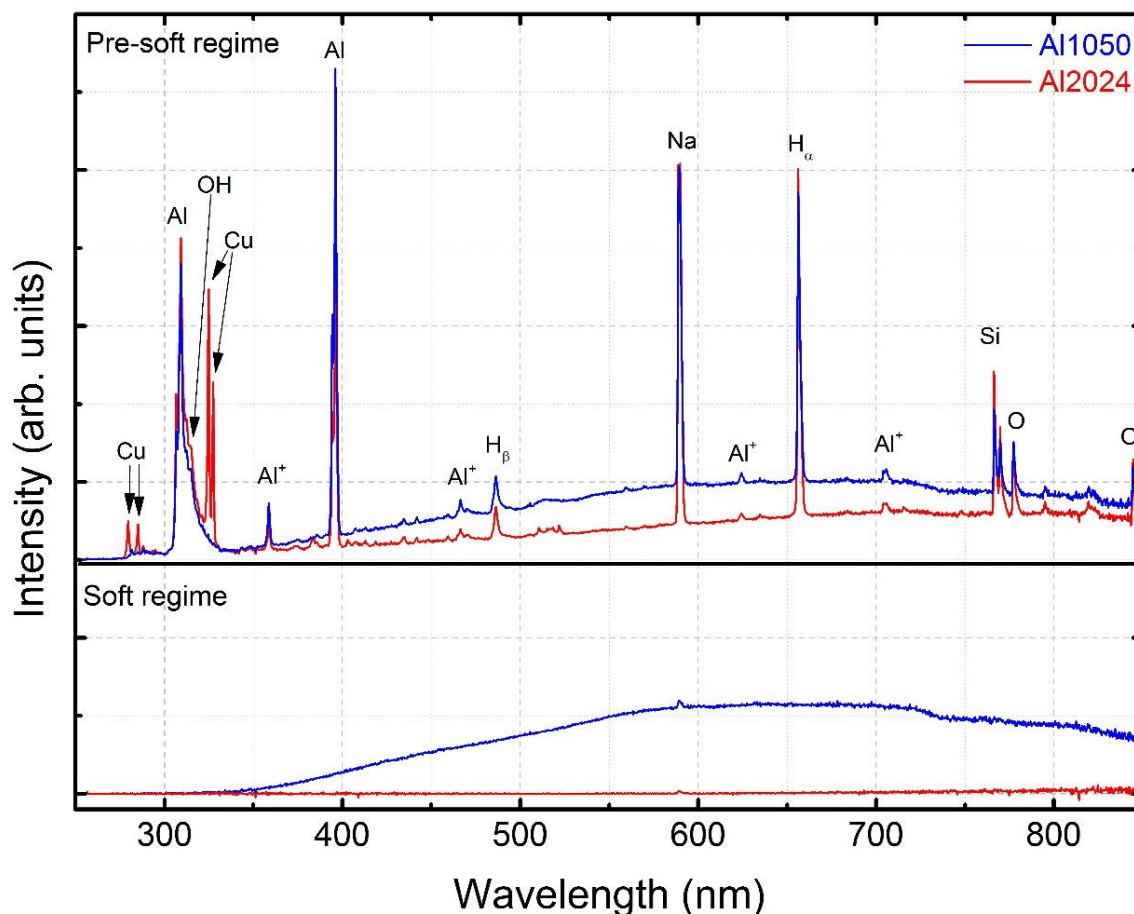


Figure IV-7. Emission spectra recorded during the PEO treatment of the 1050 and the 2024 aluminium alloys prior and after the transition to the “soft” regime.

Furthermore, in order to verify that this broad continuum is emitted during the anodic polarization of the current pulse and not during the cathodic one, time-resolved spectra were acquired in the course of one pulse period of the current (in the range of 400 – 800 nm in wavelength). Figure IV-8 depicts the obtained spectra prior to transition and after the establishment of the “soft” regime. It clearly confirms the fact that the emission continuum takes place only during the anodic polarisation of the current which is in good accordance with the synchronised fast video recordings presented previously (Fig. IV-4).

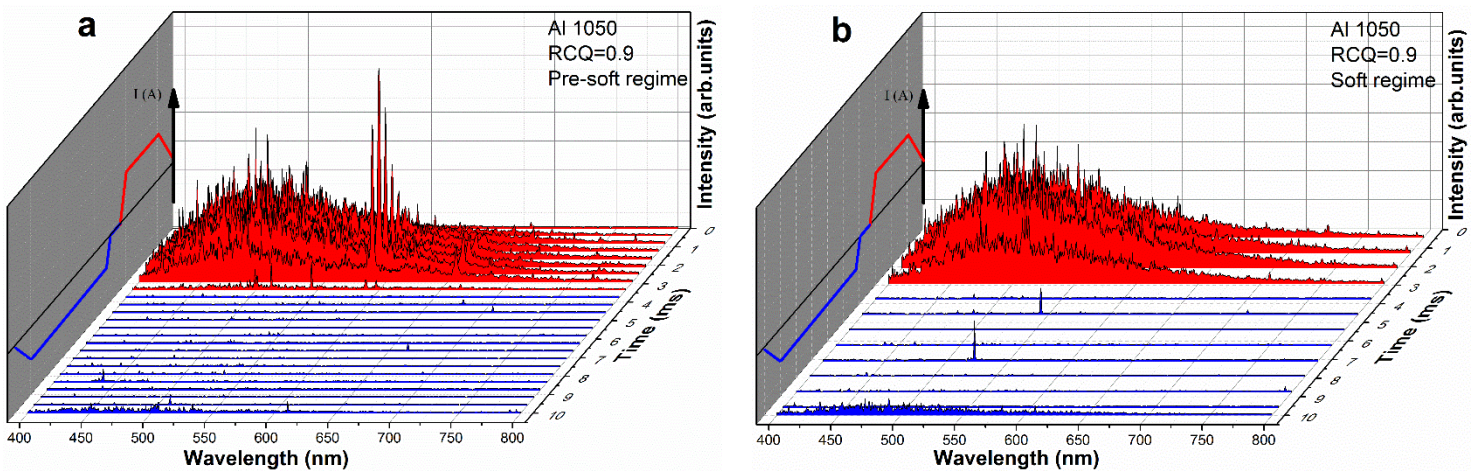


Figure IV-8. Time-resolved spectra recorded (over one pulse period of the current) during the PEO treatment of the 1050 aluminium alloys a) before the establishment of the “soft” regime (17-20 min) and b) during the “soft” regime (46-49 min).

In the literature, broad continuum spectra are associated with a galvanoluminescence phenomenon during anodising processes of aluminium [116–121]. The source of this luminescence is attributed to the “flaws” in the forming oxide layer. Tajima *et al.* [122] has reported that anodizing processes with inorganic electrolyte, luminescence strongly depends on surface pre-treatment, while it is unaffected with organic electrolytes. Results of Kasalica *et al.* [117] confirm this behaviour and, additionally, they identify transitions in molecules, such as AlH, AlO, Al₂ and AlH₂, possibly localised in pores of the γ alumina structure, as the source of this luminescence. In their investigation, Klapkiv *et al.* [24] attributed the continuum spectrum to “free-free (bremsstrahlung radiation) and bound-free (collision-radiative recombination of electrons) transitions”. The intensity of the continuum is the sum of these two types of radiation ($J_{\Sigma} = J_{\Sigma}^{ff} + J_{\Sigma}^{bf}$). They showed that in general, this decreases with the oxide growth, is due to the fact that charge and mass transfer into the plasma are decelerated. An exception to this was the treatment in LiOH electrolyte, which was explained by the reduction of the number of MDs per unit area and thus, leading to increased local current densities. However, this was not the case in our experiments with Al1050, where, on the contrary, the density of these light sources remains high (Fig. IV-4 d) and the intensity of the continuum increases even during the “soft” regime (Fig. IV-7).

IV.4.2b Electron (T_e), rotational (T_{rot}) and gas (T_{gas}) temperatures

The analysis of the OES spectra gives quantitative information on the excited species in the plasma of the micro-discharges. It allows determining different characteristic temperatures such as the electron temperature and the rotational temperature of one chemical species, the latter being a good

estimate of the gas temperature into the plasma phase. In addition, analysis of the spectra also gives the plasma density also known as the electron density.

The electron temperature can be determined by using the Boltzmann plot method which is based on the estimation of the intensity of the emission lines of a given species. In most cases, an assumption of a thermodynamic equilibrium (TE) or at least local thermodynamic equilibrium (LTE) is required.

The emitted power density is given by:

$$I_{mn} = h\nu_{mn}A_{mn}N_m \quad (\text{W/m}^3) \quad (\text{Eq. IV-1})$$

where I_{mn} is the power density of the emitted line corresponding to transition from an excited level m with energy E_m to a lower level n with energy E_n , h is the Plank’s constant, ν_{mn} and A_{mn} the frequency and the Einstein’s coefficient for spontaneous emission, respectively, and N_m the density of population of the excited level m .

Assuming LTE, all excited states of the species can be assumed to satisfy the Boltzmann’s distribution. Consequently, N_m can be expressed as:

$$N_m = \frac{N_0 \cdot g_m}{Z} \cdot \exp\left(\frac{-E_m}{k_B T}\right) \quad (\text{Eq. IV-2})$$

where N_0 is density of the ground state, g_m the degeneracy of the state m , Z the partition function, k_B the Boltzmann’s constant and T the excitation temperature. With the consideration of LTE, the excitation temperature can be representative of the electron temperature (T_e).

Combining the above relations one can obtain:

$$\ln\left(\frac{I_{mn}\lambda_{mn}}{g_m A_{mn}}\right) = \ln\left(\frac{hcN_0}{Z}\right) - \frac{E_m}{k_B T_e} \quad (\text{Eq. IV-3})$$

where c is the speed of light in vacuum. Numerical values on transition probabilities (A_{mn}), wavelengths (λ), energy levels (E_m) and degeneracy (g_{mn}) were obtained from NIST database [123].

In equation IV-3, the term on the left-side relation (containing the intensity I_{mn}) is proportional to the energy level. Plotting this quantity as a function of E_m and linearly fitting provides a slope coefficient that is inversely proportional to the electron temperature T_e . Figure IV-9 illustrates an example of such calculation based on the measurements of the intensity of the O^+ emission lines. It’s worth noting that the accuracy of this method increases with the number of emission lines that are considered as well as with the increase of the E_m energy range.

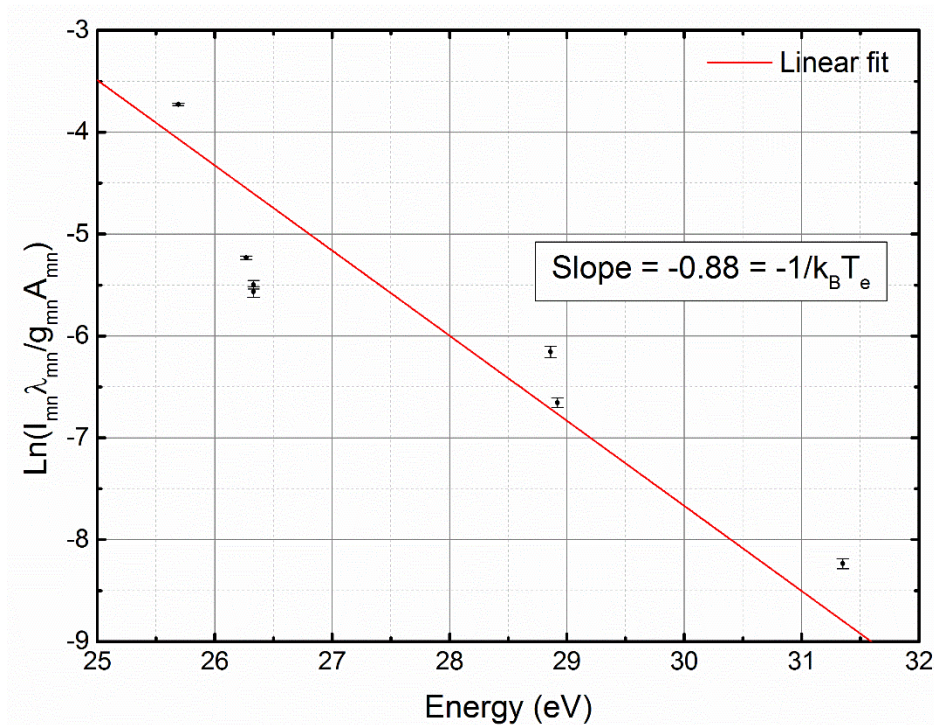


Figure IV- 9. Example of a Boltzmann plot using the oxygen ions (O^+) emission lines for the estimation of the electron temperature T_e .

Similarly, the rotational states can be assumed to be in local thermodynamic equilibrium and satisfy the Boltzmann distribution. Thus, plot method can be applied on molecules to determine the rotational temperature (T_{rot}). However, from practical point of view, this is done not by the Boltzmann plot but by fitting the experimental emission lines while having the temperature T_{rot} as fitting parameter. In the condition of LTE and high pressure, this rotational temperature can be assimilated to the gas temperature ($T_{gas} \approx T_{rot}$) in the plasma [124–127]. In our experiments, electron temperature was calculated based on the intensity of the oxygen ion (O^+) emission lines in the range of 370-475 nm, while the rotational temperature was estimated using the emission lines from the hydroxyl radical (OH) species at 306-318 nm. Calculations were performed both under the “arc” and the “soft” regime conditions.

The results are depicted in Fig. IV-10, that presents the evolution of electron (T_e) and gas (T_{gas}) temperature with processing time of Al2024.

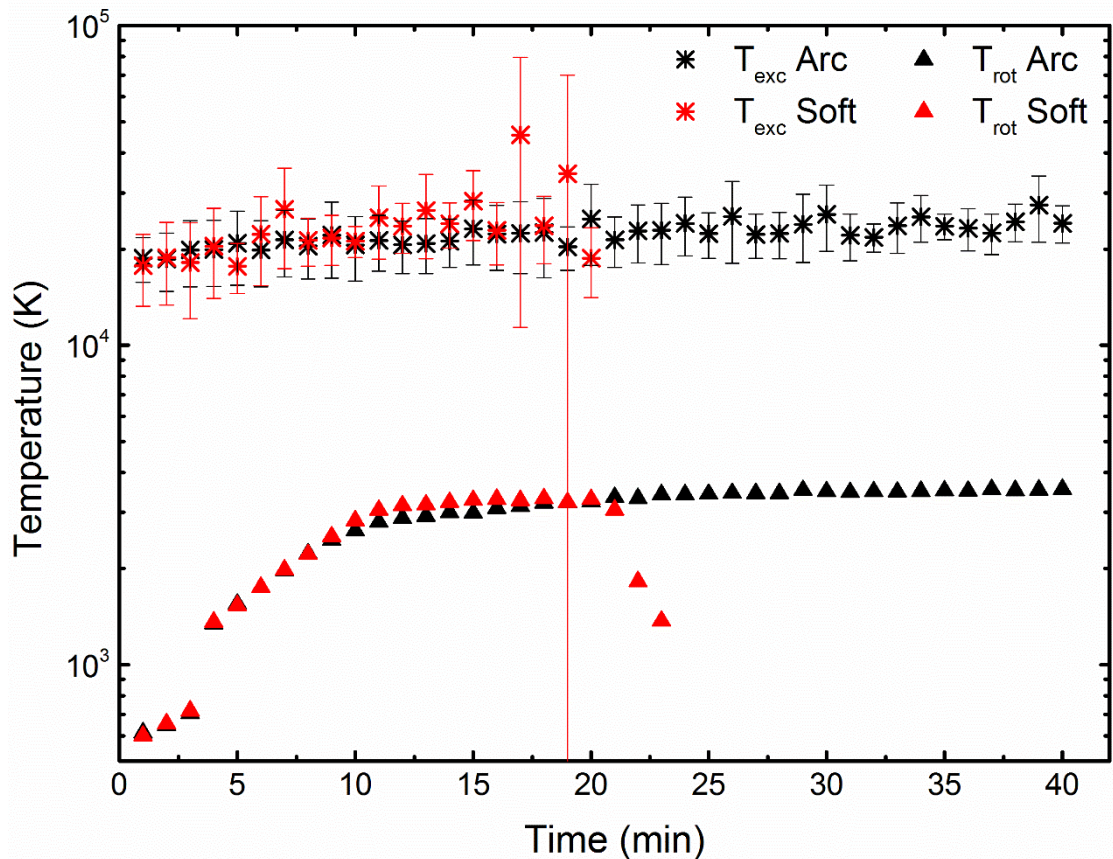


Figure IV- 10. Evolution of the electron ($T_e \approx T_{exc}$) and the gas ($T_{gas} \approx T_{rot}$) temperatures during the PEO treatment of a copper-alloyed 2024 aluminium alloy in “arc” and “soft” regime conditions both conducted in the *electrolyte 1*.

Calculations of electronic temperature (T_e), show that its values exhibit a broad dispersion, ranging between $T_e = 18000 - 25000$ K. In literature, values of electron temperature calculated from various elements (e.g. Al, Al^+ , O^+ , Mg, Ti) present in the plasma, range from as low as 3000 K to 33000 K [21,23,42,70,72,75,76,128].

Regarding the gas temperature, it was found to be approximately at $T_{gas} \approx T_{rot} = 3500 \pm 50$ K for both “arc” and “soft” regimes. Despite the increasing trend observed at the beginning of the treatment (up to ~ 7 min), these values are not considered very accurate, due to strong interference from aluminium emission lines, and should not be taken into consideration. Similarly, for the “soft” regime conditions (red triangles), values after 20 min are not considered due to the gradual extinction of the micro-discharges and thus the very low intensity of the OH emission lines.

IV.4.2c Electron density N_e

The electron density in the plasma of the micro-discharges is determined by estimating the broadening of emission lines. Several mechanisms are responsible for broadening of emission lines

such as the natural broadening (which arises from the finite lifetime of an atom in an excited state), the Doppler broadening (which is caused by the thermal movement of the emitters), the pressure broadening (which is due to the collisions of emitters with neutral atoms or molecules) and the Stark broadening (which arises from the interactions of emitters with the surrounding charged species, *i.e.* ions or electrons). In addition, the broadening caused by the spectrometer should also be taking into account.

Due to its sensitivity to electron density and temperature, Stark broadening is used for the determination of the electron density. In the present study, we used the results of A. Descoeur [129] who established a direct relationship between electron density and Stark broadening for hydrogenic species:

$$N_e = 8.8308 \cdot 10^{16} \cdot (\Delta\lambda_s)^{1.6005} \quad [\text{cm}^{-3}] \quad (\text{Eq. IV-4})$$

where N_e the electron density and $\Delta\lambda_s$ the Stark width.

In the case of non-hydrogenic species, the electron density is given by the following relation [107]:

$$\Delta\lambda_s = 2 \cdot w \cdot \left(\frac{N_e}{10^{16}}\right) + 3.5 \cdot A \cdot \left(\frac{N_e}{10^{16}}\right)^{\frac{1}{4}} \cdot \left[1 - 1.2 \cdot N_D^{-\frac{1}{3}}\right] \cdot w \cdot \left(\frac{N_e}{10^{16}}\right) \quad [\text{nm}] \quad (\text{Eq. IV-5})$$

where w (in nm) is the electron impact parameter, A (in nm) the ion broadening parameter and N_D the number of particles/atoms in the Debye sphere.

The first term of equation IV-5 corresponds to broadening due to electron-electron collisions while the second one due to electron-ion. For an electron density range of $N_e = 10^{17} - 10^{15} \text{ cm}^{-3}$ the second term equals to $7.82 \cdot 10^{-5} \text{ nm}$ and $2.4 \cdot 10^{-8} \text{ nm}$, respectively. As the contribution of the second term is negligible, this can be reasonably omitted, leading, thus to the simplified expression:

$$\Delta\lambda_s = 2 \cdot w \cdot \left(\frac{N_e}{10^{16}}\right) \quad [\text{nm}] \quad (\text{Eq. IV-6})$$

Values for the impact parameters w were obtained from tables provided by H. R. Griem [130,131].

In the present investigation, in order to calculate N_e , we considered the emission lines of H_α at 356.3 nm, Al at 396 nm and Al^+ at 704 nm. If H_β emission line of the Balmer series is usually used, instead of the H_α line, it remains that its very low intensity did not allow an accurate estimation of N_e . The H_α emission line, however, exhibits a strong self-absorption, which in turn leads to an

overestimation of the electron density. In addition, we studied the emission lines of Al at 396 nm and Al⁺ at 704 nm.

Considering the equations (Eq. IV-4) and (Eq. IV-6), the main difficulty lies in measuring the Stark broadening $\Delta\lambda_s$. As mentioned, there are various mechanisms that may be responsible for the broadening of the spectral lines. Broadening caused by the spectrometer and Doppler effect results into Gaussian profile of the emission line, while the rest of the mechanisms lead to Lorentzian profile. If all of them take place, the resulting profile follows a Voigt function, which is the convolution of these two profiles. The broadening measurements are performed through the full-width at half maximum (FWHM) of each contribution, Gaussian and Lorentzian.

The contribution of the spectrometer is a technical characteristic of the apparatus used and is equal to 0.08 nm in our case. Natural ($\Delta\lambda_{\text{nat}} \approx 10^{-5}$ nm) and Doppler ($\Delta\lambda_D \approx 0.026$ nm at 3000 K) broadenings are negligible and in our conditions and pressure broadening reaches values as high as 0.05 nm for the lowest temperature of $T = 900\text{K}$ (based on the relation $\Delta\lambda_p = 5.736 \cdot T^{-0.7}$ [132]). As shown previously, the temperature largely exceeds this value during these experiments. So, having this information and fixing the known values during the fitting process of experimental data by Voigt profile, we can obtain the Stark broadening contribution ($\Delta\lambda_s$). However, although the Voigt function fits adequately the emission lines for other elements, in the case of hydrogen line the Voigt fit is not satisfactory. This problem was tackled by Jovovic *et al.* [38,102] who used two Voigt functions instead of one. An example of such procedure is depicted in Fig. IV-11.

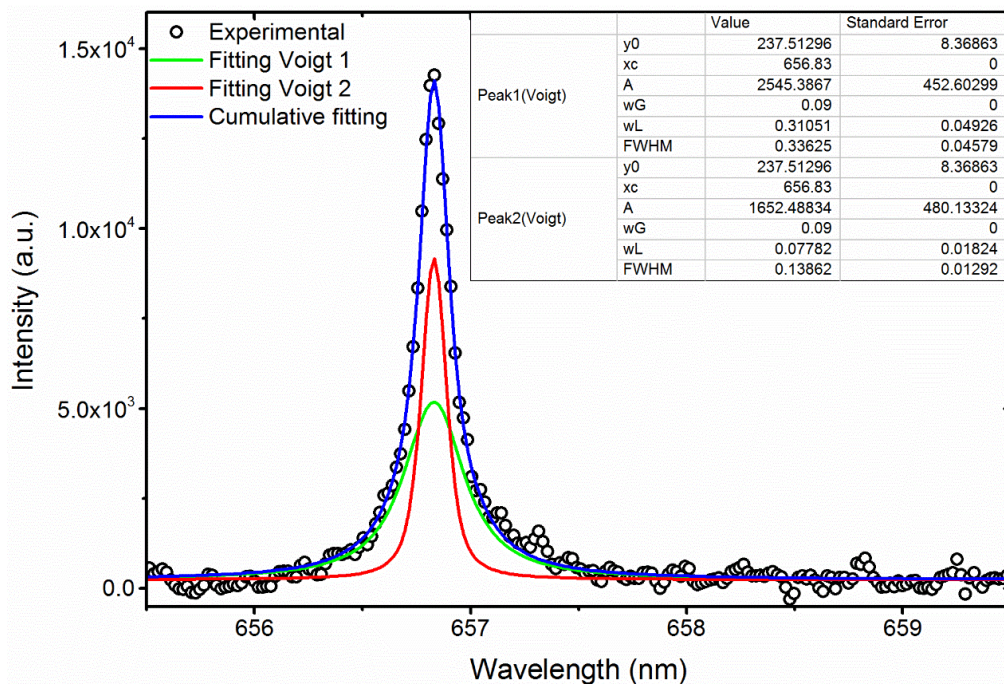


Figure IV- 11. Example of fitting of H_α emission line using two Voigt functions.

The convolution of these two functions provides an accurate fitting of the experimental data, but the use of such method results in two distinct values of $\Delta\lambda_s$, which implies the existence of two different electron densities and, thus, requires the assumption of two different types of micro-discharges. This might have been possible to confirm by recording and characterising an individual discharge. However, this was not possible in our experimental set-up. Indeed, the recorded signal is a result from multiple discharges originating from various sites of the surface. In addition, in order to achieve adequate signal to noise ratio, the acquisition time of the spectrometer is much higher than the lifetime of a discharge (or even cascades of discharges) So, in practice measurements of average values are performed in this way. However, resulting to two distinct average values from one measurement contradicts the concept of a mean value. Nevertheless, this method is used by multiple groups for determination of electron density [23,38,75,76,102,104].

Determination of the electron density, in either “arc” (Fig. IV-12) or “soft” (Fig. IV-13) conditions leads to values between 10^{14} cm^{-3} to $2 \cdot 10^{17} \text{ cm}^{-3}$, which are relatively constant during the process. Calculations from emission lines of Al and Al^+ are in good agreement, providing electron densities around the value of 10^{17} cm^{-3} . This is partially in disagreement with the A. Nominé’s earlier findings [107], which showed a clear distinction between the values obtained from neutral and ionised aluminium species. In addition, following the aforementioned method, we obtained two values from the hydrogen line analysis, none of which coincides with the ones obtained from aluminium species. Nevertheless, the results are within the typical electron density range reported in the literature [21,23,66,76].

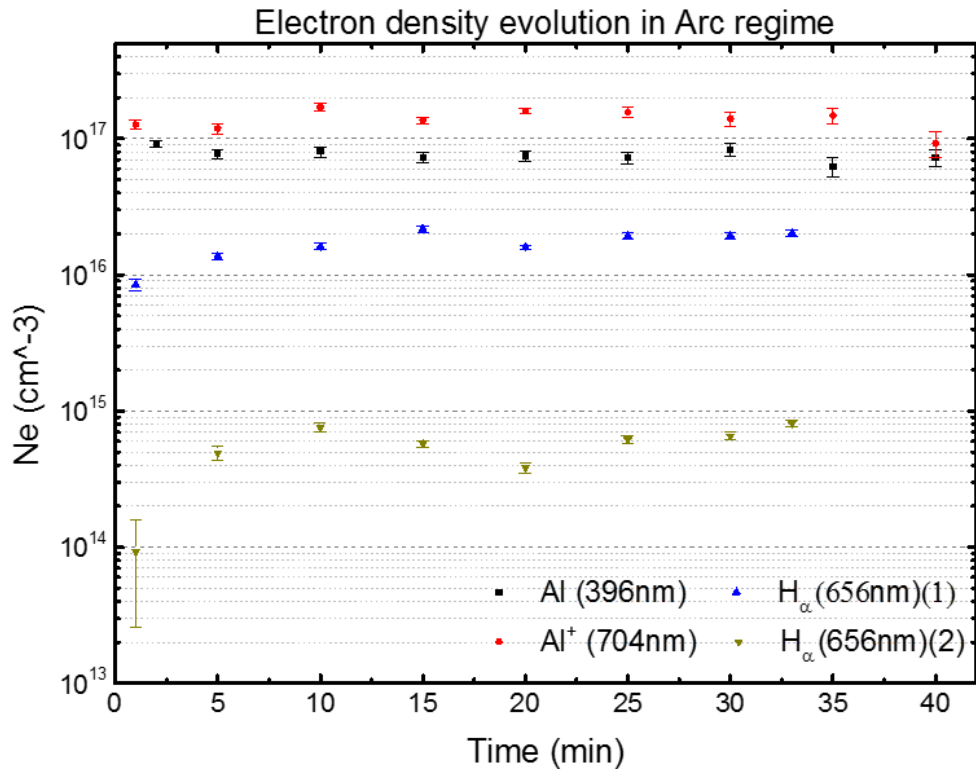


Figure IV- 12. Evolution of the electron density during the PEO process of a 2024 aluminium substrate in the “arc” regime and conducted in the *electrolyte 1*.

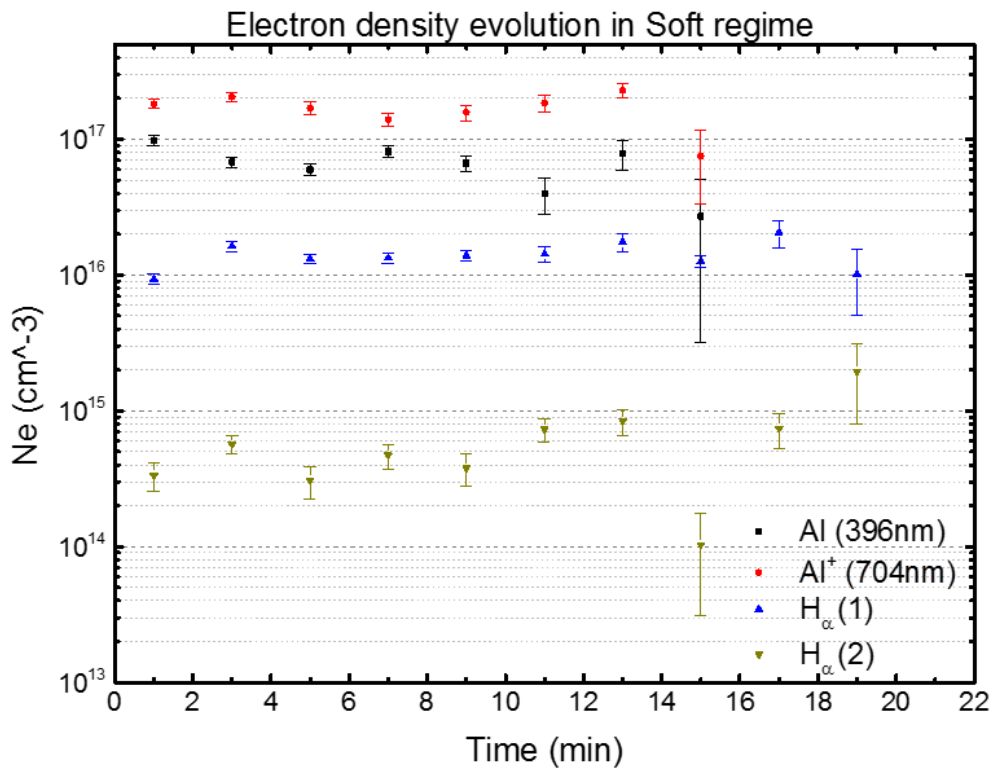


Figure IV- 13. Evolution of the electron density during the PEO process of a 2024 aluminium substrate in the “soft” regime and conducted in the *electrolyte 1*.

IV.5 Ex-situ characterisation of the PEO coatings

The PEO coatings grown on the low-alloyed 1050 and on the copper-alloyed 2024 aluminium alloys were compared from a microstructural point of view. Influence of the electrolyte (*electrolyte 1* and *electrolyte 2*) as well as the influence of the electrical regime conditions applied (“arc” and “soft”) on the formed microstructures were also discussed.

IV.5.1 X-ray diffraction measurements

Fig. IV-14 presents the X-ray diffraction patterns obtained from the two aluminium alloys processed in the *electrolyte 1* for 50 min. For each alloy, indexation of peaks shows the presence of the α -, γ - and δ - alumina polymorphs. Intensity of peaks suggests a larger amount of the α -alumina than for the γ - and δ -alumina. The unusual presence of the δ -alumina polymorph could be explained by transitional phase from γ - to α - that occurs at temperatures between 900 to 1000 °C [133,134].

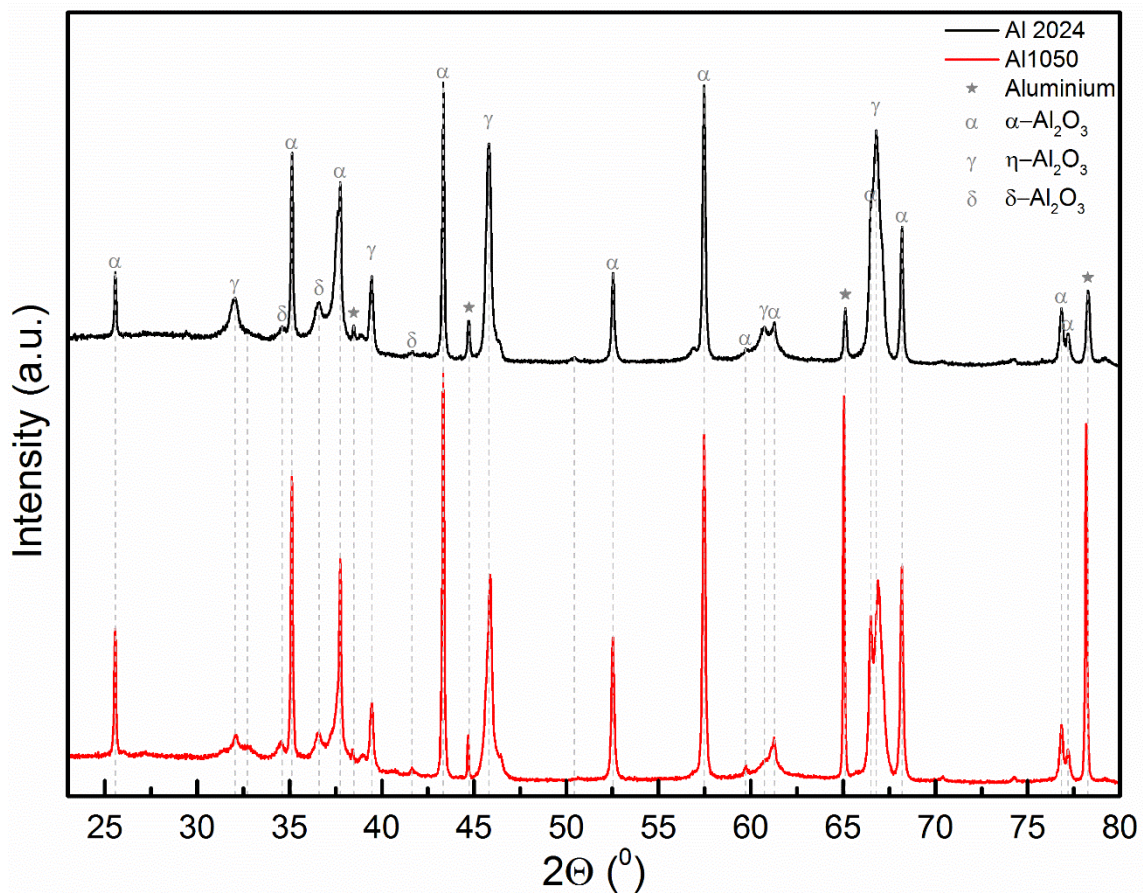


Figure IV- 14. X-ray diffraction patterns of the PEO oxide layers produced on the 1050 and 2024 aluminium alloys after processing for 50 min under the “soft” regime conditions and in the *electrolyte 1*.

Fig. IV-15 presents the XRD spectra recorded on the PEO coatings formed in the electrolyte 2, before and after the establishment of the “soft” sparking regime. The α - and γ - alumina polymorphs are present into the coatings. Peaks of mullite ($\text{Al}_6\text{Si}_2\text{O}_{13}$) also appear. This can be explained by a higher concentration of silicon into the electrolyte 2 than in the electrolyte 1.

At the same time, intensity of the α -alumina peaks is higher after the establishment of the “soft” regime which suggests an increase in the volume proportion of corundum during the “soft”- regime. This is in good agreement with recent works [26,135].

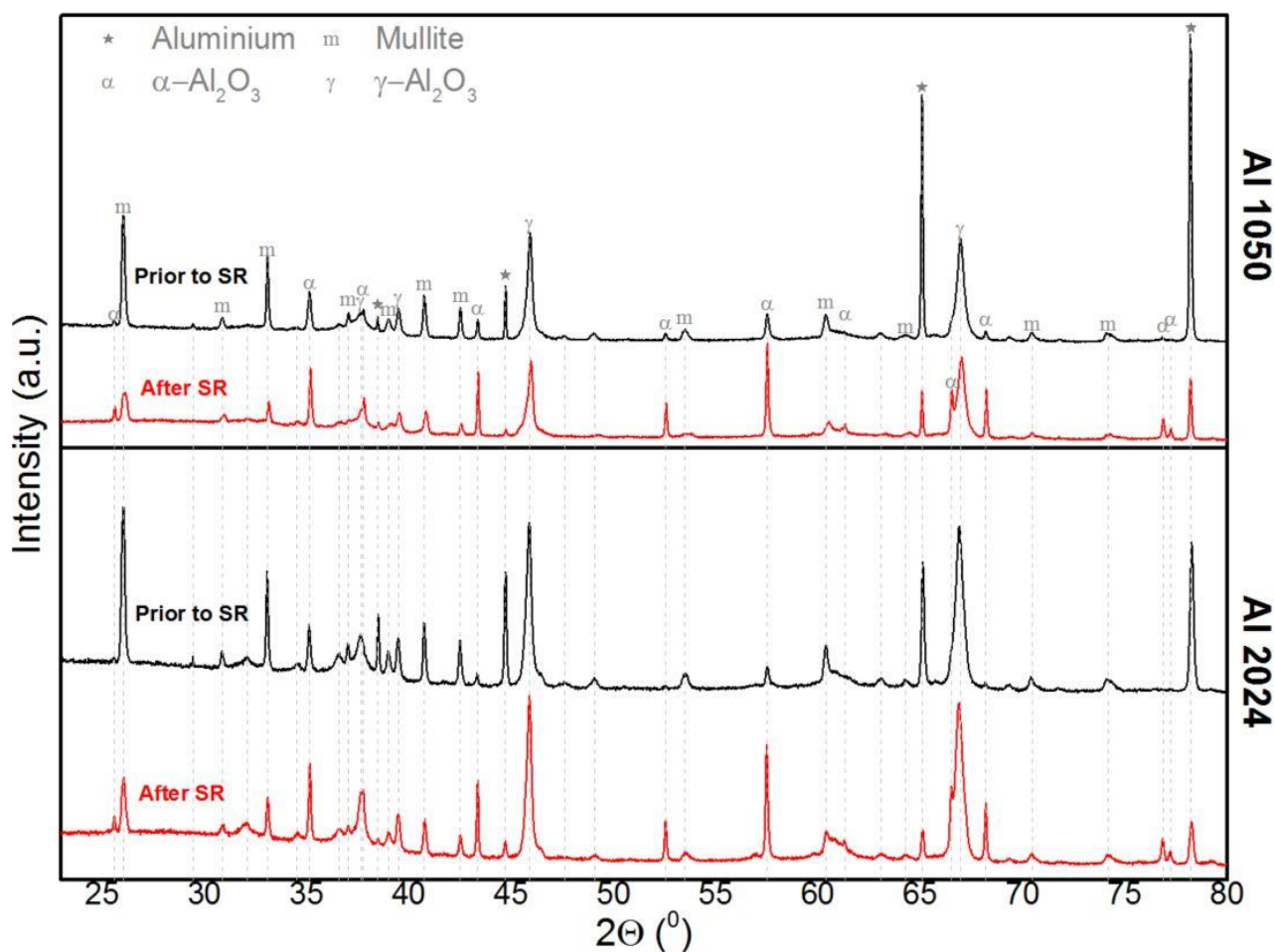


Figure IV- 15. X-ray diffraction patterns of the PEO oxide layers produced on the 1050 (upper) and 2024 (lower) aluminium alloys under the “soft” regime conditions and in the *electrolyte 1*. Black patterns correspond to treatments performed before the transition to “soft” regime and red patterns correspond to treatments performed until the end of the process (50 min).

IV.5.2 Morphology and elemental composition of the PEO coatings

SEM cross-section micrographs in Figure IV-16 illustrate typical morphologies of the PEO oxide layers produced on the two aluminium alloys investigated. The coatings consist of two sublayers. As

known and in accordance with the literature [3,7,77], the outer layer is generally characterised by large scale interconnected porosities, while the inner one exhibits a dense compact structure after processing in “soft” regime conditions. Occasionally, network of interconnected large cavities that creates a vertical channel through the dense layer might be observed (indicated in Fig. IV-16b). This is likely the result of intense micro-discharges (type B) that took place earlier, during “arcing” regime, and remained unfilled through the rest of the process.

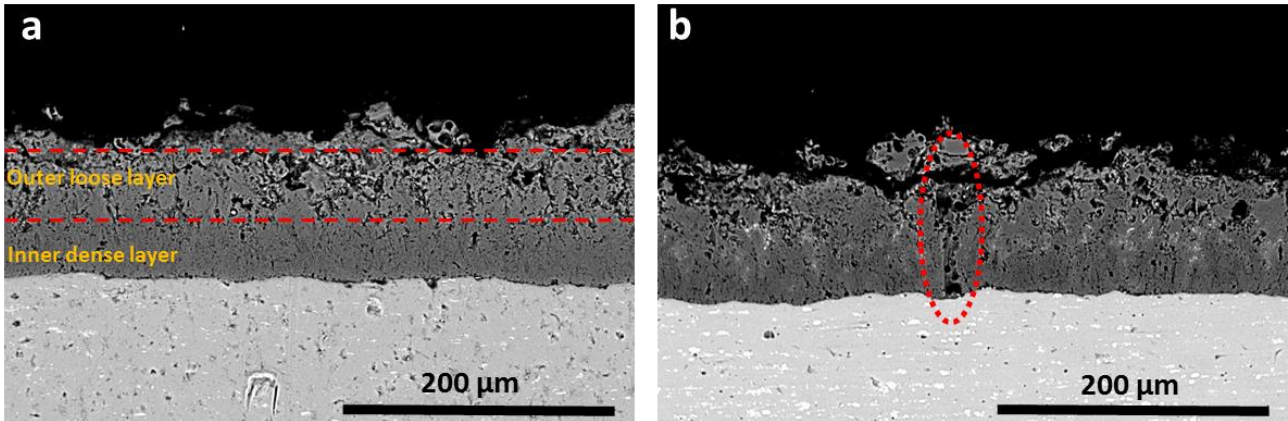


Figure IV- 16. Cross-section SEM micrographs of PEO coatings produced on a) a 1050 aluminium substrate and b) a 2024 aluminium substrate under the “soft”-regime conditions and in the *electrolyte 2*.

Elemental analyses performed by energy dispersive X-ray spectroscopy (EDX) on these cross-sections are presented in Fig. IV-17 and Fig. IV-18. Similarly to chapter III, the coatings consist mainly of aluminium and oxygen, which are homogeneously distributed throughout the oxide layer. On the contrary, silicon (Si), potassium (K) and sodium (Na), originating from the electrolyte, are deposited at the outmost sublayer.

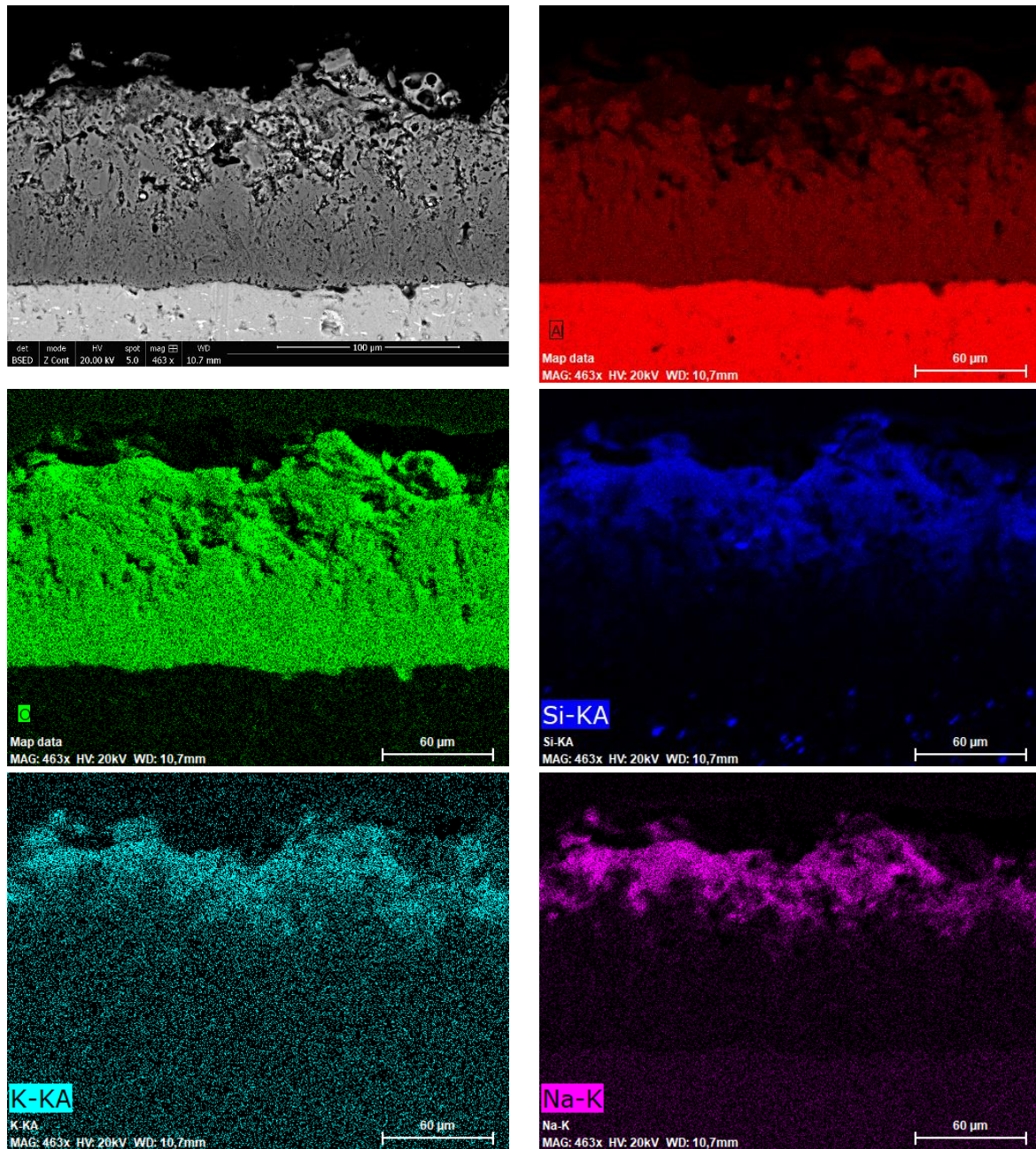


Figure V- 17. SEM cross-section micrograph of a PEO coating produced on a 1050 aluminium alloy (within the “soft” regime conditions and in the *electrolyte 2*) and the corresponding EDX elemental map distribution of Al, O, Si, K and Na elements.

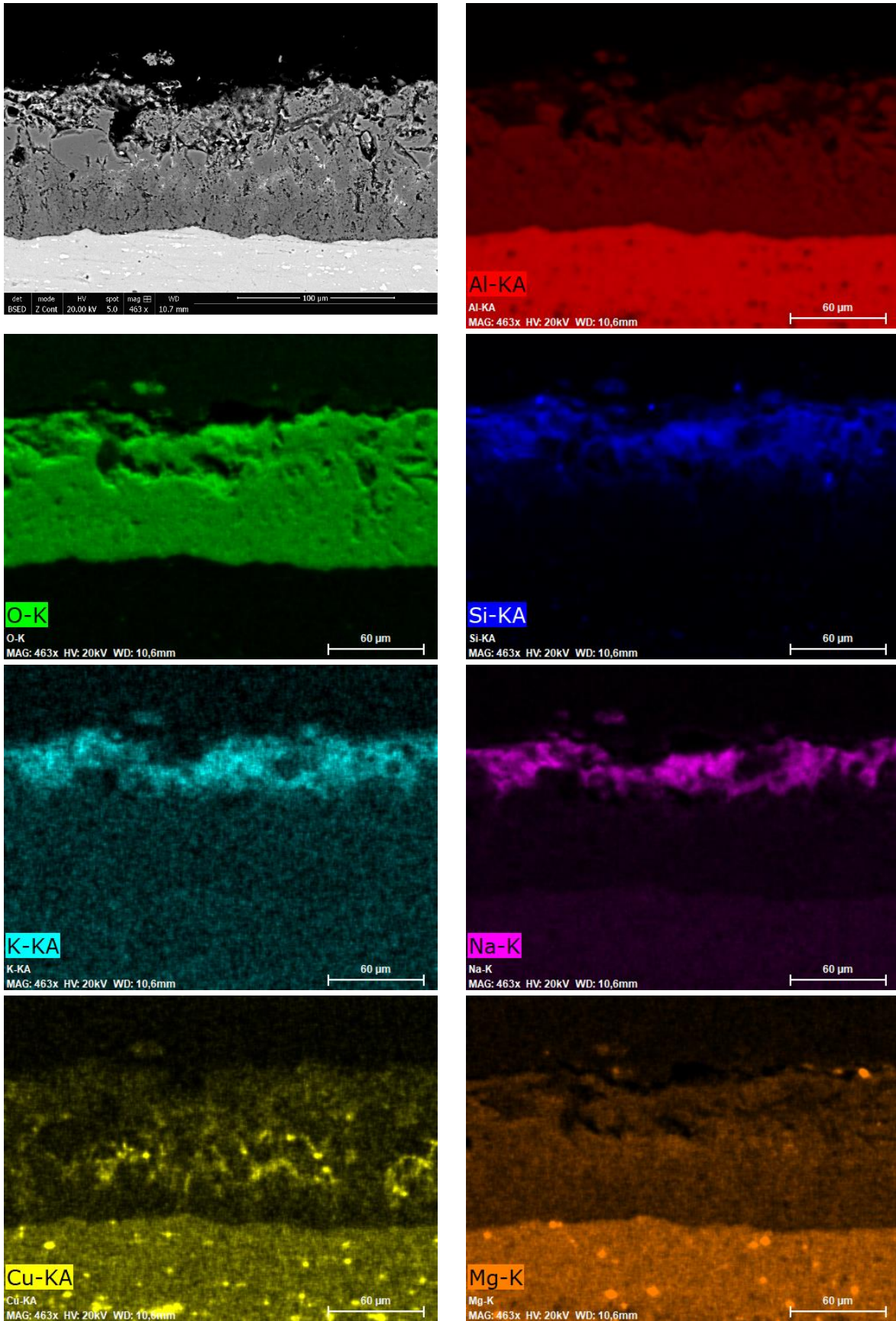


Figure IV- 18. SEM cross-section micrograph of a PEO coating produced on a 2024 aluminium alloy (within the “soft” regime conditions and in the *electrolyte 2*) and the corresponding EDX elemental map distribution of Al, O, Si, K and Na, Cu and Mg elements

As the main difference of aluminium 2024 is its content in copper, elemental map of Cu is also presented in Fig. IV-18. A gap in the copper concentration appears at the substrate/oxide interface. Copper is not distributed evenly throughout the coating but seems to be mainly located at a distance of approximately 40 μm from the substrate, forming an intermediate layer inside the overall PEO coating. This observation was cross-checked in various locations over the coating by performing scan-line profile measurements along the perpendicular direction to the surface Figure IV-19 shows one scan-line profile which clearly illustrates the higher concentration of copper in the centre of the oxide layer.

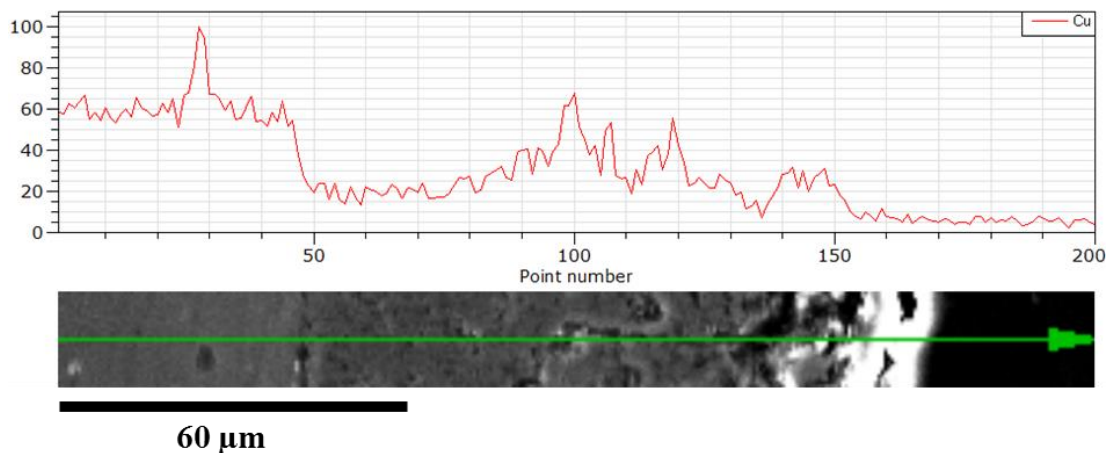


Figure IV- 19. Scan profile of the Cu element throughout a PEO oxide coating produced by on a copper-alloyed 2024 grade aluminium under the “soft”-regime conditions and in the *electrolyte 2*.

IV.6 Interaction of MDs with the surrounding environment

To further investigate the micro-discharges, and particularly the unusual subsistence of light spots on the surface of the quite pure 1050 aluminium alloy during the “soft” regime, a series of specific synchronised high speed camera recordings were conducted. For this purpose, a close comparison between the “arc” (RCQ = 1.5) and the “soft” (RCQ = 0.9) processing conditions was considered. A surface of approximately 200 mm^2 was recorded by setting the acquisition frequency of the camera at 100 kfps². Such recording conditions provides a time resolution of 10 μs and imposed a spatial resolution of $4.4 \cdot 10^{-3} \text{ mm}^2$. PEO treatments were processed in the *electrolyte 1* Micro-discharges appearing during the “arc” sparking regime (before establishment of the “soft” sparking regime) are usually intense (large size). They are accompanied with a subsequent collapse of the gas bubbles at their vicinity. Indeed, following every discharge (or cascade of discharges), a large amount of energy is released in the form of a shockwave that propagates through the top of the discharge channel, at

² fps: frame per second

the oxide/electrolyte interface. In the present experiment, the main objective was to monitor the micro-discharges over the processed surface with their simultaneous effect on the surrounding environment, mainly the dynamic of the gas bubbles that are located at the vicinity of micro-discharges. Note that a specific image processing software (TRACK by APREX Solutions) was implemented to analyse the obtained video frames, as illustrated in Fig. IV-20. By adjusting the detection parameters in the image processing software, it is possible to detect and follow both the discharge events (a) and the gas bubbles (b). In such a way, some correlations between the micro-discharges and their effect on the dynamic of the gas bubbles can be drawn.

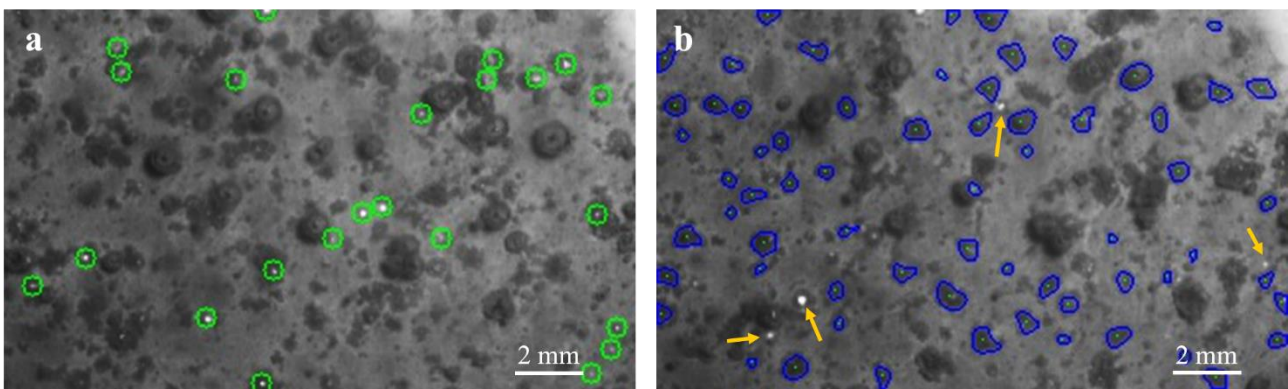


Figure IV- 20. Image analysis of high speed video images obtained during the PEO treatment of the 1050 aluminium alloy within the “soft” regime conditions. Detection of (a) micro-discharges and (b) gas bubbles located over the processed surface. Yellow arrows in (b) indicate micro-discharges while blue edges represent the shape of the surrounding bubbles.

Figure IV-21 shows an example of the effect of micro-discharges on the surrounding gas bubbles. When no current is applied, these bubbles remain immobile (or maintain a low velocity due to the electrolyte stirring) with a quite well-defined spherical shape. During the anodic polarisation of the processed material, micro-discharges occur and induce both deformations of the spherical shape of the surrounding bubbles (as seen in Fig. IV-21) or variations in their velocities (or acceleration).

Here, it is worth specifying that the automatic analysis of frames is based on detection parameters (e.g. the contrast threshold) the accurate discrimination of two distinct events remains very sensitive to the process. Since the recorded surface is illuminated by an external light source during recording, rapid changes caused by light reflection or shadows of the gas bubbles themselves can lead to misleading detection. In addition, collisions and mergers of two individual gas bubbles into one or creations of new ones need to be identified. To avoid such detection artefacts, it was decided to follow only the velocity of the detected bubbles and to provide velocity distributions. To minimise erroneous detections, and consequently, false calculations, we relied mostly on a statistical approach by

monitoring larger surface areas and maximising the number of the gas bubbles that are being recorded.

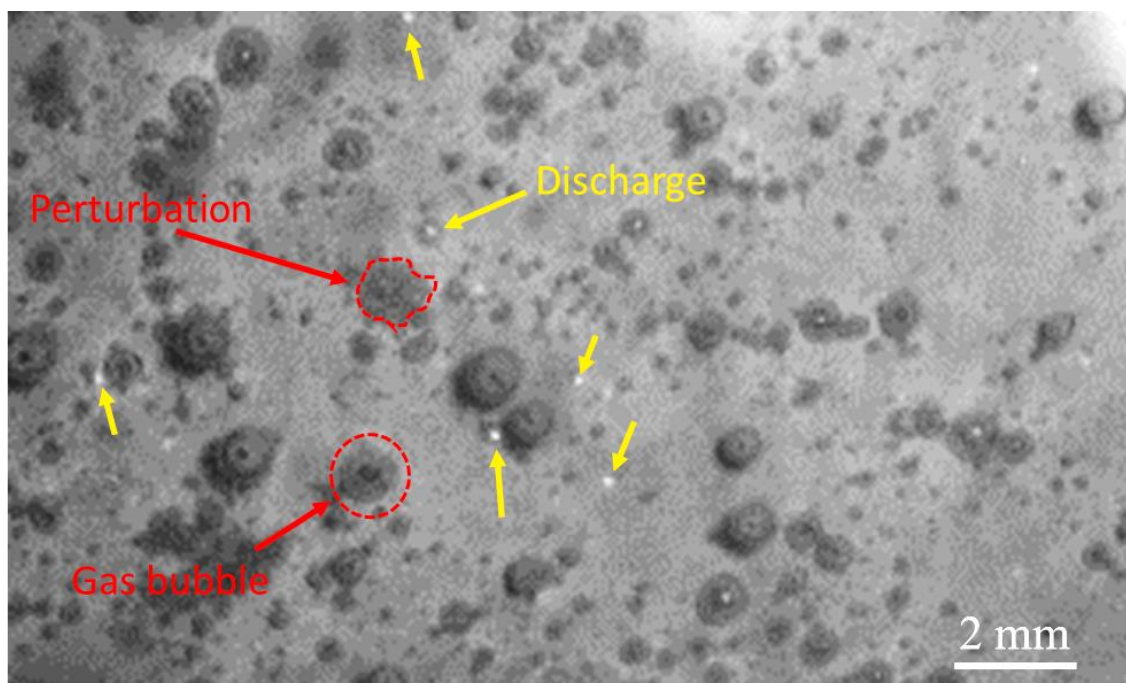


Figure IV- 21. Frame recorded during fast video imaging that illustrates the effect of micro-discharges on the surrounding gas bubbles.

The results of these synchronised recordings in the course of the treatment are summarised in Figure IV-22. This figure shows the anodic voltage evolution for the two investigated electrical conditions (RCQ = 0.9 and 6.0). The velocities of the gas bubbles, recorded during five consecutive periods of the current pulse and at various moments during a treatment, are also given in the insets of the Fig IV-22. During the “arc” sparking regime (Fig. IV-22a and c), when strong micro-discharges dominate the process, one can observe that bubbles exhibit high velocities during each anodic pulse of the current. Although the majority of the detected bubble presents a velocity in the range of 60-70 mm/ms, velocities up to 120 mm/ms have been also observed

Interestingly, over one pulse of the anodic current, the time at which the bubbles start to move with high velocities is in good accordance with the delay of the micro-discharges appearance, as described by Martin *et al.* [67] and as discussed in the previous chapter. Indeed, with high RCQ conditions (black voltage curve), a shorter delay in the micro-discharges appearance is observed than the one with low RCQ (blue). This is reliable with the gas bubble velocities which are detected earlier (Fig.IV-22 a) for high RCQ than for the low RCQ (Fig. IV-22c). However, one can also observe smaller number of detections of relatively high velocities scattered throughout the recordings. Their origin might lay either in true existence of high velocity gas bubbles, caused by the constant stirring

of the electrolyte, or, as well, in erroneous recording due to false detection. As mentioned, the detection is very sensitive to changes in pixel intensity and despite the attempts to optimise the parameters, an absolutely accurate detection was not achieved. A closer and focused on fewer gas bubbles recording, with improved illuminating conditions, could provide better insight to this matter. Nevertheless, the periodic increased density of high velocities that appear during every anodic alternation implies a direct correlation of these perturbations with the intense micro-discharges.

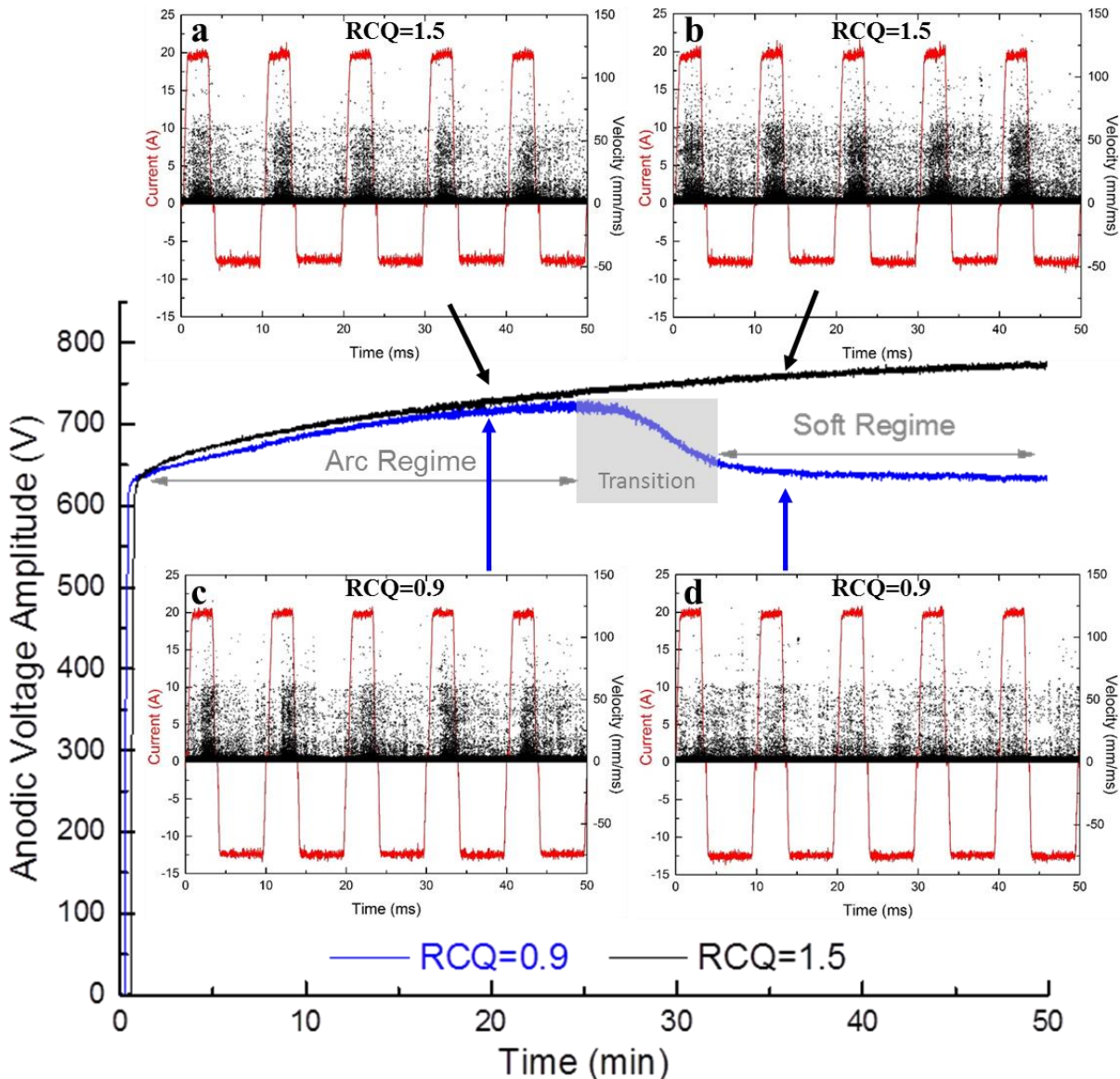


Figure IV- 22. Synchronised recordings of gas bubble dynamics with the applied current pulses in the course of the PEO treatment. The upper and lower insets correspond to processes conducted with high (RCQ = 1.5) and low (RCQ = 0.9) charge quantity ratio values, respectively.

As the process continues, and in the case of the “arc” sparking conditions (RCQ = 1.5), the treated surface still experiences strong micro-discharges taking place throughout the oxide layer thickness.

In fact, as the thickness of the coating increases, the discharges gradually decrease in number but become stronger in terms of size. As seen in Fig. IV-22b, this behaviour clearly induces stronger effects on the dynamic of the surrounding gas bubbles. Indeed, the density of the detected bubbles with high velocities gradually increases with the processing time (a). On the contrary, after the establishment of the “soft” regime (blue voltage curve), the average velocity of the bubbles significantly decreases (Fig. IV-22d) and only some minor detections of high velocity bubbles are still observed homogeneously scattered irrespective of the applied pulses (anodic or cathodic).

However, and as we have seen in section 3 of this chapter, light emission continues to take place periodically with the anodic pulses after the establishment of the “soft” regime for this 1050 aluminium alloy. Figure IV-23 illustrates recordings of 10 consecutive pulses obtained at 50 min of processing time with RCQ = 1.5 (a) and RCQ = 0.9 (b). It shows synchronised detections of number of light spots (or micro-discharges) and velocities with the applied current pulses. These simultaneous detections evidence the correlation between the plasma discharge events, their light emission and the perturbations caused on the gas bubbles.

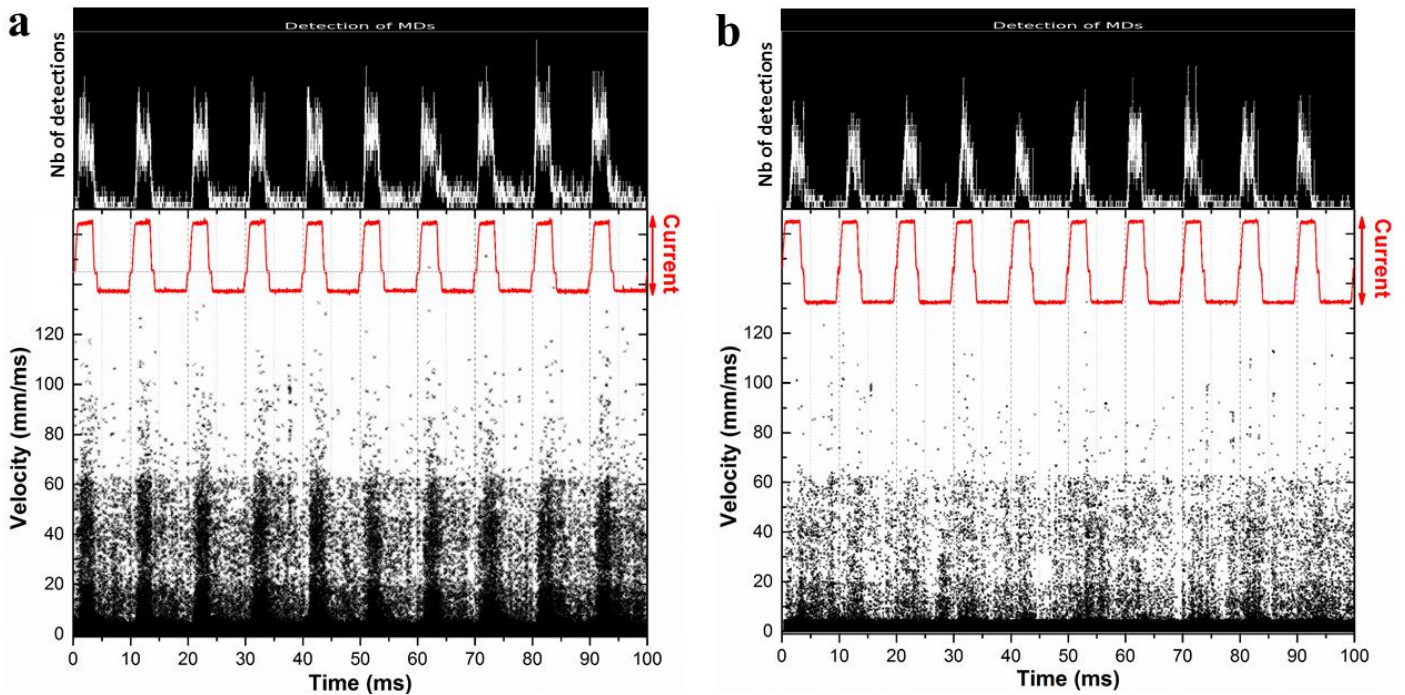


Figure IV- 23. Synchronised detections of gas bubble perturbations and light emission with the applied current pulses at 50 min of processing in a) “arcing” (RCQ = 1.5) and b) “soft” (RCQ = 0.9) conditions.

Once again, as intense micro-discharges continue to occur throughout the total thickness of the oxide layer during the “arc” sparking regime (Fig. V-23a), the light emissions are followed by intense

perturbations of the gas bubbles as confirmed by the high velocity detections. In contrast, in Fig. IV-23b, despite the process operating in “soft” regime (at 50 min), light emission is still emitted periodically and absolutely synchronised with the anodic current pulses, but no apparent effect is observed on the dynamics of the gas bubbles.

The plausible reasons of this observation will be discussed in the following section.

IV.6 Phenomenological interpretation

A phenomenological interpretation of the previous observations is proposed in this last section. A descriptive mechanism explaining the aforementioned results is discussed and a schematic illustration of this proposed mechanisms is given in Fig. IV-24.

At the early stage of the process, regardless the electrical conditions, the processed surface experiences intense micro-discharges that appear in “cascades” [136]. They take place throughout the overall thickness of the layer (named as type-B by Cheng *et al.* [104]) and they are accompanied with strong optical and acoustic emissions. Ignition of a micro-discharge is also associated with the formation of a shockwave that propagates in the electrolyte (Fig. IV-24 a). Gas bubbles that are on the path of the shockwave are suddenly affected. They suddenly change in shape, vibrate and they are accelerated. Between two micro-discharges, bubbles return to their original spherical shape and return to their low velocity. This mechanism is illustrated in Figures IV-24a.1-5 where consecutive frames obtained from the high speed video recording are shown. Micro-discharges are marked with red while the pre-existing gas bubble over the oxide surface is in yellow. When a discharge starts, a small gas dome appears over the discharge channel (a.1), which expands to its maximum (a.3, a.4) and collapses once the discharge is over (a.5). As a consequence, the surrounding gas bubble (yellow) is disrupted and deformed during this period until it finally relaxes again and return to its shape. In addition to deformation, changes in velocity are also observed. On the path of the pressure shockwave, the gas bubble experiences a sudden acceleration leading to high short lived velocities in the timescale of microseconds, as they were presented in Fig. IV-22 and Fig. IV-23.

These intense micro-discharges usually result in coatings with relatively large cavities which are rich in elements from the electrolyte, as they are interconnected through a network of pores that are of nano- and micro-meter size [91] (Fig.IV-24b).

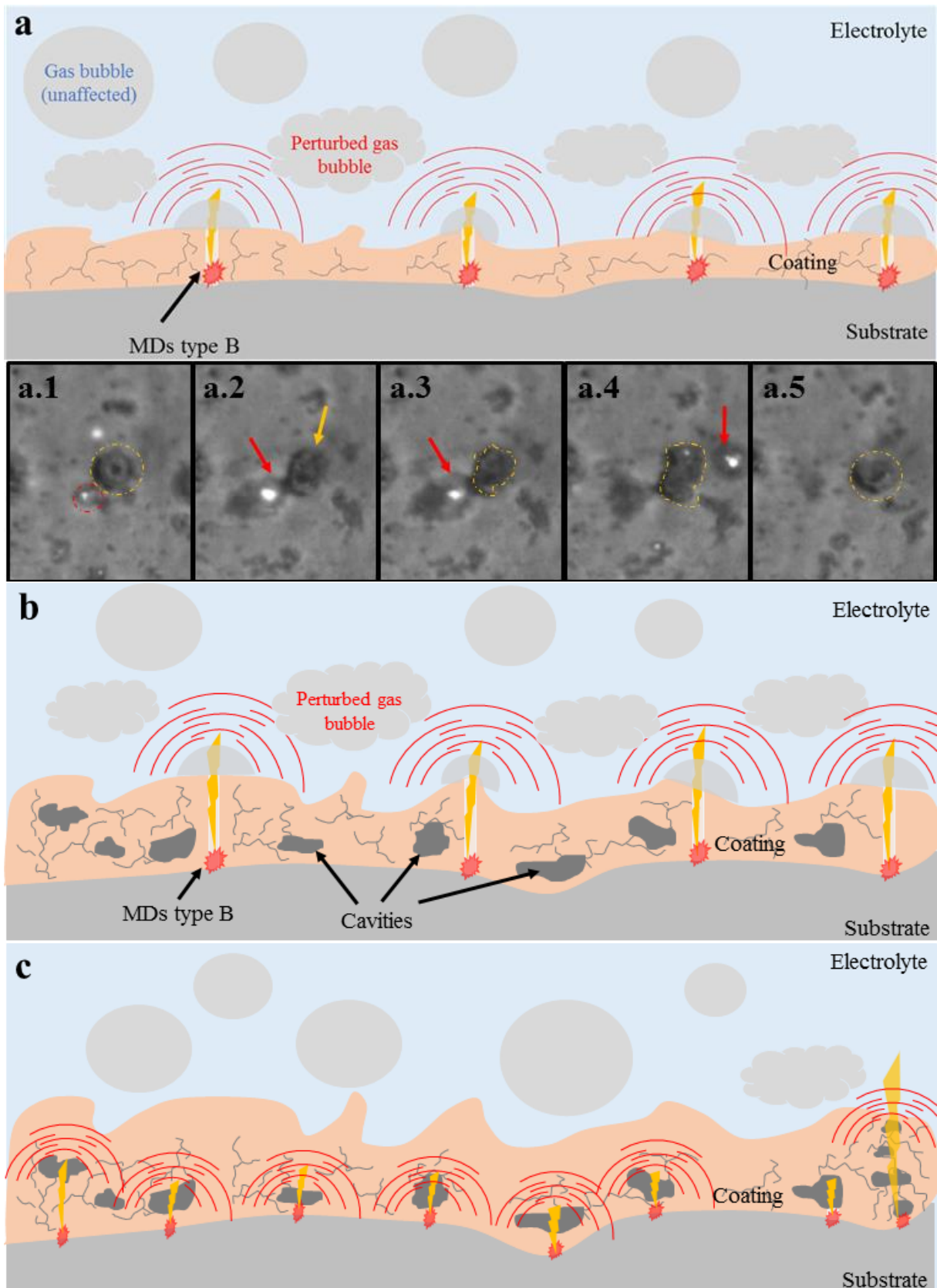


Figure IV- 24. Schematic illustration of the mechanism and the interactions between MDs and gas bubbles during PEO of Al1050. a) corresponds to the early stage of the process, b) prior to establishment of “soft” regime and c) during “soft” regime.

As the process continues, the oxide layer gradually grows and become thicker. Therefore, the overall electrical impedance of the system increases. Based on the model of electrical charge accumulation [67], this higher impedance requires a greater amounts of charges at the oxide/electrolyte interface to induce a discharge throughout the overall layer. However, under the electric field during anodic polarisation, it is possible that discharges are facilitated through the existing cavities in the oxide layer. The existence of such type of discharges has been proposed by Hussein *et al.* [23,101] and Cheng *et al.* [64,104]. As these cavities are surface-connected through the network of pores, there is a constant supply of ionic species from the electrolyte. Electrical discharges are prone to occur at the weakest points, such as impurities and structural defects. Under this consideration, they would preferentially take place at these cavities rather than throughout the overall oxide layer (Fig. IV-24c). This is consistent with our experimental observations, as in such case, the energy released after these discharges would propagate, absorbed and transformed by the surrounding oxide layer without reaching the surface. This is indirectly confirmed in Fig. IV-23b by the absence of interaction between the “light emitting events” and the gas bubbles perturbations. Moreover, such type of mechanism can explain the continuity of the oxide growth during “soft” regime by an inward growth of the coating. Recent findings of Wu *et al.* [78] and Wang *et al.* [137] confirm such hypothesis and demonstrate the growth towards the substrate, by studying the coating /substrate interface. Nevertheless, some B-type discharges might still take place throughout the overall layer via closely interconnected cavities which can facilitate such discharges (as shown in Fig. IV24c). These might be responsible for some of the perturbations recorded in either Fig. IV-22d or Fig. IV-23b during “soft” regime. But they are believed to be a small minority compared to the total number of the detected “light-emitting events”.

In addition, it has been observed that these “softer” light emissions occur also during the “arcing” stage as well, concomitantly with the intense micro-discharges. In fact, these light spots ignite approximately 0.7-1 ms earlier that the violent micro-discharges, which are accompanied with gas evolution. This is shown in Fig. IV-25 which presents image frames obtained from video recording at 20 min of processing of aluminium 1050 in “soft” regime conditions. At this moment, “soft” regime has not been established yet, thus type-B discharges are expected to dominate the process. However, as can be seen in Fig. IV-25a and b, ignition of “softer” discharges takes place first all over the processed surface with no indications of gas evolution at this moment. It is only after 0.72 ms that the first intense micro-discharge (red in Fig. IV-25c) is observed, followed by a dome-like growth and collapse of the gas bubble above the discharge channel. The process then continues with both types of discharges (Type-B and D) occurring simultaneously (d).

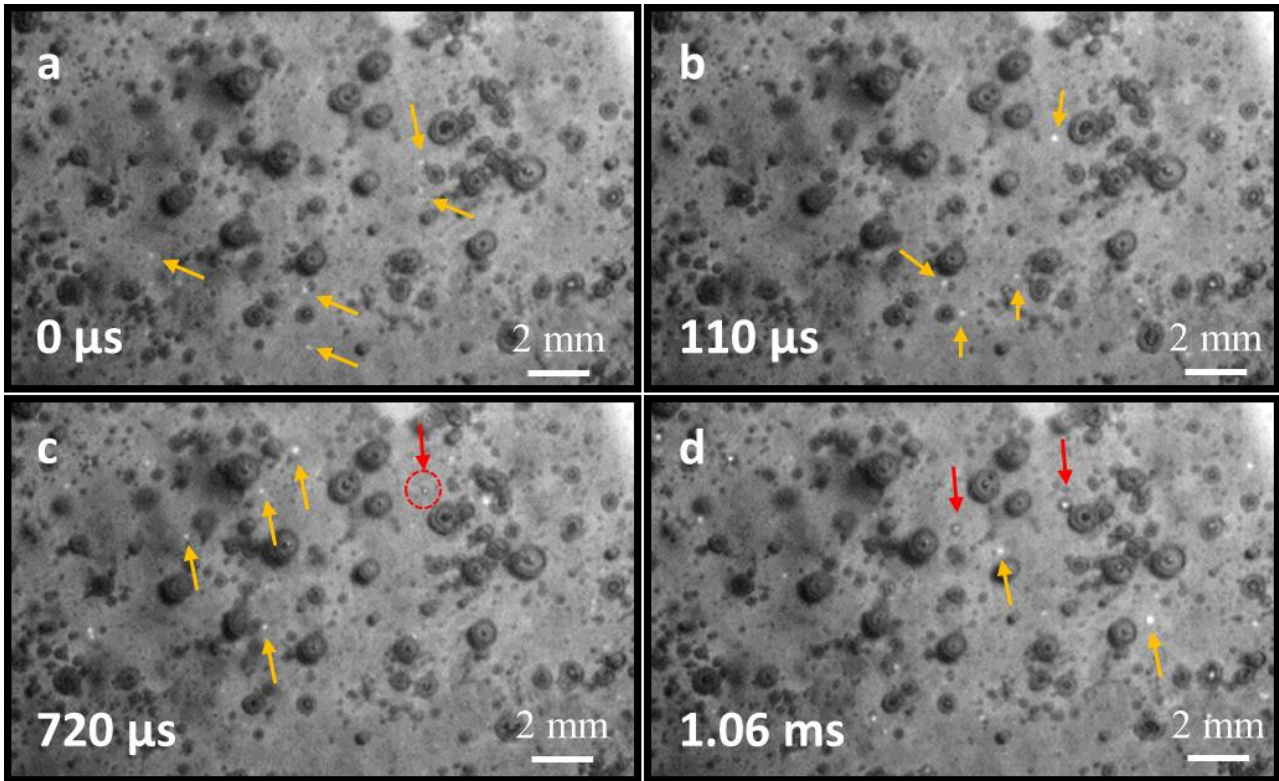


Figure IV- 25. Image frames obtained from fast video recording during PEO treatment of Al 1050 under “soft” regime conditions at 20min of processing time. Yellow arrows show possible micro-discharges taking place inside the oxide coating (Type-D) while the red ones correspond to intense MDs occurring throughout the total layer (Type-B).

These findings further support the concept that dielectric breakdown occurs at the weakest point of the layer and as such, under the anodic polarisation, is likely to occur earlier inside these cavities and later, during “soft” regime, dominate the process.

In the case of copper-alloyed aluminium 2024, the visual absence of these internal micro-discharges during “soft” regime could be attributed to the presence of copper in the coating as shown in Fig. V-18. Copper is oxidised mainly in its most stable forms, as cuprous (Cu_2O) and cupric (CuO) oxide, both exhibiting dark colours (dark red and black, respectively). However, in literature, the band gap of such compounds is reported to range between 1.7 - 2.6 eV [138–143], corresponding to a wavelength range of approximately 730 - 476 nm, respectively. This results to copper oxide being a strong absorber at lower wavelengths and exhibiting an increase of transmittance from 500 - 700 nm, thus, leading to a “filtering” effect. However, this was not observed. In the range of our measurements (250 – 850 nm) (Fig. V-7), no signal was recorded after the transition to “soft” regime. This fact excludes the influence of copper oxide on the appearance of inner micro-discharges on Al 2024 during “soft” regime. Nevertheless, other phases, such as copper aluminium oxide (Al_2CuO_4), may also be

formed in the coating. A further detailed investigation would be necessary to provide more information, regarding this aspect.

IV.7 Conclusions of Chapter IV

This chapter was dedicated to the study of PEO process by investigating two different substrates and utilising various characterisation techniques in order to obtain a better insight into the process itself and the phenomena taking place, mainly regarding the nature and properties of the micro-discharges during “soft” regime.

We have shown how the type of the electrolyte affects the discharge events and their distribution over the processed surface and, consequently, their effect on the growing oxide layer. Transition to “soft” regime exhibited a peculiar behaviour, being affected more by the treated material rather than the used electrolyte. A homogeneous growth and a roughly twofold increase in thickness was observed when using the more concentrated electrolyte 2. In addition, the use of this electrolyte led to a significant decrease in anodic voltage, which probably has an impact on the energy consumption of the system during PEO.

Fast video recordings of the processed surface during “soft” regime revealed periodical ignitions of light spots with the anodic pulses. This was further investigated and confirmed by means of optical emission spectroscopy, which showed the presence of a broad continuum for the pure aluminium sample during this stage. It was shown that these light spots co-exist with the intense MDs even during the “arcing” stage and, in fact, ignite earlier.

Finally, by studying the interactions of micro-discharges with the surrounding environment, a correlation between discharge events and the gas bubble dynamics was established. This indirect investigation indicated that the source of the light spots, detected during “soft” regime on pure aluminium, is localised deep inside the growing oxide layer. The proposed mechanism suggests the occurrence of mainly internal micro-discharges (Type-D) in “soft” regime, which drive the process in continuation of the oxide growth.

Chapter V - Formation of PEO coatings in the “soft” regime conditions

V.1 Introduction of the chapter V

As reported in the chapter I, pioneer works have shown that the suitable setting of the current parameters during PEO of aluminium allows a particular “soft” regime to appear [19,106]. The appearance of this “soft” regime is mainly promoted by the use of a bipolar current at the electrodes for which the ratio of charge quantity RCQ ($RCQ = Q_p / Q_n$) is lower than one, preferably in the range of [0.8–1]. Despite the gradual disappearance of visible micro-discharges over the processed surface and a gradual reduction in the acoustic emission, appearance of the “soft” regime results in an increase in growth kinetic and a reduction of the porosity while the process energy consumption is reduced by 20–30 %. Nevertheless, the mechanisms that govern the transition from the detrimental “arc” regime to the beneficial “soft” regime are not well understood yet. More specifically, the relationship that exists between the PEO processing conditions, the discharge mechanisms and the resulting PEO coatings remains not well understood.

To this end, a fine description of the specific morphology of the PEO coatings grown under the “soft”-regime was conducted. Particularly, this chapter focuses on the formation of PEO coatings grown on aluminium in a silicate-rich electrolyte within the specific “soft” regime conditions. The microstructure of the PEO coatings was fully described at different scales, mainly at the sub-micrometre scale using high resolution transmission electron microscopy (HR-TEM). To complement, optical emission spectroscopy (OES) was carried out to estimate some thermodynamics parameters (especially the temperature of the material under the micro-discharges) that could explain phase transitions. Finally, based on an experimental approach that combined material and optical characterisations, a growth mechanism based on a metastable solidification route of a silicon-enriched alumina melt was proposed and discussed.

It is also worth mentioning that this present study is the continuation of preliminary observations of A. Nominé [107] who pointed out for the first time the formation of particular lamellar nanoscale morphology inside the “pancake” structure during the “soft” regime. By proposing a mechanism of its formation, the present study goes beyond Nominé’s experimental observations.

V.2 Specific experimental conditions

V. 2.1 Elaboration of specific samples in the PEO “soft” regime conditions

The samples used in this study consisted of an Al 2024 aluminium alloy (see Table II-2). They were processed in a typical electrolyte consisting of potassium hydroxide ($[\text{KOH}] = 1 \text{ g}\cdot\text{L}^{-1} \approx 0.018 \text{ mol}\cdot\text{L}^{-1}$) and anhydrous sodium silicate ($[\text{Na}_2\text{SiO}_3] = 1.65 \text{ g}\cdot\text{L}^{-1} \approx 0.014 \text{ mol}\cdot\text{L}^{-1}$) diluted in deionized water. As the use of the current controlled power supply allows to optimally set and control the anodic and cathodic current amplitudes, the ratio of the positive to negative charge quantity ($\text{RCQ} = Q_p / Q_n$) was set at 0.9 in order to allow the occurrence of the “soft” regime in the course of the process [19,106]. The current frequency and the anodic current density were set at 500 Hz and $40 \text{ A}\cdot\text{dm}^{-2}$, respectively.

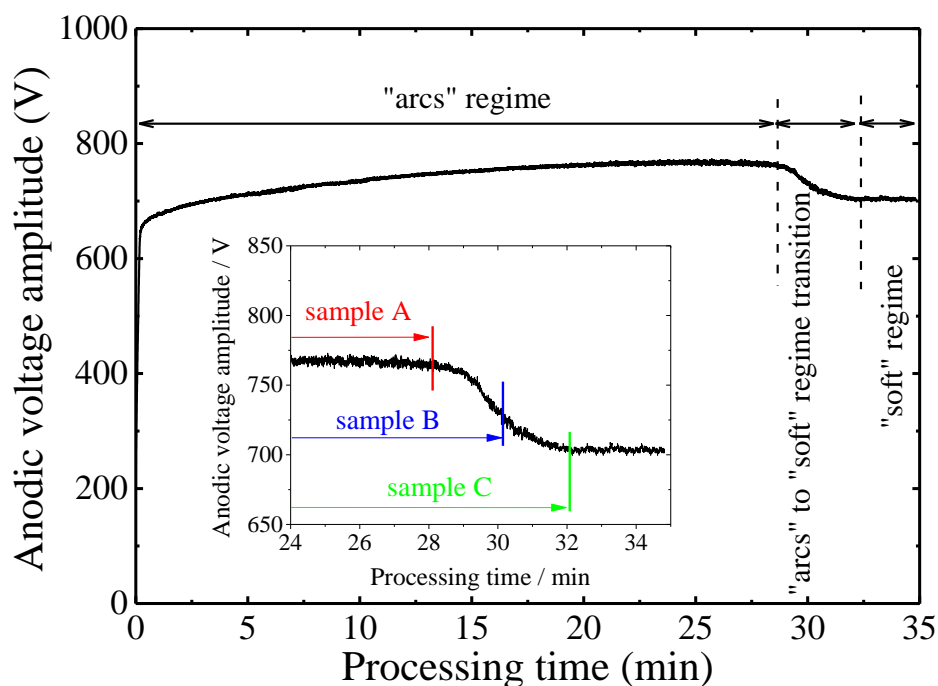


Figure V-1. Voltage-time response of a Al2024 aluminium alloys PEO processed within the “soft” regime electrical conditions ($Q_p / Q_n = 0.9$, $f = 500 \text{ Hz}$, $j = 40 \text{ A}\cdot\text{dm}^{-2}$). Inset depicts the processing time of the samples A, B and C.

As previously reported in the Chapter I, the transition from the “arc” to the “soft” regime is characterised by a gradual drop of the anodic voltage amplitude in the course of the treatment. This voltage transition is also directly correlated with a change of the optical and acoustic behaviour of the discharges which gradually turned to tiny discharges with shorter lifetimes [19,20]. This phenomenon is typical of bipolar PEO treatment conducted in “soft” regime conditions. Fig. V-1 which shows the typical evolution of the anodic voltage amplitude with the processing time evidences that this

transition starts at approximately 28 min and is fully established at about 32 min. Based on this voltage-time response presented, three samples were differently processed. Sample A was processed until the end of the “arc” regime (process stopped at 28 min). Sample B was processed until the moment of transition from “arc” to “soft” regime (process stopped at 30 min). Sample C was processed until the “soft” regime was fully established (process stopped at 32 min).

V.2.2 Ex situ characterisation of the PEO coatings

At the micrometre scale, the produced PEO oxide layers were observed by scanning electron microscopy (SEM). For each processed sample, the top-most surface and the cross-section were examined using secondary electrons (SE) and backscattered electrons (BSE) detection modes. The elemental composition of samples was determined by EDX measurements at different locations on the top-most surface of the coatings and the phase identification of the oxide layers was performed by XRD measurements. The relative volume content of the α - Al_2O_3 phase with respect to the η - Al_2O_3 was deduced from XRD peak adjustments and calculated from the integrated intensity of α - Al_2O_3 peaks compared to the integrated ones of both α - and η - Al_2O_3 [28]. Additionally, the phase characterization of the top-most surface region of the oxide layers was carried out by grazing incident XRD (GIXRD). It must be mentioned here that, from a crystallographic point of view, γ - and η - Al_2O_3 belong to the same space group ($\text{Fd}\bar{3}\text{m}$) and exhibit the same lattice parameter (0.790 nm) making it difficult to discriminate each other by conventional XRD measurements. In the present study, in a better accordance with the JCPDS cards, the η - Al_2O_3 is suggested to be present in the produced PEO coatings instead of the γ - Al_2O_3 .

At the sub-micrometre scales (between 1 to 0.01 μm), the microstructure of the produced oxide layers was investigated by high-resolution transmission electron microscopy (HR-TEM). In scanning mode (STEM), EDX analysis was performed using an energy-dispersive X-ray spectrometer with a probe size of 1 nm. EDX element distribution maps were recorded over an area of $512 \times 512 \text{ nm}^2$ (1 measurement point per nm). In addition, an EDX line-scan profile consisting of 40 measurement points distributed over a line of 330 nm in length was also recorded with an acquisition time of 1 min per measurement point.

V.2.3 In situ characterisation of the PEO process

Optical emission spectroscopy (OES) measurements were performed during the PEO process, using a 1800 gr/mm grating (resolution of $\sim 0.07 \text{ nm}$). The optical emission spectra were recorded

within the wavelength range of 200–900 nm. To ensure that the maximum light intensity was collected and to avoid absorption of near-UV wavelength radiations by the glass window of the PEO treatment cell, an appropriate optical fibre connected to the entrance slit of the spectrometer was immersed in the electrolyte and located at ~30 mm from the sample.

V.3 Results on the *ex situ* characterisation of the PEO coatings

V.3.1 Characterisation at the micrometre scale

Indexing of the XRD patterns in Fig. V-2a revealed that oxide coatings are composed of crystalline aluminium oxides α -Al₂O₃ and η -Al₂O₃ in various proportions. The transition to the “soft” regime is concomitant with the appearance of α -Al₂O₃ diffraction peaks whose intensity increases gradually as the “soft” regime proceeds. Indeed, just before the appearance of the “soft” regime (sample A), the coating is mainly composed of η -Al₂O₃ ($7 \pm 3\%$ vol. α -Al₂O₃), while the one processed until the “soft” regime is completely established (sample C), exhibits the highest content of α -Al₂O₃ ($18 \pm 3\%$ vol. α -Al₂O₃). This observation is in good agreement with previous studies which also showed a gradual enrichment in α -Al₂O₃ through the inner sublayer of the PEO coating when the process switched into the “soft” regime [17,113].

The aluminium peaks on the XRD patterns (noted Al in Fi. V-2) are due to the scattering of the aluminium substrate beneath the oxide layer. When the “soft” regime started, the intensity of the Al-peaks starts to decrease, suggesting that the oxide coating became thicker and more compact as the “soft” regime occurred. The grazing incidence XRD (GIXRD) pattern recorded on sample B is presented in Fig. V-2b. The absence of aluminium peaks in this pattern confirms that Al peaks detected in Fig. V-2a originate from the substrate. It also confirms that no crystalline aluminium exists in the PEO coating. In addition, the GIXRD pattern shows that the top-most surface of the grown oxide layer is composed of an amorphous material and crystallised phases. These crystalline phases consist of a mixture of alumina and mullite, the latter being a solid solution phase of alumina (Al₂O₃) and silica (SiO₂) in the Al₂O₃-SiO₂ binary system [144]. The presence of mullite in PEO coatings was previously reported by Dehnavi *et al.* [37,103,113] who also showed that the mullite phase was mainly located in the outer sublayer of the PEO coatings.

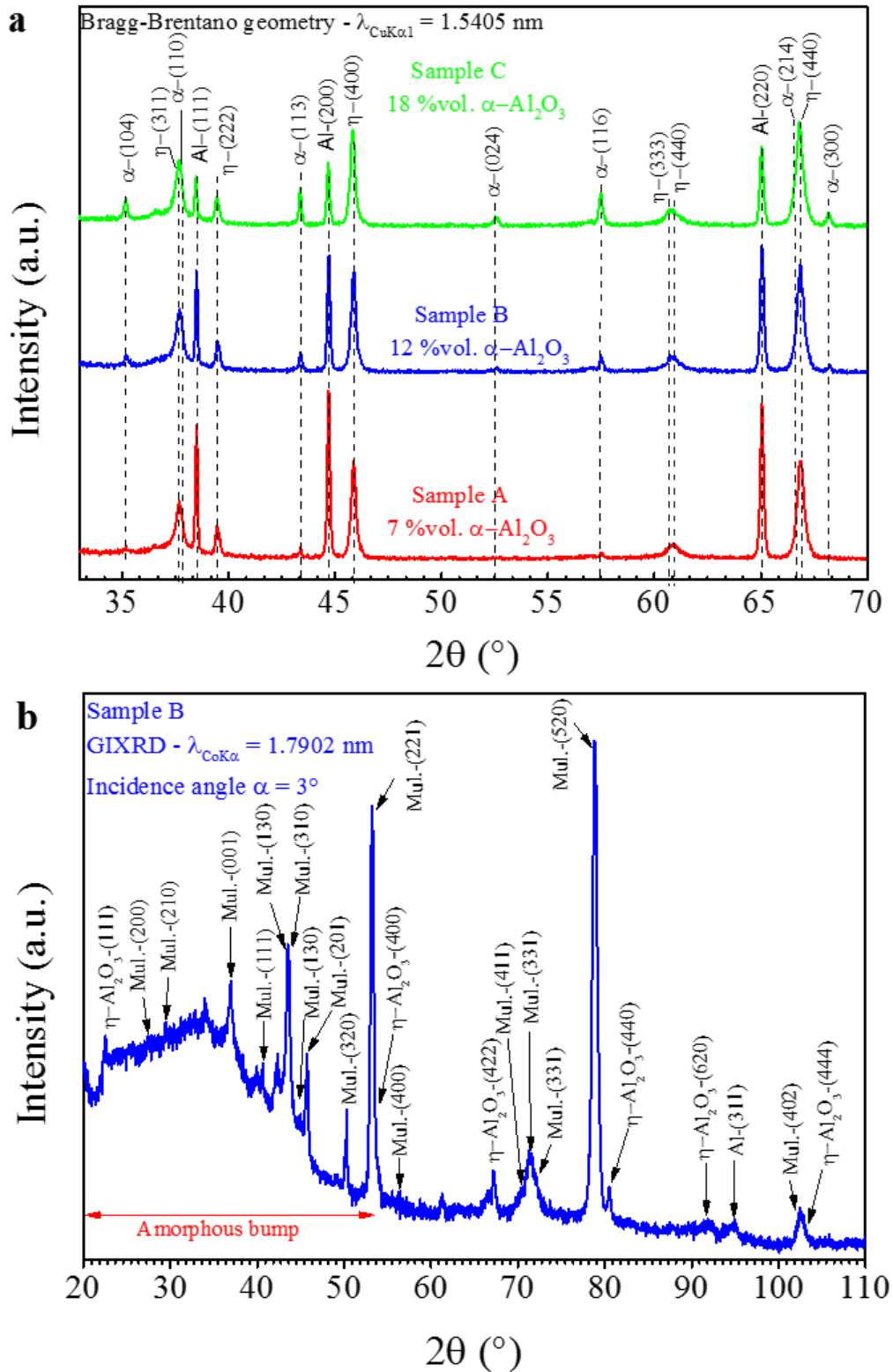


Figure V-2. a) XRD patterns of the processed samples with the calculated $\alpha\text{-Al}_2\text{O}_3$ content (in % vol.). (Al for aluminium, α for $\alpha\text{-Al}_2\text{O}_3$, η for $\eta\text{-Al}_2\text{O}_3$. b) GIXRD pattern of the processed sample B. (Mul. for mullite).

SEM micrographs of the cross-sections and the top-most surface of the processed samples are shown in Fig. V-3. With the transition from “arc” to “soft” regime, the morphology of the PEO

coatings gradually transforms into a more compact and thicker oxide layer ($26 \pm 8 \mu\text{m}$, $31 \pm 5 \mu\text{m}$, $55 \pm 5 \mu\text{m}$ thick for samples A, B and C, respectively).

For the sample A, processed before the occurrence of the “soft” regime (Fig. V-3a and 3d), the morphology is characterised by large and unfilled oxide layer bulges. As previously described in Chapter I, these bulges, commonly referred to as “pancake”-like structures [135], are typical of PEO coatings grown within the “arc” regime and they are caused by strong electrical MDs. The EDX spectrum recorded on the dome of the hollow “pancake” structure shows it mainly consists of Al ($\approx 31\%$ at.) and O ($\approx 67\%$ at.) (Fig. V-3g), which is consistent with the detection of alumina from GIXRD measurements (Fig. V-2b). A small amount of Si ($\approx 1\%$ at.) coming from the electrolyte was also detected, while the presence of Au ($\approx 1\%$ at.) is due to the gold sputtered coating on the surface prior to SEM observations.

For the sample B (Fig. V-3b and 3e), collected during the transition from the “arc” to “soft” regime, the cavity of the “pancake” structure is mainly filled with some solidified material. The EDX spectrum recorded on this site shows it consists mainly of Al ($\approx 24\%$ at.) and O ($\approx 63\%$ at.), but also Si ($\approx 7\%$ at.), Ca ($\approx 1\%$ at.), K ($\approx 1\%$ at.), Na ($\approx 1\%$ at.), Mg ($\approx 1\%$ at.) and Au ($\approx 1\%$ at.) (Fig. V-3h). At the same time, the growth of an interconnected network of a “sponge-like” morphology was observed around and across “pancake” structures on the topmost surface of sample B (Fig. V-3e). This “sponge”-like morphology, highly porous and with filaments, seems to incorporate elements from both the electrolyte, e.g. O ($\approx 54\%$ at.), Si ($\approx 13\%$ at.), Ca ($\approx 5\%$ at.), K ($\approx 2\%$ at.) and Na ($\approx 1\%$ at.), and from the Al substrate, e.g. Al ($\approx 18\%$ at.), Cu ($\approx 4\%$ at.) and Mg ($\approx 2\%$ at.) (Fig. IV-3i). This observation is in good agreement with previous studies that showed that the formation of this “sponge”-like structure usually appears concomitantly with the transition to “soft” regime whatever the processing conditions applied [20,26,85,114,135].

For sample the C (Fig. V-3c and 3f), once the “soft” regime is fully established, this “sponge”-like structure still continues to grow until it covers the entire surface of the sample as already reported [85,114]. Consequently, the previous “pancake” structure is progressively modified into a porous outer sublayer as the process goes on. Although this “sponge” structure may exhibit poor mechanical properties in terms of hardness and wear resistance due to its high porosity, several studies reported an interest in this outer sublayer. Particularly, some authors demonstrated that this “sponge” structure promotes the incorporation of (nano-) particles from the electrolyte to the oxide layers, and can endow the PEO coatings with new functionalities, such as hydrophobicity and biocompatibility [48,58,145].

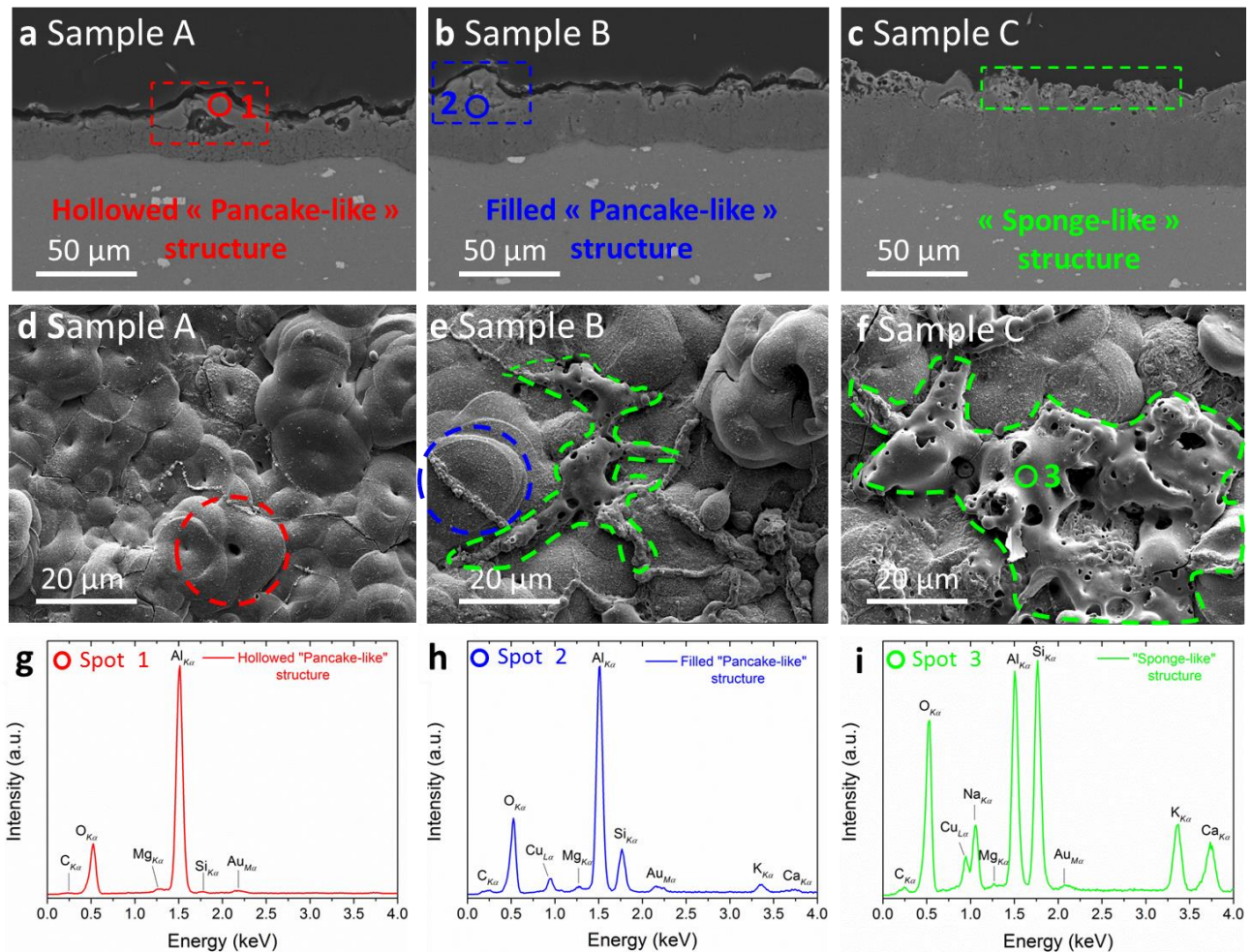


Figure V-3. SEM micrographs recorded on the cross-section (first row) and top-most surface (second row) of the samples processed: (a) and (d) just before the “soft” regime appearance (sample A), (b) and (e) during the transition from “arc” to “soft” regime (sample B) and (c) and (f) after the complete establishment of the “soft” regime (sample C). EDX spectra recorded (g) on the hollow “pancake”-like structure (red area 1), (h) on the filled “pancake”-like structure (blue area 2) and (i) on the “sponge”-like structure (green area 3).

V.3.2 Characterisation at the sub-micrometre scale

The microstructure of sample B was thoroughly characterised at a sub-micrometre scale using TEM. For this, a thin slice of ~ 60 nm in thickness was prepared from the surface using a FIB facility. This foil was vertically extracted through a filled “pancake” structure, as illustrated in Fig. V-4a. The bright-field STEM (BF-STEM) micrograph in Fig. V-4b shows two regions: a thin “sponge”-like outer sublayer that seemed to cover the dome of the “pancake” structure (blue dashed lines in Fig. V-4b) and a thick denser inner sublayer (red dashed lines in Fig. V-4b). Indexing the selected area electron diffraction (SAED) pattern revealed that the “sponge”-like outer sublayer is completely amorphous (Fig. V-4c). The EDX spectrum obtained on this region shows Si and O in large amounts (Fig. V-4e), while the content in other elements from the electrolyte and from the aluminium alloy is lower.

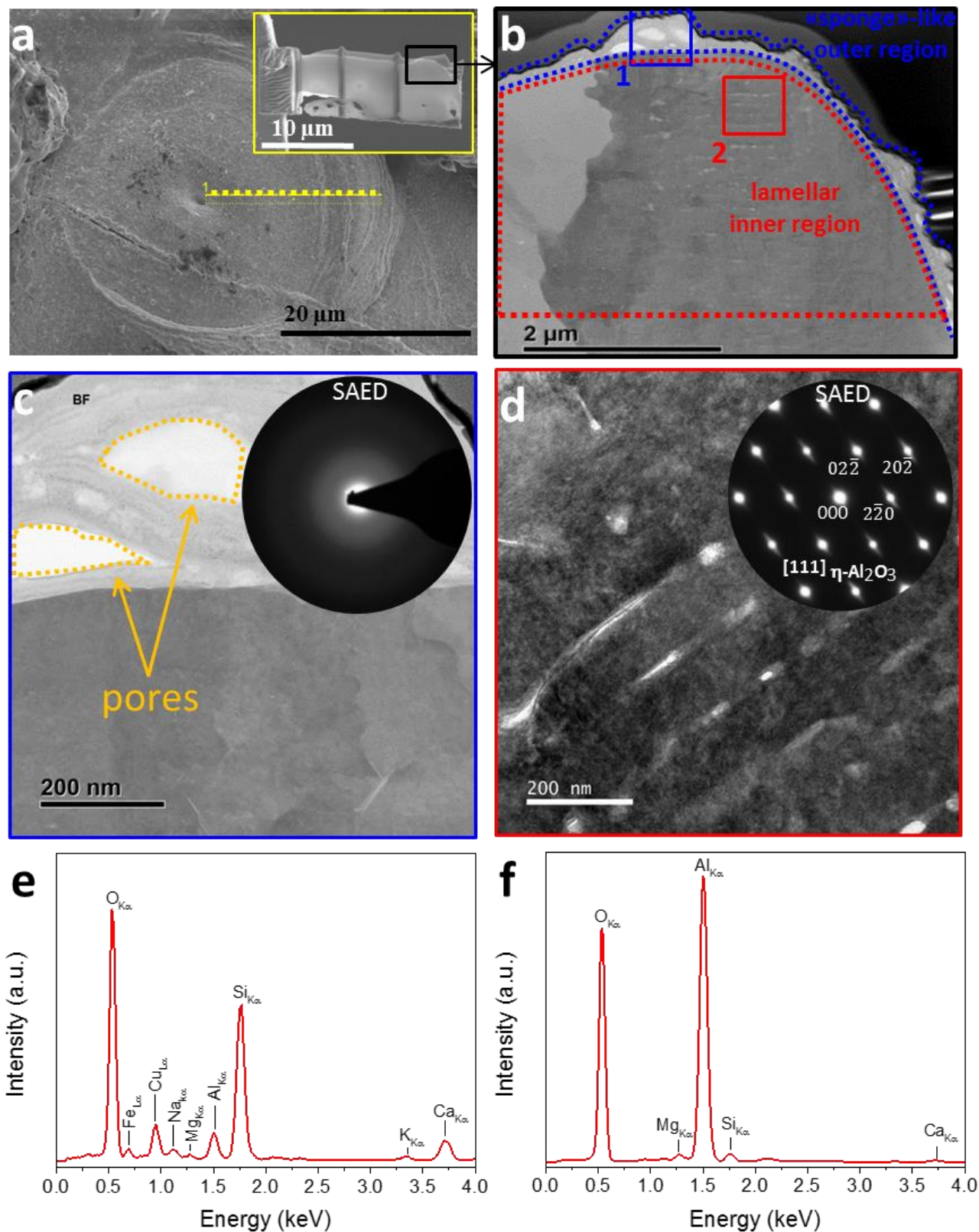


Figure V-4. (a) SEM-BSE micrograph of the top-most surface of the sample B. Dotted line shows the location of the extraction of the FIB foil cross-section. (b-d) bright field STEM micrographs of the “pancake”-like structure and the associated SAED patterns. Integrated EDX spectra for: (e) outer porous sublayer located on the dome of the “pancake”-like structure (blue square) and (f) filled cavity of the “pancake”-like structure (red square).

The formation of a thin Si-rich amorphous border on the top-most surface of the “pancake” structure is consistent with the detection of an amorphous phase with the GIXRD measurements (Fig. V-2b). In contrast, indexing the SAED pattern recorded for the filled cavity of the “pancake” structure indicates the presence of the crystalline η -Al₂O₃ phase (Fig. V-4d), suggesting that the crystalline α -Al₂O₃ phase, identified by XRD measurements (Fig. V-2a), is located deeper in the PEO coating. This observation is in good agreement with experimental results by Tilous *et al.* [7] who showed from micro-focused X-ray synchrotron diffraction measurements that the α -Al₂O₃ phase is preferentially located under the “pancake” structures. These results were partly explained by Yerokhin *et al.* [22] who simulated the temperature field in a cylindrical discharge channel by taking into account the heat dissipation into the adjacent oxide layer, the presence of the bulk Al substrate and the cooled electrolyte. With similar electrical conditions to those used here, they predicted that the η - to α -Al₂O₃ phase transition was more likely to occur in the internal sublayer than in the outer one, the latter being subject to a higher cooling rate.

In addition, the SAED pattern in Fig. V-4d also shows that each bright diffraction spot has a diffuse streak, suggesting the presence of defects in the η -alumina crystal structure. The BF-STEM micrograph of the filled cavity of the “pancake” structure reveals nanoscale lamellae (Fig. V-4d). Bright and thin lamellae alternate periodically with dark and thick lamellae. The EDX spectrum in Fig. V-4f, integrated over this lamellar arrangement, shows the presence of Al and O in large amounts and Si, Ca and Mg in lower amounts.

Fig. V-5 shows a high-resolution TEM micrograph of this lamellar structure and the associated FFT patterns recorded on both the bright and the dark lamellae. Indexing the FFT patterns confirms crystallised η -alumina. However, the presence of long and diffuse streaks on the FFT pattern recorded on the bright lamellae clearly shows that η -alumina lamellae exhibit numerous crystallographic defects, while dark lamellae are weakly-faulted crystals, as confirmed by the presence of well-defined circular spots on the corresponding FFT pattern. For this particular lamellar arrangement, a closer examination of the element distribution was done with STEM / EDX analyses. The latter were performed over a 500 nm × 500 nm square area as defined in the dark-field STEM (DF-STEM) micrograph in Fig. V-6. The thin and faulted lamellae are enriched in Si, Ca and Mg, while the thick and weakly-faulted lamellae are depleted in these elements.

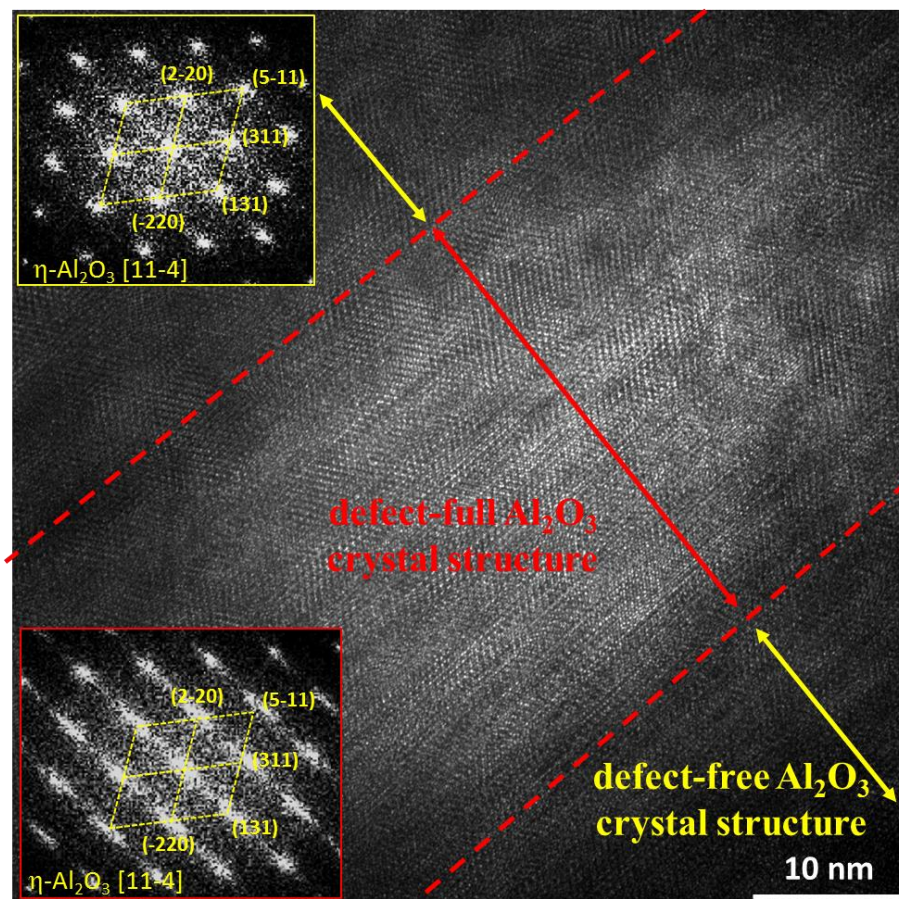


Figure V-5. High resolution TEM micrograph of the lamellar structure observed in the filled “pancake”-like structure of the processed sample B and the FFT patterns associated to the bright (red central region) and the dark lamellae (yellow lateral regions).

The EDX spectrum given in Fig. V-7a was recorded in the weakly-faulted alumina lamellae (spot #1 in Fig. V-6). The associated amount in each element is also given in Fig. V-7a. The presence of Mg, Si, and Ca can be neglected, since their respective amount is in the same range as the quantification limit of the EDX detector ($\approx 1\%$ at.). Thus, the weakly-faulted lamellae consist mainly of O (59.7% at.) and Al (39.3% at.), close to stoichiometric Al_2O_3 . In contrast, the EDX spectrum given in Fig. V-7b and recorded in the faulted lamellae (spot #2 in Fig. V-6) shows that they mainly contain O (62.8% at.), Al (18.9% at.) and Si (16.5% at.). This result clearly suggests that the faulted lamellae likely consists of the mullite phase as previously detected with GIXRD measurements in Fig. V-2b. Indeed, the presence of stacking faults in the HR-TEM micrograph in Fig. V-5 and the diffuse streaks on each electron diffraction spot in Fig. V-4d can be attributed to the formation of the mullite phase. It can be explained by considering the η -alumina structure that consists of chains of AlO_6 octahedra cross-linked with chains of AlO_4 tetrahedra. When the mullite phase is forming, SiO_4 tetrahedra randomly replaced AlO_4 tetrahedra through the initial η -alumina structure, giving rise to structural defects and a distorted η -alumina structure [144].

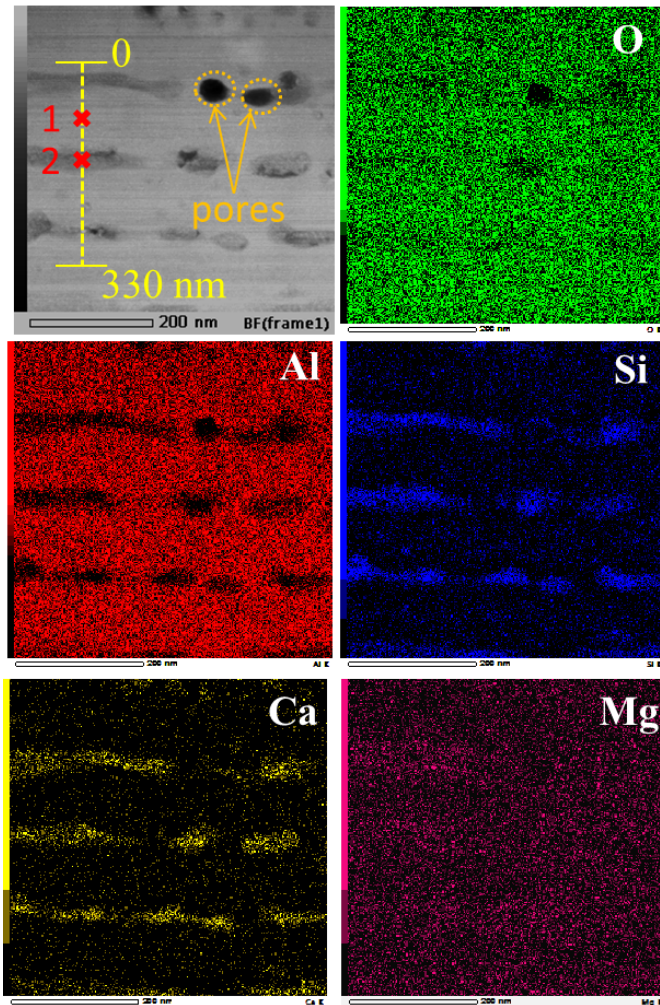


Figure V-6. Dark-field STEM (DF-STEM) micrograph recorded over a 500x500 nm square area in the filled “pancake”-like structure of the processed sample B and the associated STEM / EDX elemental maps.

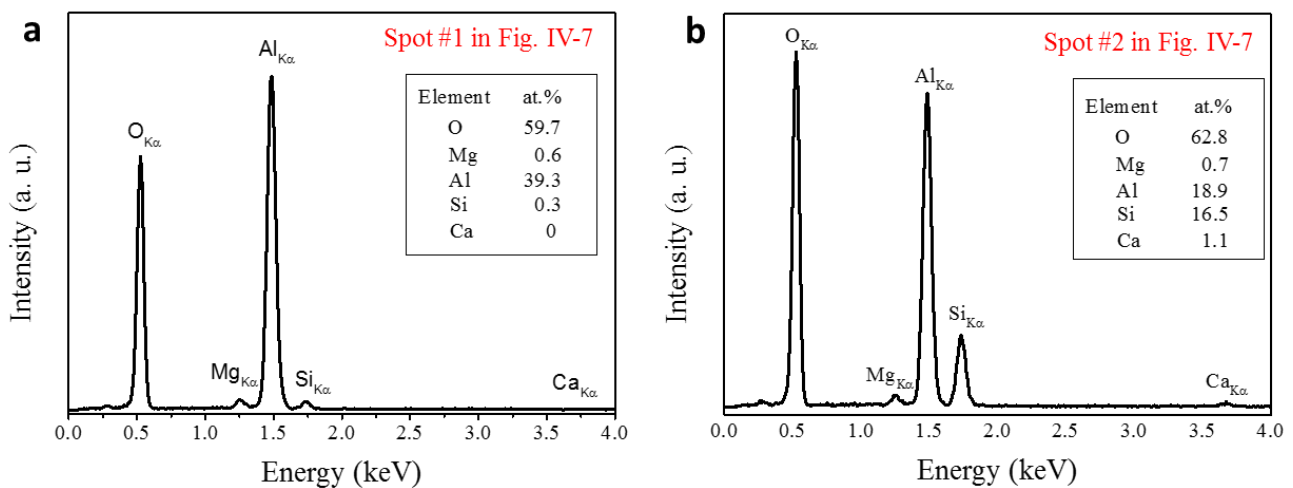


Figure V-7. EDX spectra and the associated element quantification recorded a) on the thick and defect-free lamellae (spot 1) and b) on the thin and defect-full alumina lamellae (spot 2). Locations of the spot 1 and the spot 2 are defined in the DF-STEM micrograph in Fig. V-6.

From the STEM / EDX elemental line-scan defined on the DF-STEM micrograph in Fig. V-6, the average periodicity of this lamellar nanocomposite structure was estimated at about 120 nm (Fig. V-8). The average thickness of each type of lamella was determined at 30 nm for the thin and faulted Si-rich lamellae, and 90 nm for the thick and weakly-faulted Si-poor lamellae.

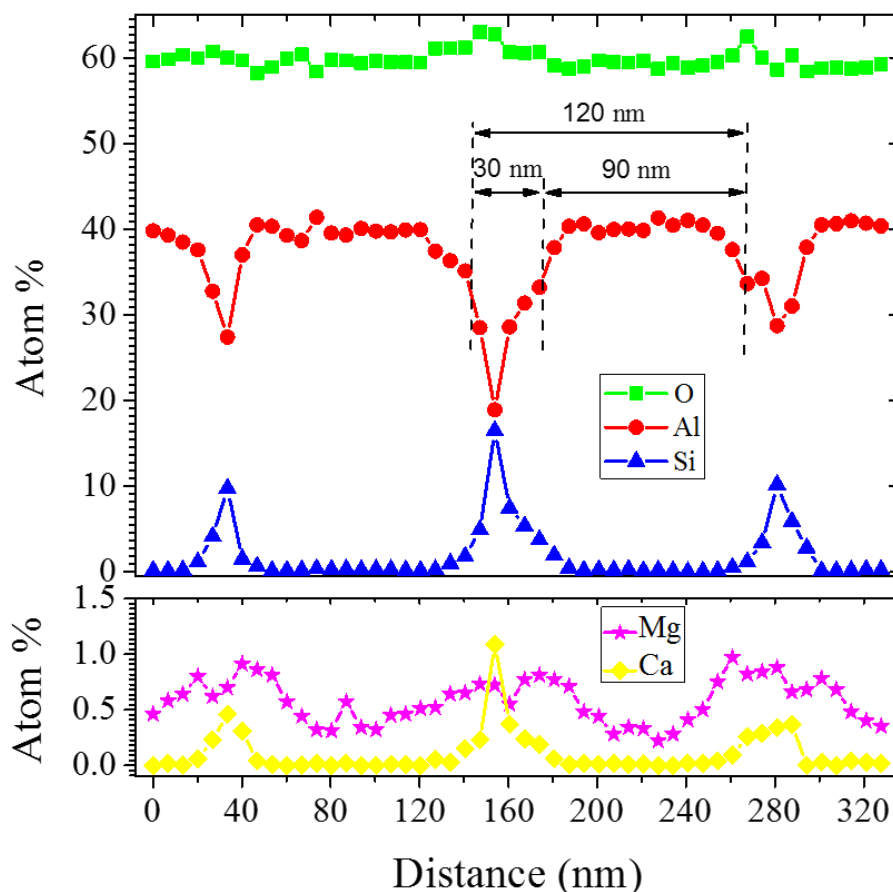


Figure V-8. The STEM / EDX element line-scan profile through the lamellar nanocomposite morphology observed in the filled “pancake”-like structure. The location of the line-scan is defined in the DF-STEM micrograph in Fig. V-6.

V.4 Results on the *in situ* characterisation of the PEO process

V.4.1 Estimation of the electron temperature in the plasma of the micro-discharges

The accurate determination of the temperature inside the micro-discharges is needed in order to describe the microstructure formation during PEO. Its value can be estimated in part by conducting optical emission spectroscopy (OES) measurements as described by Bruggeman *et al.* [146,147] and Belmonte *et al.* [148]. Fig. V-9 shows the OES spectrum recorded during the PEO processing of the aluminium alloy in a KOH/Na₂SiO₃-containing electrolyte. This spectrum was collected during the transition from the “arc” to the “soft” regime. It shows emission lines of the electrolyte species (*e.g.*

Na, H $_{\alpha}$, H $_{\beta}$, K, OH, O) and some others from the aluminium alloy substrate (*e.g.* Al, Cu). Analysis of this spectrum allows determining the excitation temperature T_{exc} using the Boltzmann plot method [146–148]. This excitation temperature T_{exc} is similar to the electron temperature T_e , provided the plasma is in thermodynamic equilibrium, at least in local thermodynamic equilibrium (LTE). The latter can be reasonably assumed for PEO discharges that consist of “arc” discharges. However, depending on the emission lines that are used, different values of T_e can be obtained. For instance, Jovović *et al.* [38] estimated T_e to ≈ 4000 K from Mg emission lines, while during the same treatment T_e has been estimated at ≈ 33000 K when using O $^+$ lines.

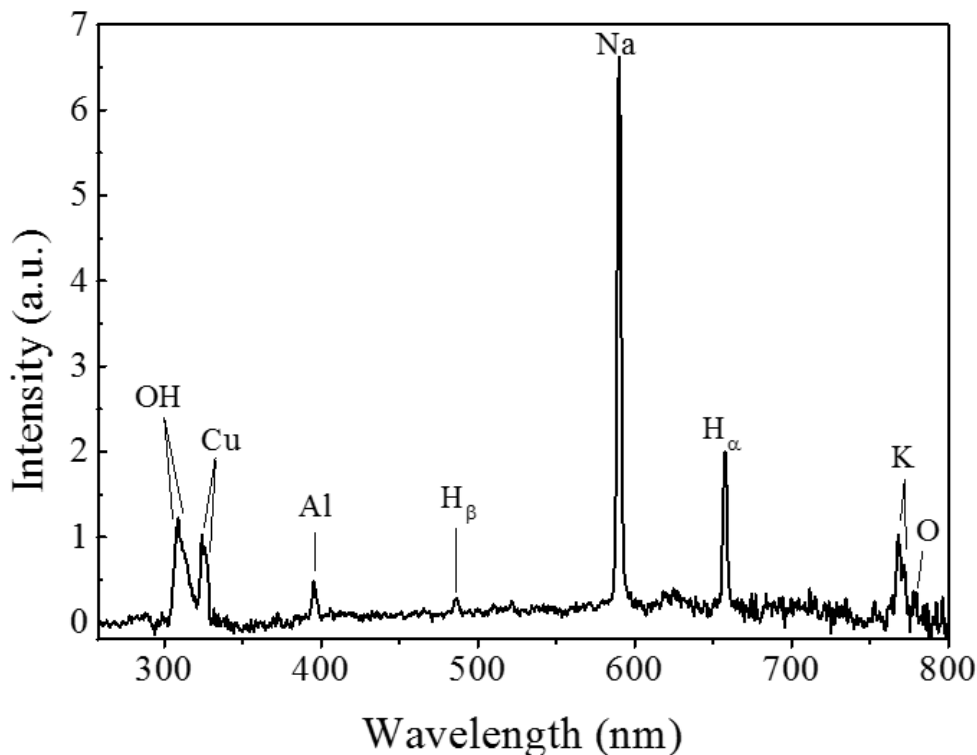


Figure V-9. Typical emission spectrum (260 nm – 800 nm) of the micro-discharges recorded during PEO of aluminium (Al2024) in silicate-rich electrolyte.

This effect was observed in the present case where T_e determined from Al $^+$ lines is $10000 \text{ K} \pm 2000 \text{ K}$, while the same determination using O $^+$ lines give an average value of $40000 \text{ K} \pm 10000 \text{ K}$ (Fig. V-10). These two temperature values can be due either to the presence of two groups of discharges with different properties, or to discharges composed of two regions, a hot and dense core and a colder and less dense outer region. All OES measurements were integrated over the whole sample surface and over several periods of the applied current. Therefore, reported T_e values were averaged values and the determination of two T_e values is still under debate in the PEO community. If T_e is usually considered as valuable information on the physical processes taking place within the

plasma, it only characterises the electrons inside the plasma and reflects neither the gas, nor the surface temperature; it is therefore unsuitable to support the possibility of phase transitions in the solid in contact with the plasma.

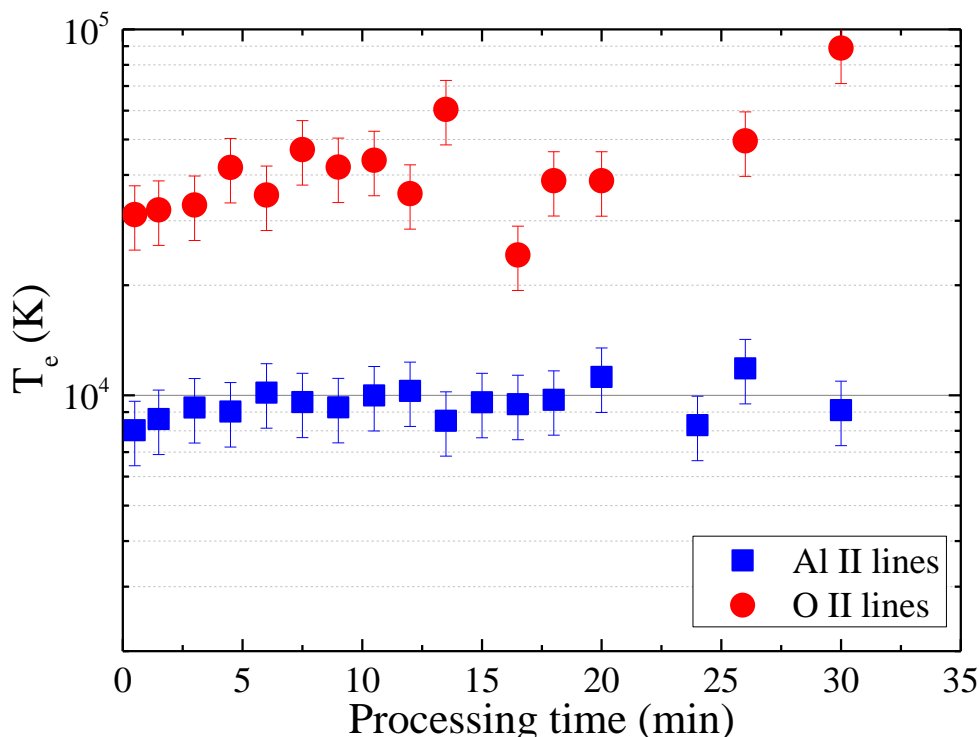


Figure V-10. Variation of the excitation temperature (assumed to be close to the electron temperature T_e) in the micro-discharges as a function of treatment time. The temperatures are estimated from the Boltzmann plots of the Al⁺ lines (noted Al II lines) and the O⁺ lines (noted O II lines).

V.4.2 Estimation of the rotational temperature in the plasma of the micro-discharges

In presence of molecules in the plasma, OES makes it possible to measure vibrational T_{vib} and rotational T_{rot} temperatures. Since rotational levels are very sensitive to Brownian motion, rotational temperature gives an excellent estimate of the gas temperature [124]. The OES spectrum during PEO processing of aluminium revealed only two molecular bands, corresponding to the transitions AlO ($B^2\Sigma^+, v' = 0 \rightarrow A^2X^+, v = 0$) at 484.2 nm and OH ($A^2\Sigma^+, v' = 0 \rightarrow X^2\Pi, v = 0$) at 306.8 nm. In the present study, the OH band was chosen because of the strong interference between H_β line and AlO band which would have jeopardised the band profile fitting. The spectrum of the OH rotational bands, given in Fig. V-11, was fitted with the rotational temperature as a fitting parameter. The best fit was obtained for a temperature of $3200 \text{ K} \pm 50 \text{ K}$, which is consistent with that obtained by Stojadinovic *et al.* ($3500 - 4000 \text{ K}$) [73,149]. It should be noted here that, for practical reasons, during the fitting process, the data points corresponding to aluminium emission lines (at $\sim 308.7 \text{ nm}$ and $\sim 309.3 \text{ nm}$) were omitted to allow better adjustment of the curve to the OH emission lines.

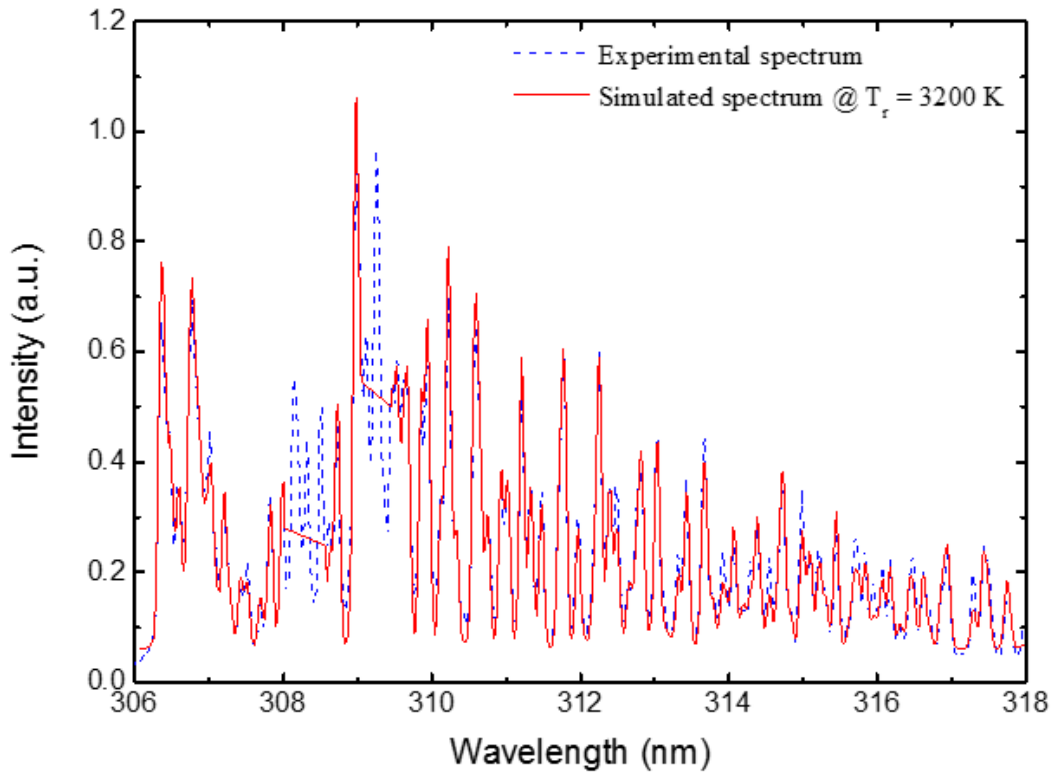


Figure V-11. Emission spectrum of the molecular OH ($A^2\Sigma^+$, $v' = 0 \rightarrow X^2\Pi$, $v = 0$) band from the micro-discharges recorded during PEO of aluminium in silicate-rich electrolyte (dotted blue line). Simulated emission spectrum for a rotational temperature T_{rot} of 3200 K (Red line). Note that emission lines of Al (transition multiplet at 308.217 nm, 309.271 and 309.284 nm) were deliberately removed from the spectrum before applying the adjustment procedure.

V.5 Discussion

The discussion hereafter focuses on the description of a melting/solidification route to explain the formation of the 1:1 mullite/alumina lamellar nanostructure that gradually filled the “pancake” cavity during the PEO “soft” regime. Estimation of key parameters determining the development of such a nanostructure is needed first, as detailed in the following sections. Estimation of the heating rate HR experienced by the solidified material under the micro-discharges, estimation of the cooling rate (CR) experienced by the alumina-siliceous melt in contact with the cooled surrounding electrolyte and estimation of the crystallisation temperature (T_c) at which the material solidification starts were successively conducted. These key thermodynamic parameters were estimated based on the combined results from the multi-scale characterisation of the “pancake” structure and from the optical characterisation of the micro-discharges. The proposed mechanism, hereafter, only focuses on the formation of the lamellar nanostructures observed inside the pancake cavity, and does not claim to be a full description of the growth mechanisms of PEO layers. Therefore, some precautions are needed and the discussion draws some assumptions. Firstly, it is assumed that the material transformations

discussed here results from the ignition of a single micro-discharge. Hence, the combined effect of several micro-discharges that could appear at the same time in a close vicinity, especially the collective thermal effect, is not taken into account. For that, further studies are needed to introduce refinements of the proposed mechanism. Secondly, the discussion focuses on the exclusive presence of O, Al and Si elements that are distributed in various proportions through the 1:1 mullite/alumina lamellar nanocomposite. Indeed, as the amounts measured for Mg and Ca elements were within the detection limit of the STEM / EDX (1% at.), their presence can be reasonably neglected. Consequently, the discussion is based on the SiO₂ - Al₂O₃ binary phase diagram that also shows metastable phases (Fig. V-12) [144]. The schematic model in Fig. V-12 illustrates the proposed mechanism of formation of the metastable 1:1 mullite/alumina lamellar nanocomposite observed in the cavity of the “pancake” structure.

V.5.1 Estimation of the heating rate (HR)

Estimation of the heating rate, noted *HR*, experienced by the solidified material under the micro-discharge was based on the optical emission spectroscopy results. As discussed above, the rotational temperature T_{rot} of the OH molecules in the plasma of the micro-discharge can reasonably be assumed equal to the gas temperature T_{gas} , $T_{gas} \approx T_{rot} \approx 3200$ K. This temperature is therefore a good estimate of the temperature that the material experiences within the micro-discharge. Considering the SiO₂ - Al₂O₃ binary phase diagram reproduced in Fig. V-12 [144], and whatever the fraction of SiO₂ in Al₂O₃, the material is liquid at that temperature value. Therefore, the PEO alumina coating, initially in a solid state at the electrolyte temperature $T_{elec} \approx 300$ K, is locally melted under the micro-discharge and reaches the gas temperature $T_{gas} \approx 3200$ K. Additionally, previous studies using ultra-fast video imaging established that the average lifetime of the micro-discharges, Δt_{MD} , is in the range of 10 μ s [21,71,136,150–152]. Thus, the heating rate *HR* can be estimated as:

$$HR \cong \frac{\Delta T_{heat}}{\Delta t_{MD}} \quad (\text{Eq. V-1})$$

where $\Delta T_{heat} \approx T_{gas} - T_{elec}$. Using the above values for T_{gas} , T_{elec} and Δt_{MD} gives $HR \approx 3 \times 10^8$ K·s⁻¹. This value is likely underestimated, since the high temperature reached in the micro-discharges did not hold over the entire MD lifetime. Indeed, Δt_{MD} includes the ignition and the extinction time during which the gas temperature was lower.

V.5.2 Estimation of the crystallisation temperature (T_c)

Estimation of the crystallisation temperature, noted T_c , at which the material solidification starts was based on the nanoscale characterisation of the 1:1 mullite/alumina lamellar arrangement that filled the “pancake” structure.

First, the volume fraction of alumina lamellae, V_{Alum} , (accordingly $V_{Mul} = 1 - V_{Alum}$ is the volume fraction of 1:1 mullite lamellae) in the nanocomposite arrangement was estimated using HR-TEM image analysis according to the parallelepiped shape of mullite identified in literature [153–155]. In the nanostructured region in Fig. V-4d, a minimum of 10 different views (400×400 nm) were considered for the estimation of the surface fraction of alumina lamellae. Thus, V_{Alum} was in the range of 75 to 85% vol. (accordingly V_{Mul} is in the range of 15 to 25% vol.) From V_{Alum} , the weight fraction of the alumina lamellae W_{Alum} in the nanocomposite arrangement (where W_{Mul} is the weight fraction of the 1:1 mullite lamellae) was calculated according to:

$$W_{Alum} = \frac{\rho_{Al_2O_3} \cdot V_{Alum}}{\rho_{Al_2O_3} \cdot V_{Alum} + \rho_{1:1 Mul} \cdot V_{Mul}} \quad (\text{Eq. V-2})$$

where $\rho_{Al_2O_3} = 3.96 \text{ g} \cdot \text{cm}^{-3}$ and $\rho_{1:1 Mul} = 3.05 \text{ g} \cdot \text{cm}^{-3}$ are the density of pure alumina and 1:1 mullite phases, respectively. Hence W_{Alum} , was estimated in the range of 79 to 88% wt. (accordingly W_{Mul} is in the range of 12 to 21% wt.). From W_{Alum} , the molar fraction of the alumina lamellae M_{Alum} in the nanocomposite arrangement (where M_{Mul} is the molar fraction of the 1:1 mullite lamellae) was calculated using:

$$M_{Alum} = \frac{W_{Alum}/A_{Al_2O_3}}{W_{Alum}/A_{Al_2O_3} + (1 - W_{Alum})/A_{1:1 Mul}} \quad (\text{Eq. V-3})$$

where $A_{Al_2O_3} = 101.96 \text{ g} \cdot \text{mol}^{-1}$ and $A_{1:1 Mul} = 162.04 \text{ g} \cdot \text{mol}^{-1}$ are the molar weights of pure alumina and 1:1 mullite phases, respectively. Thus, M_{Alum} was estimated in the range of 86 to 92% mol (accordingly M_{Mul} is in the range of 8 to 14% mol).

Second, the amounts of O, Al and Si in the pure alumina lamellae were $C_{O/Alum} = 59.7\% \text{ at.}$, $A_{Al/Alum} = 39.3\% \text{ at.}$ and $C_{Si/Alum} = 0.3\% \text{ at.}$, respectively. The amount of Si is very low and lower than the accuracy of the EDX (about 1% at.), so it is reasonable to assume that the alumina lamellae mainly consist of pure crystallised Al_2O_3 . Thus, using the $SiO_2 - Al_2O_3$ binary phase diagram [144], the molar fraction of Al_2O_3 in the alumina lamellae at room temperature (X_2 in Fig. V-12) is 100% mol. In contrast, EDX of the 1:1 mullite lamellae shows that the amounts of the O, Al and Si

were $C_{O/Mul} = 62.8\% \text{ at.}$, $C_{Al/Mul} = 18.9\% \text{ at.}$ and $C_{Si/Mul} = 16.5\% \text{ at.}$, respectively. From the amount of Si in the mullite lamellae, the molar fraction of the Al_2O_3 phase in the mullite lamellae (X_1 in Fig. V-12) was estimated at following equations (4) - (8). The amount of Si in mullite can be expressed as a function of the number of Si, Al and O atoms in the 1:1 mullite lamellae according to:

$$C_{Si/Mul} = \frac{N_{Si/Mul}}{N_{Si/Mul} + N_{Al/Mul} + N_{O/Mul}} \quad (\text{Eq. V-4})$$

where $N_{Si/Mul}$, $N_{Al/Mul}$ and $N_{O/Mul}$ can be expressed as a function of the molar fraction of the Al_2O_3 phase in the mullite lamellae (X_1) and the Avogadro's number (\mathcal{N}_A):

$$N_{Si/Mul} = \frac{1}{3}(1 - X_1)\mathcal{N}_A \quad (\text{Eq. V-5})$$

$$N_{Al/Mul} = \frac{2}{5}X_1\mathcal{N}_A \quad (\text{Eq. V-6})$$

$$N_{O/Mul} = \frac{2}{3}(1 - X_1)\mathcal{N}_A + \frac{3}{5}X_1\mathcal{N}_A \quad (\text{Eq. V-7})$$

X_1 was determined from Eq. V-(4) - (7):

$$X_1 = 1 - 3C_{Si/Mul} \quad (\text{Eq. V-8})$$

Third, the nominal molar fraction of Al_2O_3 in the molten material at 3200 K (X_0 in Fig. V-12) can be estimated from the lever rule:

$$M_{Alum} = \frac{X_0 - X_1}{X_2 - X_1} \quad (\text{eq. V-9})$$

Thus, X_0 was estimated in the range of 93 to 96% mol.

Finally, by considering both the estimated molar fraction of Al_2O_3 in the nominal composition of the molten material and a metastable solidification route due to the high cooling rate experienced by the molten material (section 4.3), the crystallisation temperature of the lamellar nanocomposite was estimated at about $T_c = 1300 \text{ K}$. On the SiO_2 - Al_2O_3 binary phase diagram reproduced in Fig. V-12 [144], this crystallisation temperature corresponds to the boundary of the liquid miscibility gap between mullite and alumina at the nominal composition of the alumina-siliceous molten material.

V.5.3 Estimation of the cooling rate (CR)

The cooling rate, noted CR , experienced by the alumina-siliceous melt in contact with the cooled surrounding electrolyte required to form the metastable 1:1 mullite / alumina nanocomposite arrangement can be estimated according to:

$$CR \cong \frac{\Delta T_{cool}}{\tau_{Si}} \quad (\text{Eq. V-10})$$

Where $\Delta T_{cool} = T_c - T_{elec} = 1000$ K is the difference between the crystallisation temperature and the electrolyte temperature, and $\tau_{Si} \cong 3 \cdot 10^{-5}$ s is the diffusion time constant of Si in the solid Al_2O_3 . τ_{Si} was calculated from the average diffusion length $\bar{\delta} \cong 60$ nm, measured from the STEM/EDX profile in Fig. V-8:

$$\bar{\delta} = \sqrt{2 \cdot D_{Si/Al_2O_3}(T) \cdot \tau_{Si}} \quad (\text{Eq. V-11})$$

where $D_{Si/Al_2O_3}(T) = 7 \cdot 10^{-11}$ m²/s is the diffusion coefficient of Si in the Al_2O_3 phase at the metastable crystallisation temperature and the corresponding estimated nominal composition X_0 between 93 and 96% mol [156,157]. As suggested by Takamori *et al.* [156] and Chiang *et al.* [157], this diffusion coefficient can be calculated from the Stokes-Einstein equation:

$$D_{Si/Al_2O_3}(T) = \frac{kT}{6\pi r_{Si}\mu} \quad (\text{Eq. V-12})$$

with $k = 1.38 \cdot 10^{-23}$ J·K⁻¹ the Boltzmann constant, $\mu = 0.1$ Pa·s, the estimated dynamic viscosity at liquidus temperature for the nominal composition X_0 [158] and $r_{Si} = 1.36 \cdot 10^{-10}$ m the equivalent radius of Si estimated from:

$$r_{Si} = \frac{1}{2} \left(\frac{V_{M,Si}}{N_A} \right)^{1/3} \quad (\text{Eq. V-13})$$

where $V_{M,Si} = 12 \cdot 10^{-6}$ m³·mol⁻¹ is the molar volume of Si, and $N_A = 6.022 \cdot 10^{23}$ mol⁻¹ the Avogadro's constant. Hence, the cooling rate was estimated at $C \approx 3.3 \cdot 10^7$ K·s⁻¹, which is in good agreement with the calculation of Yerokhin *et al.* (10^7 K·s⁻¹) [22].

V.5.4 Mechanism of melting and metastable solidification route

First of all, although the electrical parameters fulfil the “soft” regime conditions, it is well established that the PEO process always starts conventionally with an “arc” regime [19,26,159,160]. The PEO process gradually switches to the “soft” regime only after a certain processing time, usually

after 10 to 30 min depending of the process parameters. The “arc” regime is characterised by visible and intense micro-discharges (mainly with strong B-type micro-discharges according to Hussein *et al.* [23] which occur throughout the thickness of the PEO coating and induce large and unfilled discharge channels (“pancake” structures). In contrast, with the gradual appearance of the “soft” regime, visible and intense micro-discharges progressively change to tiny micro-discharges which develop inside the discharge channels that fill the “pancake” cavities. According to Cheng *et al.* [104,161,162] these tiny discharges are mainly of D-type. Consequently, with the appearance of the “soft” regime, the ignition of such discharges increasingly occurs inside the “pancake” cavity. With the ignition of a D-type micro-discharge, the solidified material that initially consisted of quite pure Al_2O_3 previously formed during the “arc”-regime is locally and rapidly heated above $T_{gas} \approx 3200$ K with a heating rate of $HR \approx 3 \cdot 10^8$ $\text{K} \cdot \text{s}^{-1}$.

At this temperature, the pure alumina solid phase transforms into liquid. In addition, the elements present in the electrolyte can be more easily accepted into the coating through the surface discharging process. The SiO_3^{2-} anions present in the electrolyte enter the discharge channels through electrophoresis under the strong electric field, and undergo various excitation and dissociation processes in the micro-discharges. Dehnavi *et al.* [37,103,113] showed that SiO_3^{2-} anions dissociated into Si atoms in the plasma core. Klapkiv [98] described the transport in the channel of O and Si atoms from the core to the shell of the plasma due to temperature gradients. After about 10 μs , which is the average lifetime of the PEO micro-discharges in “soft” regime, the micro-discharge extinguishes and the plasma transport stops suddenly. The atomic species recombine to form gaseous O_2 and liquid SiO_2 . Ultimately, just before the cooling step starts, the molten Al_2O_3 and the freshly formed SiO_2 combine in a liquid phase, resulting in an alumina-siliceous melt (Fig. V-12). It is also worth noting that after one micro-discharge, it is expected that the melt is quite exclusively composed of alumina ($X_2 \approx 100\%$ mol). In turn, after repetitive ignition/extinction cycles of micro-discharges that are known to appear in successive bursts at the same location over the substrate [151], the alumina-siliceous melt is gradually enriched in SiO_2 and reaches the estimated nominal molar fraction of Al_2O_3 between 93 and 96% mol.

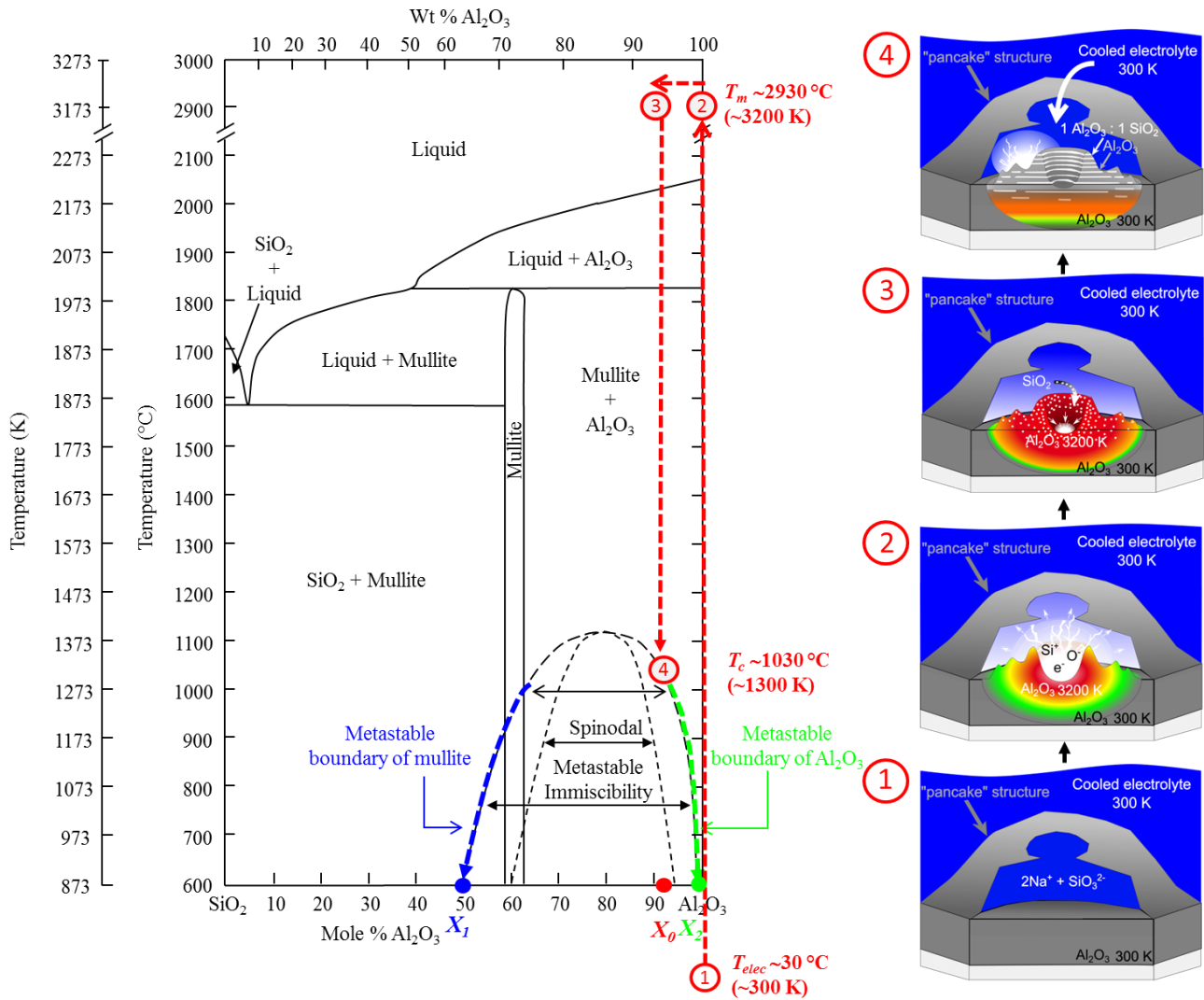


Figure V-12. Phase diagram for the Al₂O₃-SiO₂ binary system showing metastable regions in the mullite/Al₂O₃ domain and the proposed schematic representation of the formation of nanostructured metastable mullite in the “pancake” cavity during PEO of aluminium in “soft” regime condition [144]. 1: Arc discharging inside the “pancake” cavity that is associated with the propagation of a shock wave and the development of a spatial gradient of temperature about 3200 K. 2: Melting of the pre-existing solidified alumina associated with the enrichment in Si. 3: rapid quenching at about $3.3 \cdot 10^7\text{ K}\cdot\text{s}^{-1}$ due to the cooled surrounding electrolyte that filled the “pancake” cavity. 4: Mullite formation from a metastable phase transformation (solidification temperature at about 1300 K) and generation of a new arc discharging which gradually leads to the filling of the cavity.

As the micro-discharges extinguish, the pressure in the “pancake” cavity decreases and the cooled electrolyte enters into the open discharge channel. Consequently, the alumina-siliceous melt is quenched at cooling rate of $CR \approx 3.3 \cdot 10^7\text{ K}\cdot\text{s}^{-1}$. Within such severe cooling conditions, the solidification is expected to follow a non-equilibrium route as predicted by the SiO₂-Al₂O₃ phase diagram (Fig. V-12) [144]. For a nominal molar fraction of Al₂O₃ in the range of 93 to 96% mol, the solidification of the alumina-siliceous melt starts at the critical solidification temperature $T_c \approx 1300\text{ K}$ as it is defined by the boundaries of the mullite/Al₂O₃ metastable immiscibility dome in Fig. V-12.

Therefore, a mechanism of phase separation takes place due to the precipitation of metastable mullite lamellae that alternate with metastable alumina lamellae. Close to the crystallisation temperature, the metastable mullite lamellae freshly formed are enriched in alumina ($\approx 65\%$ mol Al_2O_3 ; $\approx 35\%$ mol SiO_2). Oppositely, the metastable alumina lamellae that are freshly formed are not 100% pure and contain a significant amount of SiO_2 , up to 5% mol. As the cooling process continues, and as predicted by the metastable branches of mullite and Al_2O_3 (blue-coloured and green-coloured in Fig. V-12), the metastable mullite lamellae are progressively enriched in SiO_2 while the metastable alumina lamellae are gradually depleted in SiO_2 due to diffusion in the solid state [153–155]. At 870 K (limit of the phase diagram in Fig. V-12 [144]), the alumina lamellae consist of Al_2O_3 ($X_2 \approx 100\%$ mol), while the mullite lamellae contain about 50% mol SiO_2 (50% mol Al_2O_3) that corresponds to the metastable 1:1 mullite. The molar fraction of the alumina lamellae M_{Alum} is also higher (in the range of 86 to 92% mol) than the molar fraction of the metastable 1:1 mullite M_{Mul} (in the range of 8 to 14% mol). Finally, the microstructure predicted at 870 K by the proposed solidification mechanism remains close to the microstructure observed and characterised at room temperature in the present study.

V.6 Conclusions of Chapter V

The present chapter presented the PEO processing of a 2024 aluminium alloy in a $\text{KOH} / \text{Na}_2\text{SiO}_3$ electrolyte within the well-established “soft” regime electrical conditions. The microstructure of the “pancake” structure formed during the transition from the “arc” regime to the “soft” regime was fully described at different scales. Mainly, the cavity of the “pancake” structure was closely examined using high-resolution transmission electron microscopy.

The main result shows that the beginning of the “soft”-regime was concomitant with the formation of a lamellar nanocomposite that gradually filled the cavity of the “pancake” structure. This nanocomposite consisted of Al_2O_3 lamellae (≈ 90 nm in thickness) that periodically alternated with a metastable 1:1 mullite lamellae (≈ 30 nm in thickness). Combined with optical emission spectroscopy measurements performed during the transition to “soft” regime, a growth mechanism based on the metastable solidification route of a silicon-enriched alumina melt was proposed. Under the micro-discharge, alumina was locally melted above ≈ 3200 K at a high heating rate $\approx 3 \times 10^8$ $\text{K} \cdot \text{s}^{-1}$. It was then gradually enriched in silicon due to the electrolyte decomposition and then cooled by the electrolyte at a high cooling rate $\approx 3.3 \times 10^7$ $\text{K} \cdot \text{s}^{-1}$ after the micro-discharge extinction. Within such severe cooling conditions, the solidification process followed a non-equilibrium route as predicted by the metastable SiO_2 – Al_2O_3 phase diagram. It resulted in a phase separation consisting in a nanoscale lamellar arrangement of pure alumina and 1:1 mullite lamellae.

Chapter VI - New opportunities for the Plasma Electrolytic Oxidation process

VI.1 Introduction of the chapter VI

This final chapter focuses on potential new opportunities for the Plasma Electrolytic Oxidation process. Two aspects are mainly addressed and their feasibility is presented. The first part of the chapter is dedicated to study the feasibility of producing metallic oxide (micro- and nano-) particles by using the PEO process. The second part is devoted to study the possibility of elaborating improved protective coatings by the use of a duplex surface treatment involving the cold-spray technique and the PEO process. The specific protocols used for these two studies are explained in details and the results collected are mainly based on the ex-situ characterization of the produced metallic oxide particles and the elaborated duplex coatings. Although the main purpose of this chapter is to open new fields for the PEO process, it remains that discussion of the experimental results will provide a better understanding of the inherent growth mechanisms taking place during the PEO process.

VI.2 Formation of metallic oxide particles using the PEO process

VI.2.1 Introduction

The primary interest in using the PEO process is to protect light metallic alloys by growing a protective oxide layer at their surface. Among the inherent aspects of this process, it is widely known that it produces residual particles into the electrolyte. When the process stops, they are usually found at the bottom of the electrolytic cell. It is generally accepted that their presence affects the efficiency of the PEO process and in most of the cases, the electrolyte is regularly renewed by a fresh one. Using plasma-based electrolytic processes, numerous papers deal with the formation of particles during cathodic plasma electrolysis [163,164]. When the metallic electrode is negatively biased, metallic (micro- and nano-) particles are formed within the stable plasma sheet that covered the processed electrode. Nevertheless, mechanisms governing the cathodic plasma electrolysis process singularly contrast from those encountered during plasma electrolytic oxidation during which numerous, short-lived and tiny micro-discharges appear when the working electrode is positively biased. To the best of our knowledge, no studies have focused specifically on the produced particles as well as on the mechanism of their formation during the PEO process. In this first part of this chapter, it is proposed to fully characterise the microstructure of the produced particles at different scales by using

complementary techniques (SEM, High-resolution TEM, STEM/EDX, FIB milling). Finally, on the basis of the results, a descriptive mechanism of formation of these particles is discussed.

VI.2.2 Specific experimental conditions

The PEO processed materials consisted in a low-alloyed aluminium (Al1050), a copper-rich aluminium alloy (Al-2024). Their chemical compositions are reported in Table II-2. Additionally, samples of low-alloyed zirconium (Zr-M5) were prepared (Table VI-1). The aluminium samples were cut to rectangular shape of 40 mm × 25 mm × 5 mm in dimensions, while the zirconium samples exhibited a tubular shape of 30 mm in height and 15 mm in diameter. The sample sizes were chosen to provide approximately the same processing surface ($\sim 0.28 \text{ dm}^2$) to ensure same current density applied.

Table VI-1. Chemical composition of the commercial M5 zirconium alloy (noted ZrM5)

Elements	Nb	O	Fe, S	Zr
in wt.%	1	0.14	<0.05	Balance

The samples were PEO processed in 4 L beaker containing a solution of potassium hydroxide ($[\text{KOH}] = 1 \text{ g.L}^{-1} \cong 0.018 \text{ mol.L}^{-1}$) diluted in deionised water. Unusually, and in order to avoid the pollution of the electrolyte and the dissemination of the produced particles, the electrolyte was indirectly cooled using a double wall system. As described in Fig. VI-1a, the beaker containing the electrolyte is located inside a larger tank filled with a cooled water stream. A magnetic stirrer at the bottom of the beaker ensures the homogenization of the electrolyte temperature. In these conditions, the temperature was kept below 60 °C. For each PEO treatment, the processed sample was systematically located at 90 mm apart from the working electrodes (two titanium plates of $200 \times 200 \times 1 \text{ mm}^3$ in size). PEO treatments were conducted using a pulsed bipolar current generator within the “soft” regime electrical conditions, setting the ratio of charge quantity ($RCQ = Q_p / Q_n$) to 0.9. The current pulse frequency (f) and the anodic current density (j_a) were set at 100 Hz and 37 A.dm^{-2} . The duration of the PEO treatments was set at 30 min.

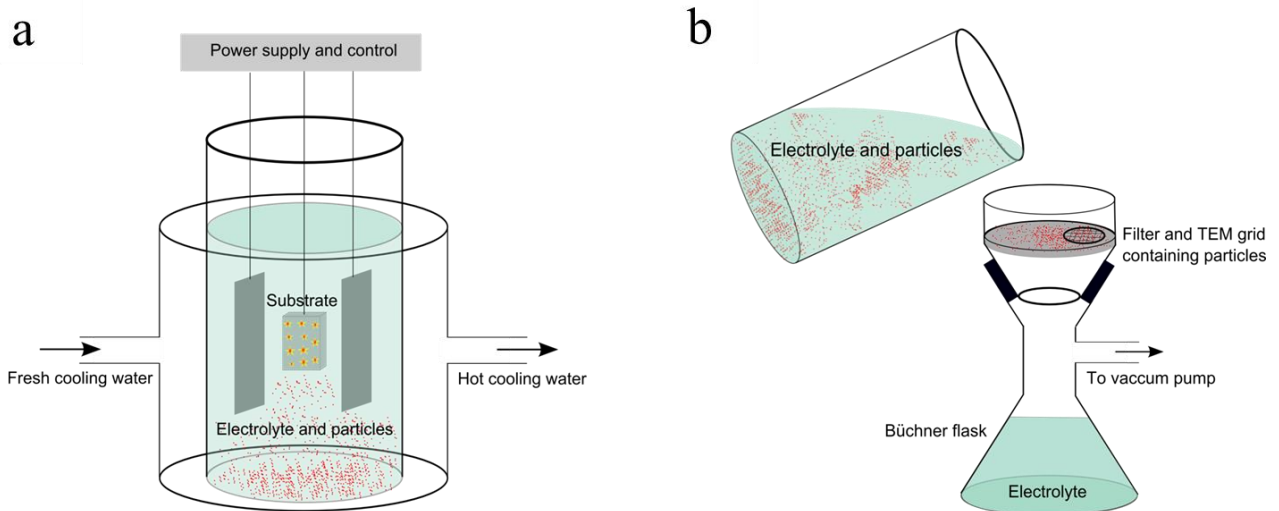


Fig. VI- 1. Schematic view of the experimental procedure that allows a) producing particles using the PEO process and b) collecting them using the Büchner filtering method.

As illustrated in Fig. VI-1b, the electrolyte containing the suspended particles was then filtered using the Büchner filtering method. The filter paper used allows retaining particles up to about 100 nm in size (Whatman® Cyclopore™ polycarbonate membrane). Additionally, a TEM grid (300 mesh nickel grid covered with a carbon film) was also placed onto the surface of the filter paper. After filtering, the filter paper and the TEM grid are then dried in an oven at 60 °C for 12 h.

Pictures of the electrolyte and the filter paper were taken before and after filtering. The particles, stopped both onto the filter paper and on the TEM grid, were observed using SEM and TEM techniques. Different magnifications were used in order to estimate the size distribution of the particles. The chemical composition and the distribution in elements of the synthesised particles were determined by EDX and STEM/EDX analyses. The phase composition of the particles was investigated by XRD measurements performed on the surface of the filter paper. High-resolution TEM observations combined with indexing of the associated FFT patterns also led to the determination of the phase composition of the produced particles. Additionally, FIB technique (Focused Ion Beam using a Ga⁺ beam) was also used to cut the produced particles in half and to characterise their internal morphology. Finally, for comparison reasons, PEO coatings grown on the different processed substrates were also characterised by SEM, EDX and XRD techniques.

VI.2.3 Results and discussion

VI.2.3a Morphology of the particles

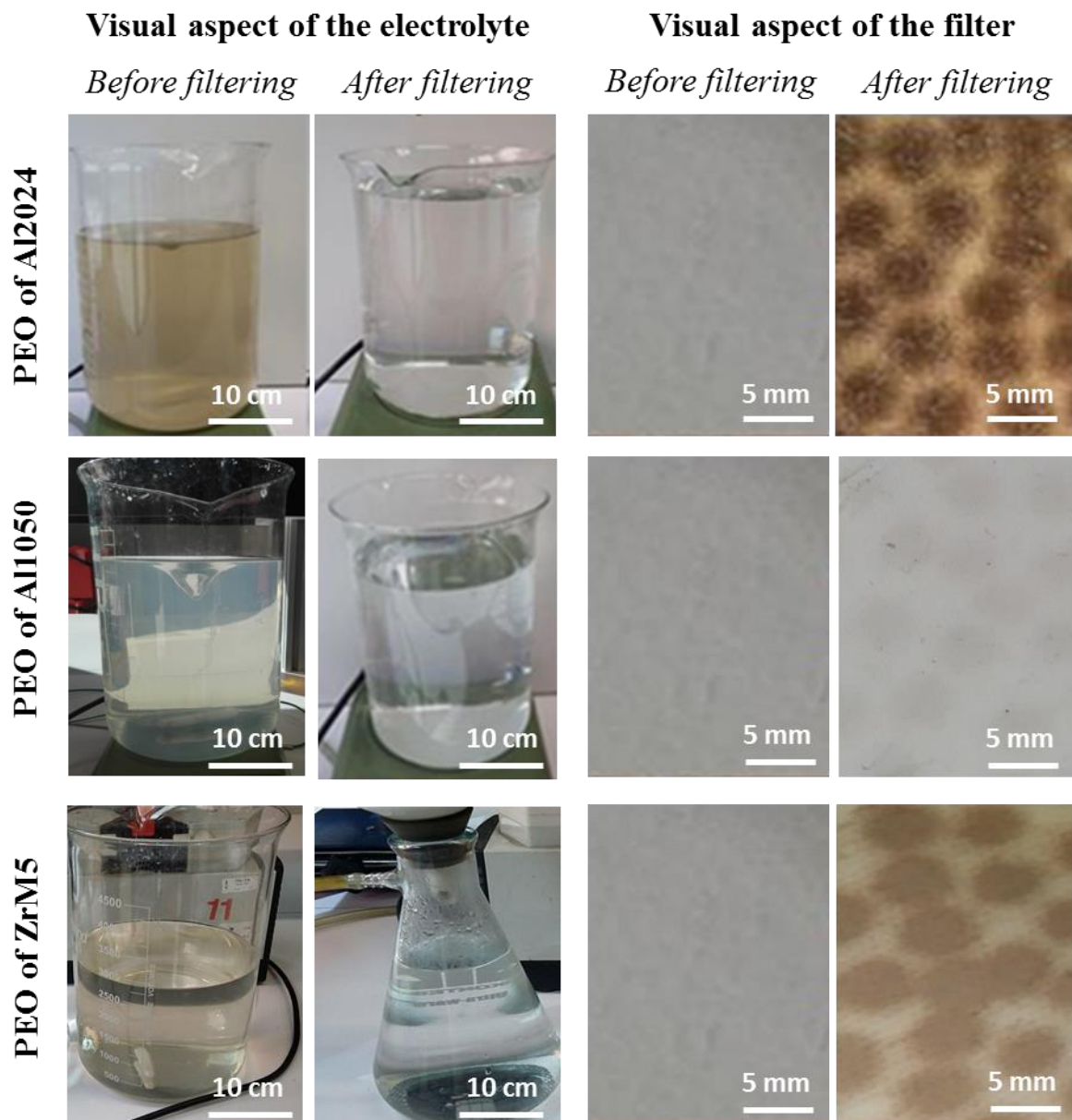


Fig. VI- 2. Visual aspect of the electrolyte (before filtering) and the filter paper (after filtering) for the PEO process of Al1050, Al2024 and ZrM5 alloys.

Fig. VI-2 shows the visual aspect of the different electrolytes and filter papers before and after filtering. Whatever the processed substrate, the electrolytes are colored before filtering while they are transparent after filtering. This suggests the presence of particles. This is also confirmed by the visual aspect of the filter paper after filtering. PEO processing of the rich-copper aluminum alloy (Al 2024) results in a brown aspect of the filter. In contrast, the filter exhibits a whitish appearance in the case

of the low-alloyed aluminum substrate. For the low-alloyed zirconium, the filter paper appears pinkish-brown colored.

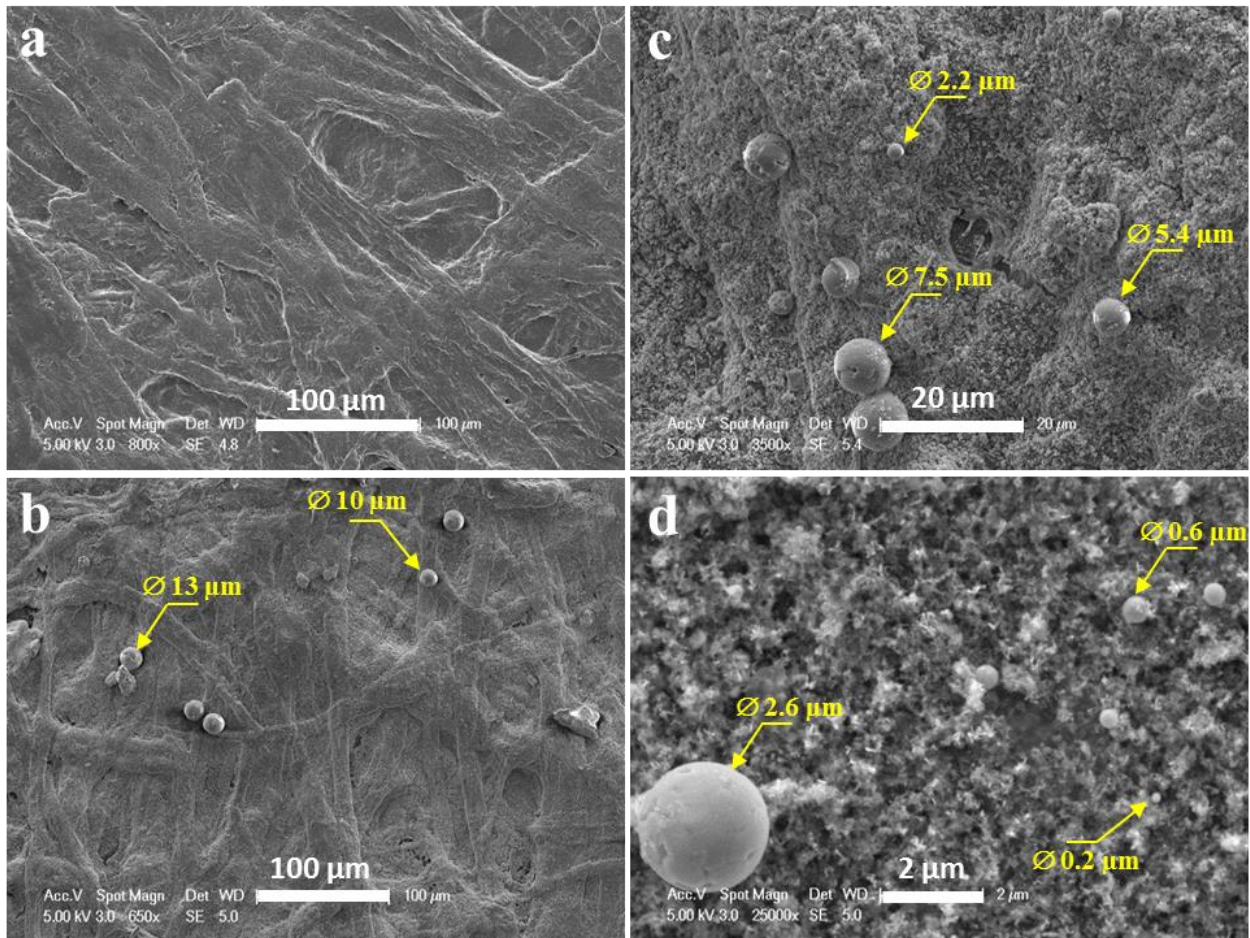


Fig. VI- 3. SEM micrographs recorded at different magnifications on the filter paper a) before filtering and b), c), d) after filtering for the PEO process of the Al2024 aluminium alloy.

Fig. VI-3 shows the SEM micrographs of the filter paper before and after filtering in the case of the PEO process of the copper-rich aluminium alloy (Al2024). Before filtering, no particle is observed at the surface of the filter paper. In contrast, particles are observed after filtering. At low magnification (Fig. VI-3a,b), particles exhibit a spherical shape with a diameter in the range of 0.1 to 10 μm . At higher magnification (Fig. VI-3d), it can be seen that particles are not perfectly spherical since some holes and cracks remain visible over their surface. It is also worth mentioning that same observations were done for the PEO process of the low-alloyed aluminium (Al1050) and zirconium substrate (ZrM5). Some of these particles were cut in half using FIB technique. Whatever the PEO processed substrate, SEM micrographs in Fig. VI-4 show that particles exhibit an internal cavity which, for certain particles, opens outwards. Interestingly, the fact that the morphology of the particles remains

the same irrespective of the processed metallic alloy suggests a formation mechanism which is inherent to the PEO process but independent of the processed material.

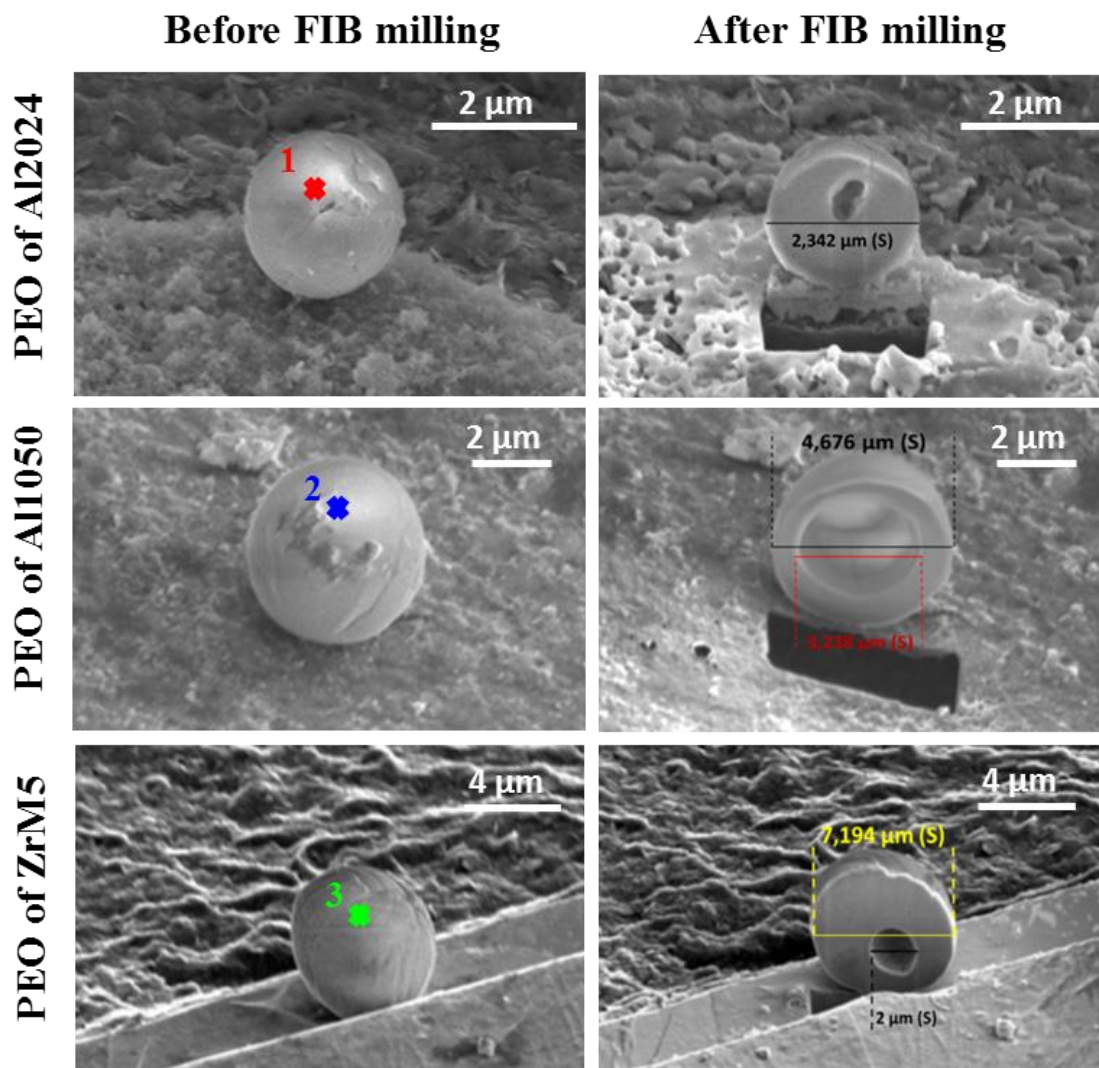


Fig. VI- 4. SEM micrographs of the produced particles on Al1050, Al2024 and ZrM5 alloys before and after FIB milling. Coloured spots indicate the locations at which EDX spectra of Fig. VI-5 were recorded.

VI.2.2b Chemical composition of the particles

The EDX spectra given in Fig. VI-5 were recorded on the centre of the particles as shown in Fig. VI-4. The EDX spectra recorded on the particles produced with the copper-rich aluminium alloy (Al2024) and the low-alloyed aluminium alloy (Al1050) shows that they consist exclusively in Al and O elements. This suggests the formation of alumina particles. The particles produced with the low-alloyed zirconium consist exclusively in Zr and O elements, suggesting in this case the formation of zirconia particles. These first analyses were confirmed by the elemental distributions and quantifications done with STEM/EDX analyses as shown in Fig. VI-6 and in Table VI-2, respectively.

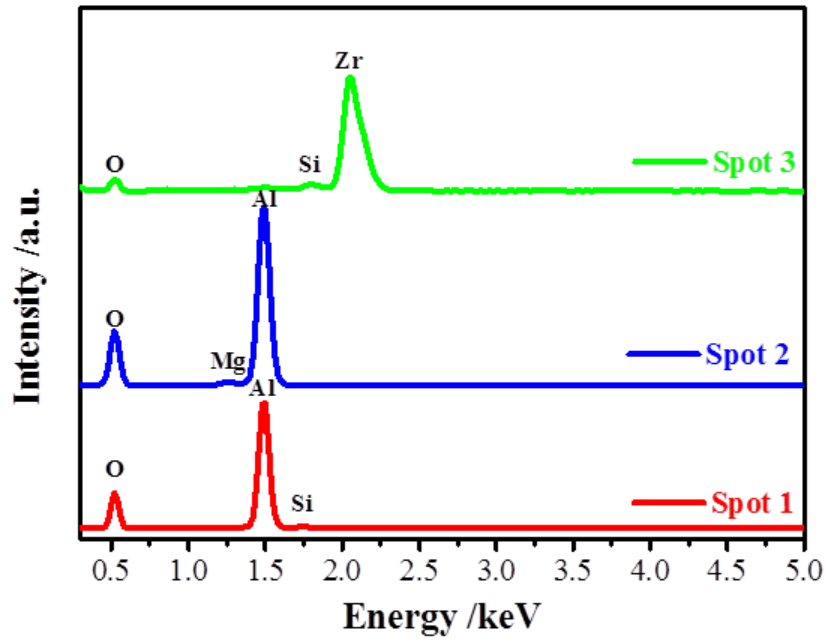


Fig. VI- 5. EDX spectra recorded on micro-particles produced during the PEO process of Al1050, Al2024 and ZrM5 alloys. Spots 1, 2 and 3 are defined in the SEM micrographs in Fig. VI-4.

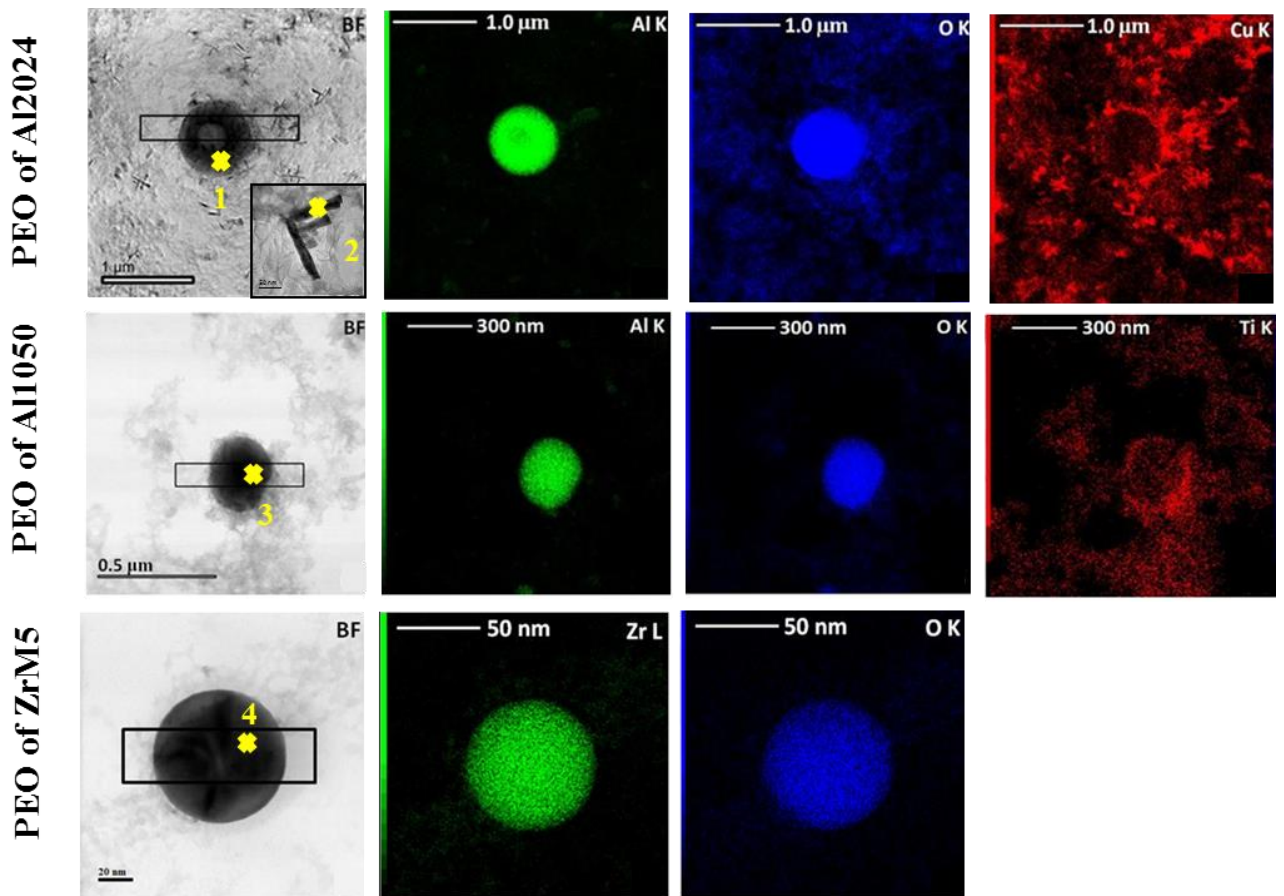


Fig. VI- 6. Bright-field STEM (BF-STEM) micrographs recorded on particles produced during the PEO process of Al1050, Al2024 and ZrM5 alloys and the STEM/EDX elemental maps.

Table VI-2. Elemental composition of the particles produced during the PEO process of Al1050, Al2024 and ZrM5 alloys.

	Al	Zr	O	Cu	Ti	C
Spot 1* (in at %)	38.4	-	58.4	3.2	-	-
Spot 2* (in at %)	1.1	-	52.3	43.5	-	3.1
Spot 3* (in at %)	41.3	-	57.7	-	1	-
Spot 4* (in at %)	-	34.3	65.7	-	-	-

* From STEM/EDX analysis performed in regions reported in Fig. VI-6.

Spherical particles formed during the PEO process of the aluminium alloys (Al1050 and Al2024) are mainly composed of Al and O. Their atomic concentration is close to the stoichiometry of alumina Al_2O_3 (Spot 1 and spot 3 in Table VI-2). The particles produced with the zirconium alloy are rich in Zr and O and their atomic concentration is close to the stoichiometry of zirconia ZrO_2 (Spot 4 in Table VI-2). Additionally, in the specific case of the copper-rich aluminium alloy (Al2024), bright-field micrographs evidence the presence of nanometre-size needles surrounding the Al, O-rich spherical particle. The STEM/EDX element quantification performed on these needles (Spot 2 in Table VI-2) reveals the presence of Cu and O in large amount suggesting that they consist of copper oxide. In contrast no similar needle was detected in the case of the low-alloyed aluminium substrate (Al1050). Finally, carbon residues are associated to the carbon film deposited on the TEM grid while titanium traces may come from the gradual erosion of the titanium counter-electrodes used during the PEO treatments.

VI.2.2c Crystallographic phases of the particles

XRD patterns of the metallic substrate, the PEO oxide coating and the filter paper (after filtering the electrolyte) for the PEO processed aluminium (Al1050 and Al2024) and zirconium (ZrM5) alloys are compared in Fig. VI-7. First of all, and whatever the processed alloy, the XRD patterns of the produced PEO coatings show the presence of Al and Zr peaks in the case of the PEO process of both the aluminium (Al1050 and Al2024) and zirconium substrates (ZrM5), respectively. They originate from the metallic substrate lying under the oxide layer due to the X-ray penetration depth that exceeds the overall thickness of the formed PEO coating. As usually encountered for the PEO process of aluminium [7,78,113] and zirconium alloys [64,161,165], the XRD patterns reveal the presence of two types of alumina (face-centred cubic η - and rhombohedral α - Al_2O_3) through the PEO coatings grown on the aluminium substrates and one type of zirconia (monoclinic ZrO_2) through the PEO layer produced on the zirconium substrate. Indexing the XRD patterns recorded on the filter papers only

evidence the presence of η - α - Al_2O_3 and ZrO_2 for the PEO process of the aluminium and the zirconium alloys, respectively. In the specific case of the copper-rich aluminium substrate (Al2024), one can note the presence of the copper oxide CuO in the corresponding filter paper (Fig. VI-7a).

XRD measurements performed on the filter papers confirm the fact that the spherical particles consist of crystallised alumina or zirconia, depending on the metallic substrate processed, while the needle shaped particles are composed of crystallised copper oxide. This result was cross-examined by performing finer TEM observations as shown in Fig. VI-8. Indeed, high-resolution TEM (HR-TEM) micrographs confirm the crystalline state of the produced particles. Moreover, indexing the associated FFT patterns confirm the presence of η - Al_2O_3 in the spherical particles produced during PEO of the Al2024 substrate. Surrounding needle shaped particles well consists of CuO. Finally, the spherical particles produced from the ZrM5 substrate are crystallised within the ZrO_2 phase.

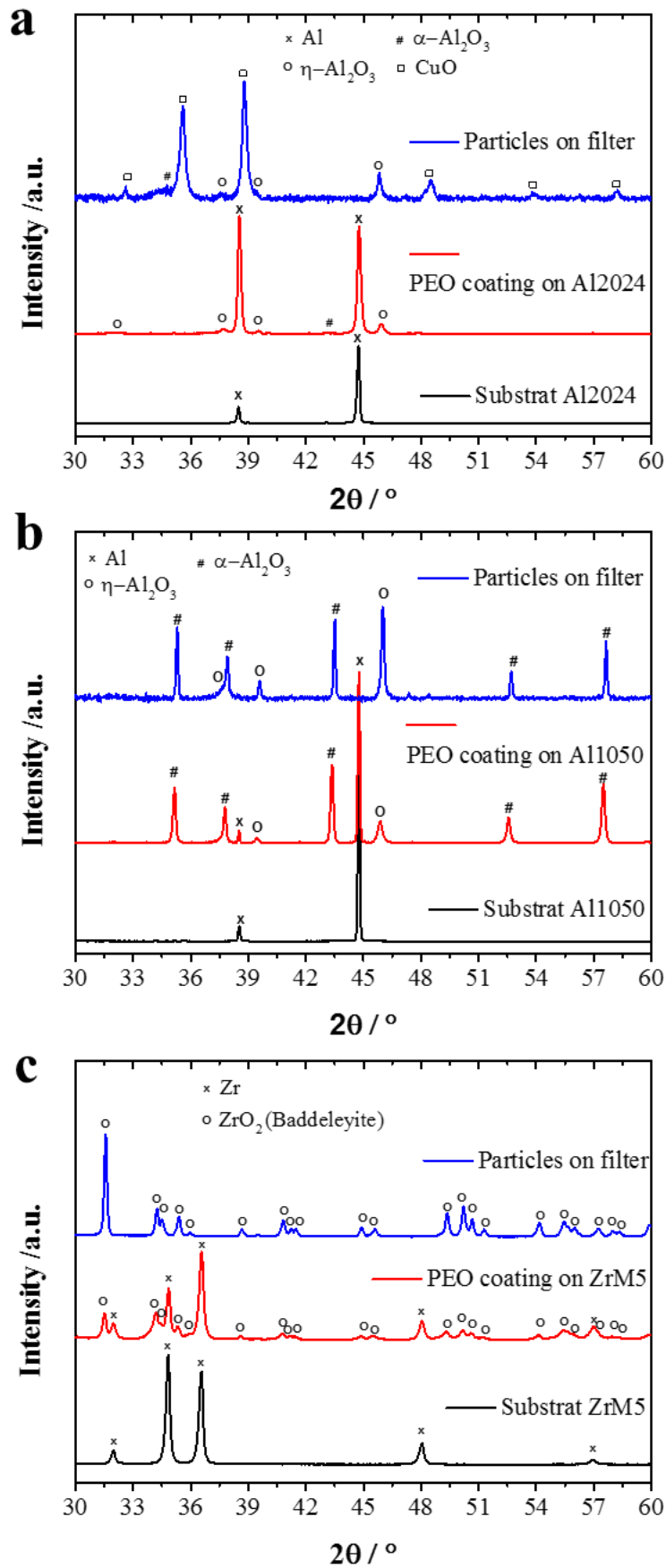


Fig. VI- 7. XRD patterns of the metallic substrate, the oxide coating and the filter paper (after filtering the electrolyte) in the case of the PEO process of Al1050, Al2024 and ZrM5 alloys.

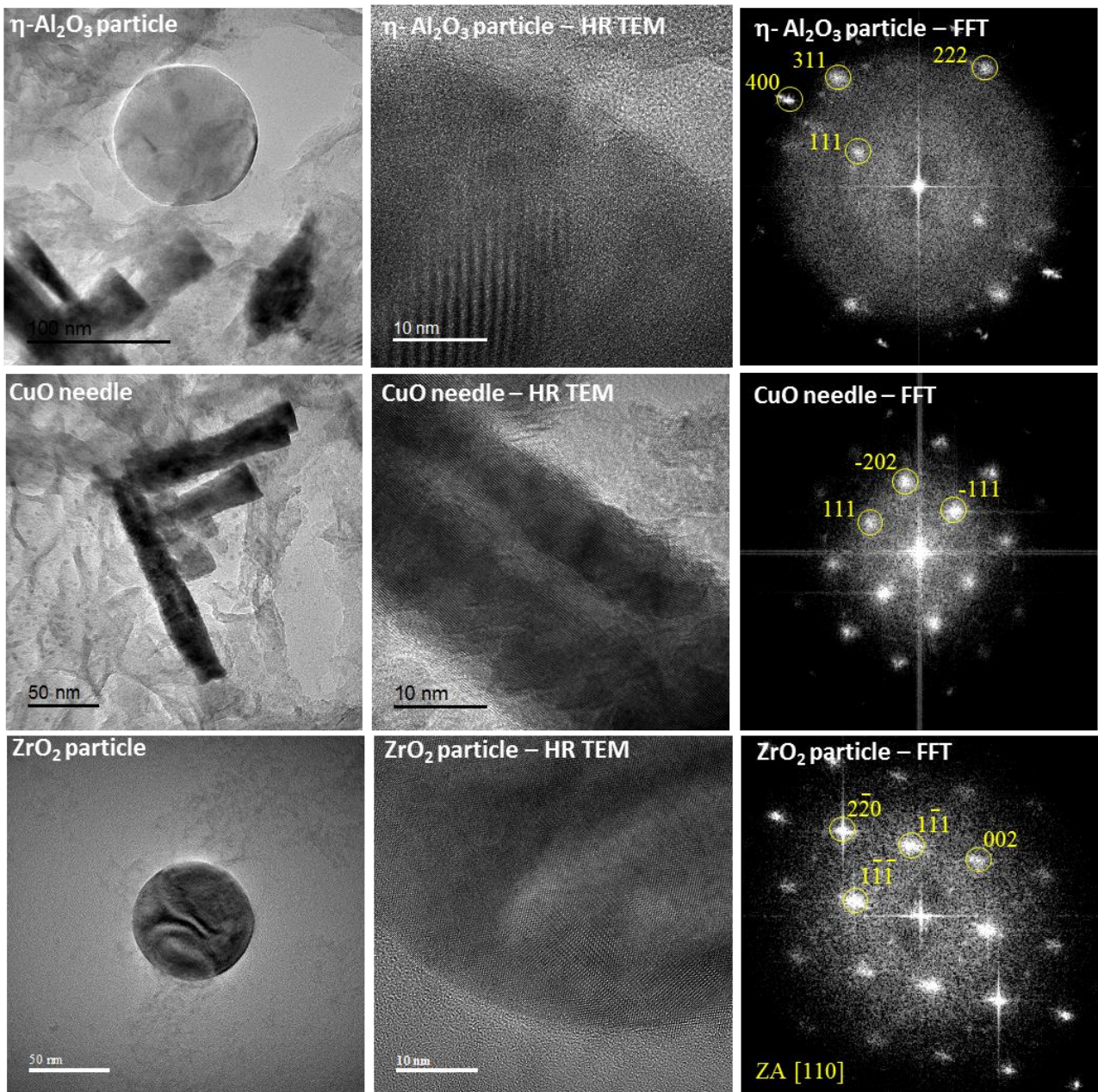


Fig. VI- 8. Bright-field TEM micrographs, high-resolution TEM micrographs and the associated FFT patterns recorded on nano-particles produced during the PEO process of Al1050, Al2024 and ZrM5 alloys.

VI.2.2d Discussion about the formation mechanism of the particles

The discussion hereafter focuses on the formation of particles during the PEO process. Particularly, a descriptive mechanism is proposed to explain their formation and their specific morphology (spherical with cracks at their surface and hollow inside). The particles being produced from the processed metallic electrode, the proposed mechanism is mainly based on a close comparison between the morphology of these particles and the morphology of the corresponding elaborated PEO coatings.

Fig. VI-9 shows the cross-section and the top-view SEM micrographs of the PEO coating elaborated on the Al2024 alloy. The observed morphology is characteristic of PEO coatings elaborated under the “arc” regime (before the appearance of the “soft” regime) with the presence of large open discharge channels forming “pancake”-like structures over the top-most surface [5,78,161,166,167].

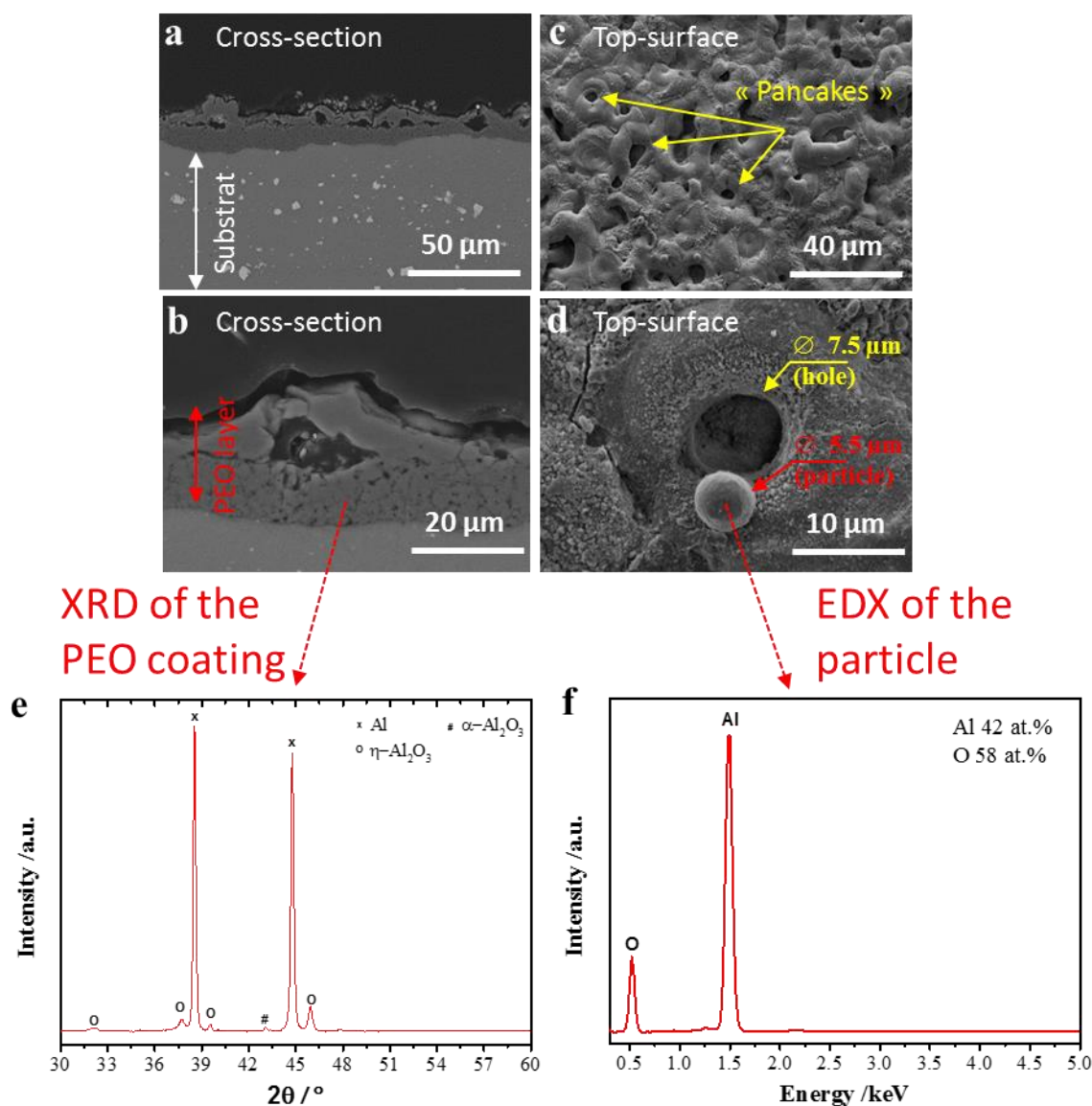


Fig. VI- 9. Cross-section and top-view SEM micrographs of the PEO coatings elaborated on the Al2024 alloy. XRD pattern of the elaborated PEO coating and EDX spectra specifically recorded on on a spherical particle attached on the top-surface of the PEO coating.

The associated XRD pattern clearly evidences the presence of two polymorphs of crystalline alumina *e.g.* α- and η-Al₂O₃. As a comparison, it was previously established that particles produced from the Al2024 alloy also consist in these two alumina polymorphs (see Fig. VI-7a). More

interestingly, a close examination of the top-surface of the coating reveals the presence of spherical particles (see Fig. VI-3d). They seem as attached at the top-surface of the coating, particularly at the vicinity of the “pancake” structure. Their spherical shape is the same as the particles observed in the filter paper. Additionally, Fig. VI-3d also shows that the attached particle exhibits quite the same size as the diameter of the “pancake” cavity. Finally, the EDX spectrum shown in Fig. VI-9f and collected on this attached particle shows that it consists mainly of Al and O suggesting the presence of crystalline alumina. Thus, a relationship between the microstructure of the produced particles and the grown PEO coating, mainly the morphology of the “pancake” structure, is established. This allows proposing a mechanism of formation of these metallic oxide particles during the PEO process of aluminium and zirconium alloys as illustrated in Fig. VI-10.

Before appearance of the micro-discharge, and as described previously with SEM observations, Fig. VI-10a presents the typical “pancake” structure that developed during the PEO “arc” regime. Nominé *et al.* have demonstrated that micro-discharges appear in “cascade” through the discharge channel of a “pancake” structure [136,152]. More recently, and by performing optical emission spectroscopy measurements, Martin *et al.* have estimated the gas temperature in the micro-discharge at about 3200 K [124,148,168]. At this temperature, the pre-formed oxide layer is locally and rapidly melted at a heating rate of about $\sim 10^8$ K.s⁻¹ (Fig. VI-10b). Troughton *et al.* have also reported the development of a pressure shockwave that radially propagates outwards from the micro-discharge [151]. It results in the vaporisation of the surrounding electrolyte and the expansion of a gas bubble. Using fast video imaging to follow the dynamic of bubbles and, by applying the Rayleigh-Plesset’s cavitation model, Troughton *et al.* estimated the pressure at about 3 bars [151]. After the extinction of the micro-discharges for which the life-time is about 10 μ s [20,67], the gas bubble continues its expansion through the cavity of the “pancake” structure as illustrated in Fig. VI-10c. Under a high pressure gradient, the molten part of the oxide is driven from the cavity of the “pancake” structure outwards where the pressure is lower (1 bar). The molten oxide can only leave through the open hole of the “pancake” dome and gradually inflates similarly to a rubber balloon (Fig. VI-10d). In contact with the cooled electrolyte, the molten oxide is rapidly cooled at a high cooling rate of about $\sim 10^7$ K.s⁻¹ [168] and solidified keeping a hollowed spherical shape. Cracks appear at its surface due to the volume retraction of the oxide during solidification (Fig. VI-10e). Then the solidified particle may either remain attached to the “pancake” or, if the electrolyte turbulence is sufficiently strong, the particle may be ejected into the electrolyte (Fig. VI-10f).

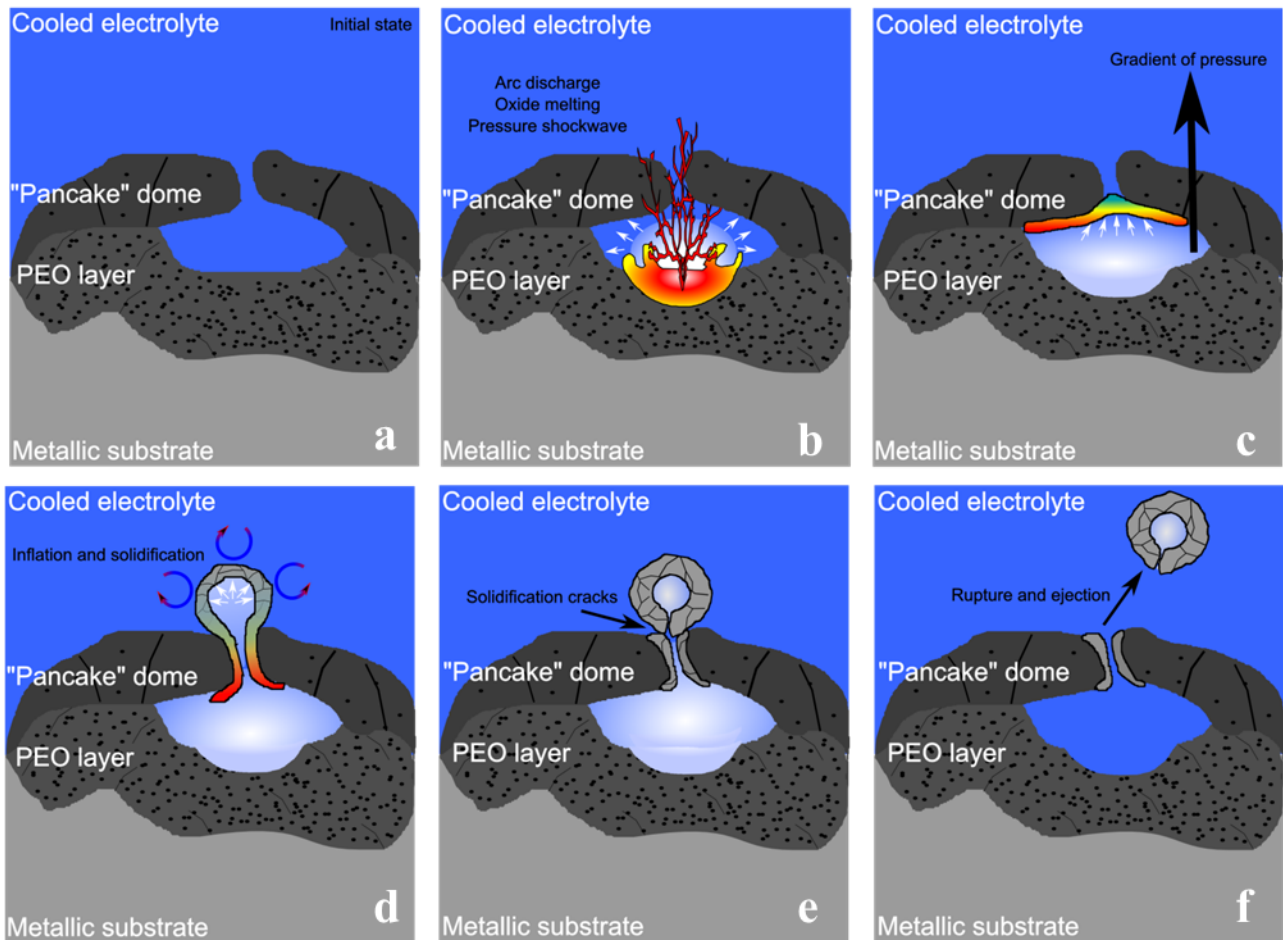


Fig. VI- 10. Schematic description of the formation mechanism of the metallic oxide particles during the PEO process of metallic substrate.

VI.2.4 Intermediate conclusion

The formation of particles during the PEO process of aluminium and zirconium alloys was investigated. The microstructure of the particles was characterised at different scales, mainly by using transmission electron microscopy. Whatever the processed material, results show that particles exhibit the same morphology, *i.e.* a hollowed spherical shape with diameters in the range of 100 nm to 10 μm . They consist of polycrystalline metallic oxide (η - and α - alumina for the PEO of aluminium alloys and zirconia for the PEO of zirconium alloy). The microstructure of the produced particles was then compared to the microstructure of the PEO coatings grown on the metallic substrates. Similarities were noted between the morphology of the particles and the typical ‘‘pancake’’-like structure. On this basis, a descriptive mechanism that could explain the formation of these particles was proposed. Ignition of a micro-discharge inside the ‘‘pancake’’ cavity induces the propagation of a pressure shockwave that pushes the molten oxide through the exit orifice of the

“pancake”. Similarly to a rubber balloon, the molten oxide forms a hollowed sphere and is rapidly solidified by the surrounding electrolyte and ejected into the electrolyte.

VI. 3 Duplex surface treatment using cold-spray and PEO processes

VI.3.1 Introduction

As previously reported in chapter I, the Plasma Electrolytic Oxidation (PEO) process is a plasma-assisted electrochemical conversion process of metallic surfaces to produce protective ceramic coatings. PEO is particularly dedicated to light-weight metals such as Al, Mg and Ti. When applied to aluminium alloys, the resulting PEO coatings exhibit improved thermal-, wear- and corrosion-resistance, because the processing conditions are optimized in such way that thick, hard, compact and adherent crystalline oxide layers can be achieved [4,15,27,169–172]. In contrast, when applied to magnesium alloys, produced PEO coatings are generally thin and porous and need in most of the cases additional sealing post-treatments [16,59,167]. Moreover, the PEO process does not allow surface protection of ferrous-based metals for which, in the electrochemical domain, electro-galvanization remains widely used at the industrial scale, although using concentrated acid (*e.g.* boric acid) and other toxic compounds (*e.g.* hexavalent chromium and cyanides). To overcome such limitations (mainly the complexity and the difficulty to PEO process magnesium alloys and ferrous-based metals), it is proposed to proceed according a duplex surface treatment involving the cold-spray technique and the PEO process. Indeed, and as illustrated in Fig. VI-11, the main idea is to spray a first coating of aluminium on magnesium and ferrous-based substrates by using the cold-spray technique and then convert this pre-deposited aluminium coating into an alumina ceramic coating by using the PEO process. The feasibility of such a duplex treatment is investigated and results are presented and discussed in the following section.



Fig. VI-11: Schematic view of a duplex treatment involving cold spray and PEO techniques.

VI.3.2 Specific experimental conditions

VI.3.2a Metallic substrates

A commercial EV31 grade magnesium alloy and a commercial S235 structural steel were used as substrates. The chemical composition of these substrates is given in Tables VI-3 and VI-4. The samples have a rectangular shape of 45 mm × 25 mm × 5 mm. For comparison reasons, it is also worth mentioning that a commercial 1050 grade aluminium alloy was also used as substrate (chemical composition is given in Table II-2). Prior to be processed, the surface of the samples is shot blasted with corundum particles under 5 bars pressure. It allows to clean the surfaces (*i.e.* removal of organic contaminations or oxidation residues) and to provide a sufficient roughness level to ensure adhesion of the aluminium sprayed coating. After shot blasting, the resulting average mean surface roughness R_a of the samples is $25 \pm 5 \mu\text{m}$ and $17 \pm 5 \mu\text{m}$ for the magnesium substrate and for the steel substrate, respectively. Table VI-5 gives the different samples produced during this study.

Table VI-3: Chemical composition of the commercial EV31 magnesium alloy

Elements	Nd	Gd	Zn	Zr	Mg
in wt.%	2.60	1.38	0.25	0.66	Balance

Table VI-4: Chemical composition of the commercial S235 structural steel

Elements	Mn	C	Si	P	S	Fe
in wt.%	1.4	0.17	0.05	0.035	0.035	Balance

Table VI-5: Conditions of elaboration of the different samples using cold spray and PEO process

Substrate	Step 1: Cold Spray (CS) (thickness of Al 1050)	Step 2: PEO process (processing time)	Reference name
Al (1050)	0 μm	8 min	Al + CS 0 μm + PEO 8 min
Al (1050)	0 μm	20 min	Al + CS 0 μm + PEO 20 min
Al (1050)	0 μm	35 min	Al + CS 0 μm + PEO 35 min
Mg (EV31)	66 \pm 15 μm	0 min	Mg + CS 66 μm + PEO 0 min
Mg (EV31)	66 \pm 15 μm	8 min	Mg + CS 66 μm + PEO 8 min
Mg (EV31)	66 \pm 15 μm	20 min	Mg + CS 66 μm + PEO 20 min
Mg (EV31)	66 \pm 15 μm	35 min	Mg + CS 66 μm + PEO 35 min
Mg (EV31)	220 \pm 25 μm	0 min	Mg + CS 220 μm + PEO 0 min
Mg (EV31)	220 \pm 25 μm	8 min	Mg + CS 220 μm + PEO 8 min
Mg (EV31)	220 \pm 25 μm	20 min	Mg + CS 220 μm + PEO 20 min
Mg (EV31)	220 \pm 25 μm	35 min	Mg + CS 220 μm + PEO 35 min
Steel (S235)	80 \pm 15 μm	0 min	St + CS 80 μm + PEO 0 min
Steel (S235)	80 \pm 15 μm	8 min	St + CS 80 μm + PEO 8 min
Steel (S235)	80 \pm 15 μm	20 min	St + CS 80 μm + PEO 20 min
Steel (S235)	80 \pm 15 μm	35 min	St + CS 80 μm + PEO 35 min
Steel (S235)	190 \pm 25 μm	0 min	St + CS 190 μm + PEO 0 min
Steel (S235)	190 \pm 25 μm	8 min	St + CS 190 μm + PEO 8 min
Steel (S235)	190 \pm 25 μm	20 min	St + CS 190 μm + PEO 20 min
Steel (S235)	190 \pm 25 μm	35 min	St + CS 190 μm + PEO 35 min

VI.3.2b Cold-spray processing conditions

In the cold-spray process, also known as cold gas dynamic spraying or high velocity particle consolidation, coatings are applied in the solid state by spraying metal powder at a high velocity upon a substrate at greatly reduced temperatures compared to thermal spray techniques [173–175]. A carrier gas, usually nitrogen or helium, at pressure as high as 4 MPa and at temperature ranging from 100 to 1000 °C, is expanded to a supersonic speed through a converging-diverging De Laval nozzle. Particles are introduced in this gas flow at the inlet of the nozzle. Depending of the processing conditions applied, as well as the morphology and the density of the sprayed particles, the metallic particles are accelerated through the nozzle at speeds exceeding 1000 m.s⁻¹. The particles impact the

substrate located approximately at 5 – 30 mm from the exit of the nozzle and form a more or less dense metal coating. The thickness of the sprayed coating is also adjusted by repeated scans over the same area. Table VI-6 gives the main parameters of the cold spray process that were used in the present study. The sprayed metallic powder consists of a commercial 1050 grade aluminium alloy for which the chemical composition is given in Table II-2. Two different ranges of coating thickness were achieved on both the magnesium and the steel substrates. For the magnesium samples, thicknesses of the aluminium layer deposited by cold spray were $66 \pm 15 \mu\text{m}$ and $220 \pm 25 \mu\text{m}$ (see Table VI-5). For the steel samples, thicknesses were $80 \pm 15 \mu\text{m}$ and $190 \pm 25 \mu\text{m}$.

Table VI-6: Cold spray process parameters

Parameters	Values
Sprayed powder	Commercial 1050 Al alloy
Powder shape	Spherical
Powder size	$10 \pm 3 \mu\text{m}$
Carrier gas type	Nitrogen (N_2)
Gas pressure	2.4 MPa
Gas temperature	340 °C
Nozzle traverse speed	$90 \text{ mm}\cdot\text{s}^{-1}$
Nozzle stand-off distance	30 mm

VI.3.2c PEO processing conditions

PEO treatments were run in a solution of potassium hydroxide ($[\text{KOH}] = 1 \text{ g}\cdot\text{L}^{-1} \cong 0.018 \text{ mol}\cdot\text{L}^{-1}$) and anhydrous sodium silicate ($[\text{Na}_2\text{SiO}_3] = 1.65 \text{ g}\cdot\text{L}^{-1} \cong 0.014 \text{ mol}\cdot\text{L}^{-1}$) diluted in deionised water. The measured pH and conductivity of the fresh electrolyte is 12.5 and $2.8 \text{ mS}\cdot\text{cm}^{-1}$, respectively. In order to limit the ageing effect of the electrolyte, a fresh electrolyte is renewed for each substrate. Two titanium counter-electrodes (plates of $200 \times 200 \times 1 \text{ mm}$ in size) were set at 90 mm from the working electrodes (Al1050, Mg EV31 and Steel S235). All the PEO treatments were conducted using a pulsed bipolar current generator within the “soft” regime electrical conditions. The ratio of charge quantity ($RCQ = Q_p / Q_n$) was set at 0.9. The current pulse frequency (f) and the anodic current density (j_a) were set at 100 Hz and $48 \text{ A}\cdot\text{dm}^{-2}$. As reported in Table VI-4, the durations of the PEO treatments were set at 8, 20 and 35 min. After treatment, the processed samples were rinsed with ethanol, dried and stored in a dry environment before ex situ characterization.

VI.3.2.d Ex-situ characterization of the coatings

Cross-sections of the treated samples were examined by SEM. To ensure consistency of the results, the centre of the samples was systematically characterised. The coating thickness was determined as an average value of 10 measurements taken on cross-section over 10 different locations (every 100 μm). Chemical composition and distribution of elements in the synthesised coatings and the phase composition was determined by EDX analysis and XRD measurements, respectively. Finally, X-ray micro-tomography measurements were carried out to characterise porosities through the cold sprayed aluminium coatings as well as through the PEO oxide layers. A Phoenix Nanotom X-ray micro-computed tomography (μCT) equipment was used to characterise the void morphology and distribution in the both the cold sprayed and PEO processed coatings. Rectangular specimens of $\sim 2 \times 2 \times 2$ mm in dimensions were characterised by X-ray μCT . The μCT equipment was composed of an X-ray tube operating up to 180 kV / 30 W and an X-ray scintillator screen which was coupled to a high-resolution Hamamatsu CCD-sensor (2300 pixels \times 2300 pixels). The μCT procedure was based on the acquisition of a series of X-ray radiographs of a sample that rotated step by step around a vertical axis perpendicular to the incident beam. Images were recorded over a period of 6 s. A total of 1440 images were recorded for scan duration of 144 min. For 3D-imaging reconstruction, a mathematical algorithm was used to reconstruct the distribution of absorption coefficients within the sample volume, and then the internal 3D volume structure of the samples. The final resolution of the 3D-images was voxels of dimensions $1.5 \times 1.5 \times 1.5$ μm . Below these dimensions, porosities were not detected.

VI.3.3 Results and discussion

VI.3.3a Establishment of the “soft” sparking regime

Fig. VI-12 shows the evolution of the anodic voltage amplitude as a function of the PEO processing time for the different duplex treatments conducted and summarized in Table VI-5. As previously reported, the “arc” to “soft” regime switching time is usually detected by the gradual drop in the anodic voltage amplitude in the course of the PEO process [19]. During the first minutes of treatment, *i.e.* in the PEO “arc” regime, Fig. VI-12 shows that the presence of a cold-sprayed aluminium coating on magnesium and steel substrates has a significant influence on the voltage amplitude value compared to the reference PEO treatment performed on the aluminium substrate (without cold-sprayed aluminium coating). For example, after 5 min, the anodic voltage amplitude is higher than 900 V for the duplex treatments while it is lower than 760 V for the reference PEO treatment performed on the bulk aluminium substrate. Moreover, for this reference treatment, transition from

the “arc” to “soft” regime appears at about 28 min. In contrast, Fig. VI-12 evidences that all the duplex treatments conducted on magnesium and steel substrates result in an earlier appearance of the “soft” sparking regime. This is particularly obvious for the thicker cold-sprayed aluminium coatings for which transition occurs before 18 min. For the thinner pre-deposited aluminium coatings, it is also apparent that the occurrence of the “soft” regime is accompanied with a sharp drop in the anodic voltage amplitude (more than 300 V).

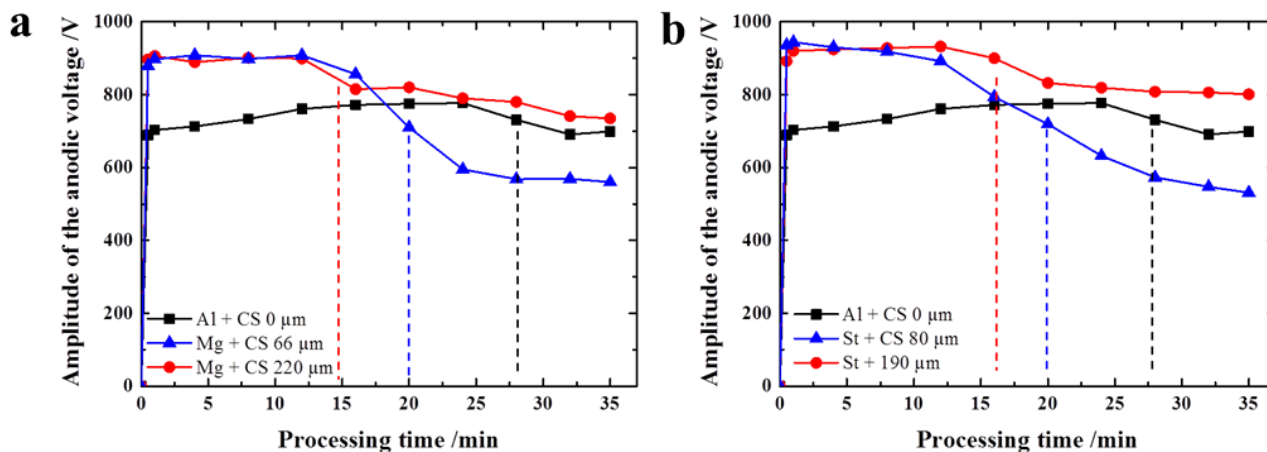


Fig. VI-12: Evolutions of the anodic voltage amplitude as a function of the PEO processing time a) for Al 1050 substrate (without cold sprayed Al coating) and Mg substrates (with 66 and 220 μm cold sprayed Al coatings) and b) for Al 1050 substrate (without cold sprayed Al coating) and steel substrates (with 80 and 190 μm cold sprayed Al coatings). Vertical dash lines indicate the PEO processing time at which the “soft” regime occurs. Reference name of each sample is given in Table VI-5.

VI.3.3b Morphology and growth kinetic of the coatings

Fig. VI-13 shows the cross-section SEM micrographs of the PEO oxide layers grown for 35 min under the different conditions defined in Table VI-5. Cross-sections views of the pre-deposited aluminium coatings on the magnesium and steel substrates are also presented in Fig. VI-13 (left-hand side column). The latter show that all the cold-sprayed aluminium coatings are porous, the size and the density of pores gradually decreasing from the top-surface to the coating / substrate interface. Thickness of the cold-sprayed aluminium coatings is also non-homogeneously distributed over the substrates mainly due to their initial roughness achieved during the surface preparation with shot blasting. For the reference aluminium substrate (without cold-sprayed aluminium coating), the cross-section SEM micrographs show the typical morphology of PEO coatings produced on aluminium alloys during the “arc” regime (at 8 and 20 min) and the “soft” regime (at 35 min). The “pancake”-like structure is the usual feature of PEO layers grown under the “arc” regime” while a “sponge”-like structure known to incorporate elements from the electrolyte (*e.g.* Si, Na and K) is more developed over top-surface with the “soft” regime. It is also apparent that with the transition from the “arc” to

the “soft” regime which occurs at about 28 min for the reference aluminium substrate, the morphology gradually transformed into a more compact and thicker oxide layer.

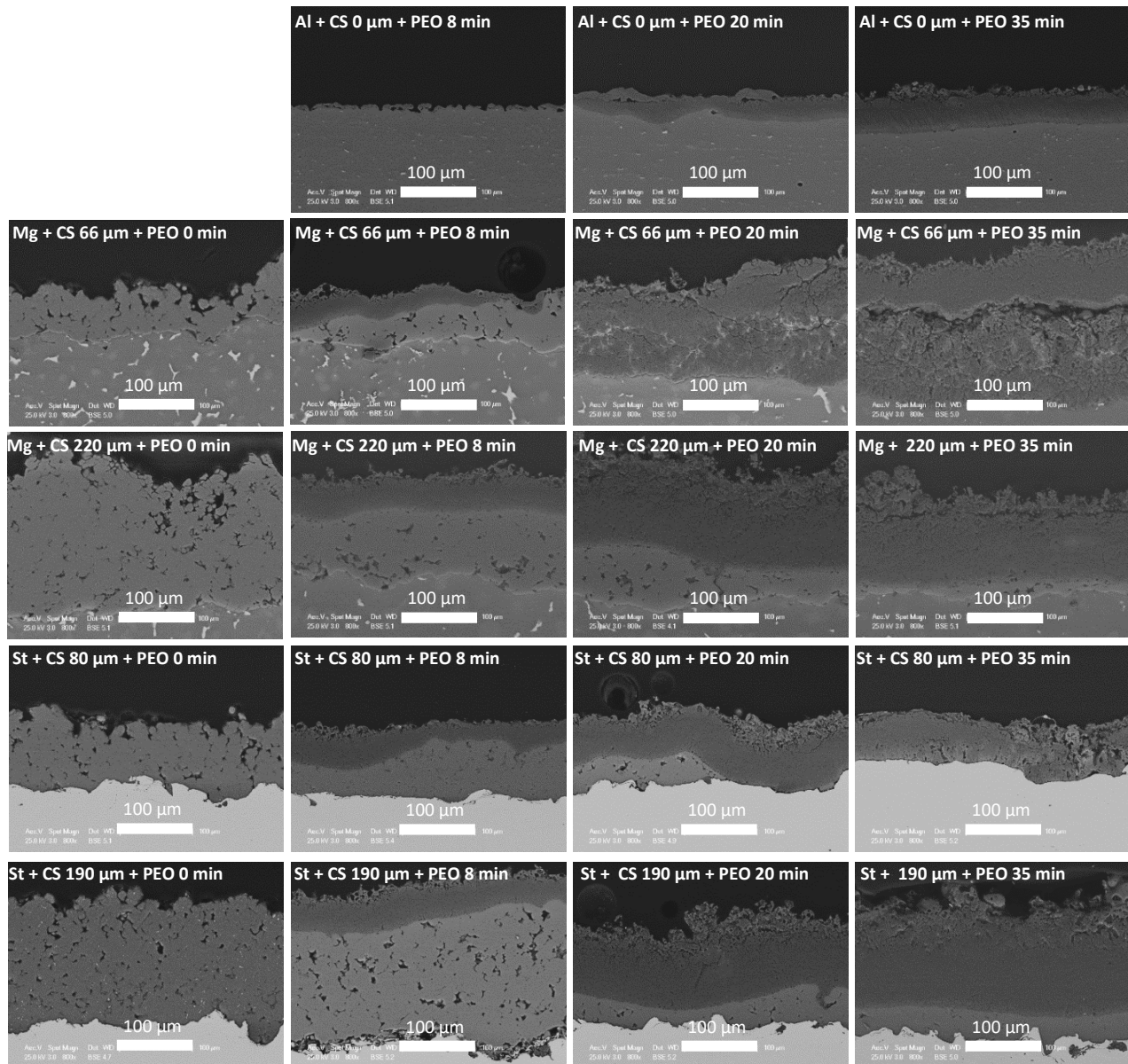


Fig. VI-13: Cross-section SEM micrographs of the cold sprayed and PEO processed samples for different PEO processing time (0, 8, 20 and 35 min). Reference name of each sample is given in Table VI-5.

Interestingly, Fig. VI-13 clearly shows the possibility to grow a PEO oxide layer through the aluminium coating pre-deposited on both magnesium and steel substrates. Whatever the nature of the metallic substrate (*e.g.* magnesium or steel), the thickness of the cold-sprayed aluminium coating and the processing time, it appears that duplex treatments result in thicker and more compact PEO oxide layers compared to the reference PEO treatment performed on the aluminium substrate (without cold-sprayed aluminium coating). Additionally, the top-surface of the PEO oxide layers grown for 20 min

already exhibit a sponge-like structure which is characteristic of PEO coatings elaborated under the “soft” regime. This is in good agreement with previous observations established from the voltage-time responses which demonstrated an earlier transition to the “soft” regime by using duplex treatments. It is also worth noting that, for the thinner cold-sprayed aluminium coatings (below 80 μm in thickness), thickness of the PEO oxide layers reaches and even exceeds the thickness of the pre-deposited aluminium coating. Particularly for the magnesium substrate, the PEO oxide layer is clearly thicker than the pre-deposited aluminium coating. It suggests not only the full conversion of the sprayed aluminium into aluminium oxide but also the conversion of the magnesium substrate into magnesium oxide. This is particularly obvious at 35 min where signs of delamination can be observed exactly at the location of the former aluminium / magnesium interface. In contrast, for the steel substrate, the PEO oxide layer reaches the aluminium / steel interface at about 20 min after which growth of the oxide layer seems to stop. Interestingly, after 35 min, no delamination is observed at the interface between the elaborated PEO coating and the steel substrate. It can be explained by the initial high level of roughness over the steel surface that ensures an efficient anchor of the coating.

Fig. VI-14 depicts the evolution of the average thickness of the overall PEO oxide layer with the processing time for the different surface treatments investigated and defined in Table VI-5. It confirms an enhancement of the growth kinetic of the PEO oxide layer using duplex treatments. At 8 min, the overall PEO oxide layers formed on both the pre-coated magnesium and steel substrates are three and even four times thicker than that grown on the bulk aluminium substrate (without cold-sprayed aluminium coating). During the first minutes of process, the growth kinetic is about $1.5 \mu\text{m}\cdot\text{min}^{-1}$, values usually encountered for conventional PEO treatments on aluminium substrates, while it rises to $6 \mu\text{m}\cdot\text{min}^{-1}$ for duplex treatments investigated. For the thicker cold-sprayed aluminium coatings (up to 190 μm in thickness), a slight decrease in the growth kinetic is observed for longer processing times. Indeed, at 35 min, the growth kinetic is about $4 \mu\text{m}\cdot\text{min}^{-1}$. For thinner cold-sprayed aluminium coatings (down to 80 μm), the growth behaviour is different between the magnesium substrate and the steel one. Concerning the magnesium substrate, the growth kinetic remains unchanged throughout the duration of the PEO process ($6 \mu\text{m}\cdot\text{min}^{-1}$) and the final thickness of the PEO oxide layers ($215 \pm 20 \mu\text{m}$ at 35 min) clearly exceeds the thickness of the pre-deposited aluminium coating ($66 \pm 15 \mu\text{m}$). It means that after converting the overall aluminium pre-coating into aluminium oxide, oxidation continues through the magnesium substrate without change in the growth kinetic. Oppositely, in the case of the steel substrate, once the aluminium pre-coating is fully oxidized at about 20 min, thickening of the PEO oxide layer stops.

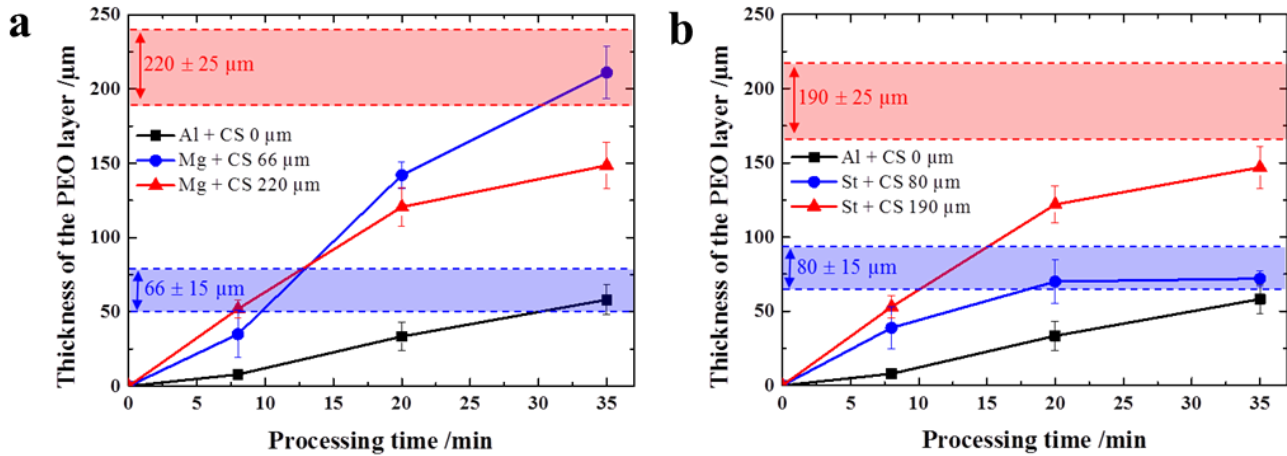


Fig. VI-14: Evolutions of the PEO oxide layer thickness as a function of the PEO processing time **a)** for Al 1050 substrate (without cold sprayed Al coating) and Mg substrates (with 66 and 220 μm cold sprayed Al coatings) and **b)** for Al 1050 substrate (without cold sprayed Al coating) and steel substrates (with 80 and 190 μm cold sprayed Al coatings). Coloured boxes indicate thicknesses of the different pre-deposit cold sprayed Al coatings. Reference name of each sample is given in Table VI-5.

VI.3.3c Chemical and crystallographic compositions of the duplex coatings

Fig. VI-15 presents specific SEM cross-section views and the associated EDX map of Al, O, Si, Ca, K, Mg and Fe distributions throughout the coatings synthesised using a conventional PEO process on an aluminium substrate (for 35 min) and using duplex treatments on both a magnesium substrate and a steel substrate (for 20 min). Fig. VI-16 shows the EDX spectra recorded at different locations over the cross-section (indicated by coloured and numbered crosses in Fig. VI-15) as well as the corresponding quantification in elements. First of all, whatever the processed substrate and as usually encountered for PEO treatments conducted on aluminium in “soft” regime, these element maps evidence that the outer sponge-like structure of the coatings incorporates elements from the electrolyte, *e.g.* O, Si, Ca and K, and from the aluminium substrate or the aluminium pre-coating, *e.g.* Al. For the aluminium substrate, without pre-deposited aluminium coating (Fig. VI-15a), the inner sublayer exclusively consists of Al and O. For the magnesium substrate with a cold-sprayed aluminium pre-coating ($66 \pm 15 \mu\text{m}$ in thickness) (Fig. VI-15b), the synthesised PEO coating can be divided into 3 sublayers that consist of a sponge-like outer sublayer enriched in Si, Ca and K, a denser intermediate sublayer rich in Al and O and, close to the magnesium substrate, an inner sublayer rich in Mg and O which also exhibits cracking mainly extended parallel to the interface. For the latter, the element quantification clearly suggests the presence of a magnesium oxide and the absence of an aluminium oxide. In the case of the steel substrate with a pre-deposited aluminium coating (Fig. VI-15c), the PEO coating shows a thick sponge-like outer sublayer and a compact inner sublayer rich in Al and O. It is also worth mentioning that the EDX measurements do not show the presence of

oxidized iron even close to the steel interface. Finally, the SEM cross-section micrograph in Fig. VI-15c particularly evidences the fact that the cold sprayed aluminium coating exhibits larger porosities than for the inner PEO oxide sublayer.

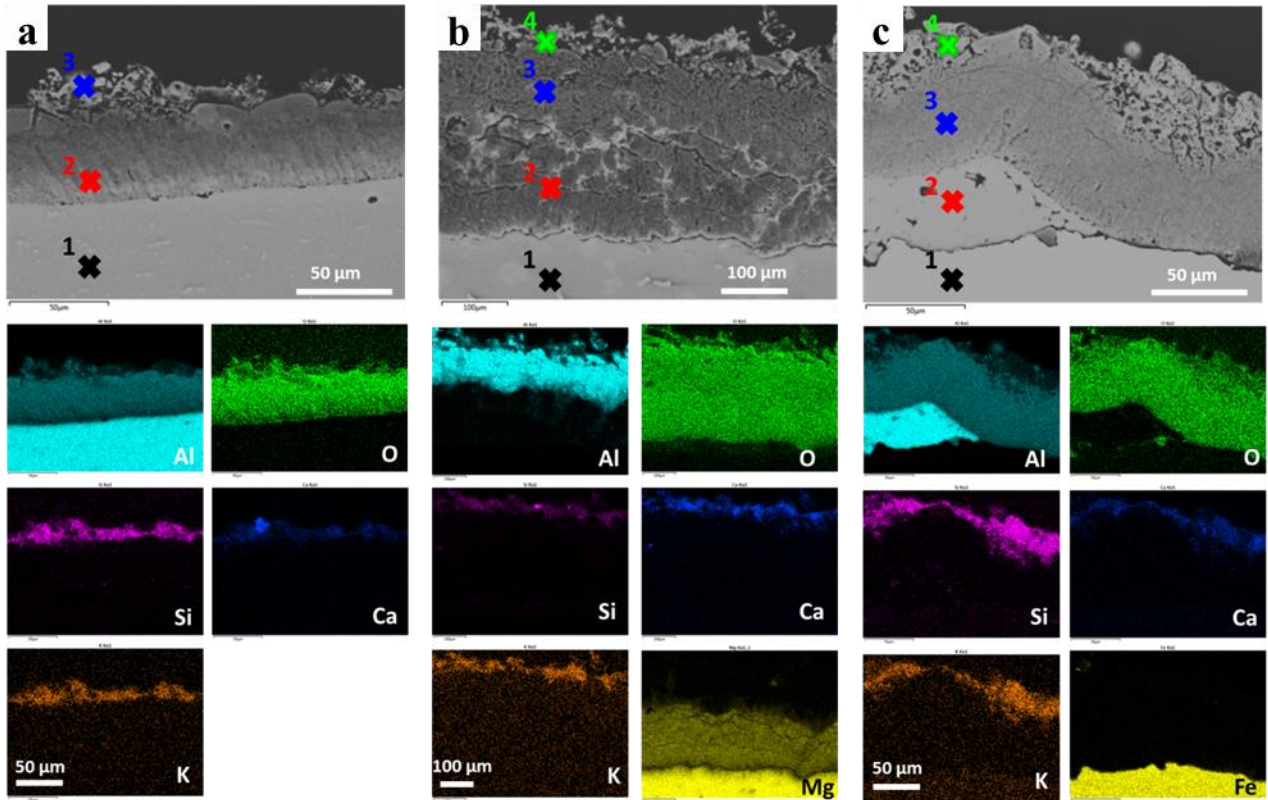
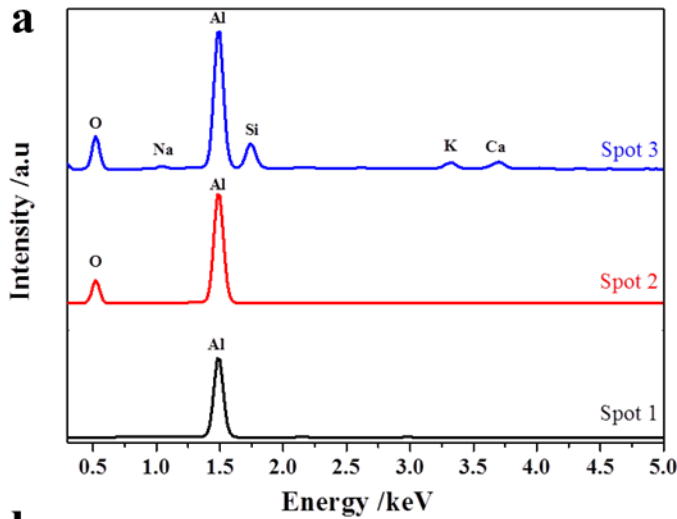
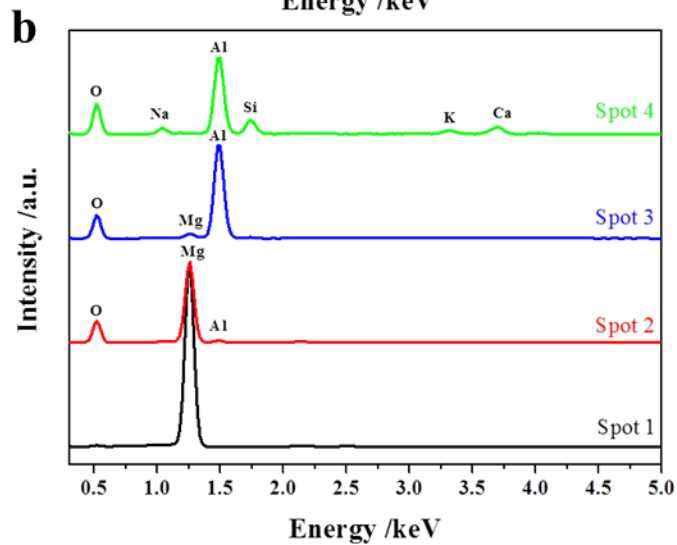


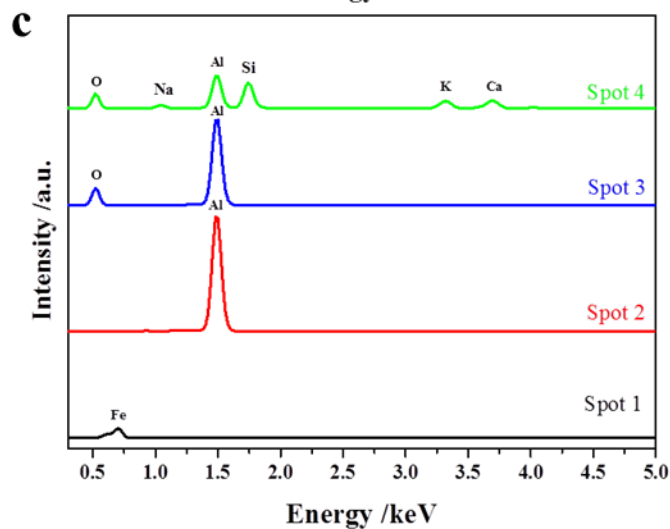
Fig. VI-15: Cross-sections SEM micrographs and the corresponding EDX element maps for the duplex coatings grown on a) an Al1050 substrate (without cold sprayed Al coating), b) a Mg substrate (with 66 μm cold sprayed Al coating) and c) a steel substrate (with 80 μm cold sprayed Al coating). Coloured spot corresponds to EDX localized measurements for which EDX spectra and the associated element quantification are given in Fig. VI-16.



Element (in wt%)	Spot 1	Spot 2	Spot 3
Al	100	57	39
O	-	43	41
Si	-	-	12
Ca	-	-	3
K	-	-	3
Na	-	-	2



Element (in wt%)	Spot 1	Spot 2	Spot 3	Spot 4
Mg	100	58	2	-
Al	-	3	54	32
O	-	39	44	45
Si	-	-	-	9
Ca	-	-	-	6
K	-	-	-	4
Na	-	-	-	4



Element (in wt%)	Spot 1	Spot 2	Spot 3	Spot 4
Fe	100	-	-	-
Al	-	100	56	27
O	-	-	44	42
Si	-	-	-	16
Ca	-	-	-	6
K	-	-	-	6
Na	-	-	-	3

Fig. VI-16: EDX spectra recorded at different locations over the cross-section of the coatings grown and the associated element quantification on a) an Al1050 substrate (without cold sprayed Al coating), b) a Mg substrate (with 66 μm cold sprayed Al coating) and c) a steel substrate (with 80 μm cold sprayed Al coating). Location of the different spots is defined in the SEM cross-section micrographs in Fig. VI-15.

In complement to the EDX analysis, XRD measurements were performed on the different samples. Fig. VI-17 shows that for all the processed samples, with or without a pre-deposited aluminium coating, the XRD patterns show the presence of Al peaks as well as crystalline α - and η -alumina peaks. Al peaks are originated from the aluminium substrate or from the cold-sprayed aluminium pre-coating. This is confirmed by the decrease in the Al peak intensity as the process goes due to the gradual thickening of the PEO oxide layer. The presence of α - and η -alumina is usual for oxide layers grown during PEO of aluminium. The transition to “soft” regime is known to be concomitant with the appearance of α -alumina. This is confirmed by the relative increase in the intensity of the α -alumina peaks with the processing time compared to the intensity of the η -alumina peaks. For the magnesium substrate with a pre-deposited aluminium coating (Fig. VI-17b), and in addition to the α - and η -alumina peaks, XRD patterns also show the presence of magnesium oxide (MgO) and forsterite (Mg_2SiO_4) peaks after 20 min processing time. It definitively confirms previous suggestion *i.e.* the oxidation of the magnesium substrate that takes place after the complete oxidation of the pre-deposited aluminium coating. Their low peak intensity is due to the fact that the MgO- and Mg_2SiO_4 -containing sublayer is located beneath the thick aluminium oxide sublayer as observed in Fig. VI-15b. Interestingly, by using a duplex treatment involving cold-spray and PEO processes on a magnesium substrate, this result also evidences the possibility to produce a composite ceramic-based multilayer on a lightweight metal. Finally, for the steel substrate with a cold-sprayed aluminium coating, XRD patterns show the presence of Al peaks as well as crystalline α - and η -alumina peaks. For longer PEO processing time, although thickening of the PEO coating stops, the relative intensity of the α - alumina peaks seems to increase compared to the intensity of the η -alumina peaks. This suggests the gradual transformation of the η -alumina into α -alumina for longer PEO processing time. This point should be the subject of further detailed investigations. In addition, Fig. VI-17c also confirms the absence of oxidized iron through the PEO coating.

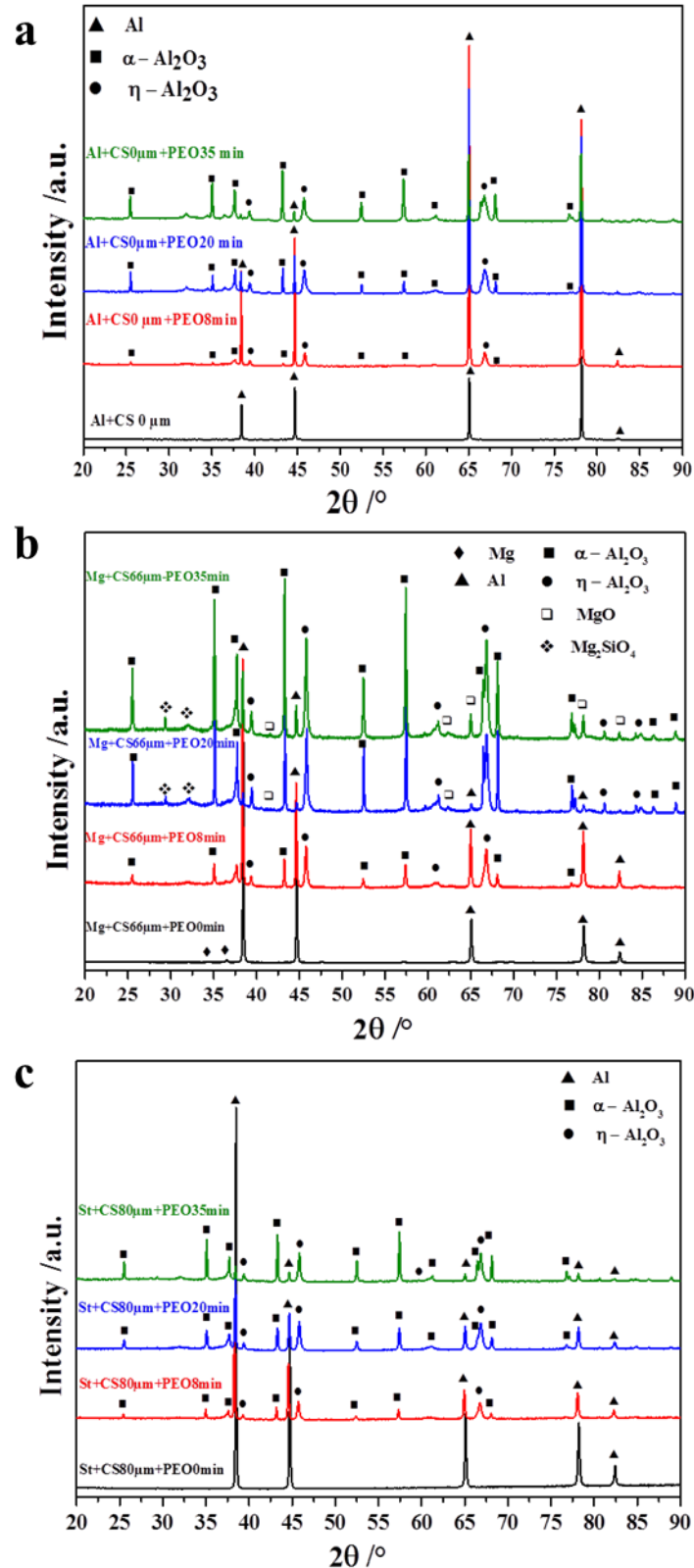


Fig. VI-17: XRD patterns (using Bragg-Brentano geometry) of the coatings synthesised using cold spray and PEO treatments at different processing time (0, 8, 20 and 35 min) for **a)** Al1050 substrate (without cold sprayed Al coating), **b)** Mg substrate (with 66 μm cold sprayed coating) and **c)** steel substrate (with 80 μm cold sprayed coating). Reference name of each sample is given in Table VI-5.

VI.3.3d Discussion about the growth mechanism of the duplex coatings

The discussion hereafter focuses on the influence of the porosity on the PEO process of aluminium. Particularly, a descriptive mechanism is proposed to explain the role played by the porosities through a pre-deposited aluminium coating on the subsequent growth of a PEO oxide layer. Indeed, previous results have shown that growth kinetic of PEO oxide layers is greatly enhanced (by a factor up to 3) when applied to cold-sprayed aluminium coatings compared to a bulk aluminium substrate. At the same time, results have also shown that the cold-sprayed aluminium coatings exhibited a high level porosity throughout their thickness. This is particularly obvious in Fig. VI-18 which shows the SEM cross-section view of a steel substrate covered with a cold-sprayed aluminium coating ($80 \pm 15 \mu\text{m}$ in thickness) and then shortly PEO processed (for 8 min processing time). Large and extended pores up to $10 \mu\text{m}$ in length are observed through the pre-deposited aluminium coating.

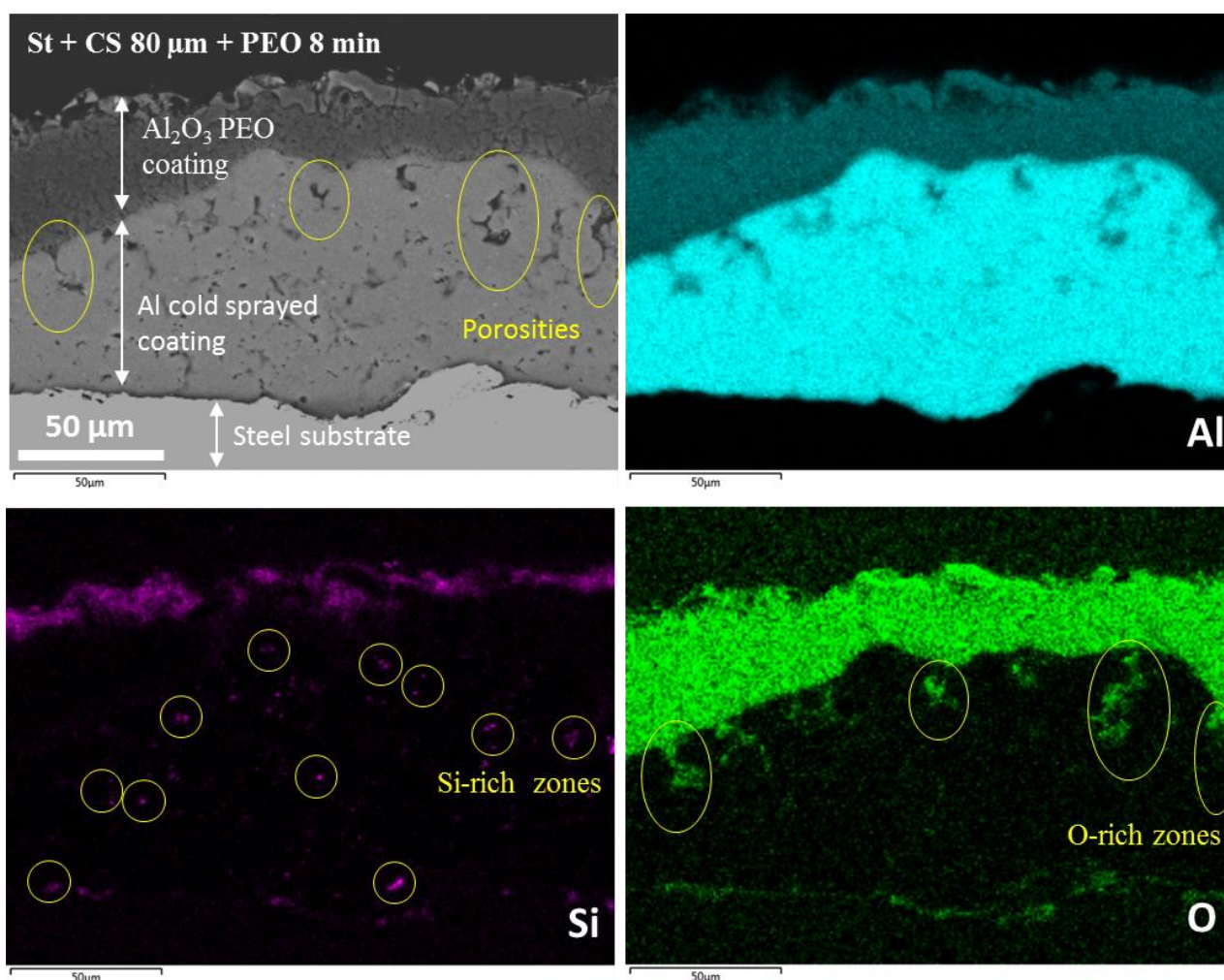


Fig. VI-18: Cross-sections SEM micrographs and the corresponding EDX element maps (Al, Si and O) of a PEO coating grown on a steel substrate (with $80 \mu\text{m}$ cold sprayed Al coating) for 8 min.

In complement to these SEM observations, X-ray micro-computed tomography (μ CT) measurements were also carried out to characterise these porosities through the cold sprayed aluminium layers but also through the PEO oxide layers. Fig. VI-19 show the three-dimensional X-ray μ CT visualizations of pores into the coating elaborated on a steel substrate pre-coated with a thick cold-spray aluminium coating ($190 \pm 20 \mu\text{m}$ in thickness) that was subsequently PEO processed for 35 min. The associated scheme allows localizing the probed volume. The PEO outer sublayer consists in small but numerous pores while the cold-sprayed aluminium coating exhibits fewer but larger pores. The average size of pores in the PEO oxide layer is below $1.25 \mu\text{m}$, which is the detection limit of the X-ray μ CT equipment (below $3.375 \cdot 10^{-9} \text{mm}^3$ in volume), while for the cold sprayed coating the maximum length path of the detected porosities varies between tens to hundreds of micrometres with an average volume of 10^{-8} - 10^{-5}mm^3 . Interestingly, and contrary to observations performed on SEM cross-section micrographs, the 3D X-ray tomography visualizations also highlight the presence of interconnected pores through the cold-sprayed aluminium coating forming a network of large porosities. At the beginning of the PEO process, when the sample is in contact with the electrolyte, it would be reasonable to expect that the presence of such open porosities allows the electrolyte to infiltrate deep into the cold-sprayed aluminium coating.

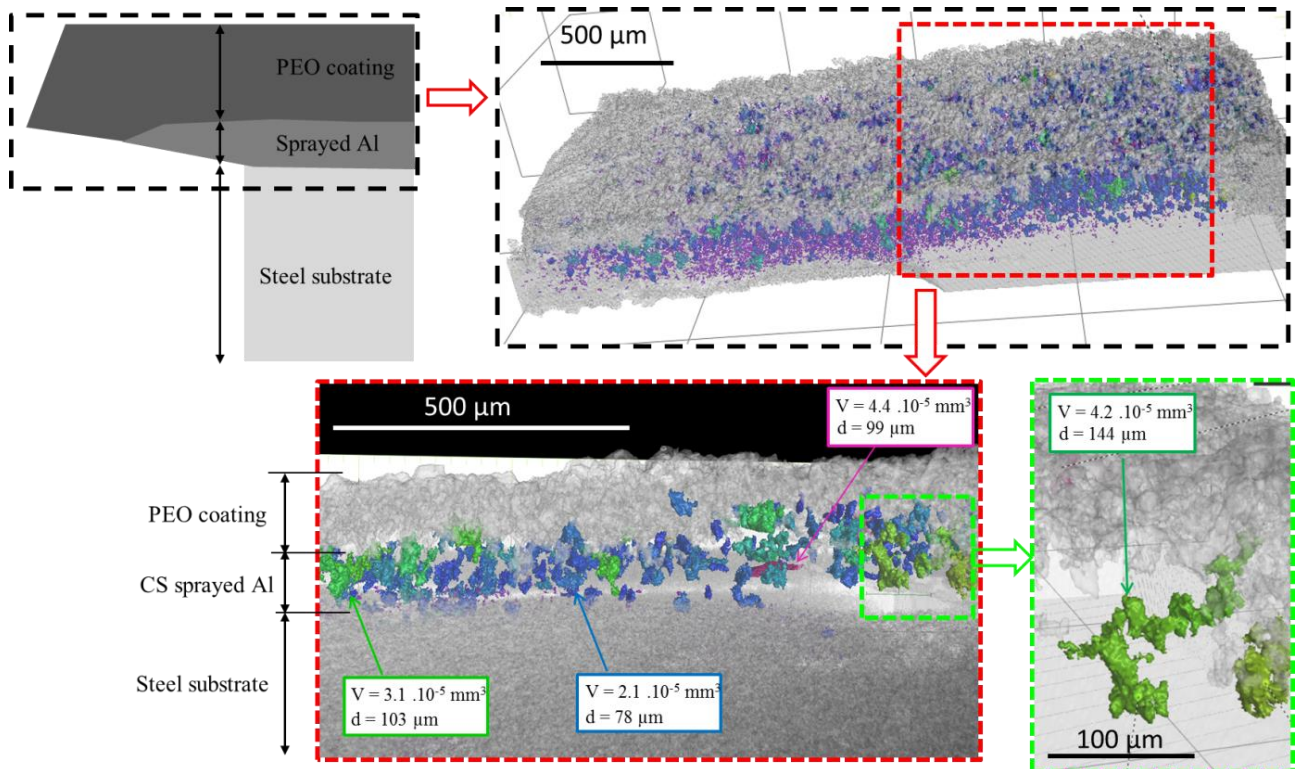


Fig. VI-19: X-ray micro-tomography images of a PEO coating grown on a steel substrate (with $190 \mu\text{m}$ cold sprayed Al coating) for 35 min.

The EDX element maps given in Fig. VI-18 confirm this statement since elements from the electrolyte, especially Si and O, are detected into the porosities of the pre-deposited aluminium coating. These elements are found far advanced from the front line of the aluminium oxidation. For these advanced sites, it suggests that conversion of aluminium into alumina has already started. This is confirmed in Fig. VI-20 which presents SEM cross-sections micrographs recorded on both the magnesium and steel substrates. One can clearly observe oxidized regions ahead from the PEO oxidation front line which clearly exhibits the same shape and size as the porosities observed by X-ray μ CT through the cold sprayed aluminium coatings.

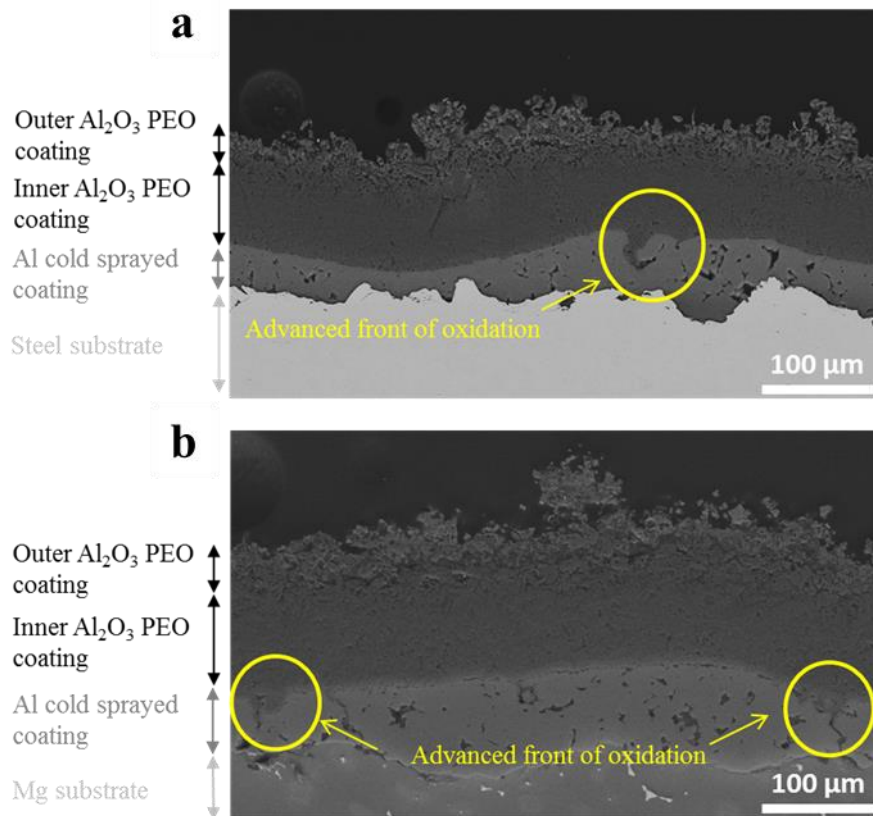


Fig. VI-20: Cross-section SEM micrographs of the cold sprayed and PEO processed samples (for 20 min) for a) a steel substrate (with 190 μm cold sprayed Al coating) and b) a Mg substrate (with 220 μm cold sprayed Al coating).

On the basis of these observations, a growth mechanism of PEO coating in porous aluminium is proposed hereafter. The schematic model in Fig. VI-21 illustrates this proposed mechanism. Before applying the current to the electrodes, the processed sample is firstly immersed in the electrolyte. This electrolyte infiltrates into the connected porosities of the cold-sprayed aluminium layer. When applying the current, and during the first seconds of treatment, the voltage increases rapidly due to

the growth of a thin insulating oxide layer over the processed surface. In the case of the sprayed coatings that exhibit open porosities, breakdown value appears at higher voltage than for the bulk aluminium substrate due to higher specific surface (see Fig. VI-12). Indeed, the accumulated charges throughout the insulating layer, needed to reach the dielectric breakdown voltage, remain higher with a higher specific surface. As the PEO process continues, the “arc” regime takes place and arcs appear over the processed surface. Strong arcs ignite but, in the case of the sprayed aluminium coating, they turn rapidly into smoother micro-discharges due to confinement of the connected porosities. These micro-discharges that appear into the porosities of the cold-sprayed coating are comparable to the D-type micro-discharges known to appear inside the PEO coating during “soft” regime [104,162]. Said differently, it is as if the porosities of the cold-sprayed coating trigger the “soft” regime resulting in its earlier appearance compared to bulk aluminium (see Fig. VI-12). Once the “soft” regime is established, a sponge-like phase enriched in elements from the electrolyte grows at the top-surface of the PEO coatings. This can explain that, after just ten minutes of PEO treatment, a well-developed sponge-like structure is observed at the top surface of the duplex coating. In contrast, for the bulk aluminium, this sponge like structure occurs later, after about 20 minutes (see Fig. VI-13). Inner micro-discharges that appear inside porosities of the pre-deposited aluminium coating gradually converted the surrounding aluminium into alumina. Thus, the growth front of the PEO oxide layer extends not only vertically as observed for the bulk aluminium but also laterally. With the processing time, the porosities are gradually filled with aluminium oxide trapping elements from the electrolyte inside the inner dense PEO oxide sublayer. This explains the presence of such elements, mainly Si, throughout the overall PEO coatings (see Fig. VI-18). In contrast, for the PEO process of bulk aluminium, the inner oxide sublayer is depleted in such elements. Finally, for the duplex treatments, the oxidized areas that consist of advanced fronts of oxidation overlap with the adjacent ones forming a thicker PEO coating compared to those observed for the PEO process of bulk aluminium.

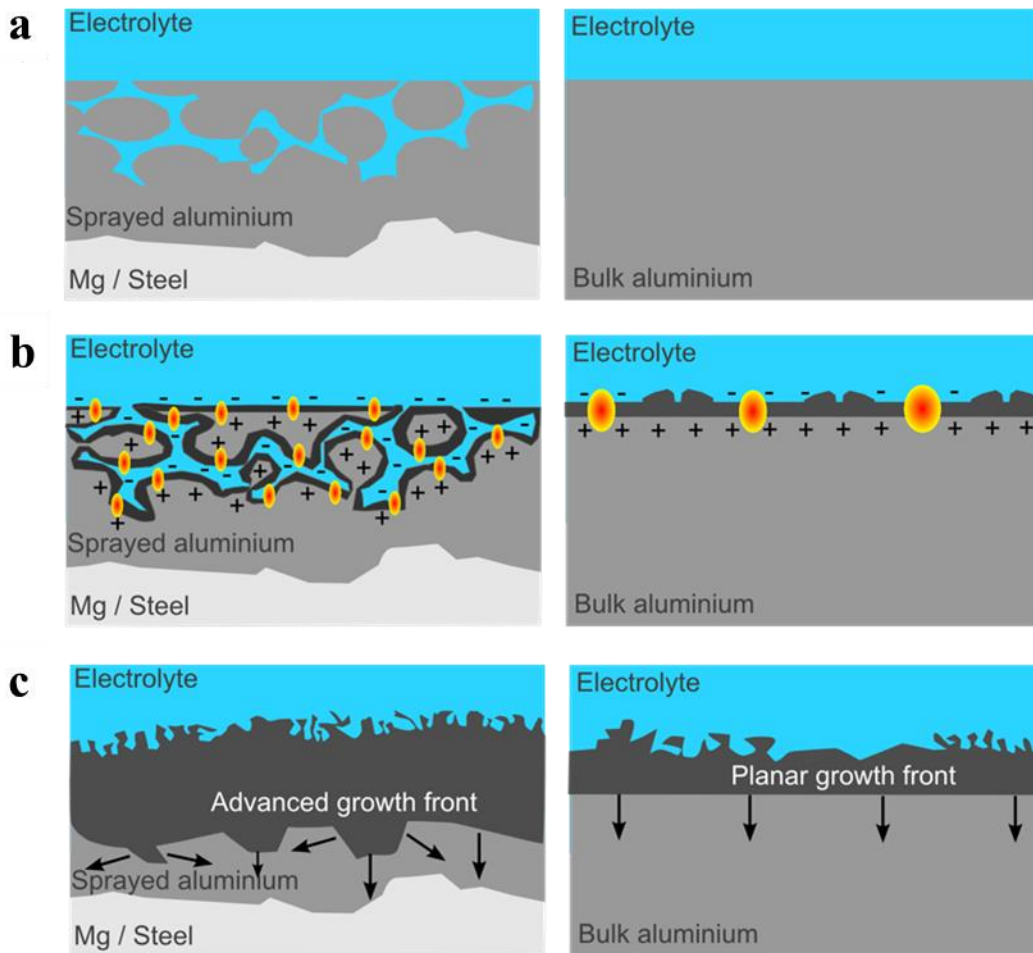


Fig. VI-21: Schematic description of the influence of the porosities inside a cold-sprayed aluminium coating on the growth of a PEO oxide layer, **a)** before applying current to the electrodes, **b)** during the first minutes of the PEO process and **c)** after long PEO processing time.

VI.3.4 Intermediate conclusion

The feasibility of duplex surface treatments involving cold-spray and plasma electrolytic oxidation techniques was investigated. For this purpose, cold-sprayed aluminium coatings with various thicknesses were pre-deposited on magnesium and steel substrates and they were then PEO processed during various processing time. Results clearly demonstrated the possibility to grow an alumina PEO coating on magnesium and steel substrates. Compared to conventional PEO treatment performed on bulk aluminium substrates, growth kinetic of the PEO oxide layer is greatly enhanced by using a duplex treatment. The role played by porosities through the pre-deposited aluminium coating was pointed out and a descriptive mechanism of growth was proposed. Such a duplex treatment offers new opportunities to protect surface of magnesium alloys and ferrous-based material for which direct PEO process remains tricky or even impossible. Further investigations should be devoted to investigate the properties of such duplex coatings, such as wear resistance and corrosion resistance.

VI.4 Conclusions of Chapter VI

This final chapter was dedicated to investigations that may bring new perspectives and opportunities to the PEO processing in terms of applicability, while simultaneously maintaining our focus to understand the process and, combined with the experimental observation, provide a consistent interpretation of the mechanisms that are taking place.

In the first part of this chapter, evidence of micro- and nanoparticle formation during PEO processing was provided. These particles exhibiting spherical geometry and a variety of sizes, are mainly metallic oxides, products of the interactions between the processing substrate and the species of the electrolyte. Production of nanoparticles by plasma in or in contact with liquids has gained much attention recently due to many promising application in biological and medical domains [164,176–178]. A better comprehension and correlation between the PEO processing conditions and the resulting oxide particles, along with optimisation of their collection, could provide new exploitation opportunities for plasma electrolytic oxidation.

In the second part, adopting a more engineering approach, the feasibility of producing thick compact oxide coatings on magnesium and steel was presented. The implementation of a duplex treatment revealed the improvement of oxide coatings formed on magnesium, in terms of both, growth kinetics and compactness of the oxide. Moreover, the possibility of elaborating protective oxide layers particularly on ferrous-based metals, which conventionally are not possible to treat by PEO, was revealed. This demonstrates that plasma electrolytic oxidation can in certain circumstances replace existing coating methods and provide improved and environmental friendly solutions.

General conclusions

The aim of this thesis was to investigate Plasma Electrolytic Oxidation (PEO) process and to contribute to a better understanding of the fundamental mechanisms that govern the process and drive the oxide growth. This was primarily done by two approaches. On one hand, by investigating the breakdown of the dielectric layer, the ignition and appearance of micro-discharges and their physical properties with various electrical parameters applied. And on the other hand, by studying the interactions of the micro-discharges at the metal / oxide / electrolyte system and their effect on the structural properties of the resulting oxide layers.

The first study was oriented towards the behaviour of the micro-discharges under varying electrical conditions, *i.e.* RCQ values, in the course of one treatment. As it had been already shown that the micro-discharges tend to exhibit a certain delay in their appearance with respect to the applied current pulse, our goal was to investigate the effect of a sudden and abrupt change on the ignition of micro-discharges. It was shown that their behaviour is governed by the dynamics of the charges in the electrolyte under polarisation and was explained based on a mechanism of charge accumulation at the growing oxide surface. Furthermore, it was shown that this mechanism depends not only on the applied electrical parameters, but also on the surface morphology of the oxide layer.

In parallel, the combination of certain conditions during the sequential processing revealed the possibility to accelerate and promote the beneficial “soft” regime earlier compared to the single-sequenced treatment. This had an impact on the physical properties of the micro-discharges, as their density and size exhibited an almost fivefold decrease. Consequently, this had an effect on the resulted oxide layer. A synergetic effect was observed, as the coating elaborated with these conditions, exhibited combined characteristics of both conditions, that is an enhanced growth rate resulting in an up to ~40% thicker coating and a compact and dense structure. Finally, it was shown that a considerable reduction in specific energy consumption can be achieved by implementing sequential PEO processing.

Further attention was given to the study of micro-discharges, through the investigation of the effect of the electrolyte on their density and distribution. Besides the decrease in anodic voltage amplitude, that can improve the efficiency in energy consumption, it was illustrated that concentrated electrolytes can lead to a more homogeneous distribution of the micro-discharges during processing, resulting to a more even and thicker oxide layer. Moreover, comparative treatments of two aluminium alloys led to interesting observations, revealing a periodic emission of light with anodic pulses during “soft”

General conclusions

regime for the copper-free aluminium alloy (Al1050), while its complete absence was noticed for the case of the copper-alloyed samples (Al2024). Optical emission spectroscopy confirmed this emission, however, with the exception of a broad continuum, no atomic emission lines were observed in the spectra. The nature of these discrete light sources, was further investigated by means of fast video recording and studying the interactions of the micro-discharges with the gas bubbles located at the vicinity of the processing surface in both “arcing” and “soft” conditions. The results showed that, regardless the conditions, at the beginning of the process, these light spots co-exist with the micro-discharges and, in fact, their ignition precedes the intense (B-type) MDs by approximately 0.7 ms. Once the “soft” regime is established, only these light spots appear on the processed surface. The interactions of the micro-discharges with the gas bubbles, allowed a correlation of the discharge events with their dynamics. The results showed intense perturbations during “arcing” regime and complete absence of them once the “soft” regime was established. These observations indicate indirectly that the source of these light spots is localised inside the growing coating. Having in mind the suggested types of micro-discharges in literature, one can assume that these light spots are the inner D-type micro-discharges, as they appear even simultaneously with the B-type during “arc” regime and dominate the process later on in “soft” regime. However, there is an uncertainty in this assumption, due to the corresponding emission spectra. Further studies should be devoted in investigating the exact nature of this light emission during “soft” regime.

From material point of view, a particular attention was given to the study of the “pancake” cavity formed during the “arc” to “soft” regime transition. A multi-scale investigation of the microstructure revealed the formation of a nanometre scale lamellar arrangement inside the “pancake”, which consists of periodic alternations of alumina and a metastable 1:1 mullite lamellae. Through optical emission spectroscopy and calculations, it was shown that during the discharge the underlying alumina is heated, melted and subsequently solidified in contact with the electrolyte at extreme rates. With these results and based on the alumina-silica phase diagram, a growth mechanism was proposed suggesting that under such severe cooling conditions the solidification process undergoes a non-equilibrium route leading to eventually to the phase separation and formation of such lamellar structure.

Lastly, although plasma electrolytic oxidation has been mostly investigated for aluminium processing and mainly for the growth of protective oxide coating, there are various opportunities in which PEO could find application. In this context, divergent work was conducted and new possibilities were sought.

It was shown that during PEO certain by-products can be obtained that originate from reactions of elements from the processing substrate and the electrolyte. In our case, it was found that metallic oxide particles of aluminium and zirconium are formed during the processing of their respective substrates. Interestingly, they all exhibit same morphology of hollow spherical shape. Cross examination of the sizes of produced particles with the surface characteristics of the elaborated coatings, allowed an interpretation of the formation mechanism of these particles. Optimisation of the processing conditions to precisely control the physical characteristics of the particles (*e.g.* their size distribution or the hollow core-shell structure) could give access to a variety of applications.

Additionally, a different approach was conceived in order to optimise or even elaborate for the first time oxide layers on substrates which are typically difficult (as for the case of magnesium) or even impossible (for the commercial steel) to produce by conventional PEO. With this goal, the duplex processing, combining a first deposition by cold spray and then the application of PEO processing, proved to be efficient in both enhancing the growth and the microstructure of the oxide layers produced on magnesium. At the same time, the results from the commercial steel prove the formation of an adherent aluminium oxide layer on the substrate, with no signs of any interfacial degradation between the alumina and steel. This method illustrates the possibility to expand the range of materials that can be treated by plasma electrolytic oxidation and extend the applicability of the process.

Despite the progress that has been achieved in plasma electrolytic oxidation, its large scale application in production lines is still restrained due to the very high energy costs. Few examples of PEO processing applications exist and are mainly confined in high level technologies. Thus, optimisation of energetic efficiency is compulsory. This cannot be achieved without a complete understanding of the fundamental processes that take place during PEO and the variety of the influencing factors. Therefore, research should be pursued to study both the plasma properties within the discharge, as well as its interactions with the material of the processing surface.

Bibliography

- [1] A. Hartwig, D. Heederik, C.L. Klein, H. Kromhout, L. Levy, D. Papameletiou, European Commission, S.A. and I. Directorate-General for Employment, *SCOEL/REC/386 Chromium VI compounds: recommendation from the Scientific Committee on Occupational Exposure Limits* (2017)
- [2] R. Smith, *Regulation (EC) No 764/2008 of the European Parliament and of the Council*, in: *Core EU Legislation*, Macmillan Education UK, London (2015) 183–186
- [3] A.L. Yerokhin, X. Nie, A. Leyland, A. Matthews, S.J. Dowey, *Plasma electrolysis for surface engineering*, Surf. Coat. Technol. 122 (1999) 73–93
- [4] A.A. Voevodin, A.L. Yerokin, V.V. Lyubimov, M.S. Donley, J.S. Zabinski, *Characterization of wear protective Al-Si-O coatings formed on Al-based alloys by micro-arc discharge treatment*, 86–87 (1996) 516–521
- [5] L.R. Krishna, A.S. Purnima, G. Sundararajan, *A comparative study of tribological behavior of microarc oxidation and hard-anodized coatings*, Wear. 261 (2006) 1095–1101
- [6] J.A. Curran, H. Kalkanci, Yu. Magurova, T.W. Clyne, *Mullite-rich plasma electrolytic oxide coatings for thermal barrier applications*, Surf. Coat. Technol. 201 (2007) 8683–8687
- [7] K. Tillous, T. Toll-Duchanoy, E. Bauer-Grosse, L. Hericher, G. Geandier, *Microstructure and phase composition of microarc oxidation surface layers formed on aluminium and its alloys 2214-T6 and 7050-T74*, Surf. Coat. Technol. 203 (2009) 2969–2973
- [8] E. Arslan, Y. Totik, E.E. Demirci, Y. Vangolu, A. Alsaran, I. Efeoglu, *High temperature wear behavior of aluminum oxide layers produced by AC micro arc oxidation*, Surf. Coat. Technol. 204 (2009) 829–833
- [9] A. Güntherschulze, H. Betz, *Neue Untersuchungen Über Die Elektolytische Ventilwirkung*, Dresden, (1931)
- [10] W. McNeill, *The Preparation of Cadmium Niobate by an Anodic Spark Reaction*, J. Electrochem. Soc. 105 (1958) 544
- [11] G.A. Makrov, G. A. Terleeva, E. K. Shulepko, *Micro arc and arc methods of protective coatings deposition*, Proceedings of Gupkin's Institute of petrochemical and gas industry, issue 185 (1985) 54-65
- [12] W. Krysmann, P. Kurze, K.-H. Dittrich, H.G. Schneider, *Process characteristics and parameters of Anodic Oxidation by spark discharge (ANOF)*, Cryst. Res. Technol. 19 (1984) 973–979
- [13] J. Yahalom, T.P. Hoar, *Galvanostatic anodizing of aluminium*, Electrochim. Acta. 15 (1970) 877–884
- [14] S.D. Brown, K.J. Kuna, T.B. Van, *Anodic spark deposition from aqueous solutions of NaAlO₂ and Na₂SiO₃*, J. Am. Cer. Soc. 54 (1971) 384–390.
- [15] X. Nie, A. Leyland, H.W. Song, A.L. Yerokhin, S.J. Dowey, A. Matthews, *Thickness effects on the mechanical properties of micro-arc discharge oxide coatings on aluminium alloys*, Surf. Coat. Technol. 116–119 (1999) 1055–1060

Bibliography

- [16] H.F. Guo, M.Z. An, H.B. Huo, S. Xu, L.J. Wu, *Microstructure characteristic of ceramic coatings fabricated on magnesium alloys by micro-arc oxidation in alkaline silicate solutions*, Appl. Surf. Sci. 252 (2006) 7911–7916
- [17] S. Xin, L. Song, R. Zhao, X. Hu, *Influence of cathodic current on composition, structure and properties of Al₂O₃ coatings on aluminum alloy prepared by micro-arc oxidation process*, Thin Solid Films 515 (2006) 326–332
- [18] A.L. Yerokhin, V.V. Lyubimov, R.V. Ashitkov, *Phase formation in ceramic coatings during plasma electrolytic oxidation of aluminium alloys*, Ceramics International 24 (1998) 1–6.
- [19] F. Jaspard-Mécuson, T. Czerwiec, G. Henrion, T. Belmonte, L. Dujardin, A. Viola, J. Beauvir, *Tailored aluminium oxide layers by bipolar current adjustment in the Plasma Electrolytic Oxidation (PEO) process*, Surf. Coat. Technol. 201 (2007) 8677–8682
- [20] J. Martin, A. Melhem, I. Shchedrina, T. Duchanoy, A. Nominé, G. Henrion, T. Czerwiec, T. Belmonte, *Effects of electrical parameters on plasma electrolytic oxidation of aluminium*, Surf. Coat. Technol. 221 (2013) 70–76
- [21] C.S. Dunleavy, I.O. Golosnoy, J.A. Curran, T.W. Clyne, *Characterisation of discharge events during plasma electrolytic oxidation*, Surf. Coat. Technol. 203 (2009) 3410–3419
- [22] A.L. Yerokhin, L.O. Snizhko, N.L. Gurevina, A. Leyland, A. Pilkington, A. Matthews, *Discharge characterization in plasma electrolytic oxidation of aluminium*, Journal of Physics D: Applied Physics 36 (2003) 2110–2120
- [23] R.O. Hussein, X. Nie, D.O. Northwood, A. Yerokhin, A. Matthews, *Spectroscopic study of electrolytic plasma and discharging behaviour during the plasma electrolytic oxidation (PEO) process*, Journal of Physics D: Applied Physics 43 (2010) 105203
- [24] M.D. Klapkiv, H.M. Nykyforchyn, V.M. Posuvailo, *Spectral analysis of an electrolytic plasma in the process of synthesis of aluminum oxide*, Mater Sci. 30 (1995) 333–343
- [25] A. Vladimirovich Timoshenko, Y. Vladimirovna Magurova, *Application of oxide coatings to metals in electrolyte solutions by microplasma methods*, REVMETAL. 36 (2000) 323–330
- [26] T.W. Clyne, S.C. Troughton, *A review of recent work on discharge characteristics during plasma electrolytic oxidation of various metals*, Int. Mat. Rev. 64 (2019) 127–162
- [27] S.V. Gnedenkov, O.A. Khrisanova, A.G. Zavidnaya, S.L. Sinebrukhov, A.N. Kovryanov, T.M. Scorobogatova, P.S. Gordienko, *Production of hard and heat-resistant coatings on aluminium using a plasma micro-discharge*, Surf. Coat. Technol. 123 (2000) 24–28
- [28] J. Martin, P. Leone, A. Nominé, D. Veys-Renaux, G. Henrion, T. Belmonte, *Influence of electrolyte ageing on the Plasma Electrolytic Oxidation of aluminium*, Surf. Coat. Technol. 269 (2015) 36–46
- [29] R.O. Hussein, X. Nie, D.O. Northwood, *Influence of process parameters on electrolytic plasma discharging behaviour and aluminum oxide coating microstructure*, Surf. Coat. Technol. 205 (2010) 1659–1667
- [30] E.V. Parfenov, A. Yerokhin, A. Matthews, *Small signal frequency response studies for plasma electrolytic oxidation*, Surf. Coat. Technol. 203 (2009) 2896–2904
- [31] A.L. Yerokhin, A. Shatrov, V. Samsonov, P. Shashkov, A. Pilkington, A. Leyland, A. Matthews, *Oxide ceramic coatings on aluminium alloys produced by a pulsed bipolar plasma electrolytic oxidation process*, Surf. Coat. Technol. 199 (2005) 150–157.

- [32] L.O. Snizhko, A.L. Yerokhin, A. Pilkington, N.L. Gurevina, D.O. Misnyankin, A. Leyland, A. Matthews, *Anodic processes in plasma electrolytic oxidation of aluminium in alkaline solutions*, *Electrochim. Acta.* 49 (2004) 2085–2095
- [33] A. Nominé, A.V. Nominé, N.St.J. Braithwaite, T. Belmonte, G. Henrion, *High-Frequency-Induced Cathodic Breakdown during Plasma Electrolytic Oxidation*, *Physical Review Applied.* 8 (2017)
- [34] G.-H. Lv, H. Chen, W.-C. Gu, L. Li, E.-W. Niu, X.-H. Zhang, S.-Z. Yang, *Effects of current frequency on the structural characteristics and corrosion property of ceramic coatings formed on magnesium alloy by PEO technology*, *J. Mat. Proc. Technol.* 208 (2008) 9–13
- [35] A. Melhem, G. Henrion, T. Czerwiec, J.L. Briançon, T. Duchanoy, F. Brochard, T. Belmonte, *Changes induced by process parameters in oxide layers grown by the PEO process on Al alloys*, *Surface and Coatings Technology.* 205 (2011) S133–S136
- [36] X. Ma, C. Blawert, D. Höche, M.L. Zheludkevich, K.U. Kainer, *Investigation of electrode distance impact on PEO coating formation assisted by simulation*, *Appl. Surf. Sci.* 388 (2016) 304–312
- [37] V. Dehnavi, B.L. Luan, X.Y. Liu, D.W. Shoesmith, S. Rohani, *Correlation between plasma electrolytic oxidation treatment stages and coating microstructure on aluminum under unipolar pulsed DC mode*, *Surf. Coat. Technol.* 269 (2015) 91–99
- [38] J. Jovović, S. Stojadinović, N.M. Šišović, N. Konjević, *Spectroscopic study of plasma during electrolytic oxidation of magnesium- and aluminium-alloy*, *Journal of Quantitative Spectroscopy and Radiative Transfer.* 113 (2012) 1928–1937
- [39] Q.B. Li, C.C. Liu, W.B. Yang, J. Liang, *Growth mechanism and adhesion of PEO coatings on 2024Al alloy*, *Surface Engineering.* 33 (2017) 760–766
- [40] S. Stojadinović, R. Vasilić, M. Petković, Lj. Zeković, *Plasma electrolytic oxidation of titanium in heteropolytungstate acids*, *Surf. Coat. Technol.* 206 (2011) 575–581
- [41] E. Matykina, R. Arrabal, P. Skeldon, G.E. Thompson, *Transmission electron microscopy of coatings formed by plasma electrolytic oxidation of titanium*, *Acta Biomaterialia.* 5 (2009) 1356–1366
- [42] S. Stojadinović, J. Radić-Perić, R. Vasilić, M. Perić, *Spectroscopic Investigation of Direct Current (DC) Plasma Electrolytic Oxidation of Zirconium in Citric Acid*, *Appl. Spectrosc.* 68 (2014) 101–112
- [43] R.H.U. Khan, A. Yerokhin, X. Li, H. Dong, A. Matthews, *Surface characterisation of DC plasma electrolytic oxidation treated 6082 aluminium alloy: Effect of current density and electrolyte concentration*, *Surf. Coat. Technol.* 205 (2010) 1679–1688
- [44] K. Wang, B.-H. Koo, C.-G. Lee, Y.-J. Kim, S.-H. Lee, E. Byon, *Effects of electrolytes variation on formation of oxide layers of 6061 Al alloys by plasma electrolytic oxidation*, *Transactions of Nonferrous Metals Society of China.* 19 (2009) 866–870
- [45] K.R. Shin, Y.G. Ko, D.H. Shin, *Effect of electrolyte on surface properties of pure titanium coated by plasma electrolytic oxidation*, *Journal of Alloys and Compounds.* 509 (2011) S478–S481
- [46] M. Shokouhfar, C. Dehghanian, M. Montazeri, A. Baradaran, *Preparation of ceramic coating on Ti substrate by plasma electrolytic oxidation in different electrolytes and evaluation of its corrosion resistance: Part II*, *Applied Surface Science.* 258 (2012) 2416–2423

Bibliography

- [47] X. Lu, C. Blawert, K.U. Kainer, T. Zhang, F. Wang, M.L. Zheludkevich, *Influence of particle additions on corrosion and wear resistance of plasma electrolytic oxidation coatings on Mg alloy*, Surf. Coat. Technol. 352 (2018) 1–14
- [48] X. Lu, M. Mohedano, C. Blawert, E. Matykina, R. Arrabal, K.U. Kainer, M.L. Zheludkevich, *Plasma electrolytic oxidation coatings with particle additions – A review*, Surf. Coat. Technol. 307 (2016) 1165–1182
- [49] H. Duan, C. Yan, F. Wang, *Effect of electrolyte additives on performance of plasma electrolytic oxidation films formed on magnesium alloy AZ91D*, Electrochim. Acta. 52 (2007) 3785–3793
- [50] M. O'Hara, S.C. Troughton, R. Francis, T.W. Clyne, *The incorporation of particles suspended in the electrolyte into plasma electrolytic oxidation coatings on Ti and Al substrates*, Surf. Coat. Technol. 385 (2020) 125354
- [51] J. Michalska, M. Sowa, M. Piotrowska, M. Widziółek, G. Tylko, G. Dercz, R.P. Socha, A.M. Osyczka, W. Simka, *Incorporation of Ca ions into anodic oxide coatings on the Ti-13Nb-13Zr alloy by plasma electrolytic oxidation*, Materials Science and Engineering: C 104 (2019) 109957
- [52] S. Stojadinović, N. Tadić, N. Radić, B. Grbić, R. Vasilić, *CdS particles modified TiO₂ coatings formed by plasma electrolytic oxidation with enhanced photocatalytic activity*, Surf. Coat. Technol. 344 (2018) 528–533
- [53] J.-M. Wang, D.-S. Tsai, J.T.J. Tsai, C.-C. Chou, *Coloring the aluminum alloy surface in plasma electrolytic oxidation with the green pigment colloid*, Surf. Coat. Technol. 321 (2017) 164–170
- [54] Y. Chen, X. Lu, C. Blawert, M.L. Zheludkevich, T. Zhang, F. Wang, *Formation of self-lubricating PEO coating via in-situ incorporation of PTFE particles*, Surf. Coat. Technol. 337 (2018) 379–388
- [55] M. Mohedano, C. Blawert, M.L. Zheludkevich, *Silicate-based Plasma Electrolytic Oxidation (PEO) coatings with incorporated CeO₂ particles on AM50 magnesium alloy*, Materials & Design. 86 (2015) 735–744
- [56] D.V. Mashtalyar, S.V. Gnedenkov, S.L. Sinebryukhov, I.M. Imshinetskiy, A.V. Puz', *Plasma electrolytic oxidation of the magnesium alloy MA8 in electrolytes containing TiN nanoparticles*, J. Mat. Sci. & Technol. 33 (2017) 461–468
- [57] B.-S. Lou, Y.-Y. Lin, C.-M. Tseng, Y.-C. Lu, J.-G. Duh, J.-W. Lee, *Plasma electrolytic oxidation coatings on AZ31 magnesium alloys with Si₃N₄ nanoparticle additives*, Surf. Coat. Technol. 332 (2017) 358–367
- [58] E. Matykina, R. Arrabal, B. Mingo, M. Mohedano, A. Pardo, M.C. Merino, *In vitro corrosion performance of PEO coated Ti and Ti6Al4V used for dental and orthopaedic implants*, Surf. Coat. Technol. 307 (2016) 1255–1264
- [59] A.V. Timoshenko, Yu.V. Magurova, *Investigation of plasma electrolytic oxidation processes of magnesium alloy MA2-1 under pulse polarisation modes*, Surf. Coat. Technol. 199 (2005) 135–140
- [60] P. Bala Srinivasan, J. Liang, R.G. Balajee, C. Blawert, M. Störmer, W. Dietzel, *Effect of pulse frequency on the microstructure, phase composition and corrosion performance of a phosphate-based plasma electrolytic oxidation coated AM50 magnesium alloy*, Appl. Surf. Sci. 256 (2010) 3928–3935
- [61] X. Zhang, Y. Zhang, L. Chang, Z. Jiang, Z. Yao, X. Liu, *Effects of frequency on growth process of plasma electrolytic oxidation coating*, Mater. Chem. Phys. 132 (2012) 909–915

- [62] A.B. Rogov, A. Yerokhin, A. Matthews, *The role of cathodic current in plasma electrolytic oxidation of aluminum: Phenomenological concepts of the “soft sparking” mode*, *Langmuir* 33 (2017) 11059–11069
- [63] P. Lukes, M. Clupek, V. Babicky, P. Sunka, *The Role of Surface Chemistry at Ceramic/Electrolyte Interfaces in the Generation of Pulsed Corona Discharges in Water Using Porous Ceramic-Coated Rod Electrodes*, *Plasma Processes Polym.* 6 (2009) 719–728
- [64] Y. Cheng, F. Wu, E. Matykina, P. Skeldon, G.E. Thompson, *The influences of microdischarge types and silicate on the morphologies and phase compositions of plasma electrolytic oxidation coatings on Zircaloy-2*, *Corr. Sci.* 59 (2012) 307–315
- [65] E. Matykina, A. Berkani, P. Skeldon, G.E. Thompson, *Real-time imaging of coating growth during plasma electrolytic oxidation of titanium*, *Electrochim. Acta.* 53 (2007) 1987–1994
- [66] S. Stojadinović, J. Jovović, M. Petković, R. Vasilić, N. Konjević, *Spectroscopic and real-time imaging investigation of tantalum plasma electrolytic oxidation (PEO)*, *Surf. Coat. Technol.* 205 (2011) 5406–5413
- [67] J. Martin, A. Nominé, F. Brochard, J.-L. Briançon, C. Noël, T. Belmonte, T. Czerwicz, G. Henrion, *Delay in micro-discharges appearance during PEO of Al: Evidence of a mechanism of charge accumulation at the electrolyte/oxide interface*, *Appl. Surf. Sci.* 410 (2017) 29–41
- [68] R. Arrabal, E. Matykina, T. Hashimoto, P. Skeldon, G.E. Thompson, *Characterization of AC PEO coatings on magnesium alloys*, *Surf. Coat. Technol.* 203 (2009) 2207–2220
- [69] S.P. Sah, E. Tsuji, Y. Aoki, H. Habazaki, *Cathodic pulse breakdown of anodic films on aluminium in alkaline silicate electrolyte – Understanding the role of cathodic half-cycle in AC plasma electrolytic oxidation*, *Corr. Sci.* 55 (2011) 90–96
- [70] A. Melhem, *Oxydation par plasma électrolytique : influence des paramètres du procédé sur le comportement des micro-décharges et conséquences sur les couches d'oxyde*, Thesis, INPL, Nancy (2011)
- [71] C.S. Dunleavy, J.A. Curran, T.W. Clyne, *Time dependent statistics of plasma discharge parameters during bulk AC plasma electrolytic oxidation of aluminium*, *Appl. Surf. Sci.* 268 (2013) 397–409
- [72] S. Stojadinović, R. Vasilić, M. Petković, B. Kasalica, I. Belča, A. Žekić, Lj. Zeković, *Characterization of the plasma electrolytic oxidation of titanium in sodium metasilicate*, *Appl. Surf. Sci.* 265 (2013) 226–233
- [73] S. Stojadinović, M. Perić, J. Radić-Perić, R. Vasilić, M. Petković, Lj. Zeković, *Luminescence of the $B1\Sigma^+-X1\Sigma^+$ band system of MgO during plasma electrolytic oxidation of magnesium alloy*, *Surf. Coat. Technol.* 206 (2012) 2905–2913
- [74] S. Stojadinović, M. Perić, M. Petković, R. Vasilić, B. Kasalica, I. Belča, J. Radić-Perić, *Luminescence of the $B2\Sigma^+-X2\Sigma^+$ band system of AlO during plasma electrolytic oxidation of aluminum*, *Electrochim. Acta.* 56 (2011) 10122–10129
- [75] X. Yang, L. Chen, Y. Qu, R. Liu, K. Wei, W. Xue, *Optical emission spectroscopy of plasma electrolytic oxidation process on 7075 aluminum alloy*, *Surf. Coat. Technol.* 324 (2017) 18–25
- [76] R. Liu, J. Wu, W. Xue, Y. Qu, C. Yang, B. Wang, X. Wu, *Discharge behaviors during plasma electrolytic oxidation on aluminum alloy*, *Mater. Chem. Phys.* 148 (2014) 284–292
- [77] S. Stojadinovic, R. Vasilic, I. Belca, M. Petkovic, B. Kasalica, Z. Nedic, Lj. Zekovic, *Characterization of the plasma electrolytic oxidation of aluminium in sodium tungstate*, *Corr. Sci.* 52 (2010) 3258–3265

Bibliography

- [78] Y. Wu, Z. Yang, R. Wang, G. Wu, D. Chen, D. Wang, X. Liu, D. Li, C. Guo, S. Yu, D. Shen, P. Nash, *An investigation of microstructure evolution for plasma electrolytic oxidation (PEO) coated Al in an alkaline silicate electrolyte*, Surf. Coat. Technol. 351 (2018) 136–152
- [79] G. Sundararajan, L. Rama Krishna, *Mechanisms underlying the formation of thick alumina coatings through the MAO coating technology*, Surf. Coat. Technol. 167 (2003) 269–277
- [80] D.T. Asquith, A.L. Yerokhin, J.R. Yates, A. Matthews, *Effect of combined shot-peening and PEO treatment on fatigue life of 2024 Al alloy*, Thin Solid Films 515 (2006) 1187–1191
- [81] R.H.U. Khan, A.L. Yerokhin, T. Pilkington, A. Leyland, A. Matthews, *Residual stresses in plasma electrolytic oxidation coatings on Al alloy produced by pulsed unipolar current*, Surf. Coat. Technol. 200 (2005) 1580–1586
- [82] P. Bala Srinivasan, C. Blawert, W. Dietzel, *Effect of plasma electrolytic oxidation treatment on the corrosion and stress corrosion cracking behaviour of AM50 magnesium alloy*, Mater. Sci. Engin.: A. 494 (2008) 401–406
- [83] R.H.U. Khan, A.L. Yerokhin, A. Matthews, *Structural characteristics and residual stresses in oxide films produced on Ti by pulsed unipolar plasma electrolytic oxidation*, Philosophical Magazine. 88 (2008) 795–807
- [84] K.E. Tillous, *Contribution à l'étude de l'aluminium et ses alliages 2214-T6 et 7050-T74 transformés par oxydation micro-arcs (OMA)*, Thesis, INPL, Nancy (2006)
- [85] E. Matykina, R. Arrabal, P. Skeldon, G.E. Thompson, *Investigation of the growth processes of coatings formed by AC plasma electrolytic oxidation of aluminium*, Electrochim. Acta. 54 (2009) 6767–6778
- [86] J.-H. Lee, S.-J. Kim, *Effects of silicate ion concentration on the formation of ceramic oxide layers produced by plasma electrolytic oxidation on Al alloy*, Jpn. J. Appl. Phys. 56 (2017)
- [87] H. Kalkancı, S.C. Kurnaz, *The effect of process parameters on mullite-based plasma electrolytic oxide coatings*, Surf. Coat. Technol. 203 (2008) 15–22
- [88] J.A. Curran, T.W. Clyne, *The thermal conductivity of plasma electrolytic oxide coatings on aluminium and magnesium*, Surf. Coat. Technol. 199 (2005) 177–183
- [89] X. Zhang, S. Aliasghari, A. Němcová, T.L. Burnett, I. Kuběna, M. Šmíd, G.E. Thompson, P. Skeldon, P.J. Withers, *X-ray Computed Tomographic Investigation of the Porosity and Morphology of Plasma Electrolytic Oxidation Coatings*, ACS Appl. Mater. Interfaces. 8 (2016) 8801–8810
- [90] X. Yu, L. Chen, H. Qin, M. Wu, Z. Yan, *Formation process of in situ oxide coatings with high porosity using one-step plasma electrolytic oxidation*, Appl. Surf. Sci. 366 (2016) 432–438
- [91] J.A. Curran, T.W. Clyne, *Porosity in plasma electrolytic oxide coatings*, Acta Materialia. 54 (2006) 1985–1993
- [92] O.A. Galvis, D. Quintero, J.G. Castaño, H. Liu, G.E. Thompson, P. Skeldon, F. Echeverría, *Formation of grooved and porous coatings on titanium by plasma electrolytic oxidation in H₂SO₄/H₃PO₄ electrolytes and effects of coating morphology on adhesive bonding*, Surf. Coat. Technol. 269 (2015) 238–249
- [93] Y. Han, S.-H. Hong, K.W. Xu, *Porous nanocrystalline titania films by plasma electrolytic oxidation*, Surf. Coat. Technol. 154 (2002) 314–318
- [94] B.R. Locke, M. Sato, P. Sunka, M.R. Hoffmann, J.-S. Chang, *Electrohydraulic Discharge and Nonthermal Plasma for Water Treatment*, Ind. Eng. Chem. Res. 45 (2006) 882–905

- [95] P. Bruggeman, C. Leys, *Non-thermal plasmas in and in contact with liquids*, J. Phys. D: Appl. Phys. 42 (2009) 053001
- [96] A. Hamdan, F. Kosior, C. Noel, G. Henrion, J.-N. Audinot, T. Gries, T. Belmonte, *Plasma-surface interaction in heptane*, J. of Appl. Phys. 113 (2013) 213303
- [97] M.D. Klapkiv, *State of an electrolytic plasma in the process of synthesis of oxides based on aluminum*, Mater Sci. 31 (1996) 494–499
- [98] M.D. Klapkiv, *Simulation of synthesis of oxide-ceramic coatings in discharge channels of a metal-electrolyte system*, Materials Science. 35 (1999) 279–283.
- [99] L.R. Krishna, A.S. Purnima, N.P. Wasekar, G. Sundararajan, *Kinetics and Properties of Micro Arc Oxidation Coatings Deposited on Commercial Al Alloys*, Metall and Mat Trans A. 38 (2007) 370–378
- [100] E. Matykina, R. Arrabal, D.J. Scurr, A. Baron, P. Skeldon, G.E. Thompson, *Investigation of the mechanism of plasma electrolytic oxidation of aluminium using ^{18}O tracer*, Corrosion Science. 52 (2010) 1070–1076
- [101] R.O. Hussein, X. Nie, D.O. Northwood, *An investigation of ceramic coating growth mechanisms in plasma electrolytic oxidation (PEO) processing*, Electrochim. Acta. 112 (2013) 111–119
- [102] J. Jovović, S. Stojadinović, N.M. Šišović, N. Konjević, *Spectroscopic characterization of plasma during electrolytic oxidation (PEO) of aluminium*, Surf. Coat. Technol. 206 (2011) 24–28
- [103] V. Dehnavi, B.L. Luan, D.W. Shoesmith, X.Y. Liu, S. Rohani, *Effect of duty cycle and applied current frequency on plasma electrolytic oxidation (PEO) coating growth behavior*, Surf. Coat. Technol. 226 (2013) 100–107
- [104] Y. Cheng, Z. Xue, Q. Wang, X.-Q. Wu, E. Matykina, P. Skeldon, G.E. Thompson, *New findings on properties of plasma electrolytic oxidation coatings from study of an Al–Cu–Li alloy*, Electrochim. Acta. 107 (2013) 358–378
- [105] Y. Cheng, M. Mao, J. Cao, Z. Peng, *Plasma electrolytic oxidation of an Al-Cu-Li alloy in alkaline aluminate electrolytes: A competition between growth and dissolution for the initial ultra-thin films*, Electrochim. Acta. 138 (2014) 417–429
- [106] F. Jaspard, *Oxydation des alliages d'aluminium aéronautiques par plasma électrolytique: caractérisation optique du procédé et étude des cinétiques de croissance des couches*, Thesis, INPL, Nancy (2005)
- [107] A. Nominé, *Micro-décharges en milieu électrolytique aqueux et leur interaction avec les matériaux: le cas du procédé d'oxydation par plasma électrolytique (PEO)*, Thesis, Université de Lorraine, Nancy (2014)
- [108] A. Nominé, J. Martin, C. Noël, G. Henrion, T. Belmonte, I.V. Bardin, P. Lukeš, *Surface Charge at the Oxide/Electrolyte Interface: Toward Optimization of Electrolyte Composition for Treatment of Aluminum and Magnesium by Plasma Electrolytic Oxidation*, Langmuir. 32 (2016) 1405–1409
- [109] A. Nominé, J. Martin, G. Henrion, T. Belmonte, *Effect of cathodic micro-discharges on oxide growth during plasma electrolytic oxidation (PEO)*, Surf. Coat. Technol. 269 (2015) 131–137
- [110] V. Dehnavi, D.W. Shoesmith, B.L. Luan, M. Yari, X.Y. Liu, S. Rohani, *Corrosion properties of plasma electrolytic oxidation coatings on an aluminium alloy – The effect of the PEO process stage*, Mater. Chem. Phys. 161 (2015) 49–58

Bibliography

- [111] A. Ghasemi, V.S. Raja, C. Blawert, W. Dietzel, K.U. Kainer, *The role of anions in the formation and corrosion resistance of the plasma electrolytic oxidation coatings*, Surf. Coat. Technol. 204 (2010) 1469–1478
- [112] A. Polat, M. Makaraci, M. Usta, *Influence of sodium silicate concentration on structural and tribological properties of microarc oxidation coatings on 2017A aluminum alloy substrate*, J. of Alloys and Compounds. 504 (2010) 519–526
- [113] V. Dehnavi, X.Y. Liu, B.L. Luan, D.W. Shoesmith, S. Rohani, *Phase transformation in plasma electrolytic oxidation coatings on 6061 aluminum alloy*, Surf. Coat. Technol. 251 (2014) 106–114
- [114] W. Gębarowski, S. Pietrzyk, *Growth Characteristics of the Oxide Layer on Aluminium in the Process of Plasma Electrolytic Oxidation*, Arch. of Metallurgy and Materials. 59 (2014)
- [115] S. Ikonopisov, *Theory of electrical breakdown during formation of barrier anodic films*, Electrochim. Acta. 22 (1977) 1077–1082
- [116] I.D. Belca, L.D. Zekovic, B. Jovanic, G. Ristovski, L. Ristovski, *The theory of galvanoluminescence in the anodic oxide films obtained by aluminum anodization in ammonium tartrate*, Electrochim. Acta. 45 (2000) 4059–4063
- [117] B. Kasalica, I. Belča, S. Stojadinović, M. Sarvan, M. Perić, L. Zeković, *Nature of Galvanoluminescence of Oxide Films Formed by Aluminum Anodization in Inorganic Electrolytes*, J. Phys. Chem. C 111 (2007) 12315–12319
- [118] K. Shimizu, S. Tajima, *Theory of electroluminescence of Al/anodic alumina/electrolyte system*, Electrochim. Acta 24 (1979) 309–311
- [119] S. Stojadinovic, I. Belca, B. Kasalica, Lj. Zekovic, M. Tadic, *The galvanoluminescence spectra of barrier oxide films on aluminum formed in inorganic electrolytes*, Electrochem. Commun. 8 (2006) 1621–1624
- [120] S. Stojadinovic, M. Tadic, I. Belca, B. Kasalica, Lj. Zekovic, *The galvanoluminescence spectra of barrier oxide films on aluminum formed in organic electrolytes*, Electrochim. Acta 52 (2007) 7166–7170
- [121] S. Stojadinović, R. Vasilić, B. Kasalica, I. Belča, L. Zeković, *Luminescence During the Electrochemical Oxidation of Aluminum*, in: S.S. Djokić (Ed.), *Electrodeposition and Surface Finishing*, Springer (2014) 241–302
- [122] S. Tajima, K. Shimizu, N. Baba, S. Matsuzawa, *Nature of luminescence during galvanostatic anodizing of high purity aluminium*, Electrochim. Acta 22 (1977) 845–849
- [123] NIST "Atomic Spectra Database", (available online): <https://www.nist.gov/pml/atomic-spectra-database>
- [124] P.J. Bruggeman, N. Sadeghi, D.C. Schram, V. Linss, *Gas temperature determination from rotational lines in non-equilibrium plasmas: a review*, Plasma Sources Sci. Technol. 23 (2014) 023001
- [125] P. Bruggeman, D.C. Schram, M.G. Kong, C. Leys, *Is the Rotational Temperature of OH(A–X) for Discharges in and in Contact with Liquids a Good Diagnostic for Determining the Gas Temperature?*, Plasma Processes and Polymers. 6 (2009) 751–762
- [126] A. Rodero, M.C. García, *Gas temperature determination of non-thermal atmospheric plasmas from the collisional broadening of argon atomic emission lines*, Journal of Quantitative Spectroscopy and Radiative Transfer. 198 (2017) 93–103

- [127] H. Nassar, S. Pellerin, K. Musiol, O. Martinie, N. Pellerin, J.-M. Cormier, *N₂⁺/N₂ ratio and temperature measurements based on the first negative N₂⁺ and second positive N₂ overlapped molecular emission spectra*, J. Phys. D: Appl. Phys. 37 (2004) 1904–1916
- [128] M. Sarvan, J. Radić-Perić, B. Kasalica, I. Belča, S. Stojadinović, M. Perić, *Investigation of long-duration plasma electrolytic oxidation of aluminum by means of optical spectroscopy*, Surf. Coat. Technol. 254 (2014) 270–276
- [129] A. Descoedres, *Characterization of electrical discharge machining plasmas*, Thesis, EPFL, Lausanne (2006)
- [130] H. R. Griem, *Plasma spectroscopy*, New York: Mc Graw Hill (1964)
- [131] H.R. Griem, *Spectral line broadening by plasmas*, Academic Press, New York (1974)
- [132] C. Yubero, M.C. García, M.D. Calzada, *On the use of the H α spectral line to determine the electron density in a microwave (2.45GHz) plasma torch at atmospheric pressure*, Spectrochim. Acta Part B: Atomic Spectroscopy 61 (2006) 540–544
- [133] T. Shirai, H. Watanabe, M. Fuji, M. Takahashi, *Structural Properties and Surface Characteristics on Aluminum Oxide Powders*, Nagoya Ceramic Research Laboratory Annual Report, vol. 9 (2009) 23-31
- [134] A.I. Osman, J.K. Abu-Dahrieh, D.W. Rooney, S.A. Halawy, M.A. Mohamed, A. Abdelkader, *Effect of precursor on the performance of alumina for the dehydration of methanol to dimethyl ether*, Applied Catalysis B: Environmental. 127 (2012) 307–315
- [135] D.-S. Tsai, C.-C. Chou, *Review of the Soft Sparking Issues in Plasma Electrolytic Oxidation*, Metals. 8 (2018) 105
- [136] A. Nominé, S.C. Troughton, A.V. Nominé, G. Henrion, T.W. Clyne, *High speed video evidence for localised discharge cascades during plasma electrolytic oxidation*, Surf. Coat. Technol. 269 (2015) 125–130
- [137] D. Wang, X. Liu, Y. Wu, H. Han, Z. Yang, Y. Su, X. Zhang, G. Wu, D. Shen, *Evolution process of the plasma electrolytic oxidation (PEO) coating formed on aluminum in an alkaline sodium hexametaphosphate ((NaPO₃)₆) electrolyte*, J. Alloy Compd. 798 (2019) 129–143
- [138] M.F. Al-Kuhaili, *Characterization of copper oxide thin films deposited by the thermal evaporation of cuprous oxide (Cu₂O)*, Vacuum, 82 (2008) 623–629
- [139] E.M. Alkoy, P.J. Kelly, *The structure and properties of copper oxide and copper aluminium oxide coatings prepared by pulsed magnetron sputtering of powder targets*, Vacuum, 79 (2005) 221-230
- [140] M. Heinemann, B. Eifert, C. Heiliger, *Band structure and phase stability of the copper oxides Cu₂O, CuO, and Cu₄O₃*, Phys. Rev. B. 87 (2013) 115111
- [141] J.F. Pierson, A. Thobor-Keck, A. Billard, *Cuprite, paramelaconite and tenorite films deposited by reactive magnetron sputtering*, Appl. Surf. Sci. 210 (2003) 359–367
- [142] K. Santra, C.K. Sarkar, M.K. Mukherjee, B. Ghosh, *Copper oxide thin films grown by plasma evaporation method*, Thin Solid Films. 213 (1992) 226–229
- [143] Y. Wang, P. Miska, D. Pilloud, D. Horwat, F. Mücklich, J.F. Pierson, *Transmittance enhancement and optical band gap widening of Cu₂O thin films after air annealing*, J. Appl. Phys. 115 (2014) 073505
- [144] R.H. Doremus, *Ceramic and glass materials: structure, properties and processing*, Springer (2008).

Bibliography

- [145] W.K. Yeung, I.V. Sukhorukova, D.V. Shtansky, E.A. Levashov, I.Y. Zhitnyak, N.A. Gloushankova, P.V. Kiryukhantsev-Korneev, M.I. Petrzhik, A. Matthews, A. Yerokhin, *Characteristics and in vitro response of thin hydroxyapatite–titania films produced by plasma electrolytic oxidation of Ti alloys in electrolytes with particle additions*, RSC Adv. 6 (2016) 12688–12698
- [146] P. Bruggeman, D. Schram, M.Á. González, R. Rego, M.G. Kong, C. Leys, *Characterization of a direct dc-excited discharge in water by optical emission spectroscopy*, Plasma Sources Sci. Technol. 18 (2009) 025017
- [147] P. Bruggeman, T. Verreycken, M.Á. González, J.L. Walsh, M.G. Kong, C. Leys, D.C. Schram, *Optical emission spectroscopy as a diagnostic for plasmas in liquids: opportunities and pitfalls*, J. Phys. D: Appl. Phys. 43 (2010) 124005
- [148] T. Belmonte, C. Noël, T. Gries, J. Martin, G. Henrion, *Theoretical background of optical emission spectroscopy for analysis of atmospheric pressure plasmas*, Plasma Sources Sci. Technol. 24 (2015) 064003
- [149] S. Stojadinović, R. Vasilić, M. Perić, *Investigation of plasma electrolytic oxidation on valve metals by means of molecular spectroscopy – a review*, RSC Advances. 4 (2014) 25759
- [150] C.S. Dunleavy, J.A. Curran, T.W. Clyne, *Self-similar scaling of discharge events through PEO coatings on aluminium*, Surf. Coat. Technol. 206 (2011) 1051–1061
- [151] S.C. Troughton, A. Nominé, A.V. Nominé, G. Henrion, T.W. Clyne, *Synchronised electrical monitoring and high speed video of bubble growth associated with individual discharges during plasma electrolytic oxidation*, Appl. Surf. Sci. 359 (2015) 405–411
- [152] S.C. Troughton, A. Nominé, J. Dean, T.W. Clyne, *Effect of individual discharge cascades on the microstructure of plasma electrolytic oxidation coatings*, Appl. Surf. Sci. 389 (2016) 260–269
- [153] Ī.A. Aksey, J.A. Pask, *Stable and Metastable Equilibria in the System SiO₂-Al₂O₃*, J. Am. Ceram. Soc. 58 (1975) 507–512
- [154] S.H. Risbud, J.A. Pask, *Mullite Crystallization from SiO₂-Al₂O₃ Melts*, J. Am. Ceram. Soc. 61 (1978) 63–67
- [155] W.M. Kriven, J.A. Pask, *Solid Solution Range and Microstructures of Melt-Grown Mullite*, J. Am. Ceram. Soc. 66 (1983) 649–654
- [156] T. Takamori, R. Roy, *Rapid Crystallization of SiO₂-Al₂O₃ Glasses*, Journal of the American Ceram. Society. 56 (1973) 639–644
- [157] Y.-M. Chiang, W.D. Kingery, *Spinodal Decomposition in a K₂O-Al₂O₃-CaO-SiO₂ Glass*, J. Am. Ceram. Soc. 66 (1983) c171–c172
- [158] R. Rossin, J. Bensa, G. Urbain, *Viscosité de la silice fondue et de laitiers liquides appartenant au système SiO₂-Al₂O₃*, CR Acad. Sci. Paris 258 (1964) 562-564
- [159] E. Matykina, R. Arrabal, P. Skeldon, G.E. Thompson, *Optimisation of the plasma electrolytic oxidation process efficiency on aluminium*, Surf. Interface Anal. 42 (2009) 221–226
- [160] F. Tjiang, L.-W. Ye, Y.-J. Huang, C.-C. Chou, D.-S. Tsai, *Effect of processing parameters on soft regime behavior of plasma electrolytic oxidation of magnesium*, Ceram. Int. 43 (2017) S567–S572

- [161] Y. Cheng, J. Cao, Z. Peng, Q. Wang, E. Matykina, P. Skeldon, G.E. Thompson, *Wear-resistant coatings formed on Zircaloy-2 by plasma electrolytic oxidation in sodium aluminate electrolytes*, *Electrochim. Acta* 116 (2014) 453–466
- [162] Y. Cheng, J. Cao, M. Mao, H. Xie, P. Skeldon, *Key factors determining the development of two morphologies of plasma electrolytic coatings on an Al–Cu–Li alloy in aluminate electrolytes*, *Surf. Coat. Technol.* 291 (2016) 239–249
- [163] Y. Toriyabe, S. Watanabe, S. Yatsu, T. Shibayama, T. Mizuno, *Controlled formation of metallic nanoballs during plasma electrolysis*, *Appl. Phys. Lett.* 91 (2007) 041501
- [164] T.A. Kareem, A.A. Kaliani, *Glow discharge plasma electrolysis for nanoparticles synthesis*, *Ionics*. 18 (2012) 315–327
- [165] Y. Cheng, E. Matykina, P. Skeldon, G. Thompson, *Characterization of plasma electrolytic oxidation coatings on Zircaloy-4 formed in different electrolytes with AC current regime*, *Electrochim. Acta* 56 (2011) 8467–8476
- [166] R.O. Hussein, D.O. Northwood, X. Nie, *Coating growth behavior during the plasma electrolytic oxidation process*, *J. Vac. Sci. Technol. A* 28 (2010) 766–773
- [167] R.O. Hussein, D.O. Northwood, X. Nie, *The influence of pulse timing and current mode on the microstructure and corrosion behaviour of a plasma electrolytic oxidation (PEO) coated AM60B magnesium alloy*, *J. Alloy Compd.* 541 (2012) 41–48
- [168] J. Martin, A. Nominé, V. Ntomprougkidis, S. Migot, S. Bruyère, F. Soldera, T. Belmonte, G. Henrion, *Formation of a metastable nanostructured mullite during Plasma Electrolytic Oxidation of aluminium in “soft” regime condition*, *Materials & Design*. 180 (2019) 107977
- [169] J. Tian, Z. Luo, S. Qi, X. Sun, *Structure and antiwear behavior of micro-arc oxidized coatings on aluminum alloy*, *Surf. Coat. Technol.* 154 (2002) 1–7
- [170] X. Nie, E.I. Meletis, J.C. Jiang, A. Leyland, A.L. Yerokhin, A. Matthews, *Abrasive wear/corrosion properties and TEM analysis of Al₂O₃ coatings fabricated using plasma electrolysis*, *Surf. Coat. Technol.* (2002) 7
- [171] L. Rama Krishna, K.R.C. Somaraju, G. Sundararajan, *The tribological performance of ultra-hard ceramic composite coatings obtained through microarc oxidation*, *Surf. Coat. Technol.* 163–164 (2003) 484–490
- [172] S.V. Gnedenkov, O.A. Khrisanfova, A.G. Zavidnaya, S.L. Sinebrukhov, P.S. Gordienko, S. Iwatsubo, A. Matsui, *Composition and adhesion of protective coatings on aluminum*, *Surf. Coat. Technol.* 145 (2001) 146–151
- [173] V. Champagne, D. Helfritsch, *The unique abilities of cold spray deposition*, *Int. Mater. Rev.* 61 (2016) 437–455
- [174] A. Moridi, S.M. Hassani-Gangaraj, M. Guagliano, M. Dao, *Cold spray coating: review of material systems and future perspectives*, *Surf. Eng.* 30 (2014) 369–395
- [175] M.R. Rokni, S.R. Nutt, C.A. Widener, V.K. Champagne, R.H. Hrabe, *Review of Relationship Between Particle Deformation, Coating Microstructure, and Properties in High-Pressure Cold Spray*, *J. Therm. Spray Tech.* 26 (2017) 1308–1355
- [176] N. Shirai, S. Uchida, F. Tochikubo, *Synthesis of metal nanoparticles by dual plasma electrolysis using atmospheric dc glow discharge in contact with liquid*, *Jpn. J. Appl. Phys.* 53 (2014) 046202

Bibliography

- [177] T. Kaneko, K. Baba, T. Haraba, R. Hatakeyama, Novel Gas-Liquid Interfacial Plasmas for Synthesis of Metal Nanoparticles, *Plasma Process. Polym.* 6 (2009) 713-718
- [178] V.S. Burakov, E.A. Nevar, M.I. Nedel'ko, N.V. Tarasenko, *Synthesis and modification of molecular nanoparticles in electrical discharge plasma in liquids*, *Russ. J. Gen. Chem.* 85 (2015) 1222–1237

Towards a better understanding of the growth mechanisms within the PEO process by a deep investigation of the micro-discharge / metallic surface interaction.

Plasma electrolytic oxidation (PEO) is an electrochemical surface processing technique that allows the growth of protective oxide films on lightweight metals (Al, Ti, Mg). Contrary to conventional anodising, PEO operates at high current density and voltage which results in the ignition of micro-discharges (MDs) over the processed surface. The aim of this work was to investigate the characteristics of the MDs under different processing parameters and to correlate these characteristics with the microstructure of the produced oxide layers in order to better understand the oxide growth mechanisms. Firstly, PEO sequenced treatments were conducted by changing the electrical parameters in the course of a treatment. Results revealed a particular behaviour of the MDs which depends not only on the applied electrical parameters but also on the morphology of the growing layer. Results also evidenced an earlier transition to the beneficial “soft” sparking regime, contributing to a significant improvement of the microstructure of the oxide layer as well as process energy consumption. Time-resolved optical characterizations of the PEO process pointed out a correlation between ignition of MDs and the dynamic of the surrounding gas bubbles at the oxide / electrolyte interface. Particularly, results proved the existence of inner MDs during the “soft” sparking regime. Secondly, a multi-scale characterization of the typical “pancake” structure formed during the transition to the “soft” regime revealed the formation of a lamellar nanocomposite structure consisting of periodical alternations of alumina and metastable 1:1 mullite lamellae. Finally, two new opportunities for the PEO process were explored. The feasibility of duplex treatment involving cold-spray and PEO technologies was demonstrated and the possibility to produce metallic oxide (nano-) particles was proposed.

Keywords: Plasma electrolytic oxidation, Aluminium, Oxide coating, Micro-discharges

Etude de l'interaction micro-décharge/surface métallique pour une meilleure compréhension des mécanismes de croissance lors du procédé PEO

Le procédé d'oxydation par plasma électrolytique (PEO) un procédé électrochimique de traitement de surface permettant d'élaborer des couches d'oxydes protectrices à la surface d'alliages métalliques légers (Al, Ti, Mg). Contrairement aux procédés d'anodisation, le procédé PEO utilise une densité de courant et une tension élevées qui donnent lieu au développement de micro-décharges (MDs) sur la surface traitée. L'objectif de cette étude était d'étudier les caractéristiques de ces MDs sous différentes conditions opératoires et de les corrélérer avec la microstructure des couches d'oxyde élaborées, pour *in fine* mieux comprendre les mécanismes de croissance. Tout d'abord, des traitements PEO séquencés ont été menés en changeant certains paramètres électriques en cours de traitement. Les résultats ont révélés un comportement particulier des MDs qui dépend non seulement des conditions électriques appliquées mais aussi de la morphologie de la couche en croissance. Les résultats ont également mis en évidence une transition anticipée vers le régime bénéfique de décharges « soft » contribuant ainsi à une amélioration significative de la microstructure de la couche d'oxyde et de la consommation énergétique du procédé PEO. Des mesures optiques résolues en temps ont permis d'établir une corrélation entre le développement des MDs et la dynamique des bulles de gaz à l'interface oxyde / électrolyte. Particulièrement, les résultats ont prouvé l'existence de MDs internes à la couche lors du régime de croissance « soft ». De plus, une caractérisation multi-échelle de la structure dite en « pancake », structure typique du régime « soft », a révélé la formation d'une structure lamellaire nanocomposite. Elle consiste en une alternance de lamelles d'alumine pure avec des lamelles de mullite 1 :1 métastable. Enfin, deux études prospectives ont été conduites autour du procédé PEO. La faisabilité de réaliser des traitements duplex combinant les procédés cold spray et PEO a été démontrée ainsi que la possibilité de produire des (nano-) particules d'oxyde métallique via le procédé PEO.

Mots-clés : Oxydation par plasma électrolytique, Aluminium, Couche d'oxyde, Micro-décharges